Non-linear dynamic analysis of shallow foundations

By

ELPIDA KATSIVELI

Department of Civil Engineering
UNIVERSITY OF BRISTOL

A dissertation submitted to the University of Bristol in accordance with the requirements of the degree of DOCTOR OF PHILOSOPHY in the Faculty of Engineering, Department of Civil Engineering.

MARCH 14, 2019

Word count: 33478

“I know there’s only, only one like you
there’s no way I could have made two.
My first, my last, my everything. ”
adapted from Barry White, 1974

ABSTRACT

Footings subjected to dynamic loads are commonly designed under the simplifying assumption of linear or equivalent-linear viscoelastic soil behaviour. Even though this approach is simple to implement and, in some cases, could take advantage of available closed-form solutions, the outcomes remain a gross approximation - especially for high excitation amplitudes such as those induced by strong earthquakes.

Although considerable research has been conducted for the case of large footing vibrations, where uplift, slippage or other types of foundation failure may occur, there remains a research gap for small to medium strain amplitudes (levels of strain between 10^{-6} and 10^{-3}), for which the soil behaviour is also non-linear, but not close to failure. To address this problem, a numerical methodology is developed herein, for the analysis and design of shallow footings, while taking into consideration shear modulus degradation and hysteretic damping increase effects for the foundation subsoil.

Non-linearities such as hysteresis and rate dependence are the main characteristics of cyclic soil behaviour. These features prove the frequency domain analyses inadequate, and more computationally demanding time domain analyses, such as those conducted in this study, are more appropriate.

The analysis methodology is based on the implementation of two numerical models, namely the Ramberg-Osgood (RO) model and the Modified Hyperbolic model (MH), as user-defined models into the explicit finite-difference code FLAC. Focus is then given on a rigid strip surface foundation subjected to harmonic oscillations, and results are presented in terms of the variation of the dynamic impedance with the dimensionless frequency of excitation. In addition, results are provided for the corresponding three-dimensional problem of a square footing resting on the surface of a soil layer over rock.

Linear elastic static and elastodynamic available solutions are first revisited and comparisons are drawn against published results following a throughout parametric investigation. Vertical, horizontal and rocking oscillations are considered, with the excitation imposed in the form of an applied harmonic displacement or a rotation atop a rigid surface strip footing. Non-linear soil behaviour is then studied, and different excitation amplitudes are considered to explore the effects of soil non-linearity in terms of governing parameters such as dimensionless depth to rock, soil plasticity index, material damping, and Poisson's ratio. Strain rate effects are also examined. The analysis is then extended to three dimensions and comparisons are made between 2-dimensional and 3-dimensional response in all excitation modes. Results are presented in the form of

dimensionless equations, graphs and charts which are suitable for use in geotechnical engineering practice. A detailed discussion on the use of Rayleigh damping in problems of this type is provided.

Finally, a case study involving field tests in a test site in California is modelled and the predictions are compared to the experimentally obtained data.

To my sisters, Evi and Mata, wishing them too,
to fulfil their dreams

Acknowledgements

This dissertation would not be possible without an entire community of people who have helped me with their technical expertise, encouragement and personal support.

I have been privileged to work with highly talented and renowned in their fields researchers during my time in the University of Bristol. I would like to first thank Prof. George Mylonakis for believing in me and giving me the opportunity to embark in this venture. He provided an inexhaustible source of information and guided me throughout the process. Needless to say, his support has been important for the completion of this thesis and I am deeply grateful. In addition, I would like to thank Dr. Dimitris Karamitros for serving as my co-advisor, for the ideas he contributed and for his guidance into using FLAC and implementing new numerical models.

I would also like to thank Dr. Xenia Karatzia for running all ISOBEM analyses presented in Chapter 4 and Dr. Lisa M. Star for providing the experimental data-set used in Chapter 7. Additionally, Dr. Flavia de Luca for her support and for serving as my PhD reviewer and Dr. Paul Vardanega for his contribution to the conference paper regarding the strain rate effects.

My journey, would not have been the same without a big support of the people around me. I would like to thank all the people I met in Queen's building, especially in 1.80 office, who made feel like home especially in the long hours. Also, I am thankful for all the people I met in Bristol, spent my time with, enjoyed conversations and discussed ideas. Just to mention a few: Ioanna Taouki, Teresa Reis, Despina Stamou, Harris Paraskevoulakos, Gzregorz Bialowas and Danica Sugic. You all know what you mean to me, your moral support kept me going throughout these years especially in the hectic months before the completion.

Last but not least, I would like to thank my immediate family members, my mother Antonia, who I, literally, owe my life to, my dear sisters, Evangelia and Stamatina to whom I am dedicating this work, my beloved uncle Spiros who has always been a role model, and my beloved grandmother who I am named after. I love you all so much, and I am thankful to share this accomplishment with you.

Naturally, the author is grateful for the financial support from the Engineering and Physical Sciences Research Council (EPRSC) throughout the past four years.

Elpida Katsiveli
March 2019

AUTHOR'S DECLARATION

I declare that the work in this dissertation was carried out in accordance with the requirements of the University's Regulations and Code of Practice for Research Degree Programmes and that it has not been submitted for any other academic award. Except where indicated by specific reference in the text, the work is the candidate's own work. Work done in collaboration with, or with the assistance of, others, is indicated as such. Any views expressed in the dissertation are those of the author.

SIGNED: ..... DATE: .....

TABLE OF CONTENTS

List of Tables

List of Figures

Figure **Page**

NOMENCLATURE

Abbreviations

FLAC	Fast Lagrangian Analysis of Continua
GVDA	Garner Valley Downhole Array
MH	Modified Hyperbolic
MR	Modulus Reduction
NEESR	Network for Earthquake Engineering Simulations Research
NIST	National Institute of Standards and Technology
OCR	Over-Consolidated Ratio
PI	Plasticity Index
PSSR	Pseudo-shear Strain Rate
RO	Ramberg-Osgood
SASW	Spectral Analysis of Surface Waves
SSI	Soil Structure Interaction
SSR	Shear Strain Rate
STA	Static Adjustment
UCLA	University of California, Los Angeles
UCSB	University of California, Santa Barbara
UoB	University of Bristol

WLA	Wildlife Liquefaction Array

Greek characters

α	curvature parameter in Modified-Hyperbolic model
α_0	dimensionless frequency
α_γ	normalised secant shear modulus equals to G_s/G_{max} when shear stress is equal to τ_1 in Ramberg-Osgood model
α_{0_1}	natural dimensionless frequency
χ_{ij}	dimensionless parameter depending on the thickness of the soil layer and on Poisson's ratio
Δx	element size
δ_{ij}	Kronecker's symbol
γ	shear strain
γ_c	shear strain maximum absolute value
γ_r	pseudo-reference strain in Modified-Hyperbolic model
λ	Lame's parameter
ν	soil Poisson's ratio
ω	excitation angular frequency
ϕ_{1-5}	constants proposed by Darendeli
π	mathematical constant (= 3.14159265359)
ρ	mass density
τ	shear stress
τ_1	characteristic shear stress in Ramberg-Osgood model
τ_c	shear stress maximum absolute value
θ	rocking oscillations amplitude

ξ	damping ratio

Latin characters

$\bar{K}_h$	non-linear dynamic lateral stiffness
$\bar{K}_v$	non-linear dynamic vertical stiffness
$\bar{K}_{h,elastic}$	linear dynamic lateral stiffness
$\bar{K}_{rx,elastic}$	linear dynamic rocking stiffness
$\bar{K}_{rx}$	non-linear dynamic rocking stiffness
$\bar{K}_{v,elastic}$	linear dynamic vertical stiffness
A	contact area between foundation and soil
B	footing half-width
C_h	horizontal dashpot
C_{rx}	rocking dashpot
C_v	vertical dashpot
f_1	natural frequency
$F_{1,2}$	frequency-dependent displacement functions, dependant on Poisson's ratio according to Reissner
f_{min}	Rayleigh centre frequency
G	soil shear modulus
G_s	secant soil shear modulus
G_t	tangent soil shear modulus
G_{max}	initial (maximum) shear modulus
H	lateral load amplitude
H	soil layer thickness
i	imaginary number

I'	second moment of area about the central horizontal axis
I''	second moment of area about the central vertical axis
I_p	plasticity index
K	bulk modulus
k'_v	coefficients of soil reaction (units force per length cube) depending on soil type
K_h	static horizontal stiffness
K^*_h	dynamic horizontal stiffness
k_i	coefficients of soil reaction (units force per length cube) after Barkan [12]
K_v	static vertical stiffness
K^*_v	dynamic vertical stiffness
K_{rx}	static rocking stiffness
K^*_{rx}	dynamic rocking stiffness
$k_{v,h,rx}$	dynamic stiffness modification coefficient
l	wavelength
M	moment amplitude
N	number of elements per wavelength
P	load amplitude
R	radius of disc footing
s	distance of lateral boundaries from footing corner
s_{ij}	deviatoric stress
T	function of stress or strain, describes the hysteretic response, quantity needed to implement numerical models into FLAC
t	time

t_n	viscous normal tractions of dashpots involved in the non-reflective boundaries proposed by Lysmer and Kuhlemeyer
t_s	viscous shear tractions of dashpots involved in the non-reflective boundaries proposed by Lysmer and Kuhlemeyer
u	lateral oscillations amplitude
V	vertical load amplitude
v	vertical oscillations amplitude
V_c	compression velocity
V_p	P-wave velocity
V_s	shear wave velocity
V_{La}	Lysmer's analog velocity
w	positive parameter in Ramberg-Osgood model controlling shear modulus

CHAPTER 1

INTRODUCTION

In the *Introduction* a description of the problem targeted in this thesis is provided. Additionally, the objectives of the study are presented and the thesis outline is given as a brief description of the chapters to follow.

1.1 Formulation of the problem

The configuration examined is illustrated in 1.1 as a weightless strip footing of half-width B, resting on a soil stratum of thickness H, density ρ, shear wave velocity V_s, shear modulus $G = \rho V_s^2$, damping ratio ξ, and Poisson's ratio ν. The footing is subjected to lateral, vertical and rocking oscillations of amplitude u, v and θ, respectively, induced by a concentrated harmonic source of loading, as shown in Figures 1.2 (a), 1.3 (a) and 1.4 (a), respectively. Both the footing and the bedrock underlying the soil layer are assumed to be perfectly rigid, while the soil is modelled either as (i) a linear or (ii) a non-linear material.

For every response mode, the dynamic soil-foundation system can be analysed using a set of springs and dashpots, the characteristics of which are functions of the input excitation frequency, ω. This frequency dependence originates from the infinite dynamic degrees of freedom of the soil mass and the associated wave propagation phenomena, which are now condensed to a finite set of degrees of freedom atop the footing. The corresponding dynamic spring of stiffness $\bar{K}_{ij}$ and dashpot with coefficient C_{ij} [3] are illustrated in Figures 1.2 to 1.4. The subscript ij indicates the mode of excitation, namely

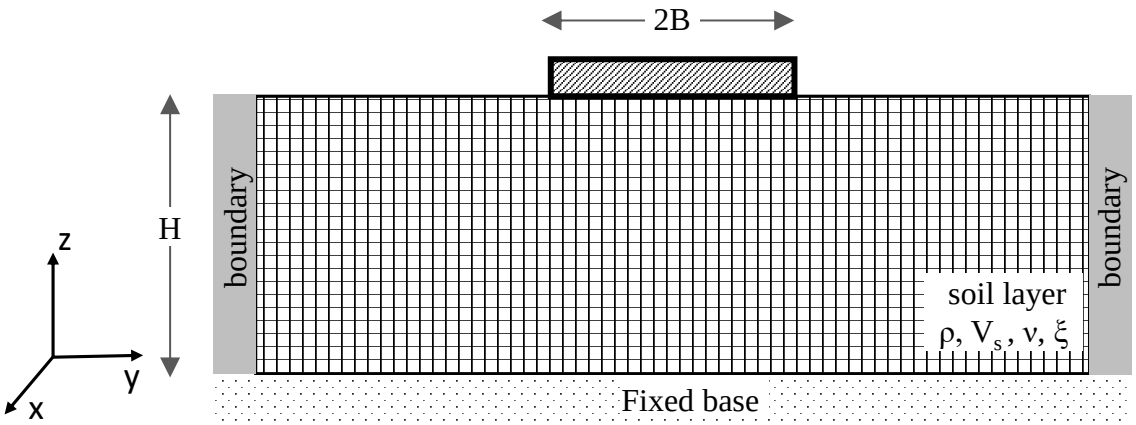

Figure 1.1: Problem description; massless, rigid footing resting on soil layer

hh (or simply *h* for non-embedded footings) for horizontal oscillations, *vv* (or *v*) for vertical and *rx* for rocking.

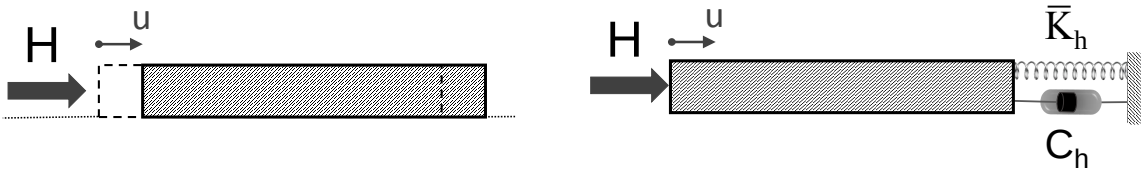

(a) (b)

Figure 1.2: (a) Rigid footing subjected to horizontal loading and (b) spring-dashpot analogue for horizontal oscillations (right)

When a footing is subjected to a harmonic lateral or vertical loading or moment, with amplitude F, V, or M, respectively, and frequency ω, a harmonic steady-state response occurs. In the linear regime, this response has the same frequency as the harmonic loading, but is not in phase. Using complex notation and for the lateral case, the above can be written as

$$F(t) = Fe^{i\omega t} \tag{1.1}$$

and

$$u(t) = ue^{i\omega t} \tag{1.2}$$

where F and u are vectors which are generally not in phase; considering F to be real valued, u in Equation 1.2 is typically complex. Therefore, the dynamic impedance can be

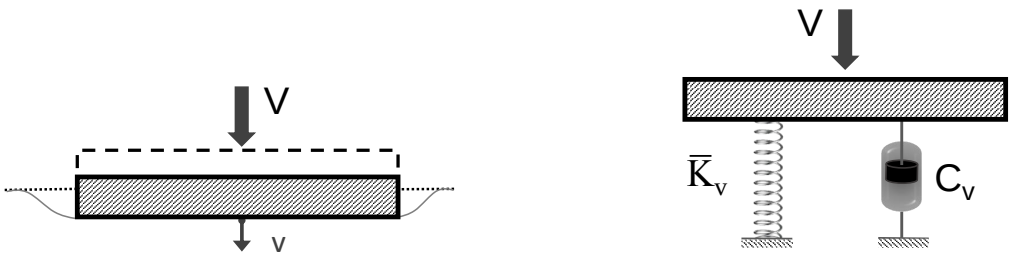

(a) (b)

Figure 1.3: (a) Footing subjected to vertical loading and (b) spring-dashpot analogue for vertical oscillations

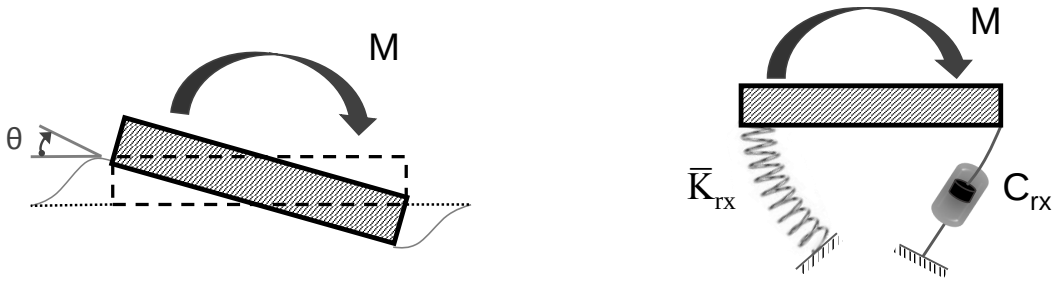

(a) (b)

Figure 1.4: (a) Footing subjected to moment and (b) spring-dashpot analogue for rocking oscillations

expressed in the following form

$$K_h^* \equiv \frac{F(t)}{u(t)} = \bar{K}_h + i\omega C_h \tag{1.3}$$

in which the complex exponents in Equations 1.1 and 1.2 cancel out from the numerator and the denominator. Note that this cancellation is not possible with ordinary trigonometric functions, which highlights the usefulness of using complex notation in the particular problem.

Alternatively, the impedance can be presented in terms of the damping ratio of the foundation, ξ

$$K_h^* = \bar{K}_h (1 + i2\xi) \tag{1.4}$$

where

$$\xi \equiv \frac{\omega C_h}{2\bar{K}_h} \tag{1.5}$$

A third possibility is to employ the loss angle , ψ, in the form

$$K_h^* = |K_h^*| e^{i\psi} \tag{1.6}$$

where

$$|K_h^*| = \sqrt{\bar{K}_h^2 + \omega^2 C_h^2} \tag{1.7}$$

and

$$\psi \equiv Arctan\left(\frac{\omega C_h}{\bar{K}_h}\right) \tag{1.8}$$

Note that special treatment is needed in the numerical analysis, to identify the relevant quarter plane of the unit vector $e^{i\psi}$ in equation 1.6.

Combining Equations 1.5 and 1.8 one can easily derive the expression

$$\psi = Arctan(2\xi) \tag{1.9}$$

The above expressions apply for all modes of excitation (translational and rotational with replacing force with moment and displacement with rotation).

In this study, the non-linear steady-state soil response is evaluated with the help of simple numerical models. The results are presented in terms of dynamic stiffness $\bar{K}_{ij}$ and damping ratio C_{ij} to facilitate use in engineering practice.

A case study is also examined to evaluate the experimental results of a real-scale SSI problem.

1.2 Practical application

The PhD research presented is applicable on the seismic assessment of inertial interaction of foundations, offshore foundation design and design of foundations subjected to machine vibrations typically in industrial buildings, for small to medium strains. Failure, defined as any change that can cause total or partial damage to the foundation such as uplifting, liquefaction, plasticity, is not considered in this study.

1.3 Research objectives and method

The principal objective of the work presented in this dissertation is to study the problem of shallow foundations accounting for the non-linear behaviour of the underlying soil. The objectives and methods that guided this research are:

- To implement available numerical constitutive models into finite difference code and investigate their capability to describe the soil non-linear behaviour.
- To calibrate the previously identified numerical models against available sets of experiments described in the form of modulus reduction curves and damping coefficient.
- To review available linear solutions to calculate impedance and expand the field of application to higher soil shear strains.
- To explore the applications of the calibrated numerical models to case studies and to calculate the non-linear impedances of foundations.
- To fit experimental data provided by full scale experiments to available numerical models and therefore numerical codes in order to gain a better insight into Soil-Structure Interaction (SSI) effects.

1.4 Thesis Outline

After the introduction chapter (i.e. this chapter), the thesis is composed by six main chapters, where the main novelties are presented, and a conclusive chapter wrapping up the main points of the research. The document is structured as follows:

Chapter 2 provides a review of available analytical, numerical and experimental research relevant to the topic of this dissertation. The Chapter is divided into two

main parts: in the first part a review of past analytical, empirical and experimental works and the parameters affecting the behaviour of soil under static and cyclic loading conditions, are presented. The second part reviews a number of numerical models to describe the non-linear soil behaviour under dynamic loading under small and medium strains. Specific attention is given to available experimental data in order to calibrate the models.

Chapter 3 describes the geotechnical numerical modelling software, FLAC by Itasca [13], in two and three dimensions which was employed to carry out the analyses in this study. An introduction to finite difference methodology and to time domain analysis is provided. Finally, the implementation of user defined numerical models into FLAC is presented.

Chapter 4 revisits available linear elastic solutions in the literature and provides the calibration of the finite difference mesh. Model parameters such as mesh dimensions, fixities and element size are investigated, and conclusions are drawn on the credibility of current design charts.

Chapter 5 presents an investigation of the effect of different governing parameters on the response of the footings investigated earlier. Two main parameter groups are studied: (a) Soil parameters including soil layer thickness, shear modulus, plasticity index (for clay), and Poisson's ratio. (b) Loading parameters associated with lateral, vertical and rocking oscillations.

Chapter 6 presents a brief verification of the 3D analysis by extending the 2D solutions to three dimensions. In addition, the elastic response of square footings is examined and comparisons are made with solutions available in the literature. Furthermore, the non-linear response on square foundations is investigated.

Chapter 7 includes comparative studies between numerical 3D analyses against experimental data. The experimental data used were collected under the auspices of the Network for Earthquake Engineering Simulations Research (NEESR) project which have been orchestrated by University of California, Los Angeles. The Chapter begins with a brief description of the sites and the structure tested and continues with a detailed presentation of the modelling procedure in three dimensions.

Chapter 8 summarises the main points of research alongside the key findings and the contribution of this study. The numerical methodology application is also included and recommended dimensionless design charts are presented. Finally, the limitations of this study are acknowledged and recommendations for further research are extended.

CHAPTER 2

LITERATURE REVIEW

This chapter presents a review of available analytical, numerical and experimental research relevant to the topic of this dissertation. The Chapter is divided into two main parts: in the first part a review of past analytical, empirical and experimental works, and the parameters affecting the behaviour of soil under static and cyclic loading conditions, are presented. The second part reviews a number of numerical models to describe the non-linear soil behaviour under dynamic loading in small and medium strains. Specific attention is given to available experimental data to calibrate the models.

2.1 Original Contributions

The literature review is divided in four main eras according to the time the research was undertaken and published and the equipment and mathematical tools available. In rough chronological order those can be named the *Empirical* era, the *Elastic Solutions* era, the *High Quality Experiments* era, and the *Computational Mechanics* era. Original contributions in the analysis and design of shallow foundations are described in the following four subsections.

2.1.1 Empirical era

The *Empirical* era encompasses all the early research conducted mainly in the pre-World-War-II Germany and the Soviet Union (Barkan [12]). The industrialisation of the western Europe created the need to explore foundation vibrations induced by machine operation and associated wave propagation in the foundation soil. The knowledge was mainly gained from experience and observation of industrial installations. Based on their performance and a sparse amount of experiments, application-specific empirical design charts and tables were produced. The results included mostly field measurements and data from simple experiment settings. Given the lack of theoretical models and proper normalisation schemes, this period will be referred to as the *Empirical* era. The most representative works have been contributed by Barkan [12, 14], Fry [15] and Margason et al [16], and they are discussed herein.

Barkan [12] studied foundations under dynamic loading induced by machine operation under the assumption of linearly elastic, or equivalently elastic soil behaviour. He collected and interpreted data from full-scale footings of industrial plants in the Soviet Union. Although he published his findings in 1948, his work only reached the Western world in 1962 when an English translation of his book became available [14]. By that time it was still the first guiding book in the field of machine vibrations and wave propagation for practising civil and mechanical engineers.

Barkan [12] based his research on a Winkler-type foundation system in which the supporting soil is replaced by a set of elastic springs. By fitting field measurements, Barkan provided a series of tables and empirical formulas to estimate the stiffness of the aforementioned springs for four main categories of soil ranging from weak soil to rocks.

Table 2.1: Spring constant expression for different modes of loading after Barkan [12, 14]

Mode of loading	Formulae	Correlation to k'_v
Vertical	$K_v = k'_v A$	k'_v
Horizontal	$K_h = k'_h A$	$k'_y \approx 0.5 k'_v$
Rocking	$K_{rx} = k'_{rx} I'$	$k'_{rx} \approx 2 k'_v$
Torsion	$K_t = k'_t I''$	$k'_t \approx 1.5 k'_v$

The expressions he proposed are summarised in Table 2.1 in which k'_i are coefficients of soil reaction (units force per length cube) depending on soil type given in Table 2.2. A is the contact area between the foundation and the soil, I' is the second moment of area

about the central horizontal axis and I'' is the second moment of area about the central vertical axis.

Table 2.2: Design values for k'_v coefficient converted to SI units after Barkan [12, 14]

Soil Type	Maximum static bearing capacity (kPa)	Subgrade reaction coefficient k'_z (MPa/m)
Weak soils	144	30
Soil of medium strength	144 - 335	30 - 50
Strong Soils	335 - 479	50 - 100
Rocks	479	100

His contribution was applicable to both translational and rotational modes of vibration. However, his work was only loosely based on elastodynamic theory and relied mainly on empiricism particularly with reference to the values of k'_i coefficients.

Fry [15] published a report with US Army Corps of Engineers in Waterways Experiment Station in their effort to design radar foundations. They presented data from steady state vibration experiments and highlighted the methodology to obtain them. They explored the case of rigid disc footings of various areas resting on two different soil types: silty clay and fine sand. The foundations were subjected to vertical, rocking and torsional forced sinusoidal vibrations which were generated by eccentric masses. The collected data were presented in tables at the same report without further interpretation.

Margason et al [16] published a study to validate the elastic halfspace theory against post-construction measurements. The study investigates five different vibrating foundations. The results are compared against predicted response based on available analytical formulae at the time (1960's). Two of the cases accounted for steady-state harmonic rocking loads, and another two for transient moment loads. The last case represented a passively isolated foundation slab undergoing a simple transient excitation test. They examined resonant amplitudes, geometric damping and frequency of maximum response. Margason et al [16] proved that the correlation between measured vibrations of full-scale industrial foundations and predicted vibrations is good. However, they highlighted unreliable results in torsional vibrations.

Even though many efforts have been made to study the effect of vibration on foundations response, the *Empirical* era is characterised by the lack of digital equipment to record and store the data and the limited understanding of soil behaviour. For those reasons, the data obtained before the 1990's have limited practical use today and should

be used with caution. The aforementioned problems have been overcome in the *High Quality Experiments* era.

2.1.2 Elastic solutions era

The elastic solutions era can be split into two main areas regarding the nature of the loading applied in foundation: static or dynamic.

2.1.2.1 Static elastic solutions

A brief summary of key contributions in chronological order is presented in Table 2.3.

The first problem to ever been tackled in geotechnical engineering is the point load acting within an elastic body of infinite extent. Lord Kelvin [17] gave the solution to this in spherical coordinates in 1848. Although it had little impact to researchers of that era, his solution is still used in the boundary element method.

Probably the most useful in geomechanics problem was solved some 30 years later in 1878 by Boussinesq. That is the problem of a static, vertical point load acting on the surface of a homogeneous elastic halfspace.The solution to the aforementioned problem was published in a series of brief papers [18–20]. Some years later, in 1885, Boussinesq [28] also provided an analytical closed-form solution for the case of a rigid circular footing resting on the surface of an elastic halfspace under the assumption of a smooth interface (disk being free to slip, not accounting shear tractions).

The more complicated problem of a horizontal point load acting at the surface of an elastic halfspace was first solved by Cerruti [21, 39]. The complexity of this problem stems from the lack of radial symmetry which leads to diffential equations in three spatial variables. Following Cerruti, Boussinesq managed to solve the same problem [28] and confirm Cerruti's solution without the latter knowing Cerruti's work.

A similar to Boussinesq's problem of a vertical point load on the surface of an elastic halfspace but acting at an infinitely long line rather than at a point was studied by Flamant [22]. Based on Boussinesq's solution and the principle of superposition, Flamant managed to calculate the stresses in the interior of the halfspace. His results presaged the idea of a pressure bulb and constitutes the first plane-strain solution where out-of plane strains and displacements are zero.

The more obscure problem of circular and rectangular loads has been treated by the mathematician Love [25] in 1929. Love provided solutions in terms of displacements and stress inside and on the surface of homogeneous, isotropic halfspace.

Table 2.3: Summary of some elastostatic solutions for footings and point loads.

Problem description	**Reference**	**Year**
Fullspace		
Point load	Kelvin [17]	1848
Homogeneous halfspace		
Vertical point load	Boussinesq [18–20]	1878
Horizontal point load	Cerruti [21]	1882
Line load	Flamant [22]	1892
Vertical disc and bell loads	Terazawa [23]	1916
Rectangular vertical loads	Schleicher [24]	1926
Disc and rectangular loads	Love [25]	1929
Vertical and Horizontal line loads inside halfspace	Melan [26]	1932
Vertical and Horizontal point loads inside halfspace	Mindlin [27]	1936
Disc on halfspace		
Vertical stiffness of disc	Boussinesq [28]	1885
Rocking stiffness of disc	Borowicka [29]	1943
Torsional stiffness of disc	Reissner & Sagoci [30]	1944
Horizontal stiffness of disc	Mindlin [31]	1949
Strip footing on halfspace		
Rocking stiffness of strip foundations	Muskhelishvili [32, 33]	1953
Homogeneous, elastic soil layers		
Rectangular loads in layer over rock	Steinbrenner [34]	1934
Vertical point load on layers over halfspace	Burmister [35]	1945
Non-homogeneous halfspace		
Rigid punch on non-homogeneous solid	Kassir [36]	1974
Point and line loads on non-homogeneous halfspace	Booker et al [37, 38]	1985

In 1932, Melan [26] took Flamant's research a step further and dealt with the problem of vertical and horizontal line loads acting anywhere in the elastic halfspace. Mindlin [27] solved the corresponding three-dimensional problem for point loads four years later, and provided closed-form expressions for the displacements (Green's functions).

Borowicka [29] studied, in 1943, the problem of eccentric vertical loads on circular and strip rigid footings. He derived analytical expressions for the vertical settlement and the stress distribution under the footing based on Boussinesq's published work. By using his expression one can derive the static rocking stiffness for smooth disc foundations given in Table 2.4. In the same paper he attempted to give the solution for the smooth strip footing resting on halfspace by integrating Boussinesq's solution. However, the formula was wrongly multiplied by Poisson's ratio squared hence the correct solution for the strip footing is credited to Muskhelishvili who derived it analytically some years later.

A significant step further was Burmister's et al [40] study on elastic layered systems. This study was followed by a more extensive sequel of papers by Burmister in 1945 [35, 41, 42]. His first studies regarded only the case of incompressible materials of Poisson's ratio, ν, equals to one half and under the assumption of a smooth interface between two elastic layers. In the last two publications, Burmister extended his solution for a rough interface between the layers in a three layered system and for arbitrary Poisson's ratio.

As part of a study of torsional oscillations of a disc resting on an elastic halfspace, Reissner and Sagoci [30] derived the torsional static stiffness of a disc. Following the theory of elasticity, they calculated the stresses and displacements on the surface and the interior of a homogeneous isotropic, elastic halfspace.

Almost seven decades after Cerruti, Mindlin [31] gave the first solution to swaying loads acting on cylindrical rigid foundations. Geotechnical engineers credit him the horizontal stiffness of discs resting on halfspace given in Table 2.4. With Mindlin's contibution the static stiffness of disc foundations resting on an elastic halfspace is complete.

A summary of the original analytical solutions for the stiffness of a rigid disc resting on a halfspace is tabulated in Table 2.4. It is worth noticing that the solutions with a disc resting on halfspace were published years after the respective solutions of problems with a point load acting directly at halfspace were determined.

For plane strain conditions, the stiffness per meter length (L) can be expressed as

$$\frac{K_{ij}}{2L} = \chi_{ij} \cdot GB^m \tag{2.1}$$

Table 2.4: Static stiffness of rigid disk resting on elastic halfspace

Loading Mode	**Expression**	**Reference**
Vertical	$K_v = \frac{4GR}{1-\nu}$	Boussinesq [28]
Rocking	$K_{rx} = \frac{\pi GR^3}{3(1-\nu)}$	Borowicka [29]
Torsion	$K_t = \frac{16GR^3}{3}$	Reissner & Sagoci [30]
Horizontal	$K_h = \frac{8GR}{2-\nu}$	Mindlin [31]

where ij is the index indicating the mode of loading; rx for rocking, $i = j = vv$ (or v) for vertical and $i = j = hh$ (or h) for swaying; χ_{ij} is a dimensionless parameter depending on the thickness of the soil layer and on Poisson's ratio, B is the half-width of the footing (equal to R for circular foundations) and m a pertinent exponent to match dimensions.

For the rocking mode of loading, ($ij = rx$), the stiffness is defined as the ratio of moment to the resulting rotation angle or

$$K_{rx} \equiv \frac{M}{\theta} \tag{2.2}$$

By dimensional arguments, m in Equation 2.1 is equal to 2. Moreover, χ_{rx} in Equation 2.1 has a finite value regardless of the thickness of the soil layer. Please note that the translational modes have zero static stiffness (i.e. $\chi_{vv} = \chi_{hh} = 0$) for halfspace conditions ($H \to \infty$) in Figure 1.1.

On the plane strain problem of a strip massless footing resting on halfspace, Muskhelishvili in 1953 [33] provided an analytical solution in the form of moment and rotation angle. He considered rocking loads and both smooth and rough interface between the strip foundations and the soil. His book was translated to English from Russian 10 years later, in 1963 and Poulos and Davis cited his work in their book in 1974 [43] by referencing the equations for infinite strip resting on halfspace ignoring traction (smooth interface)

$$\theta = \frac{(\chi+1)M}{2\pi GB^2} \tag{2.3}$$

and for the case of rough foundation

$$\theta = \frac{(\chi+1)M}{2\pi GB^2}\frac{1}{1+4\beta^2} \tag{2.4}$$

where

$$\chi = \frac{\lambda+3G}{\lambda+G} \tag{2.5}$$

$$\beta = \frac{\ln \chi}{2\pi} \tag{2.6}$$

and Lame's parameter

$$\lambda = \frac{2\nu}{1-2\nu} G \tag{2.7}$$

From the above one can easily derive the rocking stiffness assuming a smooth foundation-soil interface which is widely used today

$$K_{rx} \equiv \frac{M}{\theta} = \frac{\pi}{2} \frac{GB^2}{(1-\nu)} \tag{2.8}$$

and for the case of a rough interface

$$K_{rx} = \frac{\pi}{2} \frac{GB^2}{(1-\nu)} \left[1 + \left(\frac{\ln(3-4\nu)}{\pi} \right)^2 \right] \tag{2.9}$$

The stiffnesses from Equations 2.8 and 2.9 are plotted in Figure 2.1 and compared for increasing values of Poisson's ratio. It is evident that the foundation is stiffer when the interface between the soil and the footing is rough and for Poisson's ratio under 0.4. For Poisson's ratio equal to 0.5, (incompressible soil) the soil-foundation interface conditions do not influence the stiffness of rocking footings.

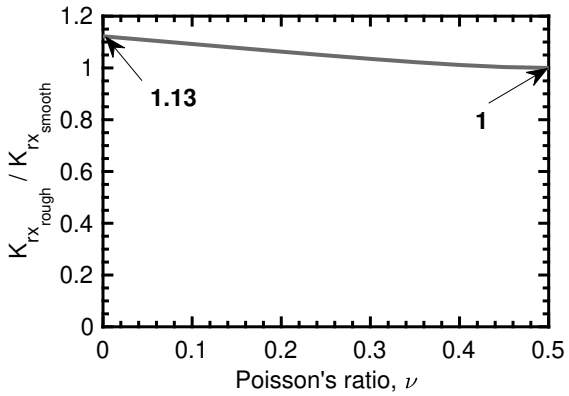

Figure 2.1: Influence of Poisson's ratio on the static rocking stiffness and the foundation soil interface

The stiffness of strip footings resting on halfspace is finite for the rocking mode of loading. For the translational modes of loading the static stiffness is zero, while the torsional stiffness is undefined.

It is worth mentioning that Eason et al [44] followed by Hanson and Puja [45] solved the integrals and provided the necessary tools to treat the case of horizontal disc loads and provide analytical solution.

Until the study of Kassir and Chuaprasert [36], the elastic solutions addressed only the case of homogeneous soil layers or a halfspace. Kassir and Chuaprasert explored the axisymmetric problem of a rigid punch in contact with a non-homogeneous elastic isotropic solid. The shear modulus is taken as a function of depth and Poisson's ratio is kept constant.

Following, Booker et al [37, 38] looked into non-homogeneous soil material, an elastic material in which the elastic modulus with depth but for constant Poisson's ratio, ν, equal to one third. The elastic modulus is given in the form of $E(z) = C \cdot z^{\alpha}$, where C is a constant and α is the non-homogeneity parameter. For α equal to 1 the elastic modulus is increasing linearly with depth, for α greater than zero but smaller than 1 the modulus is changing exponentially with depth while for α equal to zero the soil is considered homogeneous. They solved the problem for point and line loads, and subsequently extended it to strip and circular footings.

The aforementioned early elastic solutions are described extensively in a number of books e.g. [46–48] and a recent review article by Kausel [49].

2.1.2.2 Elastodynamic solutions

While static stiffness seem to have been adequately explored almost seven decades ago, the dynamic corresponding problem has been studied to a much lesser extent. This section provides an overview of the contributions in the field of soil dynamics in shallow foundations. A summary of some elastodynamic solutions is given in Table 2.5.

The problem of point forces varying with time in an boundless medium was solved by Sir George Gabriel Stokes in 1849 [50]. Stokes solution treated both the case of time-harmonic forces and the case of static forces. This solution established the base of the Boundary Element Method and influenced the field of SSI. Stokes solution was also implemented in geophysics and acoustics. An important peculiarity of the Stokes solution is that it is a closed-form throughout space in both time and frequency domains. It is the dynamic counterpart to Kelvin's problem.

The first attempt to describe the vibrations of a homogeneous, elastic halfspace is credited to Lamb [51]. Lamb formulated the classical problem of horizontal and vertical concentrated loads applied onto the surface of an elastic halfspace, often referred to as the dynamic Boussinesq problem. The basis of the "elasto-dynamic" theory was formed by

Table 2.5: Summary of some elastodynamic solutions for point loads and footings.

Problem description	**Reference**	**Year**
Fullspace		
Point forces varying with time	Stokes [50]	1849
Vibrations of a homogeneous elastic halfspace		
Description of the problem of horizontal and vertical vibrations on halfspace	Lamb [51]	1904
Vertical oscillations ($\nu = 0.25$)	Pekeris [52]	1955
Horizontal oscillations ($\nu = 0.25$)	Chao [53]	1960
Vertical oscillations for arbitrary ν	Mooney [54]	1974
Complete solution to Lamb's problem	Richards [55]	1979
Review	Kausel [56]	2012
Massless disc vibrations on halfspace		
Vertical vibrations of disc (uniform stress distribution)	Reissner [57]	1936
Vertical vibrations of disc (rigid-base stress distribution)	Quinlan [58]	1953
Vertical vibrations of disc (parabolic stress distribution)	Sung [59]	1953
Single degree of freedom system representation	Hsieh [60]	1962
Vertical oscillations of a rigid disc	Lysmer [61]	1968
Torsional vibrations on flexible foundations	Reissner [62]	1937
Torsional vibrations on rigid foundations	Reissner & Sagoci [30]	1944
Rocking oscillations of disc footings	Bycroft [63]	1956
Overview	Richart [64]	1962

Lamb's problem. Although, his approach was used in seismology and geophysics, Lamb provided the first analytical solution for a point load acting on an elastic halfspace in terms of displacements and stresses.

Solutions to the Lamb's problem were provided more than half a century after the original publication, by Pekeris [52] and Chao [53]. Both Pekeris and Chao produced closed-form expressions for the displacements evoked by a vertical and a horizontal load, respectively. However, their expressions are only valid for Poisson's ratio, ν, equal to 0.25. For the vertical case of loading, Mooney [54] extended Pekeris solution to account for different Poisson's ratios. Finally, Richards [55] provided the complete solution to Lamb's problem in terms of displacements on the surface of the halfspace and along the vertical axis under the load, for both loading modes and for any value of Poisson ratio. A compact set of exact formulae is provided in Kausel [56] using Laplace transforms.

2.1.2.3 Massless rigid footing resting on halfspace

Moving from the problem of loads acting inside a medium or on the surface of a halfspace, and in increasing level of complexity, the problem of a massless rigid footing resting on the halfspace is examined. This family of problems maintains its simplicity due to the axisymmetry, yet, they are much harder to solve as they involve mixed boundary conditions expressed in terms of both stresses and displacements.

The first to contribute is Reissner [57] who derived an analytical solution for vertical vibrations of a massless circular disc resting on an elastic halfspace. By that time, the German society of soil mechanics (DEGEBO) started to use mechanical oscillators to measure soil properties in situ. Influenced by these advancements, Reissner studied the dynamic response of a vibrating footing, and provided an analytical solution for the periodic vertical displacement at the centre of the footing, and established expressions for the amplitude of oscillator motion. In order to simplify the mixed boundary value problem, he considered the contact pressure distribution between soil and footing to be uniform. He also considered a perfectly elastic soil medium (no material damping). Reissner casted his solution for the vertical displacement in the form:

$$v = \frac{V}{GR} \cdot (F_1 + iF_2) \cdot \exp i\omega t \tag{2.10}$$

where V is the amplitude of the total force applied on the disc, ω the excitation angular frequency, G the shear modulus of the halfspace, R the radius of the disc and F_1, F_2 the frequency-dependent displacement functions that also depend on Poisson's ratio.

However, Reissner's results could not predict the dynamic response of footings in field experiments. Both parties can be held responsible for this disagreement: the experiments at the time were violating the assumed conditions (harmonic loading and elastic medium) while Reissner 's solution was problematic (an error was later found in the calculations [59] and the assumption of uniform contact pressure was not realistic). Although his study was based on unrealistic simplifications, Reissner set the foundations of the use of elastic halfspace theory in foundation dynamic problems and formed the base for further analytical studies in footing vibrations. Last but not least, Reissner introduced the familiar dimensionless frequency factor, $a_0 \equiv 2\pi f R/V_s$ which is widely used today in dynamic design charts. It can be determined as the amount of dimensionless time the shear wave travels a distance of $2\pi R$.

Following Reissner's publication, Quinlan [58] and Sung [59] extended the solution to account for the effect of changes in pressure distribution on the contact area. They studied three contact pressure distributions: uniform, parabolic and the distribution corresponding to a rigid base. Quinlan developed an approximate solution for the rigid base distribution while Sung presented solutions for all three cases in terms of displacement at the centre of the disc footing. The response curves are only important on a qualitative manner and provide insight in the influence of contact pressure distribution on the response of vibrating system. They do not capture the amplitude of the motion but the trend is very similar. Additionally, they described the damping in the system through one of Reissner's displacement function.

Almost a decade after Quinlan's and Sung's work, Hsieh [60] reorganised and simplified Reissner's solution, in the general form of the damped single degree of freedom system as shown in Eqs. 2.11.

$$V = C_v \frac{dv}{dt} + K_v v \tag{2.11}$$

where

$$C_v = \frac{R^3}{a_0}\sqrt{G\rho}\left(\frac{-f_2}{f_1^2+f_2^2}\right) \tag{2.12}$$

and

$$K_v = GR\frac{f_1}{f_1^2+f_2^2} \tag{2.13}$$

where V is the vertical force and C_v, K_v, are the corresponding dashpot and spring, respectively.

The main difference of the spring term and the damping term between a damped single-degree-of-freedom system and Hsieh's solution is that in the latter both the terms are a function of the excitation frequency (i.e. frequency dependant stiffness and damping). In the same study, Hsieh investigated and described the damping and stiffness functions for rocking, horizontal, and torsional oscillations.

Not long after, Lysmer [61] contributed an approximate solution for the case of a rigid circular footing subjected to dynamic vertical motion. In his study, a disc footing is assumed to consist of a series of concentric rings. Each ring carries a uniform pressure of a different magnitude than its adjacent ring resulting to a constant deflection under the footing. Following this simplification, Lysmer calculated the dynamic response of a footing when subjected to harmonic loading. Additionally, he developed response curves for a constant force and the rotating mass excitation.

Lysmer's research was significant to the scientific world because he established the connection between the elastic halfspace theory and the mass-spring-dashpot system, and contributed values for the damping and spring coefficients.

Following the advancements in vertical response of footing vibrations, torsional oscillations got in spotlight. Reissner [62] and Reissner & Sagoci [30] presented analytical solutions considering a surface circular footing resting on elastic halfspace. First, Reissner assumed a linear increase in shearing stress starting from zero at the centre of the disc and extending to a maximum value at the periphery. In the second study, Reissner and Sagoci, assumed a linear increase of the displacement from the centre of the disc to the edge. This setup reproduces a rigid circular footing vibrating vertically through its centre.

There are three main differences in the response of the footing when subjected to vertical and torsional oscillations: the torsional response is not sensitive to the value of Poisson's ratio, torsion is an uncoupled motion that can be studied independently, and the energy is dissipated in the form of elastic shear waves while in the case of vertical vibrations compressional and surface Rayleigh waves are additionally developed. Moreover, the radiation damping is significantly lower [65].

Switching our attention to rocking oscillations, Bycroft [63] contributed analytical solutions. He found that rocking of a rigid circular footing resting on an elastic halfspace produces an unrealistically high vertical stress under the edge of the footing that soils cannot sustain. That is because the the ideal elastic medium is stiffer than a soil support with the identical shear modulus and elasticity theory produces singularities at corners/edges of footings. He commented that the actual maximum rotation amplitude is

greater than what he proposed and the frequency at the maximum amplitude is lower.

The use of the aforementioned elastic halfspace theories for analysis and design of vibrating footings has been described by Richart [64] and Hsieh [66]. Since then, a considerable amount of research has been devoted on footings under dynamic loading, caused by both earthquakes and machine operation. A summary of early and more recent contributions has been presented by Kausel in [49] and [56] and in Mylonakis et al [3] and NIST [67], respectively.

2.1.3 High Quality Experiments era

The beginning of the *High Quality Experiments* era can be traced in the 1970's following the formulation of unverified theoretical and numerical solutions available to be tested. Experimental testing is vital for the verification and implementation of the suggested modelling methods. The beginning of this era is marked with the publication of a concise review of foundation vibrations solutions by Richart, Hall and Woods [47]. In addition, data acquisition equipment was evolved to provide reliable readings.

The *High Quality Experiments* era is characterised by carefully designed laboratory and field tests in contrast with the previous era, in which most of the data obtained were post-construction measurements (usually presented in a non-normalised form). Dimensionless graphs were widely introduced in the 1970's making the experiments relevant to a wider range of structures. The conclusions drawn from this era provide an advancement in soil-structure interaction (SSI) knowledge.

Experimental verification with the purpose to assess the foundation impedance functions, that are the stiffness and damping characteristics of footing problems can be split in two categories: 1. full or medium scale foundations tested in the field and 2. scaled laboratory models.

The advantage of laboratory models is the full control of the soil properties and the boundary conditions. However, free-field boundary conditions cannot be reliably reproduced. As a result, radiation damping does not exist due to the wave reflections on the walls of the container. Generally, laboratory models are preferred to investigate non-linear soil-structure interaction effects.

In contrast, in the full scale field testing the soil is tested in situ offering realistic boundary conditions. However, because of the presence of the water the results can be deceiving. Another problem with field testing is the uncertainty in the measurement of the shear wave velocity. Although it is common practice to use geophysical methods to

determine the shear wave velocity, the resolution is limited near the ground surface. In addition, seismic velocities neglect confinement resulted by the weight of the structure.

A brief summary of the existing field and lab experiments in the literature is given in Tables 2.6 and 2.7, respectively. A concise description follows.

Novak [68, 69] and Beredugo and Novak [70] conducted a series of small- and large-scale field experiments on vibrating foundations in the 1970's following the findings of Fry [15] in Waterways Experiment Station. The field experiments were conducted on a deep deposit of silt (loess loam). Square pads made of steel (surface) and concrete (embedded) with an area ranging from 0.5 to 1.5 m^2 and mass ranging between 1 to 4 tonnes, were examined. The foundation pads were subjected to horizontal, vertical and torsional harmonic oscillations produced either by an unbalanced mass or a mechanical, Lazan, vibrator.

The results were presented in the form of displacement amplitude versus excitation frequency, in absolute units. A decrease in resonance frequency with excitation intensity was observed and the variation of the undamped natural frequency with displacement amplitude was produced, which reflects non-linearity of the restoring forces. That is an important finding because it explains the inaccuracy of theoretical predictions when experiments are evaluated and compared against theory. A 20 to 25% difference in stiffness of rigid footings was observed.

More than a decade later, Novak published a review [71] of the experiments and made comparisons with theoretical predictions using the halfspace theory. He noticed a reduction in resonance frequency with increasing excitation intensity as well as a variation of undamped natural frequency with amplitude.

The study found that the experimental results were in good agreement with the halfspace theory for the case of horizontal and rocking oscillations. For vertical and torsional response the experimental results were poorly predicted. More specifically, in vertical oscillations the measured stiffness was almost twice as high as the computed one, but the trend was similar. Also, the predicted damping was twice as large as the measured damping. The disagreement in results was attributed to redistribution of stresses in the soil and in poor judgement of the soil layering.

Switching our attention to torsional response, the results are very different from theory. Specifically, the measured natural frequency was found to be half of the calculated counterpart, and theory overpredicts the resonant amplitudes.

Table 2.6: Summary of field experiments reported in literature since 1970

Shape	**Dimensions**	**Soil Description**	**Excitation**	**Motion analysed**	**Reference**	**Year**
square	$0.7m$ to $1.25m$	silt	harmonic Lazan oscillator	horizontal rocking vertical torsion	Novak, Beredugo [68–71]	1970
square	3m	alluvium with boulders $V_s = 305m/s$	shaker on the ground	horizontal rocking	Lin & Jennings [72]	1984
square	25m	medium dense sands and gravel $V_s = 300m/s$	shaker on roof	horizontal rocking	Luco & Wong [73]	1988
square rectangular	$1.3m \times 1.3m$ $1.2m \times 1.1m$	$V_s = 120m/s$ $V_s = 75m/s$	shaker on foundation	horizontal rocking	Crouse et al [74]	1990
circular	D=10.8m	$V_s = 300$	shaker on roof & foundation	vertical rocking horizontal	De Barros & Luco [75]	1995
square	4.1m	$V_s = 198m/s$	shaker on roof	horizontal rocking	Tileylioglu et al [76]	2011
rectangular	$4.28m \times 2.13m$	soft soil $V_s = 100m/s$ sandy silt $V_s = 190m/s$	shaker on roof & foundation	vertical horizontal rocking	Star et al [77]	2015

Table 2.7: Summary of lab experiments reported in literature

Shape	Dimensions	Soil Description	Excitation	Motion analysed	Reference	Year
square rectangular circular	$0.11m \times 0.26m$	moist sand	suddenly released static force	vertical torsion rocking horizontal	Erden, Stokoe, Dobry [78–80]	1974
square	$0.04m$	dry Nevada sand	centrifuge passive/active force	vertical torsion rocking horizontal	Gadre & Dobry [81]	1998
rectangular	$0.4m \times 0.95m$	coarse Leighton sand	shaking table	rocking vertical horizontal	Maugeri et al [82]	2000
circular	$D = 0.03m$	saturated dense sand	sinusoidal cyclic force	rocking vertical horizontal	Ghosh & Madabhushi [83]	2007
rectangular	$0.03m \times 0.14m$	Nevada sand	cyclic force base shaking	rocking	Gajan & Kutter [84]	2008
rectangular	$4.28m \times 2.13m$	rigid base lab floor	forced vibration on roof	n/a	Star et al [77]	2015

The differences caused due to the slippage between the footing and the soil, a phenomenon which is ignored in the elastodynamic theory.

Subsequently, Erden [78] ran over twenty small laboratory experiments considering surface and embedded foundations at various depths to investigate the influence of shape and embedment in dynamic response as part of his PhD thesis at the University of Texas at Austin. The study was later completed in 1985 with over thirty new experiments [79]. All the aforementioned experiments took place in a cylindrical container with both a depth and radius of $1.5m$. The container was filled with homogeneous, moist, dense sand surrounded by a thin layer ($0.305m$ deep) sawdust to model homogeneous halfspace and avoid reflection of waves emitted from the footing vibrating. Circular, square and rectangular foundations with aspect ratio up to 6 were investigated. The footings underwent steady-state and transient vertical, torsional and coupled swaying-rocking loads.

The contact surface area was around $0.07m^2$ and the height of the test footings was $0.46m$. The shear wave velocity was measured at $85m/s$ on the surface and $107m/s$ at a depth greater than $0.3m$. Static forces were applied on the pad and subsequently they were suddenly released to result in a free-vibration. The response was monitored through velocity transducers.

The outcomes were later discussed in Dobry et al [85] in an effort to experimentally evaluate the halfspace analytical method to predict the dynamic response of arbitrarily shaped foundations. This study identified a high level of agreement with associated discrepancies ranging between 10 to 15% on the natural frequencies of the footings, 10% on damping ratios in vertical vibrations and 15 to 20% in torsional. The increase in radiation damping for long footings predicted in theory was confirmed. Although, the damping was originally suggested to be 2%, it was assumed to be 2.5% for fitting purposes. Overall, the study is a validation of the halfspace theory. The measured damping ratios were similar to material damping. However, in circular, square and rectangular (long direction) footings the observed response was half of the predicted. This discrepancy can be attributed to wave reflections at the boundaries for lateral and rocking loading. This issue can be mitigated if only the first few loading cycles (before the reflected waves influence the response) are taken into consideration in the calculations.

Some years later, Gazetas and Stokoe [86] compared the aforementioned study against algebraic formulae and dimensionless charts reported in [7]. A good agreement was found for the damped natural frequencies for vertical and swaying-rocking oscillations. The agreement for radiation damping was not as encouraging but it was explained

by unpredicted reflections of the waves at the container walls and the interface between sand and sawdust.

Another field experiment was conducted by Lin and Jennings [72] who tested an one-story ($3m$ high) model structure supported on square foundations embedded from 0 to $1.5m$ deep. The footings were subjected to vertical and horizontal forced vibrations. The vibrations were produced by a shaker on the ground for a limited range of frequencies, between 7 to 70 Hertz. Horizontal and rocking impedances were presented and discussed in comparison to theoretical values. They found a very good agreement in terms of the horizontal and rocking impedances for the surface footings between their result and values obtained from analytical solutions. Nevertheless, the embedment factors that were found experimentally were, overall, higher than predicted.

Luco et al and Wong et al [73, 87, 88] investigated horizontal and rocking vibrations of large ($25m \times 25m$) embedded square footings. The tests were specifically designed to isolate the effects of soil-structure interaction. To achieve this, a nine-storey reinforced concrete building was analysed. They concluded that about one third of the total movement of the roof is accounted in the rigid-body motion associated with translation and rocking of the foundation during forced vibration tests. Additionally, they found that the inertial forces developed by translation and rocking of the footing caused almost the entire deformation of the superstructure at the fundamental frequencies.

Almost simultaneously, Crouse et al [89, 90] conducted field experiments to investigate the effect of coupling stiffness terms on the calculation of rocking and swaying stiffness. The experiments took place in South Carolina at an accelerograph station on a stiff clayey to medium sandy silt soil layer with a shear wave velocity of $150m/s$. The test foundation was a rectangular concrete pad with dimensions $1.2m \cdot 1.2m \cdot 0.6m$, partially embedded. An eccentric mass shaker was used to produce unidirectional harmonic forces. The excitation frequency ranged from 5 to 50 Hz.

To test the effect of off-diagonal stiffness terms, two settings are needed: horizontal loading over the centre of gravity and vertical loading away from the centre of gravity (rotational forces). The results were produced in terms of real and imaginary impedance parts for swaying and rocking versus frequency and were presented graphically in absolute units.

The rocking and lateral impedances were computed in three different ways taking into consideration the results of (A) the first, (B) the second experiment or (C) both the experiments. In the first two cases the computation of stiffness is possible only if the cross coupling terms are assumed to be zero. In the third case, the off-diagonal terms

are taken into account but were not computed in that research according to [89, 90] (remained unknown).

They found that between cases A, B, C the discrepancies were generally less than 25%. However, for the case of lateral stiffness and for excitation frequencies less than $30Hz$ the difference of the results computed accounting the second experiment (B) exceeded that by far. A possible explanation could be that the pad's motion at low frequencies was minimal, thus the recordings are not to be trusted. Another observation is the negative damping observed in the case of rocking for excitation frequencies less than $50Hz$. This can only be explained as an experimental error in phase measurements and not as a real phenomenon. To this end, those results were ignored.

The study concluded that the influence of the off-diagonal terms is minimal and can be ignored in the computation of rocking and lateral foundation stiffness. However, these experiments can only be relevant to similar structures and excitation frequencies as the results are presented in absolute units and generalised conclusions cannot be supported. If the coupling terms are ignored, one experiment is enough to compute both the rocking and the lateral stiffness. From this study it is shown that the first experiment is more appropriate for that, and large lateral forces and moments could be applied simultaneously.

In another experiment series at CDMG and USGS accelerograph stations Crouse and Hushmand [91] publish experimental findings. During the experiment, square and rectangular concrete foundations were subjected to forced-harmonic vibrations. The soil underlay consisted of moderately stiff alluvial deposits and soft deposits whose soil stiffness varies with depth. The excitation frequencies range from 0 to $60Hz$. A year after Crouse et al [74] discuss the findings and compare them with theory. In comparison, the halfspace theory overestimates the shear wave velocity.

De Barros and Luco [75] studied circular foundations of around $5m$ radius subjected to forced vibrations by a shaker, either fixed on the roof or on the foundation. They studied a large model structure of a nuclear reactor for a wide range of frequencies from 2 to 20 Hz. However, due to the high uncertainty in the value of shear modulus and shear wave velocity of the soil, dimensionless graphs were not produced.

Maugeri et al [82] published experimental results on the non-linear soil-structure interaction under seismic loads. The experiments were conducted at the Earthquake Engineering Research Centre Laboratory (EERC) at the University of Bristol using a 6-axis shaking table and a flexible container. Experiments performed on a surface footing resting on a dry coarse Leighton Buzzard sand. The footing was subjected to a vertical

eccentric load (to produce moments) and to a sinusoidal acceleration disseminated from the shaking table. The dynamic response of both the soil and the foundation has been monitored and later discussed by Massimino et al in [92]. The results were later used for modelling purposes by Paolucci [93].

Moreover, Tileylioglu et al [76] tested a large-scale, squared foundation structure resting on silty sand. The bedrock has been found at a depth of more than forty (40) times the halfwidth of the foundation. Thus it was assumed that the footing is resting on a layered halfspace. The structure was subjected to low-amplitude forced vibrations for a frequency range from 5 to 15 Hz. The vibrations emanate by a uni-axial shaker fixed at the top slab of the structure. In that study, frequency dependent horizontal and rocking impedances were obtained. The results are in satisfactory agreement with the available numerical models for surface foundation lying on a halfspace in terms of stiffness, but stronger damping was evident.

A recent experimental investigation was carried out by researchers at the University of California at Los Angeles (UCLA) under the auspices of the Network for Earthquake Engineering Simulations Research (NEESR) project. The experiment consisted of a simple structure, subjected to vibrations by four sources. A linear mass shaker provided small-amplitude vibrations while being attached either at the roof or at the base slab (foundation level) in both translational directions (x and y) and some accidental torsion as well. An eccentric mass shaker, attached on the roof level provided larger-amplitude vibrations in x and y direction. Vibroseis vehicle, a shaker truck, shook the ground at a distance of 20 m from the test structure. In addition to the aforementioned sources, natural earthquakes (free-field data) were recorded. The collected data include accelerations, displacements and soil-foundation contact pressures. The examined structure consists of a 4.28 m by 2.13 m reinforced concrete foundation and a top slap connected by steel columns with the option to be configured with braces. The structure was constructed and tested in two different field sites. The two field sites are characterised by shear-wave velocities of 95 m/s (very soft clays and silts) and 190 m/s (medium dense sands), respectively. The same structure without the foundation mat tied directly to the floor has been constructed and tested in the UCLA Structural Engineering Laboratory to simulate fixed-base condition. A detailed description of the experiment is given by Star et al [77] followed by an evaluation from system identification of structures [94]. The specific experiment is further discussed and modelled in Chapter 7.

2.1.4 Computational Mechanics era

The *Computational Mechanics era* begins with the advancements in the computational equipment and the development of the finite difference, finite element, and boundary element methods. Due to the machine restricted capabilities resulting in large computational time, in the early period of the specific era (mid 1960's to mid 1990's), early results are based on a limited number of elements. Available results include simple footing geometries (strip and circular footings) resting on elastic, homogeneous strata.

With the progress in computational mechanics, advanced numerical schemes and constitutive models began to appear, including the case of sands. Most of the research in the modern *Computational Mechanics era* is focused on the behaviour after yielding ("plastic flow"). Phenomena such as liquefaction of saturated sand, uplifting and overturning have been thoroughly studied. There seems to be a research gap on the soil behaviour from small to medium shear strains.

In rough chronological order Luco and Westmann [9, 95], Gazetas [2, 65, 96], Wong and Luco [97], Jakub and Roesset [98], Pais and Kausel [1], Wolf [99–101] have contributed results – including closed-form expressions for stiffness calculations.

2.1.4.1 Linear response

In the early 1970's Luco and Westmann [95] presented a study about circular foundations resting on an elastic halfspace under dynamic loads produced by machine operation. Dynamic compliances were plotted versus dimensionless frequency. All four loading cases were examined, torsion, rocking, vertical and horizontal loads, independently, but also the coupling terms between the horizontal and rocking oscillations were considered, and numerical results have been published. The stress distributions under the circular footing and the corresponding compliances were evaluated.

A year after, Luco and Westmann [9] studied the equivalent two-dimensional problem of evaluating the response of a surface rigid strip footing resting on an elastic halfspace. The footing is subjected to vertical, lateral, and rocking harmonic forces. The footing is perfectly bonded to the halfspace (rough interface). Singular integral equations theory was used to reduce the problem to the numerical solution of two integral Fredholm equations. The problem was solved for Poisson's ratio equal to 0.5 (incompressible material). They also presented approximate results for other Poisson's ratios. The results of this study were compared with the corresponding results of a smooth interface between the footing and the halfspace. They showed that the differences in the soil-foundation

interface affect impedances mostly for the vertical and the rocking loading case and for small Poisson's ratios.

The first numerical code, SHAKE, was developed in the 1970's to model dynamic soil behaviour and to compute linear response of oscillating footings. SHAKE, introduced by Schnabel et al in 1972 [102], is based on one-dimensional wave propagation solutions produced by Kanai [103], Roesset and Whitman [104], and Tsai and Housner [105]. SHAKE uses an equivalent linear method to simulate dynamic soil behaviour of horizontally layered strata subjected to vertically propagating shear waves. A recent application of SHAKE to study the problem of free-field non-linearities has been discussed in Gerolymos et al [106].

Wong and Luco [97] presented a numerical procedure to evaluate the harmonic compliance functions for an arbitrary-shaped rigid footing resting on an elastic halfspace. Vertical, rocking and horizontal modes were considered to act on a rigid rectangular foundations. In addition a rigid hollow square foundation subjected to vertical oscillations was investigated. The results were compared with available studies at the time and they concluded that the common assumption of a uniform stress distribution on the footing-soil interface as well as the evaluation of the displacements solely at the centre of the foundation results in higher foundation compliances. Additionally, they found that the hollow vertical compliance of a square footing is similar to the compliance of a solid square footing.

Novak [107] solved the plane strain problem of an infinitely long cylinder using a linear viscoelastic analytical approach and provided closed-form solutions. He defines a soil reaction approach to harmonic motion of the embedded cylindrical footing and includes material damping in his solution. He studied the problem of lateral, vertical, rocking and torsional loading. The footing rests on a homogeneous, isotropic, infinite soil with frequency independent material damping (hysteretic). Separation is ignored. The problem accounted only the case of small displacements due to harmonic vibrations. The results are presented in the form of stiffness and damping charts versus dimensionless frequency. Novak found that material damping reduces stiffness and increases total damping. Also, material damping is particularly significant in torsional and rotational modes at low frequencies. Moreover, it should not be ignored as the results could be unrealistic for low values of damping. For Poisson's ratio greater than 0.45 the horizontal stiffness can decrease at low frequencies and even become negative. This phenomenon is caused because the force and the displacement can attain more than 90° phase difference and this can be more significant in the presence of material damping.

Some years later, Gazetas [96] presented a semi-analytical procedure to estimate the static and dynamic compliance of surface rigid strip footings subjected to harmonic loads and moments placed on horizontal soil layers. The layers considered to be homogeneous and cross-anisotropic. Gazetas based his solution on an experimentally established relationship as a function of the parameters of an anisotropic soil. His solution is taking into account the boundary conditions at the layer interfaces and the surface. He presented a broad parametric investigation in compliance plots versus the dimensionless frequency introduced by Reissner [57]. Simple but approximate formulae were also given for resonant frequency factors and static displacements . He concluded that soil anisotropy is key on the evaluation of static and dynamic stiffness. In addition, he found that cross-anisotropic soils result in lower static displacements and dissimilar dynamic compliances compared to isotropic deposits.

Not long after, Gazetas [65] published a review of the state-of-the-art regarding the analysis of foundations subjected to dynamic loads produced be machine operation. Arbitrary shaped surface and embedded footings were analysed, including circular, strip and rectangular foundations. The footings were placed either on soil layer over halfspace, or the halfspace or on soil layer over halfspace. In the same publication, the effect of commonly used dimensionless parameters associated with soil properties and foundation geometry is thoroughly examined. Fitted formulas for the evaluation of static stiffness were given and dynamic impedance components were shown in dimensionless plots. The effects of soil in-homogeneity, non-linearity and anisotropy were briefly discussed. Gazetas extended this study later and provided more dimensionless graphs in [2, 7]. His publication [7] has been later experimentally supported in the companion paper by Gazetas and Stokoe [86] with reference to Erden experimental data [78].

In 1988, Pais and Kausel [1] studied the static stiffness of rigid rectangular footings resting on the surface of a halfspace. The cases of vertical, horizontal, rocking and torsional static and dynamic loads were investigated. Some year later, Gazetas [2] studied the same problem and proposed slightly altered fitted formulas. The aforementioned formulas were later revisited by Mylonakis et al [3]. The proposed elastic static solutions for vertical, lateral and rocking modes of loading and for the case of square footings are given in Table 2.8. The corresponding dynamic stiffness and radiation damping formulas are shown in Tabel 2.9

There are several ways to calculate the dynamic stiffness for footings subjected to dynamic loading. The selection of the appropriate way or program depends on the following three parameters: footing shape, type of soil, foundation type (surface, embedded

Table 2.8: Solutions for elastic static stiffness of rigid square footings resting on the surface of a halfspace (adapted from Pais and Kausel [1], Gazetas [2] and Mylonakis et al [3]).

Mode of Loading	Pais and Kausel [1]	Gazetas [2], Mylonakis et al [3]
Vertical	$K_{v,elastic} = \frac{4.7\ GB}{1-\nu}$	$K_{v,elastic} = \frac{4.54\ GB}{1-\nu}$
Horizontal	$K_{h,elastic} = \frac{9.2\ GB}{2-\nu}$	$K_{h,elastic} = \frac{9\ GB}{2-\nu}$
Rocking	$K_{rx,elastic} = \frac{4\ GB^3}{1-\nu}$	$K_{rx,elastic} = \frac{3.6\ GB^3}{1-\nu}$

Table 2.9: Elastic solutions for dynamic impedance componennt, stiffness and radiation damping, of rigid square footings resting on the ground surface (adapted from Pais and Kausel [1]).

Mode of Loading	Stiffness	Radiation damping
Vertical	$k_{v,elastic} = 1 - \left(\frac{0.6\alpha_0^2}{10+\alpha_0^2}\right)$	$\xi_m = \frac{4\psi}{K_{v,elastic}/GB}\left(\frac{\alpha_0}{2k_{v,elastic}}\right)$
Horizontal	$k_{h,elastic} = 1$	$\xi_m = \frac{4}{K_{h,elastic}/GB}\left(\frac{\alpha_0}{2}\right)$
Rocking	$k_{rx,elastic} = 1 - \frac{0.55\alpha_0^2}{2+\alpha_0^2}$	$\xi_m = \left[\frac{(4\psi/3)\cdot\alpha_0^2}{K_{rx,elastic}/GB^3\cdot(1.8+\alpha_0^2)}\right]\left(\frac{\alpha_0}{2k_{rx,elastic}}\right)$

or deep). There are numerous closed-form expressions and graphs available to determine the footing stiffness. Equations 2.14 , 2.15, 2.16 show some of those expressions used to calculate the vertical, lateral and rocking static stiffness of shallow foundations, respectively, as found in literature [2].

$$\frac{K_v}{2L} \simeq \frac{0.73G}{1-\nu}\left(1+3.5\frac{B}{H}\right) \tag{2.14}$$

$$\frac{K_h}{2L} \simeq \frac{2G}{2-\nu}\left(1+2\frac{B}{H}\right) \tag{2.15}$$

$$\frac{K_{rx}}{2L} \simeq \frac{\pi GB^2}{2(1-\nu)}\left(1+0.2\frac{B}{H}\right) \tag{2.16}$$

The graphs in Figure 2.2 were published by Gazetas [2], and are restated in Mylonakis et al [3], to calculate dynamic stiffness for surface foundation subjected to lateral and

vertical dynamic loading.

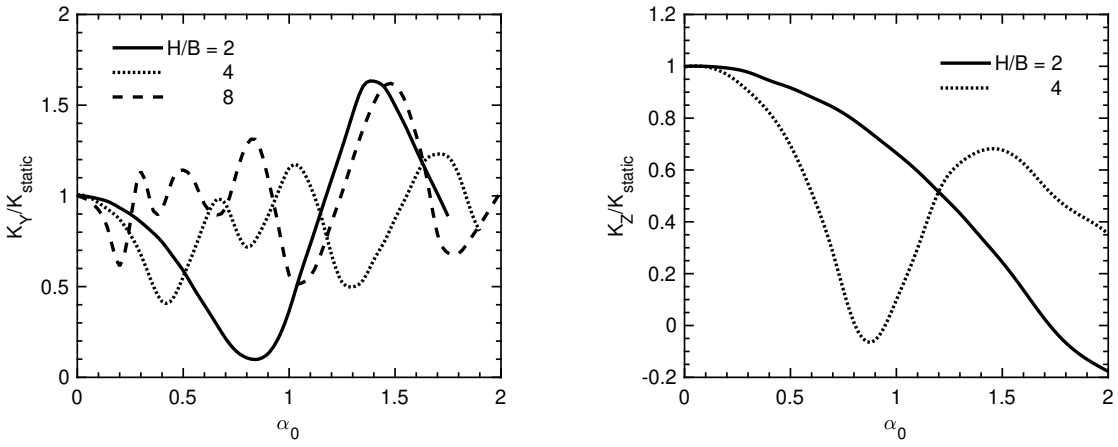

(a) (b)

Figure 2.2: Dynamic stiffness for rigid surface foundations on homogeneous stratum over bedrock ((a) Lateral, h and (b) Vertical, v – right). Reproduced from Gazetas [2]

where:

$$\alpha_0 = \frac{\omega B}{V_s} \tag{2.17}$$

is the familiar dimensionless excitation frequency introduced by Reissner [57], ω being the cyclic excitation frequency and V_s the shear wave propagation velocity of the soil layer. This expresses the ratio of the footing width to the imposed wavelength.

In the same publications an expression to calculate dynamic stiffness for surface foundation ("dynamic stiffness modifier") subjected to rocking dynamic loading is given as:

$$\bar{K}_{rx}/K_{rx} = 1 - 0.2\alpha_0 \tag{2.18}$$

More recently, Mylonakis et al [3] reviewed kinematic and inertial interaction effects associated with seismic soil-foundation-structure interaction. During earthquake shaking, travelling seismic waves cause soil deformations. These imposed displacements are transferred towards the foundation and consequently to the main structure. Inertial forces are generated by the induced motion resulting in dynamic stresses on the foundation and then on, the underlying and surrounding soil. As a result, deformations induced by the superstructure develop in the soil. The above phenomena evolve in a repeated mode while foundation and superstructure undergo further dynamic displacements.

In presence of earthquake action, soil-structure interaction can be divided into two discrete yet concurent phenomena: inertial and kinematic interaction. Soil displacements which are caused by earthquake ground motion away from the foundation are known as free-field motion. The associated foundation motion (particularly in presence of stiff foundations and embedment) does not fully match with free-field motion, which causes scattering of the incident waves known as kinematic interaction. Besides, further displacements are imposed in the ground as a result of inertial forces transmitted from the superstructure. This process is known as inertial interaction.

Kinematic effect is more dominant at low levels of ground shaking causing a reduction in foundation motion and the development of a rotational component. Nevertheless, when stronger shaking commences and due to soil modulus degradation and gaping effects, the radiation damping is limited. Inertial interaction becomes prevailing resulting in big strains and displacements concentrated near the surface as described by Wolf [99].

Wolf [99] formulated the basic equation of motion in time domain to analyse the soil-structure interaction. He focused on the problem of rigid disc placed on an elastic halfspace and provided flexibility coefficients using a cone model. Material damping is also accounted by means of a three-parameter Kelvin-Voigt model. He found that for frequency close to infinity the flexibility is zero.

Some years later, Meek and Wolf [108, 109] focused on the dynamic response of a strip footing placed on a uniform soil layer over bedrock. They employed a modified cone model theory in the time domain to calculate the translational and rotational stiffness. The cutoff frequency is also captured.

A year after, Wolf and Meek [101] implemented the modified cone model to approximate the dynamic stiffness of a circular footing resting on the surface of a soil layer over flexible bedrock. The methodology was similar to the aforementioned case of a layer over rigid bedrock performed in the time domain, but with altered wave reflection parameter. This cone accounted for the reflection at the free surface and the reflection-refraction at the interface between the soil layer and the bedrock. They provided results for the static stiffness for a broad range of soil and rock properties. In addition they found a satisfactory agreement between the the cone model calculations and exact solution is satisfactory in terms of dynamic stiffness.

Anastasopoulos et al [110] used a two-parametric modified version of Armstrong and Frederick [111] model to analyse the cyclic response of shallow foundations subjected to strong rocking oscillations. The model is based on a simple non-linear kinematic hardening model which follows the plastic flow and von Mises yield criterion. Finite element

software, ABAQUS, is used for the numerical modelling with an in-build subroutine. The results are compared with available experimental data from centrifuge tests from UC Davis and the part of the TRISEE project conducted in ELSA facility in ISPRA, Italy (large-scale). Soil stiffness was taken constant with depth, interface elements stiff in compression and with zero tensile strength are used, that allow separation; slippage is controlled by the Mohr-Coulomb criterion. The displacement is applied quasi-statically. The agreement is satisfactory. The two model parameters are calibrated against the $G-\gamma$ curves suggested by Ishibashi and Zhang [112]. The proposed model cannot reproduce the volumetric behaviour of sand and the development of pore pressures in clay. Therefore, it is mostly appropriate for clay under undrained conditions. The aforementioned model is most appropriate for reproducing the low-strain stiffness and ultimate shear strength of soil and soil-foundation systems.

2.1.4.2 Non-linear response

Much less work has been reported on non-linearities of the dynamic impedance functions of footings. One of the few studies reported on footing dynamic impedance non-linearities was presented by Jakub and Roesset in the 1970's [98, 113]. In their study, the soil is modelled as homogeneous or inhomogeneous medium over rigid base with having a depth of $1B$, $2B$ and $4B$, with B being the half-width of the footing. The non-linear constitutive soil behaviour was simulated by means of a Ramberg-Osgood model and iterative linear analyses are performed. One of the Ramberg- Osgood model parameters, w, was kept equal to 2, while the second one, α_γ, was variable to account the wide range of common soil stress – strain relations. They found that an approximation to the rocking and horizontal impedances of a rigid strip can be obtained from the available linear viscoelastic solutions, provided that the "effective" values of the secant modulus and damping are calculated in accordance to Ramberg-Osgood model.

In another interesting study, Borja [114] found that soil non-linearity resulting from an external harmonic load increases the foundation motion and generates low-frequency resonances even in a homogeneous halfspace. The first non-linear response analyses under dynamic loading are presented by Borja and co-workers [114–116]. Starting with the fully symmetrical problems of vertically oscillating circular and square foundations resting on elasto-viscoplastic halfspace, Borja et al [115] studied the non-linear behaviour of soil. Finite-element analysis in two and three dimensions is run in SPECTRA code, an enhanced non-linear version of DLEARN. The deviatoric elasto-viscoplastic model of Duvaut and Lions was employed. In that study radiation boundary conditions were

not used. The reflected waves were tackled through mesh and element size and by adjusting the analysis duration. Borja was the first to recognise that dynamic response is generally non-linear hysteretic and irreversible. Borja solved the axisymmetric problem of a vertically oscillating circular foundation (2D) and the three-dimensional problem of vertically oscillating square foundation (3D). The analyses were run in the supercomputer centre of San Diego. The soil was assumed to have a Poisson's ratio of 0.3 and a shear wave velocity of 200 m/s. The foundation is considered rigid and the mass is ignored in the computations. The footing is loaded harmonically resembling machine vibrations. Borja noticed the difference in behaviour of linear homogeneous halfspace where the motion amplitude is decreasing with the excitation frequency and the non-linear behaviour where resonance occurs and the motion amplitude is increased dramatically. He explained the phenomenon by using a single-degree-of-freedom oscillator analog.

In the 21^{st} century soil non-linearity has been established by various researchers. Stewart et al [117], Phillips et al [118, 119] and more recently Groholski et al [120] studied the non-linear soil behaviour.

Phillips et al [118] dealt with the common problem in site response non-linear analysis to match experimentally obtained modulus degradation and damping curves. For large strains the damping is generally overestimated. They introduced a damping reduction factor, which alters the hysteresis loops following the extended Masing rules, and a fitting methodology for modulus reduction and damping curves. A hyperbolic model was used to implement the damping reduction factor in the one-dimensional analysis software DEEPSOIL.

Phillips et al [119] presented two soil damping formulations implemented in non-linear site response analysis in one-dimension for small and large strains. One of the two formulations is based on a frequency-independent viscous damping matrix which reduces the over-damping at high frequencies. The other formulation includes a reduction factor to modify the extended Masing rules in order to match measured modulus reduction and damping curves simultaneously over a wide range of shear strains.

Groholski et al [120] introduced a general quadratic/hyperbolic model in which the non-linear behaviour is regulated by a curve-fitting equation as a function of the shear strains. The effiency of the general quadratic/hyperbolic model compared to a hyperbolic model is shown by means of total-stress site response analyses. They highlighted the significance of accurately simulating the maximum shear stress in a non-linear constitutive model to avoid false estimation of the computed site response.

There are research contributions investigating the highly non-linear behaviour of the

soil leading to failure provided by Gazetas et al [121], Adebar et al [122] and Gajan et al [84]. For the sake of brevity and context, only one study [121] is discussed herein.

Gazetas et al [121] investigated surface rigid foundations subjected to large overturning moments of various shapes: circular, strip and rectangular using ABAQUS on two and three dimensions. The soil underlying the foundation is an inelastic homogeneous clay deposit.

Three stages of the foundation performance were shown: the initial elastic response where the footing is fully bonded, the nearly elastic but non-linear response where separation starts to occur, and lastly the full mobilisation of the footing where soil bearing failure mechanisms develop. The results are presented in terms of non-linear effective rotational stiffness charts in general dimensionless format.

The analyses were conducted following the selective reduced-integration technique. This technique provides accurate solutions only in the case of incompressible materials. The interface elements are modelled to not carry tension. A high friction coefficient was selected to prevent sliding-a response most common in slender systems with rocking dominated response. The boundaries were placed just outside the pressure bulb (3B). For static analyses, the boundaries were either set free or fixed and they were located close to the foundation. In the dynamic analyses transmitting boundaries were placed at large distances to avoid wave reflections. The soil behaviour was modelled through a constitutive model that combines the von Mises failure criterion, a non-linear kinematic and isotropic hardening law, and a plastic flow rule. The resulting stress-strain curves were calibrated against Vucetic and Dobry for $PI = 30$. The validation of the constitutive model was gained in terms of footing moment capacity and accumulated settlement cyclic loading against centrifuge experiments conducted at UC Davis and computed static ultimate vertical force for a strip footings against the analytical solution by Prandlt.

The observed soil behaviour can be summarised as follows: for very small angles of the rotation θ a linear elastic soil behaviour is maintained and tension is sustained under the foundation. The stiffness can be calculated by closed-form expressions available in literature. For larger values of θ, the non-linear soil response past the $\gamma \geq 2 \cdot 10^{-4}$ threshold depends on PI. While for further increasing θ footing behaviour depends on FS defined as $FS = N_{uo}/N_u$ where N_{uo} is the bearing capacity under purely vertical static loading and N_u applied vertical load.

2.1.5 Key remarks

A significant step in dynamic analysis is the determination of the dynamic stiffness and damping ("impedances") of a massless foundation. There are six foundation impedances corresponding to the modes of vibration: three translational (along x, y and z axes) and three rotational (around the same axes). The term is widely used in mechanical engineering to measure the resistance to motion of a structure when subjected to harmonic forces.

In its original definition, impedance relates actions to associated response velocities; in translational modess, it is measured in units of $[F/L \cdot T]$. In soil dynamics, dynamic impedance is defined as the ratio of a harmonic force (or moment) to the corresponding harmonic displacement (or rotation). The acting force (or moment) and the ensuing displacement (or rotation) are generally out of phase, and are described by complex numbers. Accordingly, the dynamic impedance is complex valued and can be cast in the form:

$$K = \bar{K} + i\omega C \tag{2.19}$$

Both the real and the imaginary parts are functions of frequency. The real component reflects stiffness, $\bar{K}$, while the imaginary component, ωC, reflects damping due to radiation and material energy dissipation in the soil. The real part of the dynamic impedance can be determined regardless of the type of soil behaviour (linear elastic or non-linear hysteretic). When the footing is statically loaded, the real part of stiffness is the ratio of peak load over peak displacement (or moment over rotation angle) which take place simultaneously. On the other hand, when a footing is subjected to dynamic (harmonic) loading, the stiffness is derived as the fraction of load (or moment) at which the maximum displacement (or rotation) is reached over that displacement.

In the realm of the sub-structuring approach, for every degree of freedom (mode of excitation), the dynamic soil-foundation system is replaced by a set of springs and dashpots which are functions of excitation frequency, ω. The physical interpretation of dynamic stiffness in all three degrees of freedom is illustrated in Figure 2.3. Frequency dependence in both the springs and dashpots parameters (K and C) originates from the infinite dynamic degrees of freedom of the soil layer which have been condensed to the finite set of degrees of freedom atop the footing as shown in Figure 2.3.

Most of the research has been conducted with the assumption of an elastic or equivalent elastic material (numerically and analytically). There are research contributions investigating the highly non-linear behaviour of the soil [121] that leads to failure. The research gap that the current work is investigating is identified in the non-linear be-

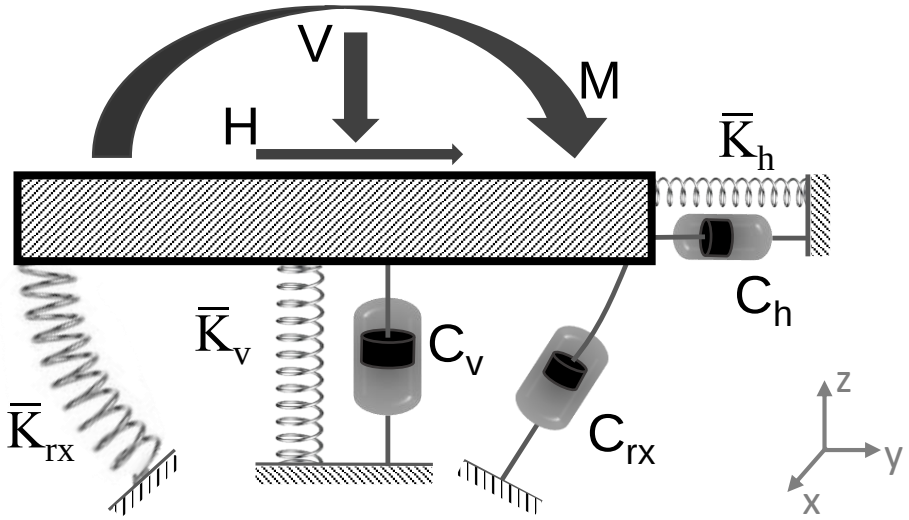

Figure 2.3: Physical interpretation of dynamic stiffness in vertical, horizontal and rocking mode of vibration.

haviour of soil before failure for small to medium shear strains. In other words, this research is looking into the soil behaviour between linear elastic and fully non-linear failure mechanisms.

2.2 Modelling cyclic soil behaviour

2.2.1 Theoretical background

Soil response is a function of the mechanical properties of the soil and the type of loading, static or dynamic. The response of soil when subjected to dynamic and cyclic loads is determined in a major degree by soil properties such as shear wave velocity, mass density (and consequently shear modulus), damping and Poisson's ratio. Of the aforementioned properties, shear modulus and damping are affected by effective stress, strain level and over-consolidation ratio and they are naturally more significant to characterise the cyclic soil behaviour.

2.2.1.1 Non-linear soil behaviour

Soil response analysis requires the definition of cyclic stress-strain relationships, commonly defined by a backbone or skeleton curve at an element level and soil damping properties [117, 123, 124]. A schematic definition of the monotonic backbone curve, also know as first loading, is presented in Figure 2.4 and it is expressed by Eq. 2.20.

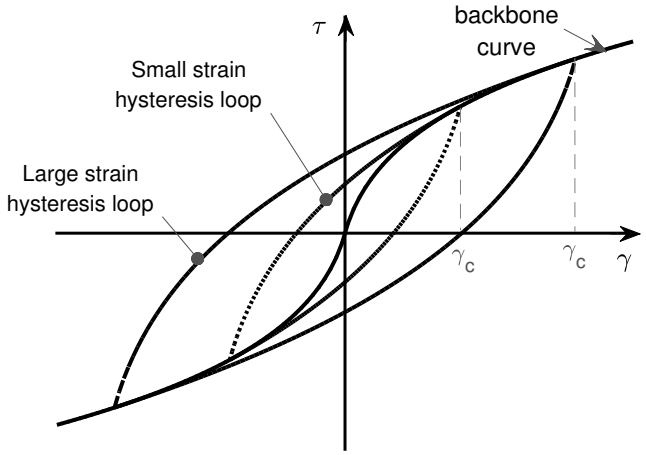

Figure 2.4: Schematic definition of backbone curve and small-strain and large-strain hysteresis loop.

$$\tau = f(\gamma) \tag{2.20}$$

For cyclic stress of relatively large amplitudes, the stress-strain curve comprises a hysteresis loop. Depending on the strain level, γ_c, the hysteresis loop expands to

concentric parabolic shaped loops as seen in Figure 2.4. For a load reversal at $\gamma = \gamma_c$ and $\tau = \tau_c$, the equation of the stress-strain curve for the unloading is described by

$$\frac{\tau - \tau_A}{2} = f\left(\frac{\gamma - \gamma_A}{2}\right) \tag{2.21}$$

while the reloading branch of the hysteresis loop is described by

$$\frac{\tau + \tau_A}{2} = f\left(\frac{\gamma - \gamma_A}{2}\right) \tag{2.22}$$

The aforementioned rules that describe the unloading and reloading parts of the loop are called the Masing rules. Masing rules [125] and extended Masing rules [126–128], are used in addition to the skeleton curve to specify the unloading-reloading and cyclic degradation soil behaviour.

The Masing rules [125] are described briefly below:

- For initial loading, the stress-strain curve is described by the backbone curve.
- The unloading curve of any cycle begins with the same shape as the shape of the negative initial loading backbone curve multiplied by a factor of two. The same applies to the reloading curve in connection with the positive part of the initial loading skeleton curve.

The above rules have been extended to include [126–128]:

- For the case when either the unloading or the loading curve exceeds the maximum reached strain and cuts across the backbone curve, it follows the backbone curve until the next stress reversal.
- For the case when either the unloading or the loading curve intersects an unloading or loading curve from a previous hysteresis loop, the stress-strain curve follows that of the previous cycle.

Both the backbone curve and the hysteresis loop are functions of the same soil properties and they are describing the non-linear soil behaviour. The elastic characteristics are defined through the backbone curve and the energy dissipation properties are indicated by the hysteresis loop. Due to non-linearity, the backbone curve is not a straight line, and the hysteresis loop does not have rounded edges.

For small shear strain levels (less than 10^{-6}) the soil behaviour is considered linear elastic and the soil is then modelled with the maximum shear modulus (G_{max}). For

medium strain levels (between 10^{-6} and 10^{-2} the soil response is considered non-linear and tangent shear modulus, G_t, or secant shear modulus, G_s, are used to define the soil behaviour and the constitutive stress - strain behaviour. A schematic definition of the shear moduli is given in Figure 2.5. The inclination of the loop is inherently associated with soil stiffness which, by definition, is described at any point during the loading process by the tangent shear modulus G_t. Naturally, G_t varies during a loading cycle. An average value to describe the inclination of the loop can be approximated by the secant shear modulus G_s.

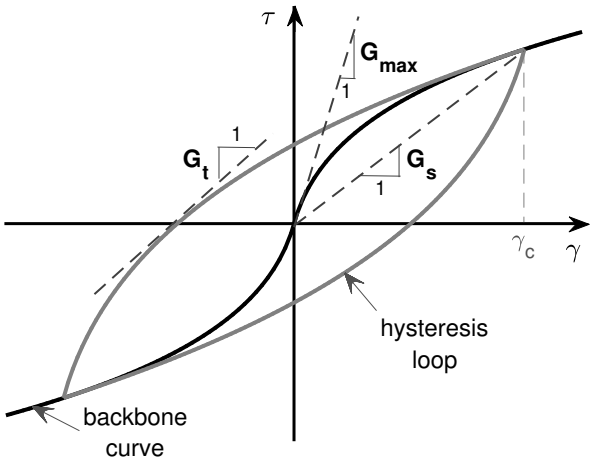

Figure 2.5: Schematic definition of maximum (G_{max}), tangent (G_t) and secant(G_s) shear modulus.

Another property to describe the shape of a hysteresis loop other than the inclination, is the breadth of the loop. The breath of the hysteresis loop is related to the energy dissipation and it is naturally linked to the damping ratio, ξ. Damping ratio, ξ, is defined as [123, 124]

$$\xi = \frac{W_D}{4\pi E_{el}} = \frac{1}{2\pi}\frac{A_{loop}}{G_s\gamma_c^2} \tag{2.23}$$

where W_D is the dissipated energy and it is equal to the enclosed area in the hysteresis loop A_{loop}, E_{el} is the maximum strain energy and it is calculated by the area enclosed in the triangle $0-(\gamma_c,0)-(0,\tau_c)$. A schematic definition of the aformentioned parameters is given in Figure 2.6.

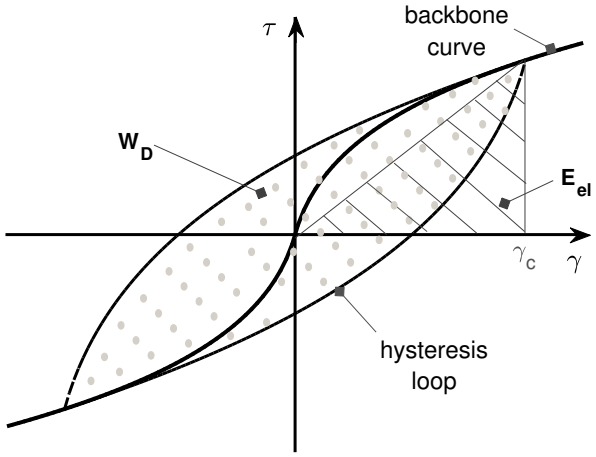

Figure 2.6: Schematic illustration of the stored elastic energy, E_{el}, and the energy dissipation, W_D, during a hysteretic loop

2.3 Description of numerical models

Numerical models are often employed when closed-form solutions are not available. Constitutive models play a central role in numerical modelling. Each constitutive model is a simplification of the soil behaviour which is inspired by experimental observation. Increasing the complexity increases the model parameters that must be defined (from experiments or in situ testing).

Constitutive models are used to represent the initial stress-strain backbone curve in non-linear site response analyses.

There are two methods to model non-linear soil behaviour: (1) the shear strain method where shear strain is given as an explicit function of shear stress and (2) the shear stress method where shear stress is given as an explicit function of shear strain. This section includes a description of models using both methodologies and their limitations are discussed.

2.3.1 Ramberg-Osgood model

Ramberg and Osgood [10] developed a perfectly hysteretic model to represent the relation between stresses and strains evolving in soil under cyclic loading. Originally, the formula was developed for metal alloys to define the stress-strain relationship of specific materials in terms of four parameters. It easy to show that with appropriate adaptations, this

formula can also be used to describe the non-linear behaviour of sand, as well as the hyperbolic stress-strain relation in clay at small and medium strain ranges. The original form of the shear stress-shear strain equation for the backbone curve is

$$\gamma = \frac{\tau}{G_{max}} \left[1 + \left(\frac{1}{\alpha_\gamma} - 1 \right) \left| \frac{\tau}{\tau_1} \right|^{w-1} \right] \tag{2.24}$$

where the characteristic shear stress, τ_1, and the initial shear modulus, G_{max}, are model parameters, while α_γ , w are constant values determined by curve fitting. More specifically, α_γ can be interpreted as a normalised secant shear modulus equals to G_s/G_{max} when shear stress is equal to τ_1, and w is a positive parameter controlling the shear modulus.

It is worth noting that equation 2.24 provides the shear strain as a function of shear stress. Shear stress, in contrast, cannot be explicitly calculated from strain. This can make certain non-linear analyses time consuming because stress determination would be laborious and would require iterations. It's worth mentioning that there have been some efforts to invert the equation [129] but except for a handful values of the parameter w, the results are only approximations. Ishihara [123] states that Ramberg-Osgood type models represent adequately a soil backbone curve at certain conditions for small to medium strain ranges.

For cycling loading and according to Masing rules [125] and extended Masing rules [126–128], equation 2.25 expresses the unloading-reloading stress-strain relationship

$$\gamma - \gamma_c = \frac{\tau - \tau_c}{G_{max}} \left[1 + \left(\frac{1}{\alpha_\gamma} - 1 \right) \left(\frac{|\tau - \tau_c|}{2\tau_1} \right)^{w-1} \right] \tag{2.25}$$

where τ_c and γ_c are the maximum absolute value of shear stress and strain, respectively, within the loop. An illustration of the backbone curve and the hysteresis loop is presented in Figure 2.7.

The secant shear modulus and the corresponding hysteretic damping coefficient for a cycling loading varying with shear stress can be calculated from equations 2.26 and 2.27 [5]

$$\frac{G_s}{G_{max}} = \frac{1}{1 + \left(\frac{1}{\alpha_\gamma} - 1 \right) \left(\frac{|\tau - \tau_c|}{2\tau_1} \right)^{w-1}} \tag{2.26}$$

$$\xi = \frac{2}{\pi} \left(\frac{w-1}{w+1} \right) \left(1 - \frac{G_s}{G_{max}} \right) \tag{2.27}$$

The formula for the secant shear modulus is relatively more accurate than the one for damping, since the model yields unrealistically low values of damping at low shear

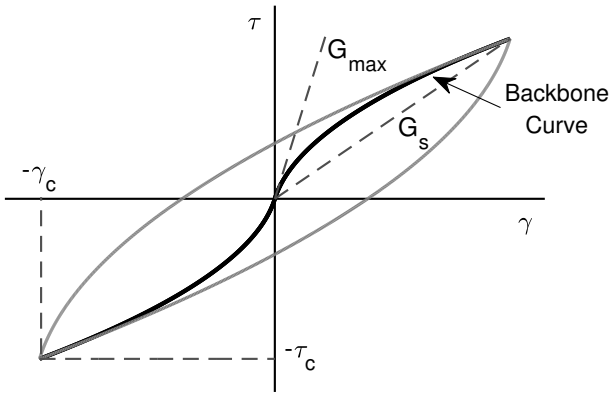

Figure 2.7: Hysteretic shear stress-shear strain Ramberg-Osgood loop. Graphical definition of shear moduli G_{max} and G_s, maximum values γ_c, τ_c and backbone curve

strain ranges [119]. This is not experimentally verified, therefore the reliability of the model is low under small deformations. However, this is a common issue in numerical models.

The effect of the two main parameters, α_γ and w, on the shape of secant modulus degradation and damping curves is depicted in Figure 2.8 and Figure 2.9, respectively.

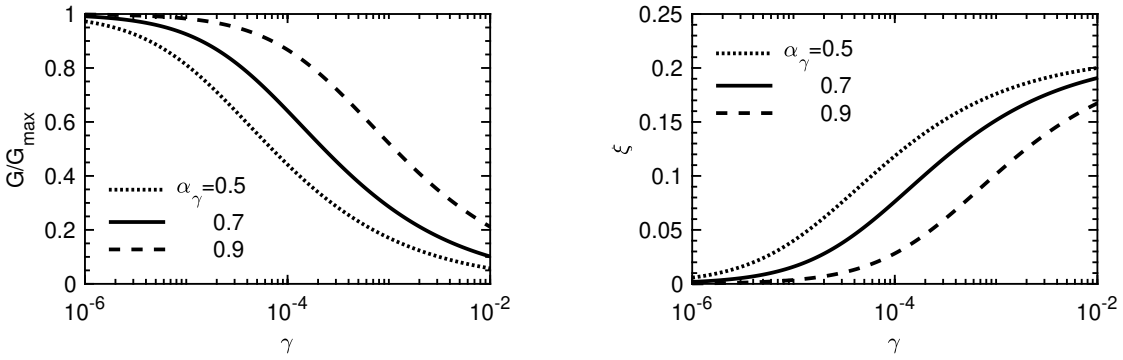

(a) (b)

Figure 2.8: Illustration of the effect of positive parameter α_γ on the shape of (a) modulus reduction and (b) damping curves

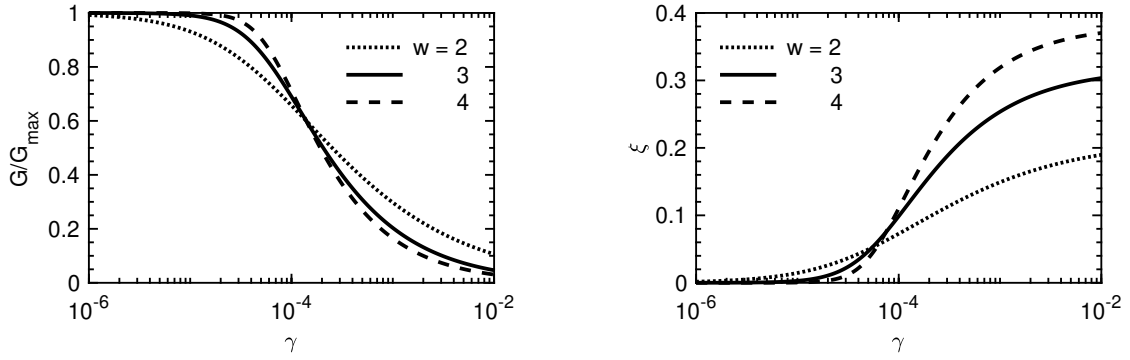

Figure 2.9: Illustration of the effect of positive parameter, w expressing the decrease rate of the secant shear moduli, on the shape of (a) modulus reduction and (b) damping curves

The Ramberg-Osgood model is widely used by researchers in numerical modelling of non-linear soil behaviour. Jakub and Roesset [98] have conducted a parametric study of the effects of soil non-linearity on the dynamic impedance functions of a rigid strip foundation. Vucetic [130] used a Ramberg-Osgood backbone curve with modified Masing criteria to describe the degradation of marine clay under cyclic loading. More recent studies by Papadimitriou [5], Karamitros et al [131] and Durante et al [132] implemented Ramberg-Osgood shear stress-shear strain models to simulate shear modulus degradation and hysteretic damping increase in small and medium shear strain amplitudes. The parameter w was kept constant (equal to 2) in all aforementioned studies, thus simplifying the model to only three parameters .

2.3.2 Hyperbolic and Modified Hyperbolic models

The hyperbolic model is based on the early stress-strain relationships by Konder and Zelasko [133]. Based on their research outcomes, Duncan and Chang [134] introduced the model for axial soil behaviour with a sets of soil properties allowing for a simple way to describe soil non-linearity at small axial strains. Following, Hardin and Drnevich [135] proposed the relationship given in Equation 2.28 to calculate shear stress as a function of shear strain

$$\tau = \frac{\gamma}{\frac{1}{G_{max}} + \frac{\gamma}{\tau_{max}}} \tag{2.28}$$

where τ_{max} is the shear strength of the soil. The above equation describes the backbone curve of the hyperbolic model. The corresponding normalised secant shear modulus as a function of shear strain attains the form

$$\frac{G}{G_{max}} = \frac{1}{1+\frac{\gamma}{\gamma_{ref}}} \tag{2.29}$$

where $\gamma_{ref} = \tau_{max}/G_{max}$. The effect of the reference strain on modulus reduction and damping curves is illustrated in Figure 2.10.

By applying Masing's rule to a hyperbolic model, Ishihara [123] derived the following expression to determine the damping ratio, ξ, at each strain level

$$\xi = \frac{4}{\pi} \times \left[1+\frac{1}{\gamma_c/\gamma_{ref}}\right] \times \left[1-\frac{\ln\left(1+\gamma_c/\gamma_{ref}\right)}{\gamma_c/\gamma_{ref}}\right] - \frac{2}{\pi} \tag{2.30}$$

where γ_c is the cyclic shear strain amplitude. According to Equation 2.28, for large values of γ, shear stress τ, approaches asymptotically the shear strength τ_{max}. This behaviour does not agree well with the laboratory data for small and medium shear strains.

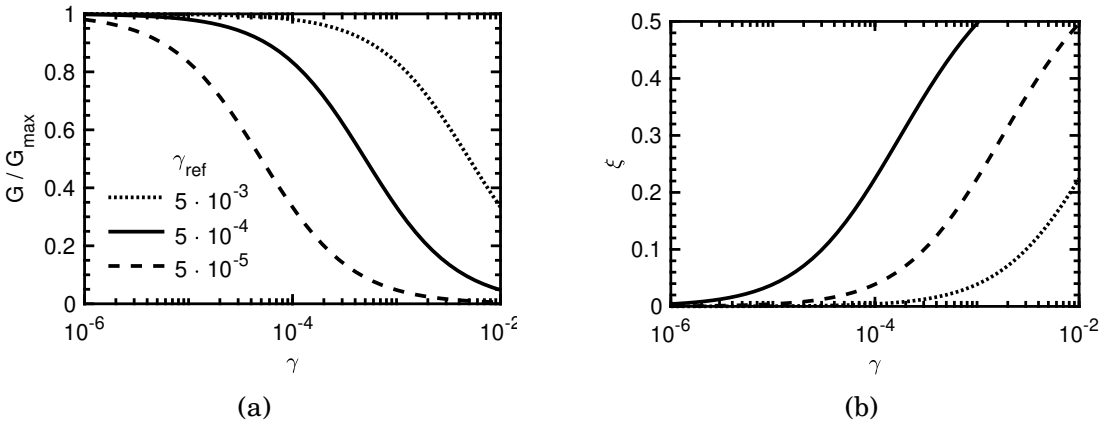

Figure 2.10: Illustration of the effect of reference strain, γ_{ref}, on the shape of (a) shear modulus reduction and (b) damping curves following the hyperbolic model.

A modified form of the hyperbolic model, named modified hyperbolic (MH) model and described by Equation 2.31 has been adopted by various researchers [4, 119, 136]. The modified hyperbolic model introduces a new parameter in Equation 2.29 and hence increases the complexity of the model. In addition, the reference strain is redefined and

no longer depends on soil shear strength. The secant shear modulus degradation curve is expressed in Equation 2.31

$$\frac{G}{G_{max}} = \frac{1}{1+\left(\frac{\gamma}{\gamma_r}\right)^{\alpha}} \tag{2.31}$$

where γ_r is a pseudo-reference strain and α is a curvature parameter. From the equation 2.31 it is trivial to define "pseudo-reference strain" as the value of shear strain where the secant shear modulus, G, is half the maximum shear modulus ($G/G_{max} = 1/2$).

Assuming Masing behaviour, Darendeli [4] calculated approximately the damping ratio as a function of the MH model parameters α and γ_r. The effect of the curvature parameter α and the "pseudo-reference strain" γ_r on the shape of the modulus reduction and damping curves are shown below in Figures 2.11 and 2.12, respectively. From the aforementioned figures it is apparent that both parameters have a physical meaning: α controls the steepness of the curve about γ_r which is the shear strain for which $G/G_{max} = 0.5$.

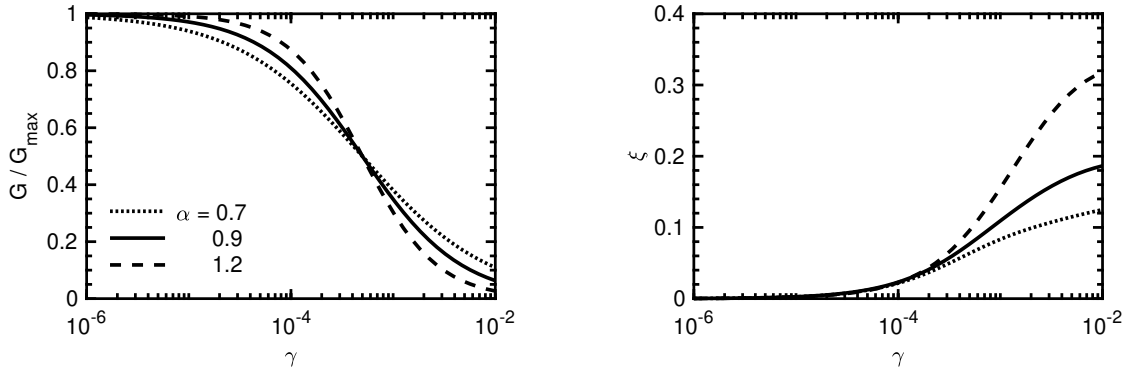

(a) (b)

Figure 2.11: Illustration of the effect of curvature coefficient, α, on the shape of (a) shear modulus reduction and (b) damping curves following the modified hyperbolic model; $\gamma_r = 5 \times 10^{-4}$.

The backbone curve of the modified hyperbolic model is given by equation 2.32 and it is depicted in Figure 2.13

$$\tau = \frac{G_{max}\gamma}{1+\left(\frac{\gamma}{\gamma_r}\right)^{\alpha}} \tag{2.32}$$

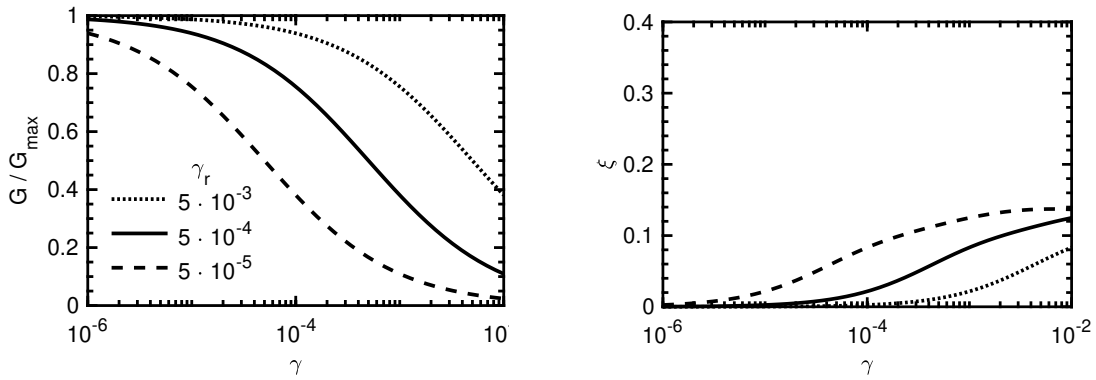

Figure 2.12: Illustration of the effect of pseudo-reference strain, γ_r, on the shape of (a) shear modulus reduction and (b) damping curves following the modified hyperbolic model; $\alpha = 0.7$.

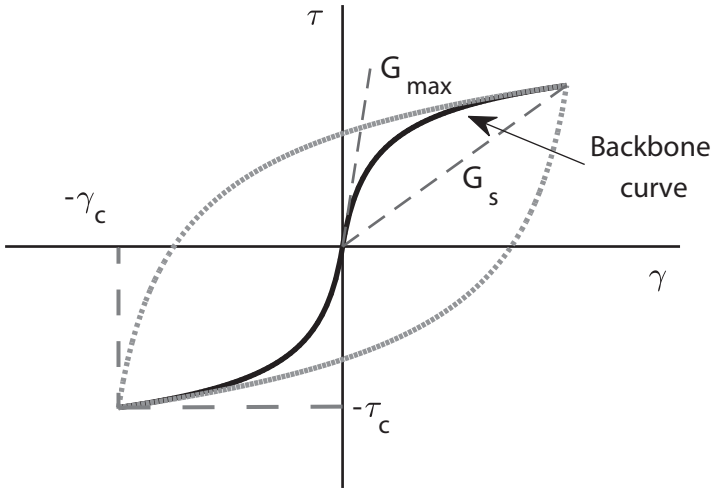

Figure 2.13: Hysteretic shear stress - shear strain loop according to modified hyperbolic model.

Following Masing and extended Masing rules, one can obtain the unload-reload equations to describe the hysteretic loop

$$\tau - \tau_c = \frac{G_{max}\left(\gamma - \gamma_c\right)}{1 + \left|\frac{\gamma - \gamma_c}{2\gamma_r}\right|^{\alpha}} \tag{2.33}$$

The loop alongside the backbone curve to define modified hyperbolic model, are illustrated in Figure 2.13 qualitatively.

The advantage of the modified version of the hyperbolic model over the original one is that it allows a better fitting to experimental data to describe soil behaviour more accurately for small and medium shear strain amplitudes.

2.4 Calibration of numerical models

The shape of the modulus reduction curves described in the previous subsection 2.3 depends on the material under investigation. In the absence of extensive soil testing data, it is common practice to estimate model parameters by calibrating the numerical model against MR curves from the literature. To name a few relevant studies, Seed and Idriss [137] provided experimental generic curves for granular materials. Iwasaki et al [138] presented MR curves for sand depending on the overburden pressure considering the confining stress. Vucetic and Dobry [8], Darendeli [4] and Bolton and Vardanega [139] proposed curves are presented below in further detail.

2.4.1 Vucetic and Dobry proposed curves

Vucetic and Dobry [8] conducted an extensive study on the effect of Plasticity Index, PI, on the cyclic stress-strain parameters of saturated sands with ($OCR = 0$) and clays. Their study is summarised by the MR, and material damping ratio curves versus the cyclic shear strain shown in Figures 2.14. The main outcome is that as the soil plasticity index increases the secant shear modulus stays constant at small strains and the steepness of the degradation incline decreases at larger strains. Similarly, for large plasticity indexes, the gradient of material damping curves is decreasing.

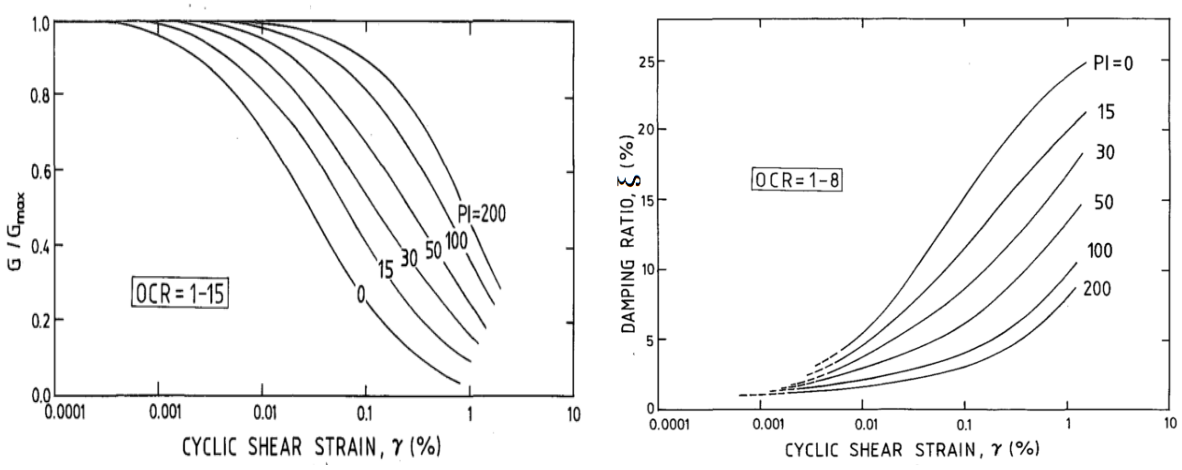

(a) (b)

Figure 2.14: (a) Modulus reduction and (b) material damping ratio curves for different plasticity indexes proposed by Vucetic & Dobry [8]

2.4.2 Darendeli fitted curves

Darendeli [4] developed a family of modulus degradation and damping versus shear strain curves based on experimental data from resonant column torsional shear (RCTS) tests conducted at the University of Texas, Austin. In his study, modified hyperbolic model (see subsection 2.3.2) is implemented to fit the experimental curves shown in Figures 2.15.

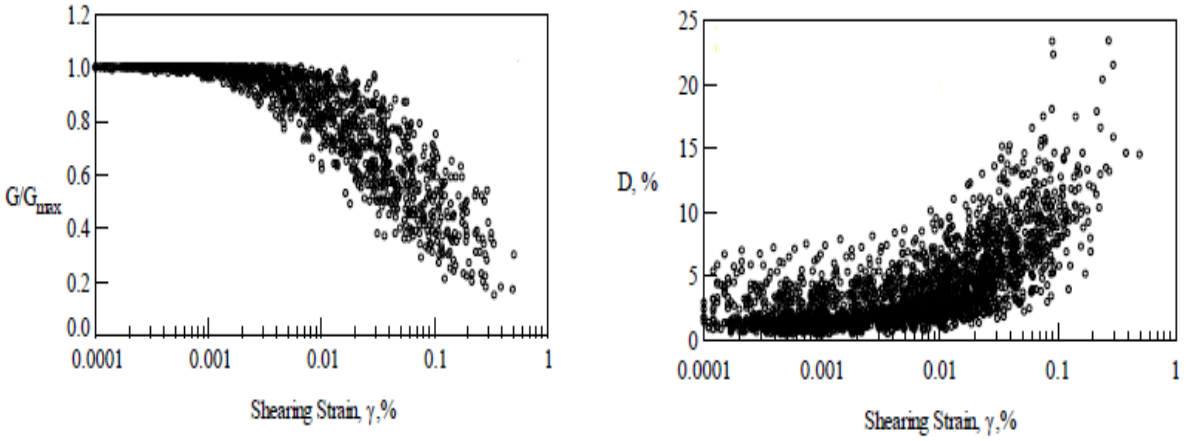

(a) (b)

Figure 2.15: Resonant column and torsional shear tests experimental data for (a) normalised shear modulus and (b) damping (source: Darendeli [4])

The proposed parameters for the modified hyperbolic model are given in Equations 2.34 and 2.35. The curvature coefficient α is taken constant and equal to $\phi_5 = 0.919$, and pseudo-reference strain γ_r is calculated as a function of soil plasticity index PI, mean effective confining stress σ'_0 and over-consolidation ratio OCR.

$$\gamma_r = \left(\phi_1 + \phi_2 \times PI \times OCR^{\phi_3}\right) \times \left(\sigma'_0 / p_\alpha\right)^{\phi_4} \tag{2.34}$$

$$\alpha = \phi_5 = 0.919 \tag{2.35}$$

where ϕ_{1-5} are constant parameters given in Table 2.10.

Darendeli [4] proposed an approximate methodology to calculate Masing damping.

$$\xi_M = c_1 \times \xi_{M,\alpha=1} + c_2 \times \xi^2_{M,\alpha=1} + c_3 \times \xi^3_{M,\alpha=1} \tag{2.36}$$

where $\xi_{M,\alpha=1}$ is the Masing damping when the curvature parameter α is equal to 1 and is calculated by the following expression

$$\xi_{M,\alpha=1} = \frac{100}{\pi}\left[4\,\frac{\gamma-\gamma_r\,ln\left(\frac{\gamma+\gamma_r}{\gamma_r}\right)}{\frac{\gamma^2}{\gamma+\gamma_r}}-2\right] \tag{2.37}$$

and c_{1-3} are functions of the α which are empirically calculated by the following expressions

$$c_1 = 0.2523 + 1.8618\alpha - 1.1143\alpha^2 \tag{2.38}$$

$$c_2 = -0.0095 - 0.071\alpha + 0.0805\alpha^2 \tag{2.39}$$

$$c_3 = 0.0003 + 0.0002\alpha - 0.0005\alpha^2 \tag{2.40}$$

The small strain damping, ξ_{min}, can be computed from the formula

$$\xi_{min} = \left(\phi_6 + \phi_7 \times PI \times OCR^{\phi_8}\right) \times {\sigma'_0}^{\phi_9} \times \left[1 + \phi_{10} ln(f)\right] \tag{2.41}$$

The total damping results as a sum of the small strain damping and a function of the modulus reduction curves. In the case of modified hyperbolic model that is [4]

$$\xi = \xi_{min} + b \times \xi_M(\gamma) \times \left[\frac{G(\gamma)}{G_{max}}\right]^{0.1} \tag{2.42}$$

where

$$b = \phi_{11} + \phi_{12} \times ln(N) \tag{2.43}$$

Table 2.10: Model coefficients, ϕ_{1-12}, for modulus reduction and damping proposed by Darendeli [4]

Parameter	**Value**
ϕ_1	0.0352
ϕ_2	0.001
ϕ_3	0.3246
ϕ_4	0.3483
ϕ_5	0.919
ϕ_6	0.8005

Parameter	**Value**
ϕ_7	0.0129
ϕ_8	-0.1069
ϕ_9	-0.2889
ϕ_{10}	0.2919
ϕ_{11}	0.6329
ϕ_{12}	-0.0057

The experimental data according to which the fitting parameters are calculated, refer to sandy and clayey soils, and up to a maximum shear strain of 3×10^{-3}. It is advised that this study should not be followed for larger strains, especially in the vicinity of the maximum shear strength [140].

2.4.3 Vardanega and Bolton parameters

Vardanega and Bolton [139] processed a database of 67 tests on 21 fine grained soils for the influence of rate effects assuming a 5% reduction per log cycle (an assumption made based on the findings of Lo Presti et al [141] and D'Onofrio et al [142]). The analysis of the database produced expressions for the reference strain linked to plasticity index (following the observations of Vucetic and Dobry [8]). For the static adjustment (strain rate of 10^{-6} Hz or less), the curvature parameter and the reference strain were shown to be linked to changes in plasticity via the empirical relationships shown as equation 2.44

$$\alpha = 0.736 \qquad \gamma_r = 2.2\left(\frac{I_p}{1000}\right) \tag{2.44}$$

For the dynamic adjustment the curvature parameter and the reference strain were shown to be linked to changes in plasticity via the empirical relationships shown as equation 2.45

$$\alpha = 0.943 \qquad \gamma_r = 3.7\left(\frac{I_p}{1000}\right) \tag{2.45}$$

which correspond to a strain rate of 10^{-2} Hz. Note that I_p is expressed numerically in both equations.

CHAPTER 3

NUMERICAL METHODOLOGY

The geotechnical numerical modelling software FLAC in two and three dimensions by Itasca was mainly employed to run the analyses in this study is described in *Chapter 3*. An introduction to finite difference methodology and to time domain analysis is provided. Following, the implementation of user defined numerical models in FLAC is presented. Finally, a brief description of the additional modelling software utilised for verification purposed, ISOBEM and PLAXIS 2D is provided.

3.1 Introduction to FLAC & FLAC3D programs

The analyses were executed by means of FLAC, a commercial software developed by Itasca. The FLAC 2D version 7 [13] is used for the two-dimensional analyses presented in *Chapter 4* and *Chapter 5* and FLAC 3D version 6 [143] for the three dimensional studies presented in *Chapter 6* and *Chapter 7*. FLAC3D extends the analysis capability of FLAC2D and uses the numerical formulation of the two-dimensional program. For the sake of brevity they will both be called FLAC hereafter.

FLAC is an abbreviation for 'Fast Lagrangian Analysis of Continua' that embodies an explicit finite difference methodology for the numerical modelling of geotechnical engineering problems. The soil is modelled as a continuum and is discretised into elements, zones, or bricks, which form a grid. The Lagrangian term denotes that the grid deforms with the material it simulates, as the incremental displacements are added to the coordinates. The grid can be any shape and elements can have any property

value in accordance to Wilkins finite volume method [144] which is incorporated. The behaviour of each element is in accordance to a prescribed linear or non-linear stress-strain constitutive law depending on the boundary conditions and the applied forces.

3.2 The explicit finite difference method

The finite difference method (FD) is a numerical technique used to solve sets of differential equations, given initial values and/or boundary values [13]. According to this method, every spatial derivative in the set of governing equations is replaced directly by algebraic expressions written in terms of the field quantities (stresses or displacements) at discrete points in space, while the variables are not defined inside the elements.

On the contrary, finite elements (FE) require field variables to vary within each element in a prescribed way. This can only be achieved through specific functions controlled by nodal parameters. Part of the formulation includes the adjustment of these parameters to eliminate errors and energy dissipation.

The main difference is that in FE method a large global stiffness matrix is produced by combining the elements stiffness matrices while in FD the equations are regenerated at each calculation step. Although the derivation process of the set of algebraic equations differs in FD and FE methods, the resulting expressions are the same. Accordingly, both methods are considered to be equivalent.

Another core difference to the FE method is the operated solution scheme. In FE implicit solution scheme based on the formation of a global matrix is the norm whereas FLAC embodies an explicit calculation method. In simple terms, in implicit solution scheme iterations are necessary to compute stresses from strains in every element in order to reach equilibrium and satisfy compatibility. In contrast, in explicit solution methods the elements do not communicate with each other during a particular solution step so the stresses are calculated from strains within one element.

The general calculation sequence used in FLAC is provided in Figure 3.1. Starting with the stresses and forces, new velocities and displacements are calculated through the equations of motion. Then, new stresses are derived from velocities through the constitutive stress-strain equations. One timestep is defined as a cycle around the loop illustrated in Figure 3.1.

It is crucial to note that each step in Figure 3.1 updates all grid variables from known values that remain 'frozen'. For instance, the upper box takes the set of stresses and forces already calculated and, for each element, computes new velocities and displacements.

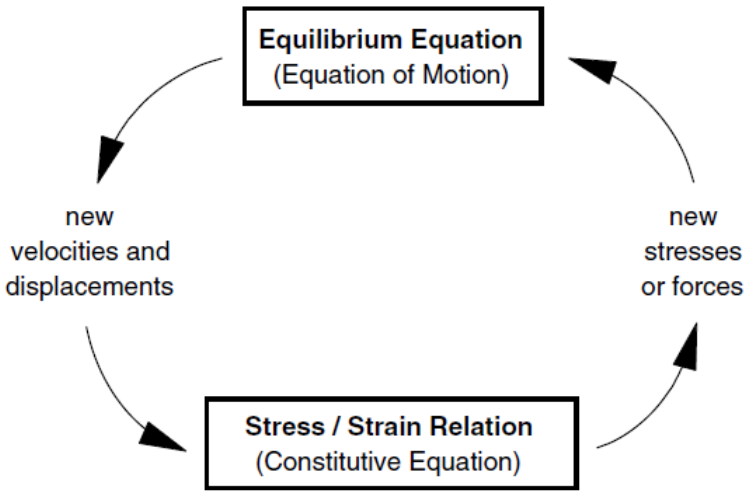

Figure 3.1: Explicit calculation style used in FLAC (Source: FLAC Manual [13])

The stresses are assumed to be fixed for the operation of the box (i.e., the newly calculated velocities do not affect the stresses). This may seem unreasonable because it is known that if velocity changes somewhere, the neighbouring elements are influenced and tend to change their stresses. However, the choice of a sufficiently small timestep guarantees that such information cannot physically propagate from one element to another in that interval. Since one cycle defines one timestep, the assumption of fixed stresses is reasonable. Naturally, after a number of cycles around the loop, disturbances can travel across neighbouring elements, just as it would happen physically.

3.3 Advantages and limitations

The chief assets of these programs are, firstly, the explicit Lagrangian calculation scheme and the mixed-discretisation zoning technique used in FLAC, that ensure that even when the physical system being modelled is not balanced, the numerical scheme is stable. Also, because no matrices (such as those assembled in FEM) are formed, large two-dimensional calculations can be made without excessive memory requirements.

In addition, FLAC allows the implementation of user-defined constitutive models (UDMs), written in C++ and compiled as Dynamic Link Libraries (DLL files). Due to the explicit nature of the integration algorithm, the main UDM function is to return new stresses given the current stress condition and the applied strain increment, namely a procedure that is rather straightforward even for complicated constitutive laws. This functionality is utilized herein, for the implementation of the Ramberg-Osgood and the

modified hyperbolic model (section 3.7).

Furthermore, FLAC includes a vigorous built-in compiler, FISH, that allows the end-user to define new functions and variables. FISH is a programming language, therefore functions entered by means of a FLAC data file are interpreted to a list of commands stored in FLAC's memory and they are performed whenever a FISH function is called upon. For instance, through FISH one can prescribe property variation in the grid, such as a non-linear increase in modulus with depth. Also it is useful when plotting and printing user defined variables or when implementing special grid generators. Last but not least, FISH permits specification of user-defined constitutive models which are proven a powerful tool. For example in the analyses presented in *Chapter 4* it was used to prescribe the model parameters according to the shear strain rates.

However, linear static simulations run faster with finite element programs than with FLAC. FLAC is most efficient to solve non-linear dynamic or large strain problems. The disadvantage of the explicit formulation (i.e., the question of required damping and small timestep limitation) are overcome to some extent by automatic inertia scaling and automatic damping that do not affect the mode of failure [13].

3.4 Critical timestep

The core requirement of the explicit finite difference scheme is a small timestep. Because for the duration of the calculation the equations operate on given, fixed values a timestep must be lower than a critical value to establish a calculation speed that is always higher than a maximum speed. The maximum speed is defined as the speed at which disturbance propagates. The aforementioned stability limitation is given in Equation 3.1

$$\Delta t < \frac{\Delta x}{V_p} \tag{3.1}$$

where Δx is the minimum element size that an elastic solid is discretised. It is calculated as $A/\Delta x_{max}$ in FLAC2D and as $V/\Delta A_{max}$ in FLAC3D. And V_p is the maximum speed at which disturbance is propagated, namely the P-wave velocity given in 3.2

$$V_p = \sqrt{\frac{K + 4G/3}{\rho}} \tag{3.2}$$

3.5 Quiet boundaries

The study of geomechanical problems naturally requires an unbounded grid. It has been shown in the literature e.g. [115] that boundary conditions can disrupt the results in dynamic solutions because of wave reflections at the artificial numerical boundaries. In order to minimise the aforementioned effect, the boundaries have to be at an adequate distance. However, larger grids naturally require higher computational time. To tackle this problem, wave reflections in FLAC can be eliminated to a degree by using viscous, quiet, or free-field boundaries. Many formulations have been suggested but the viscous - "quiet" boundaries introduced by Lysmer and Kuhlemeyer [145] are used in FLAC because they operate in time domain.

Quiet boundaries are based on the use of independent dashpots on the normal and shear (vertical and horizontal in local axes) directions. For body waves reaching the boundary at angles of incidence more than 30°, the aforementioned method is almost fully effective. For angles of incidence lower than 30°or for surface waves (Rayleigh, Love), the wave absorption is not as effective. More effective non-reflecting boundaries demand frequency-dependent elements and can only be applicable in frequency-domain analyses, or Perfectly Matched Layer (PML) boundaries which are essentially exact, yet only applicable in elastic media. Thereafter FLAC cannot take advantage of them. The non-reflecting boundaries proposed by Lysmer and Kuhlemeyer [145] involve dashpots in the normal (t_n) and shear (t_s) directions that provide viscous normal and shear tractions given by

$$t_n = -\rho \cdot V_p \cdot v_n \tag{3.3}$$

$$t_s = -\rho \cdot V_s \cdot v_s \tag{3.4}$$

with v_n, v_s being the normal and shear input particle velocity respectively, ρ the mass density of the grid, V_p and V_s the compressional and the shear wave propagation velocities, respectively.

3.6 Mechanical damping and material response

In dynamic numerical simulations, damping reproduces, in magnitude and pattern, the energy dissipation in a corresponding dynamically loaded natural system. Damping is partly caused by energy loss by virtue of internal friction in the soil material (material

damping) and partly by the radiation of waves towards infinity (radiation damping). Natural damping in soil is mainly hysteretic, which is frequency independent. However, it is hard to numerically reproduce hysteretic damping for two reasons: 1) Most simplified hysteretic functions do not damp all components equally when many waveforms are superimposed. 2) Hysteretic functions result in path-dependence, which makes results hard to interpret.

In software that utilises time domain analysis, such as FLAC, Rayleigh damping is usually implemented to provide damping that is almost frequency-independent over a specific spectrum of frequencies. Even though Rayleigh damping consists of two frequency-dependent viscous elements, the frequency-dependent effects are arranged to effectively counteract at the frequencies of interest.

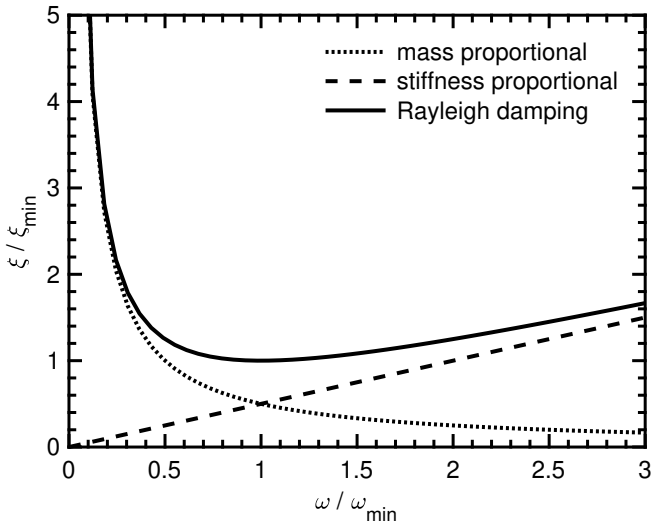

Figure 3.2: Normalised critical damping ratio versus normalised angular frequency

Originally, Rayleigh damping was implemented in the analysis of structures and elastic mediums, to dissipate the energy of the natural oscillation system modes. Therefore, the equations are normally formulated in matrices. Rayleigh damping is a function of both the mass $[M]$ and the stiffness $[K]$ system matrices. This damping formulation, originally proposed by Rayleigh and Lindsay [146], calculates the viscous damping matrix [C] as follows

$$[C] = \alpha\,[M] + \beta\,[K] \tag{3.5}$$

where α is the mass-proportional damping constant; and β is the stiffness-proportional damping constant. Both constants naturally carry dimensions. The mass-proportional

term is analogous to a dashpot connecting each FLAC grid-point to “ground”. The stiffness-proportional term is analogous to a dashpot connected across each FLAC zone. Although both terms are frequency-dependent, an approximately frequency-independent response can be obtained over a limited frequency range, with the appropriate choice of parameters, as discussed below. For a multi-degree-of-freedom system, the critical damping ratio, ξ_i , at any angular frequency of the system, ω_i, can be found from

$$\alpha + \beta\omega_i^2 = 2\omega_i\xi_i \tag{3.6}$$

or

$$\xi_i = \frac{1}{2}\left(\frac{\alpha}{\omega_i} + \beta\omega_i\right) \tag{3.7}$$

The critical damping ratio, ξ_i , can also be calculate as the fraction of critical damping for mode i with angular frequency ω_i [143].

As shown in Figure 3.2, the curve representing the sum of both mass and stiffness proportional Rayleigh damping is minimum at:

$$\xi_{min} = (\alpha\beta)^{1/2} \tag{3.8}$$

$$\omega_{min} = (\alpha/\beta)^{1/2} \tag{3.9}$$

or

$$\alpha = \xi_{min}\omega_{min} \tag{3.10}$$

$$\beta = \xi_{min}/\omega_{min} \tag{3.11}$$

And the centre frequency is defined as:

$$f_{min} = \omega_{min}/2\pi \tag{3.12}$$

In FLAC and FLAC3D, Rayleigh damping is defined with the centre frequency, f_{min} and the critical damping ratio, ξ_{min}.

Another form of frequency independent mechanical damping available in FLAC is local damping. Even though, local damping was originally designed as a means to balance static simulations, it is also applicable in dynamic simulations. However, it is advised [13] to be used with caution and simulations with Rayleigh damping should

be used for comparison. It operates by adding or subtracting mass from a gridpoint at certain times during a cycle of oscillation. During this operation, conservation of mass is satisfied as the amount added is equal to the amount subtracted. Mass is added when the velocity changes sign and subtracted when it reaches a turning point. Hence, increments of kinetic energy are removed twice per oscillation cycle (at the velocity maximum and minimum). Local damping does not need a specific centre frequency such as Rayleigh, therefore the use of local damping is simpler. A modified form of local damping—combined damping—may also be used in dynamic mode, but its performance is not well documented.

3.7 Implementation of numerical models

The models are implemented into FLAC using the following non-linear elastic formulation (expressed using Kronecker's δ symbol):

$$\dot{\sigma}_{ij} = G_t\left(\sigma_{ij}\right) \cdot \left(\delta_{ik}\delta_{kl} + \delta_{il}\delta_{jk} + \frac{2\nu}{1-2\nu}\delta_{ij}\delta_{kl}\right) \cdot \dot{\epsilon}_{kl} \tag{3.13}$$

where ν is Poisson's ratio, which is assumed to remain constant. To obtain the tangent shear modulus as a function of the current multiaxial stress state, the shear stress τ is replaced by:

$$X = \sqrt{\frac{1}{2}\left(s_{ij} - s_{ij}^{LR}\right)\left(s_{ij} - s_{ij}^{LR}\right)} \tag{3.14}$$

where s_{ij} is the deviatoric stress $s_{ij} = \sigma_{ij} - \delta_{ij}\sigma_{kk}/3$, while s_{ij}^{LR} is the deviatoric stress at the beginning of the analysis or at the last shear reversal.

It is evident from the above Equation 3.13 that implementation of the numerical models into an incremental solution algorithm such as FLAC, requires the tangent shear modulus G_t to be derived. In general terms, the tangent shear modulus in perfectly hysteretic numerical models is given as a function of the maximum shear modulus G_{max} as shown in Equation 3.15

$$G_t = \frac{G_{max}}{T} \tag{3.15}$$

where T is a function of stress or strain which describes the hysteretic response and it is the quantity needed to implement the models. For dynamic analysis, the maximum stable timestep depends on the maximum material stiffness and the minimum element size.

3.7.1 Implementation of the Ramberg-Osgood model

The multi-axial formulation of the Ramberg-Osgood stress strain is relationship can be used to simulate the hysteretic soil behaviour as described extensively in 2.3.1. Based on this formulation, the tangent shear modulus is calculated from Equation 3.15, where

$$T = \begin{cases} 1 + 2\left(\frac{1}{\alpha_1 - 1}\right)\frac{|X|}{\eta_1} & \text{for initial shearing} \\ \\ 1 + 2\left(\frac{1}{\alpha_1 - 1}\right)\frac{|X^{LR}|}{2\eta_1} & \text{after the first load reversal} \end{cases} \tag{3.16}$$

with X being a scalar measure of the deviatoric stress ratio, X^{LR} the value at last load reversal, calculated as per Equation 3.14 and η_1 a model parameter calculated by the formula

$$\eta_1 = \alpha_1 \frac{G^{LR}_{max}}{\sigma^{LR}} \gamma_1 \tag{3.17}$$

with G^{LR}_{max} the maximum shear modulus at last load reversal, σ^{LR} the isotropic stress at last load reversal and α_1 , γ_1 model parameters.

It is obvious from the aforementioned equations that in Ramberg-Osgood model, the tangent shear modulus is a function of the current shear stress state and no numerical methods are required to implement the model.

3.7.2 Implementation of the Modified Hyperbolic model

The modified hyperbolic model is described in 2.3.2. Implementation of the modified hyperbolic model into an incremental solution algorithm such as FLAC, requires the tangent shear modulus G_t to be derived from Equation 3.18

$$\frac{G_s}{G_{max}} = \frac{1}{1 + \left(\frac{\gamma}{\gamma_r}\right)^{\alpha}} \tag{3.18}$$

and given here as Equation 3.19

$$\frac{G_t}{G_{max}} = \frac{1}{G_{max}} \frac{d(G_s \gamma)}{d\gamma} = \frac{1 + (1 - \alpha)\left(\frac{\gamma}{\gamma_r}\right)^{\alpha}}{\left[1 + \left(\frac{\gamma}{\gamma_r}\right)^{\alpha}\right]^2} \tag{3.19}$$

As described in the above, user-defined models in FLAC must calculate stress increments as a function of the current stress state and the applied strain increment. As a result, Equation 3.19, where G_t is expressed in terms of the total developing strain

γ, cannot be directly applied. To obtain G_t as a function of the current shear stress τ, Equation 3.18 is substituted in $\tau = G_s\gamma$ to give

$$\frac{\tau}{G_{max}}\left[\left(\frac{\gamma}{\gamma_r}\right)^{\alpha}+1\right]-\gamma=0 \tag{3.20}$$

The tangent shear modulus G_t can be obtained by solving Equation 3.20 for γ and substituting the result back into Equation 3.19. In the case of $\alpha = 1$ or $\tau = 0$, solving Equation 3.20 is trivial. However, for $\alpha \neq 1$ and $\tau \neq 0$, no closed-form solution is available. Therefore, the Newton-Raphson procedure is incorporated in the implementation algorithm and γ is computed, iteratively, as:

$$\gamma_n = \gamma_{n-1} - \frac{\frac{\tau}{G_{max}}\left[\left(\frac{\gamma_{n-1}}{\gamma_r}\right)^{\alpha}+1\right]-\gamma_{n-1}}{\frac{\tau}{G_{max}}\frac{\alpha}{\gamma_{n-1}}\left(\frac{\gamma_{n-1}}{\gamma_r}\right)^{\alpha-1}-1} \tag{3.21}$$

Nevertheless, the function in Equation 3.20 is not monotonic, as its derivative (hence also the denominator in Equation 3.21 becomes zero for a critical value of γ, namely:

$$\gamma_{cr} = \left(\frac{G_{max}\gamma_r^{\alpha}}{\alpha\tau}\right)^{\frac{1}{\alpha-1}} \tag{3.22}$$

Therefore, to ensure convergence to the correct root γ, an appropriate value of γ_1 needs to be selected for the first iteration. For $\alpha < 1$, there exists only one positive solution which is always obtained if the initial value is $\gamma_1 > \gamma_{cr}$ (e.g., $\gamma_1 = 10^1 \cdot \gamma_{cr}$). In case where $\alpha > 1$, the modified hyperbolic model predicts a peak shear stress. The shear strain at which this occurrs can be obtained by setting $G_t = 0$ in Equation 3.19:

$$\gamma_{peak} = \left(\frac{1}{1-\alpha}\right)^{\frac{1}{\alpha}}\gamma_r \tag{3.23}$$

The peak stress can be then calculated by replacing Equation 3.23 into Equation 3.20:

$$\tau_{peak} = G_{max}(\alpha-1)^{1-\frac{1}{\alpha}}\frac{\gamma_r}{\alpha} \tag{3.24}$$

For $\gamma > \gamma_{peak}$, the tangent shear modulus becomes negative, while, using Equation 3.19, it can be easily shown that for $\gamma \to \infty$, $\tau \to 0$. As a result, for $\alpha > 1$ and $\tau < \tau_{peak}$, Equation 3.21 has two positive roots. To ensure convergence to the appropriate one, the following procedure is followed: In the beginning of each loading cycle, the initial value for the Newton Raphson iterations is selected as $\gamma_1 < \gamma_{cr}$ (e.g., $\gamma_1 = 0$). Once the peak

shear stress is reached, the initial value for each iteration is selected as $\gamma_1 > \gamma_{cr}$ (e.g., $\gamma_1 = 2\gamma_{cr}$). This algorithm has been tested extensively and has been found to always converge with an accuracy of $\gamma \pm 10^{-8}$ within 5-10 iterations.

To obtain the tangent shear modulus as a function of the current multi-axial stress state, the shear stress τ in Equation 3.21 is replaced by a scalar measure of the deviatoric stress ratio given in Equation 3.14. Finally, to allow for the formation of closed τ - γ loops, after the first shear reversal, the reference shear strain γ_r is replaced by $\gamma'_r = 2\gamma_r$.

3.8 Additional modelling software

3.8.1 Introduction to PLAXIS 2D software

PLAXIS 2D 2018 [147] is used to verify the two-dimensional linear elastic analyses presented in *Chapter 4* and confirm the vertical and lateral static stiffness calculated with FLAC. PLAXIS is a commercial software widely used in geomechanics which implements the finite element methodology for geotechnical engineering and design. It is intended to be a practical tool to be used by geotechnical engineers who are not specialising in numerical modelling and therefore it is more user-friendly compared to FLAC. However, PLAXIS capabilities are more restricted and errors are harder to track. By definition, finite element and finite difference methodologies produce the same results that is why this software is selected to verify the numerical outcomes from FLAC.

3.8.2 Introduction to IsoBEM software

IsoBEM in two and three dimensions is utilised in *Chapter 4* to verify the linear elastic horizontal dynamic stiffness of a massless strip footing resting on soil layer in collaboration with Dr. Karatzia [148]. IsoBEM is a software platform based on the Boundary Element method (BEM). BEM is a computational tool for solving a wide range of differential equations numerically. For each problem, a complete set of integral formulation, corresponding Green's function, and numerical implementation are presented in IsoBEM Theory Manual. IsoBEM can accommodate non- uniform soil properties by specifying multiple boundaries at their interfaces. These boundaries, including the ground surface, can be flat or inclined. IsoBEM is verified for applications in soil and structure interaction problems and soil dynamics [149], [150].

3.9 Data processing

Following static and dynamic analyses, forces/moments in vertical and horizontal directions and corresponding displacements/rotations are obtained. The data processing differs from static to dynamic loading and from linear to non-linear analysis. The stiffness of the foundation is by definition the fraction of force/moment over the corresponding displacement/rotation. In the linear static case this is captured as the slope of the load displacement trajectory. An example is shown in Figure 3.3 for vertical loading. In the linear case the slope remains constant regardless of the chosen parameters. Therefore, the static linear stiffness is a single value.

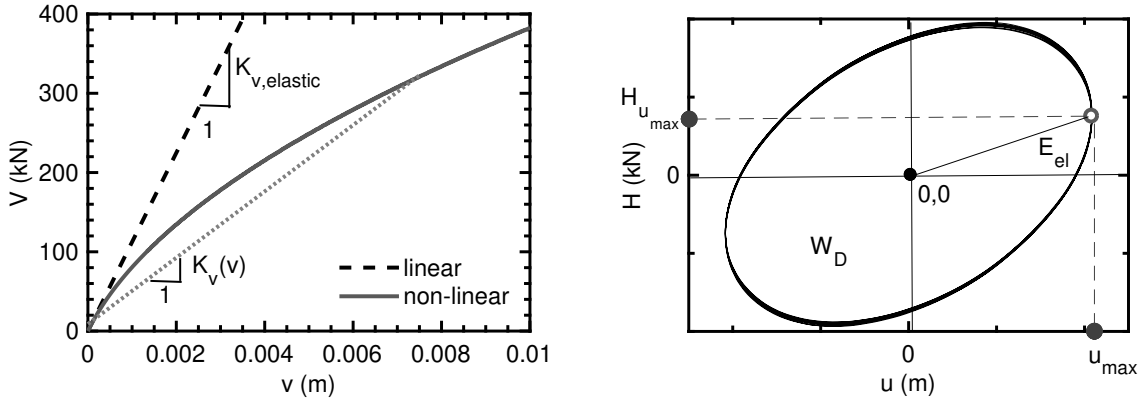

(a) (b)

Figure 3.3: (a) Example of linear and non-linear static vertical force versus settlement, and (b) Example loop; horizontal cyclic force versus horizontal displacement.

For non-linear static analyses, the stiffness is a function of the strain level and follows the stress-strain relationship defined by the constitutive model. At very small strains ($\gamma < 10^{-6}$), the stiffness must be in agreement with the aforementioned linear static stiffness also referred to as maximum stiffness in the corresponding mode of loading. For higher strain levels (e.g. higher displacement/rotation angle) the slope and consequently the stiffness is decreasing from its maximum value due to non-linearity as shown in Figure 3.3 (a) for the vertical loading case.

In dynamic analyses the data obtained are in the form of Figure 3.3 (b). For this type of loading the data processing involves the calculation of stiffness as well as damping. For the calculation of stiffness the maximum deformation and the corresponding reaction when this occurs are taken into account. The fraction of these two quantities is the

stiffness associated with the specific excitation frequency i.e.

$$\bar{K_h} = \frac{H_{u_{max}}}{u_{max}} \tag{3.25}$$

For the damping calculation the area inside the hysteresis loop is divided by the area of the triangle formed between the beginning of the axes, the maximum deformation and the reaction when the deformation is maximum. The damping ratio is given by equation 3.26 as explained in Section 2.2.1.1.

$$\xi = \frac{1}{4\pi}\frac{W_D}{E_{el}} \tag{3.26}$$

Although the effect of non-linearity if evident, there is no difference in data processing between linear and non-linear dynamic analyses.

CHAPTER 4

REVISITING LINEAR SOLUTIONS

A re-examination/revision of available linear elastic solutions in the literature is presented in *Chapter 4* and the calibration of the finite difference mesh is discussed. Model parameters such as mesh dimensions, fixities and element size are investigated and conclusions are drawn on the accuracy/credibility of current fitted formulae and design charts.

4.1 Revisiting linear static solutions

The numerical analyses have been validated against the linear static solutions which are revisited in this section. The scope of these analyses is to determine the effects of model dimensions and boundary fixities on the accuracy of the stiffness assessment. To this end, the expressions used to calculate the static stiffness of rigid strip footings resting on a homogeneous soil layer over a rigid base are re-examined (Table 4.1).

Table 4.1: Static stiffness of shallow foundations (modified from Ref. [2])

Vertical Stiffness	$K_v \simeq 0.73 \frac{G}{1-\nu}\left(1+3.5\frac{B}{H}\right)$
Lateral Stiffness	$K_h \simeq \frac{2G}{2-\nu}\left(1+2\frac{B}{H}\right)$
Rocking Stiffness	$K_{rx} \simeq \frac{\pi G B^2}{2(1-\nu)}\left(1+0.2\frac{B}{H}\right)$

It is reiterated that in the expressions in Table 4.1, B and H are the footing half width and the soil layer thickness, respectively, while G and ν are shear modulus and Poisson's ratio of the soil. Note that for $B/H \rightarrow 0$, a very deep layer, the terms in parenthesis tends to 1 and the first two formulae cease to be acceptable as the footing has zero stiffness. In this case, the last expression (due to Mushkelisvili, [32]) is exact for a smooth soil-footing interface.

The following subsections include evaluations of the effects of Poisson's ratio, element size, distance and fixities of lateral boundaries on the static stiffness for all three modes of loading. Three values of Poisson's ratio are investigated: 0.3, 0.35 and 0.40. In addition, two element sizes ($\Delta x = 0.4B$ and $0.2B$) are selected to evaluate the effect of mesh density on the response. Poisson's ratio and all other governing parameters related to material properties and geometry remain constant in the latter analyses to isolate the influence of element size.

In order to capture the influence of boundary fixities, four different sets of boundary conditions are considered, namely smooth and rough boundaries at rock level and fixed/free conditions at the lateral ends of the mesh. Specifically, the notion of a "free lateral boundary" indicates that the nodes at the edges of the model are free to move in the X and Y direction (horizontally and vertically), respectively. On the contrary, a "fixed lateral boundary" refers to side nodes with zero prescribed displacements. An intermediate state in which only the displacement across the horizontal direction is restricted is shown as "fixed horizontally". In these analyses, the bottom nodes are fixed to simulate a rough soil-rock interface at the base of the soil layer. The case of a "free to slide at the base" boundary is examined, for academic purposes, where the soil is free to slide at rock level accounting the extreme case of a smooth interface between soil and bedrock. The aforementioned effects are presented in the ensuing sections in terms of normalised stiffness versus lateral mesh size.

4.1.1 Vertical loading

Considering a vertically loaded footing, the reduction in stiffness with lateral mesh size is shown in Figure 4.1. The stiffness reaches a constant value after $s/B \approx 15$, regardless of Poisson's ratio, which indicates that the distance to the lateral boundaries does not influence vertical stiffness significantly. On the same graph, the stiffness calculated using (a) the formula of Ref [2] and (b) PLAXIS 2D numerical platform [147] are plotted. The discrepancy between the stiffness outcomes from the formula in Table 4.1 and the numerical results exceeds 30%. The outcomes are presented in Figure 4.1. The

numerical results produced by both FLAC and PLAXIS codes are in good agreement (maximum difference of less than 5%). All the results confirm the increase in stiffness with increasing Poisson's ratio.

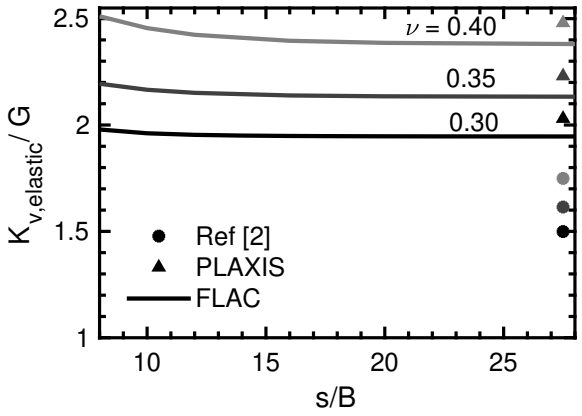

Figure 4.1: Influence of the lateral boundary distance and the Poisson's ratio on static vertical footing stiffness; $\Delta x = 0.4B$, $H/B = 8$.

Similarly to the aforementioned results, the fixities of the lateral boundaries do not influence the footing behaviour when placed at an adequate distance (Figure 4.2). On the other hand, reducing the element size from 0.4B to 0.2B results in 5% reduction in vertical footing stiffness as shown in Figure 4.3. However, this trait cannot justify the large difference between the fitted formula in Ref. [2] and the numerical results.

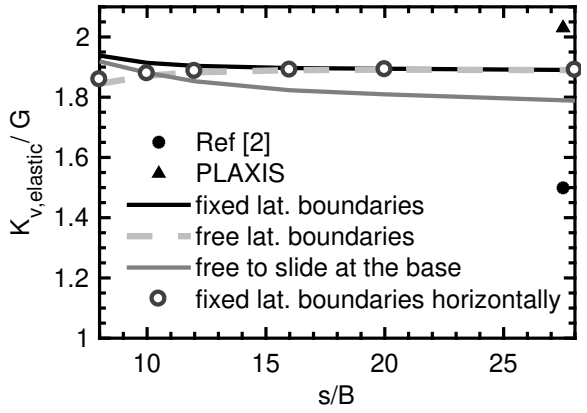

Figure 4.2: Boundary fixities effect on static vertical stiffness; $\Delta x = 0.2B$; $\nu = 0.3$, $H/B = 8$.

To evaluate the fitted formula used to calculate the vertical stiffness (Table 4.1), a closer look at the expression is necessary. The $(1 - \nu)$ term in the denominator is

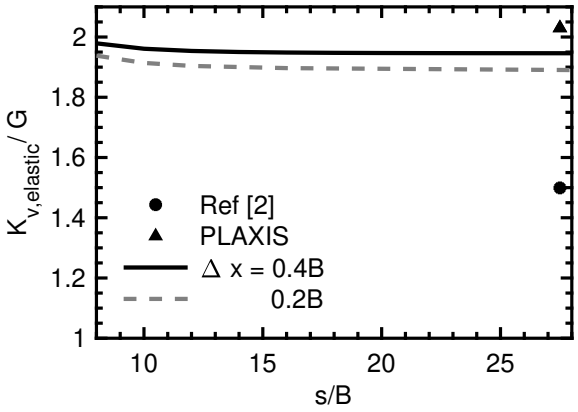

Figure 4.3: Element size effect on static vertical footing stiffness for fixed lateral boundary conditions; $\nu = 0.3$, $H/B = 8$.

part of the Boussinesq solution [18] and thus it is correctly part of the fitted formula. Therefore, the problem can be associated with the numerical values of 0.73 and 3.5 and the possibility of having the dimensionless group B/H being raised in a power other than 1.

Switching our attention to the related problem of a rigid circular disk on the surface of a homogeneous halfspace, the associated vertical and horizontal stiffnesses are given by the familiar expressions by Boussinesq (Eq. 4.1) [18] and Mindlin (Eq. 4.2) [27], respectively

$$K_v = \frac{4GR}{1-\nu} \tag{4.1}$$

$$K_h = \frac{8GR}{2-\nu} \tag{4.2}$$

Remarkably, in the extreme case of a geomaterial having zero Poisson's ratio ($\nu = 0$), vertical and horizontal stiffness are equal, $K_v = K_h$. In one postulates that the pattern at hand is the same in the plane strain mode as well, then the numerical factor in the right hand side of the vertical stiffness equation by Ref [2] should be equal to 1, as shown in Equation 4.3. It is important to note that the equality of horizontal and vertical stiffness for zero Poisson's ratio was confirmed numerically by FLAC for the plane strain case for a deep soil layer ($H > 30B$). Evidently, for a deep soil stratum, the dimensionless ratio B/H tends to 0, and thus the terms in the parentheses are on the order of 1.

$$K_v = \frac{G}{1-\nu}\left(1 + 3.5\frac{B}{H}\right) \tag{4.3}$$

Table 4.2: Comparison of numerical analyses results, literature and proposed expressions for different values of Poisson's ratio and $H/B = 8$

Expressions	$\nu = 0.3$		$\nu = 0.35$		$\nu = 0.4$	
	K_v/G	**discrep.**	K_v/G	**discrep.**	K_v/G	**discrep.**
FLAC	1.95		2.13		2.38	
PLAXIS	1.95	4%	2.24	5%	2.49	5%
Ref. [2]	1.50	23%	1.61	24%	1.75	26%
Equation 4.3	2.05	5%	2.21	3%	2.40	1%
Equation 4.4	1.94	< 1%	2.13	0%	2.36	< 1%

On the other hand, for an incompressible material such as saturated clay, $\nu = 0.5$, it turns out that the vertical stiffness in Equation 4.1 is 1.5 times higher than the horizontal counterpart which is satisfied in Equation 4.3.

However, in Table 4.2 it is noticeable that the discrepancy decreases with increasing Poisson's ratio. To capture this effect, an extra expression is introduced in which the factor 3.5 multiplying B/H is replaced by a function of Poisson's ratio as shown in Equation 4.4 below

$$K_v = \frac{G}{1-\nu}\left(1 + \frac{2}{1-\nu}\frac{B}{H}\right) \tag{4.4}$$

The difference between the proposed expressions and the results produced with FLAC in this study are shown in Table 4.2. The agreement between FLAC outcomes and Equation 4.4 is very good and it is insensitive to Poisson's ratio. However, Equation 4.4 does not fully account for the normalised soil layer thickness as shown in Table 4.3. To incorporate this effect, Equation 4.5 was derived. The discrepancies between the last expression and the numerical results are shown in Table 4.3 and are visualised in Figure 4.4.

$$K_v = \frac{G}{1-\nu}\left[1 + \frac{3.5}{1-\nu}\left(\frac{B}{H}\right)^{1.25}\right] \tag{4.5}$$

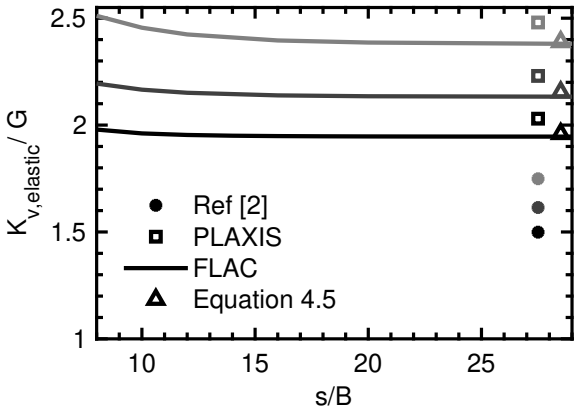

Figure 4.4: Boundary fixities effect on static vertical stiffness; $\Delta x = 0.2B$, $\nu = 0.3$, $H/B = 8$. [Modified from Fig. 4.2 to include Equation 4.5.]

Table 4.3: Comparison of results of vertical stiffness from numerical analyses, literature and proposed expressions for soil thickness; $\nu = 0.35$

Expressions	$H/B = 8$		$H/B = 4$		$H/B = 2$	
	K_v/G	**discr.**	K_v/G	**discr.**	K_v/G	**discr.**
FLAC	2.13		3.08		4.89	
PLAXIS	2.24	5%	3.19	4%	5.12	5%
Ref. [2]	1.61	24%	2.11	32%	3.09	37%
Equation 4.3	2.21	4%	2.88	6%	4.23	13%
Equation 4.4	2.13	< 1%	2.72	12%	3.91	20%
Equation 4.5	2.15	1%	3.00	2.5%	5.02	2.7%

4.1.2 Lateral loading

The normalised horizontal stiffness versus the lateral mesh size, s/B, for different values of Poisson's ratio is shown in Figure 4.5. Stiffness drops monotonically with increasing s/B, and the influence becomes asymptotic beyond $s/B \approx 20$. Higher values of Poisson's ratio naturally lead to higher stiffness. In general, an increase in Poisson's ratio by 0.05 leads to an increase in stiffness of about $4-7\%$. The fitted formula in Ref [2], may overestimate or underestimate stiffness by up to 5% depending on Poisson's ratio. This suggests that the factor $(2-\nu)$ in the denominator of the expression for K_h in Table 4.1, does not fully capture the influence of the specific parameter. To this end, a new expression is proposed herein, by replacing the factor of 2 in the parenthesis with a function of ν, as expressed in Equation 4.6. Using the new equation the agreement with the numerical results for sufficiently wide meshes becomes excellent.

$$K_h \simeq \frac{2G}{2-\nu}\left[1+3\nu\,(2-\nu)\frac{B}{H}\right] \tag{4.6}$$

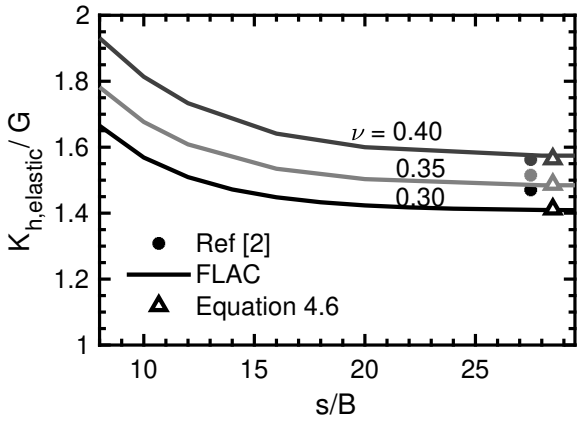

Figure 4.5: Influence of distance of lateral boundary and Poisson's ratio on the static horizontal footing stiffness; $\Delta x = 0.4B$, fixed lateral boundary conditions; $H/B = 8$.

In Figure 4.6, the sensitivity of the solution to the boundary conditions is shown. Evidently, restricting the movement of the base nodes only in the vertical direction results in 30% drop in stiffness when the footing is loaded horizontally. The other three fixity sets result in indistinguishable stiffness values when the lateral boundary is located at a sufficient distance from the footing ($s/B > 20$). Also, "fixed" and "fixed horizontally" boundary conditions lead to identical lateral footing stiffnesses. It is, therefore, suggested that only "free", "fixed" and "fixed horizontally" lateral boundaries need to be adopted and examined in the following analyses.

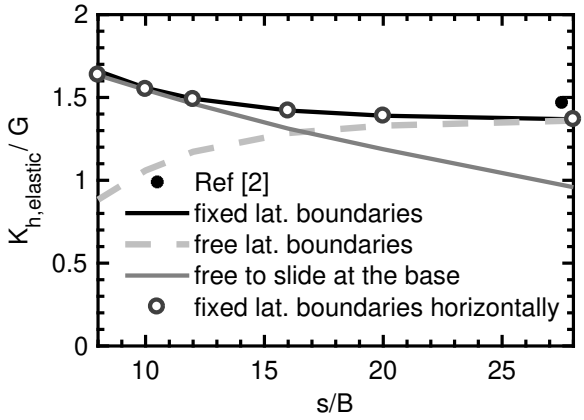

Figure 4.6: Boundary fixities effect on static horizontal footing stiffness; $\Delta x = 0.2B$, Poisson's ratio $\nu = 0.3$, $H/B = 8$.

Lastly, the effect of the element size on the horizontal stiffness is depicted in Figure 4.7. The maximum difference in stiffness between the two cases is only 2%, which justifies the use of coarser mesh. In this vein, a grid of square elements with $0.4B$ side is adopted in all ensuing analyses to evaluate the horizontal stiffness.

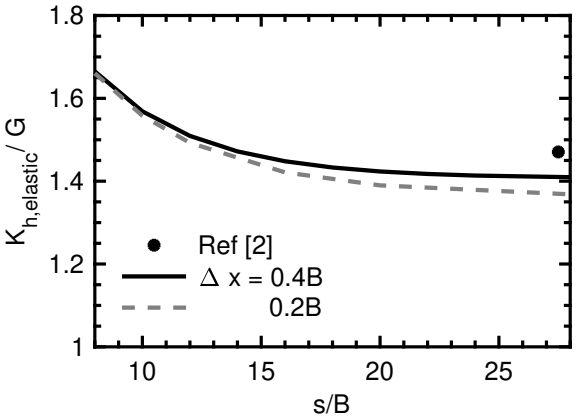

Figure 4.7: Element size effect on static horizontal footing stiffness for fixed lateral boundary conditions; Poisson's ratio $\nu = 0.3$, $H/B = 8$.

4.1.3 Rocking

Unlike horizontal stiffness, rocking response is much less sensitive to mesh size as depicted in Figure 4.8. This can be attributed to Saint Venant 's principle associated with the self-cancelling action of two adjacent vertical loads of opposite sign, that limits soil deformations in the vicinity of the footing. Naturally, foundations are stiffer for higher

values of Poisson 's ratio. The agreement with the relevant fitted formula in Table 4.1 is very good for all the cases examined (maximum discrepancy less than 3.5%). However, the difference is not consistent. For example, for $\nu = 0.4$ the fitted formula slightly overestimates footing stiffness, while for $\nu = 0.3$ and $\nu = 0.35$ the formula underestimates stiffness. These discrepancies are of minor importance from a geotechnical engineering viewpoint.

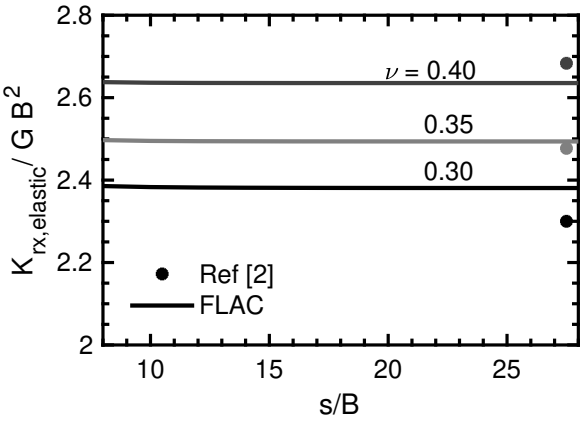

Figure 4.8: Influence of lateral boundary distance and Poisson's ratio on static rocking footing stiffness; $\Delta x = 0.4B$.

In the same vein, rocking foundations are not affected by the fixities at the lateral boundaries. As shown in Figure 4.9, almost all the considered sets of fixities produce similar rocking stiffness values with the highest divergence being 0.7% in the case of a sliding soil layer at the base. For the sake of consistency with the other loading modes, fixed boundaries are adopted hereafter.

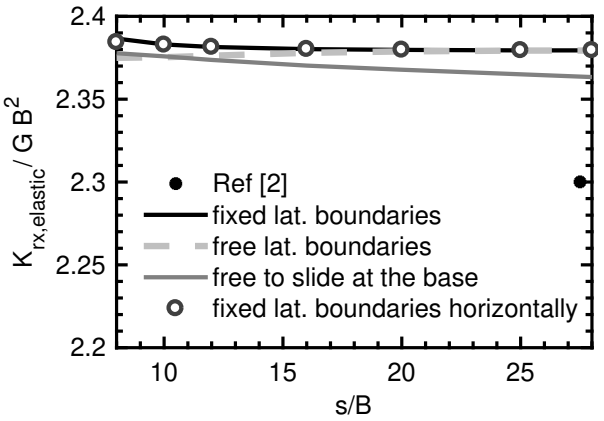

Figure 4.9: Boundary fixities effect on static rocking footing stiffness; $\Delta x = 0.2B$, $\nu = 0.3$.

In terms of element size, it is evident from Figure 4.10 that $0.4B$ long elements do not have a toll on the accuracy of the stiffness calculation. Therefore, the need of refining the grid is not important.

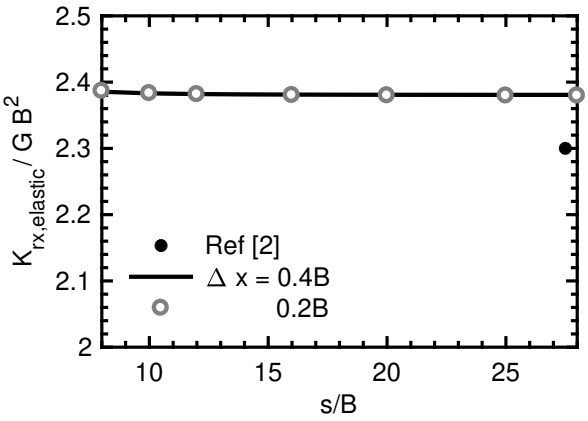

Figure 4.10: Element size effect on static rocking footing stiffness for fixed lateral boundary conditions; $\nu = 0.3$, $H/B = 8$.

4.1.4 Key remarks on linear static analyses

Summarising the observations from foregoing analyses one can draw the following conclusions:

- The influence of lateral mesh size is important in swaying, yet it is practically negligible in rocking.
- An increase in Poisson's ratio naturally leads to an increase in stiffness in all modes of loading.
- The most realistic results were obtained when both lateral and bottom boundary have restricted degrees of freedom along the horizontal, Y and vertical, Z directions.
- No noticeable differences can be observed between the two selected element sizes in swaying and rocking. This leads to the conclusion that an element size of $0.4B$ is sufficient for static horizontal and rocking analyses. In contrast, for static vertical analyses, $0.2B$ is recommended.
- For swaying foundations when s/B is equal or higher than approximately 20, the stiffness reaches a constant value no matter the boundary fixities. The corresponding value of s/B is around 15 and 8 for vertically-loaded and rocking footings, respectively. For (s/B) values lower than the aforementioned limits, stiffness is

either increasing (for free side boundaries) or decreasing (for fixed side boundaries). This can be explained as the restrictions of fixed boundaries results in a stiffer medium and vice versa.

- The expressions for the calculation of the vertical and the horizontal stiffness provided in the literature are revisited and new expressions are suggested to fully account for the influence of Poisson's ratio and soil layer thickness.

4.2 Revisiting existing elastodynamic solutions

Following static loading, linear dynamic analyses were conducted for non-dimensional frequency values, a_0, ranging between 0 and 2. The sinusoidal input motion used for the dynamic analyses is shown in Figure 4.11, in terms of the acceleration applied directly on the footing. Only the constant amplitude part of the sinusoidal motion (20 cycles) is accounted for in the stiffness and damping coefficient calculations.

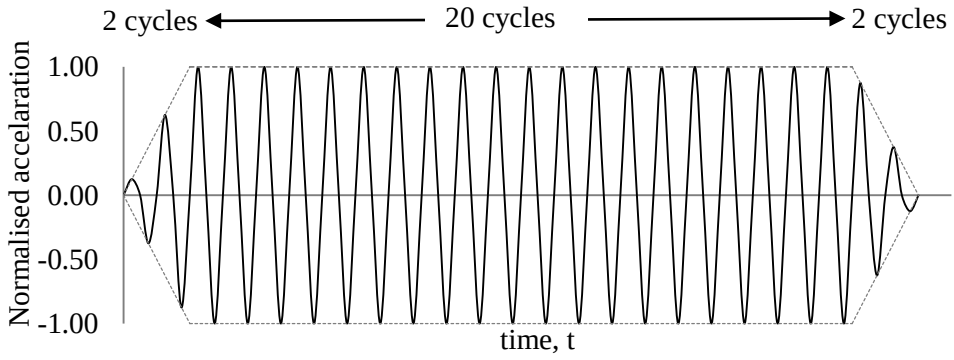

Figure 4.11: Sinusoidal input motion expressed in terms of acceleration applied directly on the rigid footing

To obtain satisfactory results, 8 to 10 gridpoints per wavelength λ are necessary. If N is the number of elements per wave length, then the requirement is $N = 8-10$. Therefore, the maximum element size for dynamic analysis is

$$s = \frac{\lambda}{N} \tag{4.7}$$

Given that

$$\lambda = \frac{V_s}{f} = 2\pi\frac{V_s}{\omega} \tag{4.8}$$

and in light of the normalised parameter α_0

$$\alpha_0 = \frac{\omega B}{V_s} \tag{4.9}$$

one could write

$$\frac{s}{B} = \frac{2\pi}{\alpha_0 N} \tag{4.10}$$

Parameter α_0 ranges from 0 to 2. For the maximum α_0 value of about 2 (high frequency analysis) the requirement is

$$\frac{s}{B} = 0.4 \;\; (N = 8) \tag{4.11}$$

Consequently, an element size of $0.4B$ is sufficient for the dynamic analyses since these are carried out for frequencies below $\alpha_0 = 2$.

4.2.1 Vertical harmonic oscillations

Considering vertical harmonic oscillations on massless footing resting on a shallow soil layer with $H/B = 2$, the normalised linear stiffness and the damping ratio are illustrated in Figures 4.12 to 4.16 versus the dimensionless frequency.

In Figure 4.12 three different types of mechanical damping are examined; namely Rayleigh, local and combined damping. The results are similar in stiffness terms, while fluctuations in the damping ratio are evident especially for the case of local damping. Combined and local types do not capture material damping, therefore Rayleigh is preferred for the following analyses.

During excitation, waves propagate away from the loaded footing, reflect at the interface between soil and bedrock and return back to surface. As a result, foundation response increases considerably at specific excitation frequencies near the natural frequencies of the soil layer. This phenomenon, where the waves are constructing causing a significantly higher response is resonance and it can be spotted in normalised stiffness graphs at zero stiffness e.g. Figure 4.12 or as a valley e.g. Figure 4.18 .

All three types of damping can capture resonance at the system's natural frequency accurately.

Rayleigh damping, as described earlier in *Section 3.6*, is defined in FLAC by the centre frequency f_{min} and the damping ratio ξ_{min}. The effect of the centre frequency in stiffness and damping is illustrated in Figure 4.13. For f_{min} greater than the natural frequency f_1, the centre frequency does not affect neither the stiffness of the foundation nor the soil

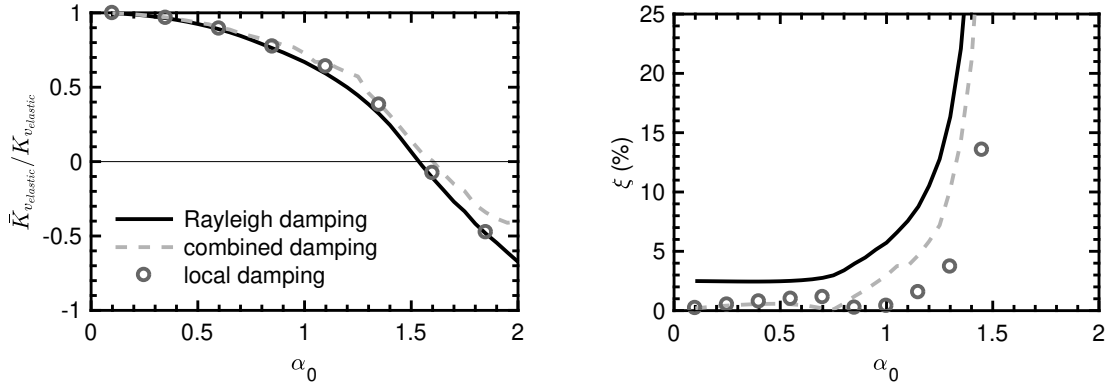

Figure 4.12: (a) Normalised linear dynamic vertical stiffness over elastic static vertical stiffness and (b) damping ξ versus dimensionless frequency for different types of damping; $H/B = 2$, $\nu = 0.30$, $\xi = 5\%$.

damping. This is not the case for smaller f_{min}, where the stiffness is overestimated and the system is over-damped before resonance occurs. Therefore, it is shown that Rayleigh damping is frequency independent over a range or predominant frequencies around the natural frequency of the system.

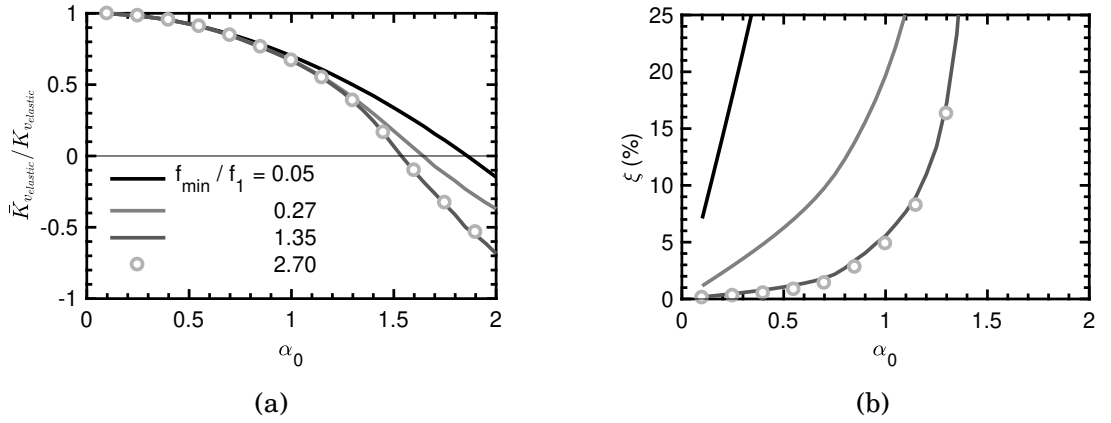

Figure 4.13: (a) Normalised linear dynamic vertical stiffness over elastic static vertical stiffness and (b) damping ξ versus dimensionless frequency for different f_{min} of Rayleigh damping; $H/B = 2$, $\nu = 0.30$, $\xi_{min} = 5\%$.

A concern is arising from Figure 4.13 as the damping is zero for small dimensionless frequencies. By changing the centre frequency, f_{min}, to the excitation frequency, f_{exc}, one can draw the plots in Figure 4.14. Although the dimensionless stiffness is indistinguish-

able between the two cases, the damping ratio differs up to $\alpha_0 = 0.6$ and does not reach the prescribed value of 5%.

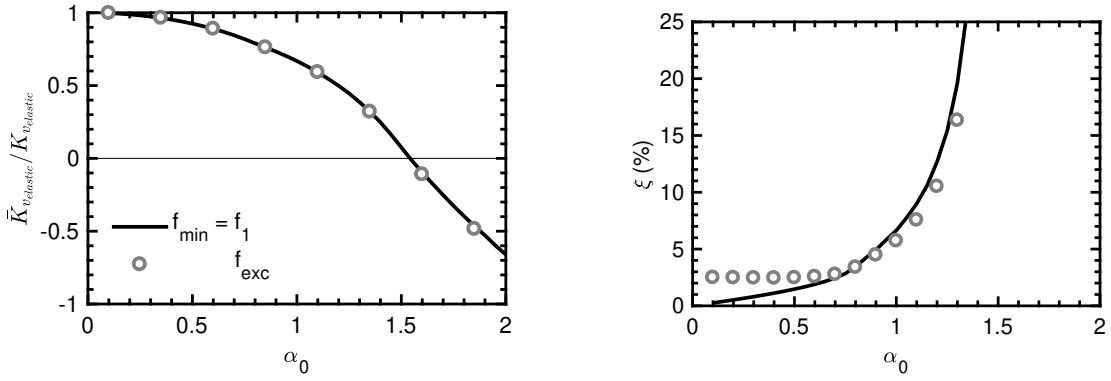

(a) (b)

Figure 4.14: (a) Normalised linear dynamic vertical stiffness over elastic static vertical stiffness and (b) damping ξ versus dimensionless frequency for different f_{min} of Rayleigh damping; $H/B = 2$, $\nu = 0.30$, $\xi_{min} = 5\%$.

To investigate this effect and the effect of the damping ratio, ξ_{min}, Figure 4.15 is explored. It is naturally evident that higher Rayleigh damping ratios result in higher system damping but the ratios do not correspond to what has been assigned to the system. In fact, for low frequencies, ξ is half the value of ξ_{min}. It is worth noticing that even for a theoretically undamped soil the system is damped closed to resonance, but this is due to wave radiation effects at the boundaries.

By separating the two Rayleigh damping components to mass-proportional damping and stiffness-proportional damping, one can get the results shown is Figure 4.16. Looking at the stiffness part, the different damping components differentiate for α_0 greater than 1.5, when the phase angle between force applied and the resulting settlement is more than 90^o. On Figure 4.16 (a), it is shown that the mass-proportional part if damping does not contribute to the overall damping of the system.

An increase in depth of the soil layer by a factor of 2, decreases the natural dimensionless frequency by the same factor, as expected. Therefore, the damping reaches extreme values and the stiffness dips for $\alpha_1 \approx 0.9$. Contrary to Figure 4.13 where stiffness appears to be unaffected by the selected centre frequency in Rayleigh damping, Figure 4.18 shows that lower values of f_{min} result in lower stiffness values beyond resonance. For f_{min} equal to the excitation frequency, the stiffness follows the same trend as for f_{min} equal to the natural frequency (Figure 4.19). However, the damping curve for low frequencies

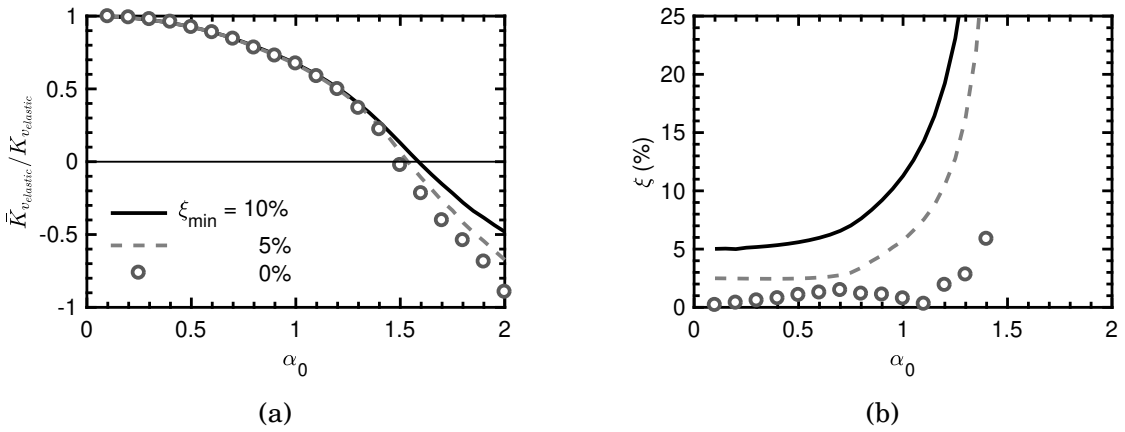

(a) (b)

Figure 4.15: (a) Normalised linear dynamic vertical stiffness over elastic static vertical stiffness and (b) damping ξ versus dimensionless frequency for variable ξ_{min} of Rayleigh damping; $H/B = 2$, $\nu = 0.30$.

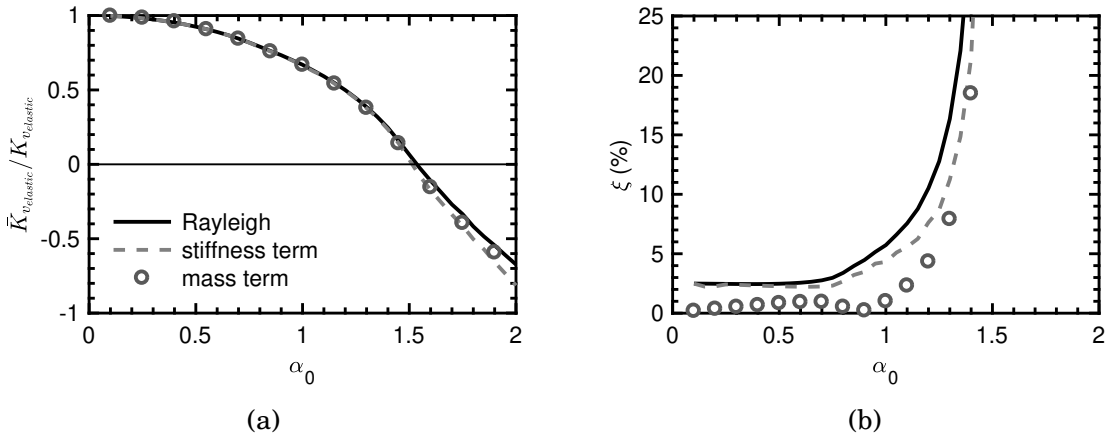

(a) (b)

Figure 4.16: (a) Normalised linear dynamic vertical stiffness over elastic static vertical stiffness and (b) damping ξ versus dimensionless frequency for mass, stiffness and total Rayleigh damping; $H/B = 2$, $\nu = 0.30$, $\xi_{min} = 5\%$.

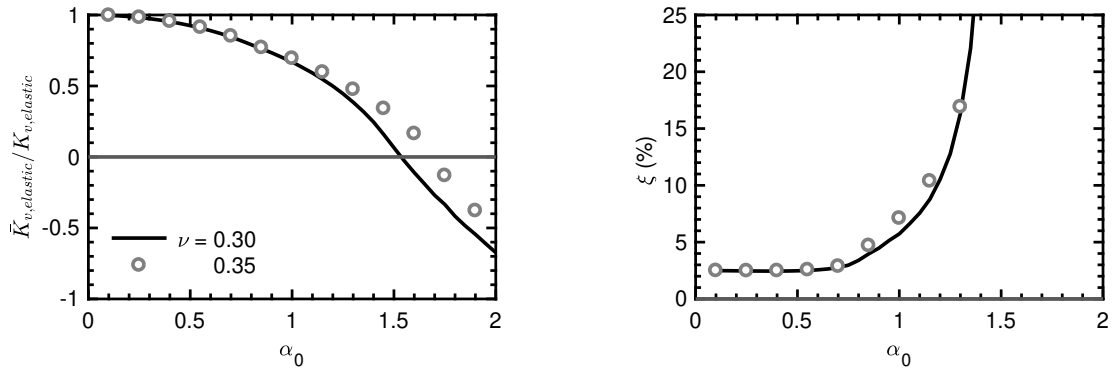

(a) (b)

Figure 4.17: Poisson's ratio influence on the (a) normalised linear dynamic vertical stiffness over elastic static vertical stiffness and (b) damping ξ versus dimensionless frequency; $H/B = 2$, $\xi_{min} = 5\%$, $f_{min} = f_{exc}$.

appears more realistic.

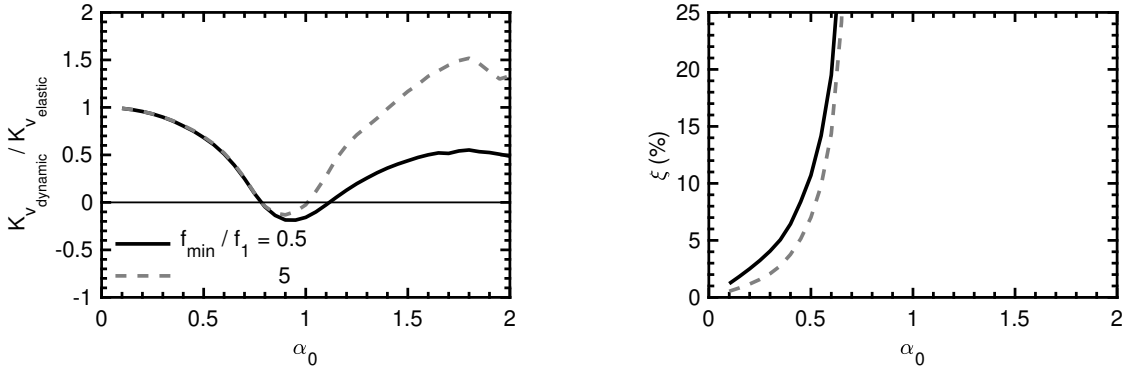

(a) (b)

Figure 4.18: (a) Normalised linear dynamic vertical stiffness over elastic static vertical stiffness and (b) damping ξ versus dimensionless frequency for different f_{min} of Rayleigh damping; $H/B = 4$, $\nu = 0.30$, $\xi_{min} = 5\%$.

The influence of Poisson's ratio on the dynamic vertical stiffness and damping is depicted in Figure 4.20. Naturally, the resonance is shifted to the right for higher Poisson's ratio and the stiffness is slightly lower. In terms of damping, Poisson's ratio has no significant effect.

The natural frequency of the system is given by the equation

$$f_1 = \frac{V_{pr}}{4H} \tag{4.12}$$

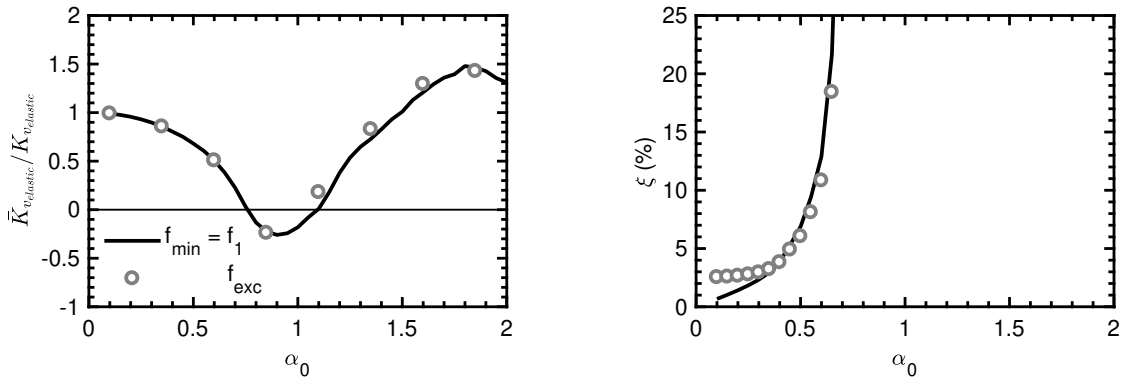

(a) (b)

Figure 4.19: (a) Normalised linear dynamic vertical stiffness over elastic static vertical stiffness and (b) damping ξ versus dimensionless frequency for different f_{min} of Rayleigh damping; $H/B = 4$, $\nu = 0.30$, $\xi_{min} = 5\%$.

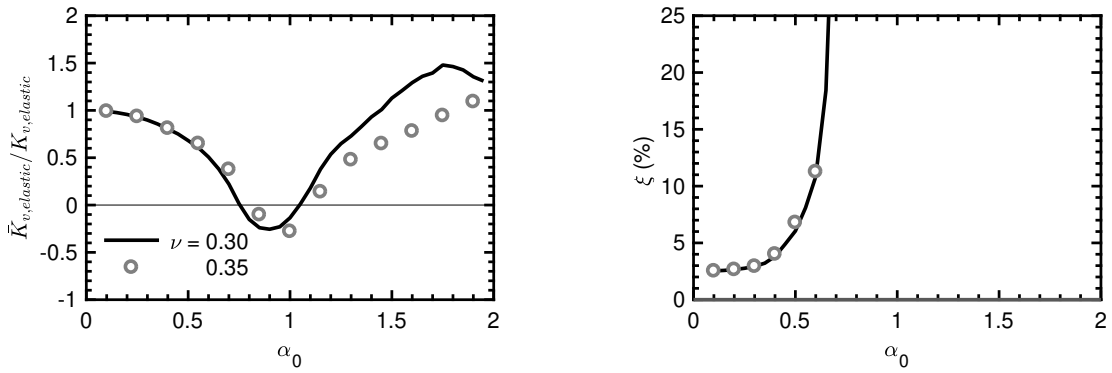

(a) (b)

Figure 4.20: Poisson's ratio influence on the: (a) normalised linear dynamic vertical stiffness over elastic static vertical stiffness and (b) damping ξ versus dimensionless frequency; $H/B = 4$, $\xi_{min} = 5\%$, $f_{min} = f_{exc}$.

with V_{pr} being the pertinent compressional wave propagation velocity and H the soil stratum thickness. In the case of vertical oscillations the wave propagation velocity could be either the P-wave propagation velocity of a homogeneous isotropic medium by

$$V_p = \sqrt{\frac{K + \frac{4}{3}G}{\rho}} = V_s \sqrt{\frac{2\,(1-\nu)}{1-2\nu}} \tag{4.13}$$

or the compression velocity proposed by Anoyatis et al [151], which is not strongly dependent on Poisson's ratio

$$V_c = V_s \sqrt{\frac{2}{1-\nu}} \tag{4.14}$$

Alternatively, V_{pr} could be the apparent prorogation velocity of compression-extension waves under a foundation, widely known as the Lysmer's analog velocity [152], expressed as a function of shear wave velocity as follows

$$V_{La} = \frac{3.4\,V_s}{\pi(1-\nu)} \tag{4.15}$$

In the light of the above, the dimensionless natural frequency is given by the equation

$$\alpha_1 = \frac{\pi}{2}\frac{B}{H}\frac{V_{pr}}{V_s} \tag{4.16}$$

A summary of the different values of α_1 is given in the Table 4.4 considering all possible compressional wave propagation velocities described above and the two soil layer thickness examined. It appears that the resonant dimensionless frequency can be calculated reasonably well using the compression velocity V_p.

Table 4.4: Natural dimensionless frequency, α_1, values using different wave propagation velocities for Poisson's ratio, ν, equal to 0.3.

Propagation velocity used in Eq. 4.16	$H/B = 2$	$H/B = 4$
FLAC numerical solution (Figs 4.17, 4.20)	1.50	0.90
P-wave propagation velocity, V_p	1.47	0.73
Anoyatis et al [151], V_c	1.33	0.66
Lysmer's analog velocity [152], V_{La}	1.21	0.61

4.2.2 Lateral harmonic oscillations

Switching our attention to lateral harmonic oscillations, the effect of Poisson's ratio and element size are investigated for three different soil layer thicknesses: H/B = 2, 4, 8. The results are presented in terms of normalised stiffness and damping curves versus dimensionless frequency.

Several peaks and valleys are observed in normalised stiffness as a result of resonance phenomena. Shear and volumetric waves emanate from the oscillating footing, reflect on the bedrock interface and return to the surface. To this end, normalised stiffness fluctuates from almost zero (0) to two (2). Normalised stiffness higher than 1 indicated that waves are destructive resulting in response smaller than the response in case of static loading. Hence, the dynamic stiffness is higher than the static.

For a soil thickness equal to the width of the footing, $2B$, Poisson' s ratios of 0.30 to 0.40 produce indistinguishable stiffness curves up to α_0 = 1.3 as shown in Figure 4.21 (a). For α_0 between 1.3 and 1.6 an increase in Poisson' s ratio results in an increase in stiffness and resonant frequency. Normalised swaying stiffness considering ν = 0.40 produce twice the stiffness of the counterpart for ν equal to 0.30 for α_0 = 1.5. The trend is flipping for α_0 greater than 1.7. On the contrary, damping curves appear to be identical in Figure 4.21 (b) regardless of Poisson' s ratio. Hence Poisson' s ratio has no influence on damping for a shallow soil layer.

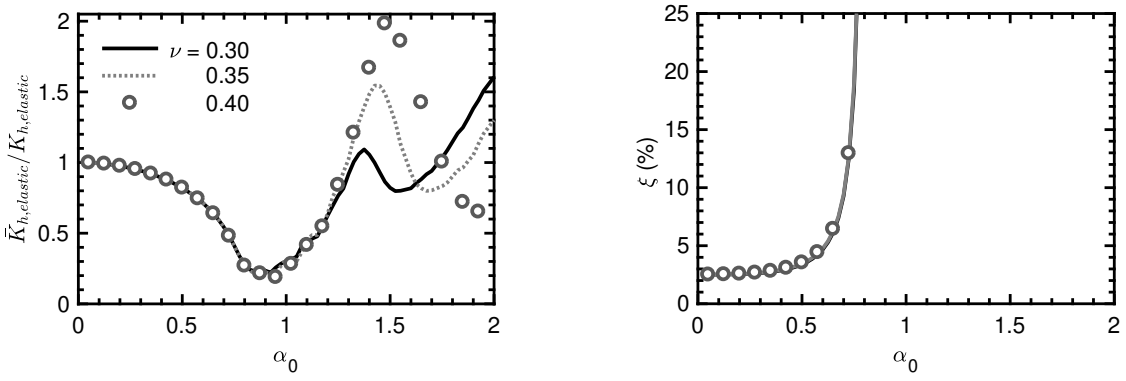

(a) (b)

Figure 4.21: Poisson's ratio influence on (a) normalised linear dynamic swaying stiffness over elastic static swaying stiffness and (b) damping ξ versus dimensionless frequency; $H/B = 2$, $\xi_{min} = 5\%$, $f_{min} = f_{exc}$, $V_s = 200\ m/s$, $\Delta x = 0.2B$.

Unlike the results for vertical oscillations, element size seems to influence considerably the lateral stiffness and damping after the first resonance as illustrated in

Figure 4.22. The difference in stiffness is increasing with α_0 beyond the first resonance and reaches around 20% for $\alpha_0 = 2$. Nevertheless, the trend remains the same in all three cases studied. On the other hand, damping is affected prior to resonance and the difference is on the order of 10%. This shows that the lateral mode of loading is more sensitive to the element size and the selection of element size should be made with caution.

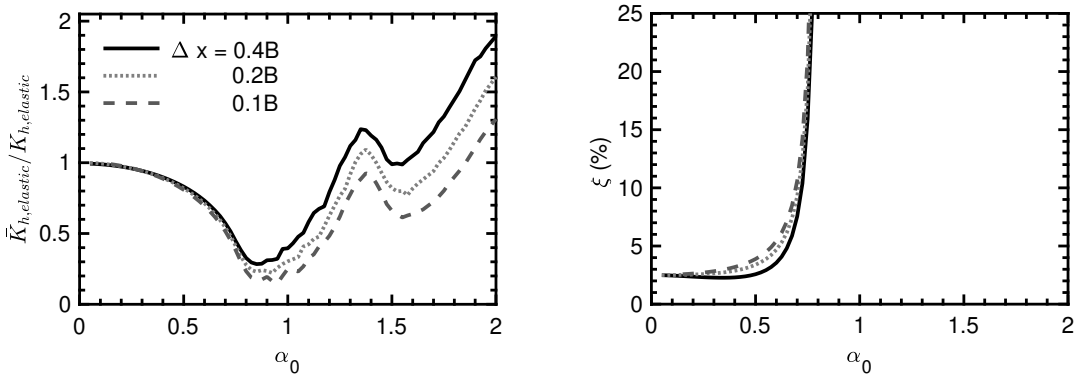

(a) (b)

Figure 4.22: Element size, Δx, influence on: (a) normalised linear dynamic swaying stiffness over elastic static swaying stiffness and (b) damping ξ versus dimensionless frequency; $\nu = 0.30$, $H/B = 2$, $\xi_{min} = 5\%$, $f_{min} = f_{exc}$, $V_s = 200\ m/s$.

Moving to a soil layer having twice the width of the footing, the results are changing slightly. Dynamic lateral stiffness curves are generally identical, unaffected by Poisson' s ratio, except for the part between the first and the second resonance (α_0 from 0.6 to 1.2). The natural dimensionless frequencies are accurately depicted on Figure 4.23 a. Following Eq. 4.17 for $H/B = 4$ those are in increasing order: $\alpha_{0_1} = 0.4$, $\alpha_{0_2} = 1.2$, $\alpha_{0_3} = 2.0$.

$$\alpha_{0_n} = n\frac{\pi}{2}\frac{B}{H} \qquad n = 1,3,5,7,... \tag{4.17}$$

An additional dip in stiffness is observed at a dimensionless frequency which seems to be affected by Poisson' s ratio and is ranging between 0.6 and 0.95. This phenomenon is also discussed in the literature [2]. As already discussed, damping is naturally unaffected by Poisson' s ratio and this is confirmed in Figure 4.23 (b).

The element size, Δx, effect is not as evident as for the case of $H/B = 2$. Stiffness is only slightly affected (by about 10%) for high excitation frequencies whilst damping is

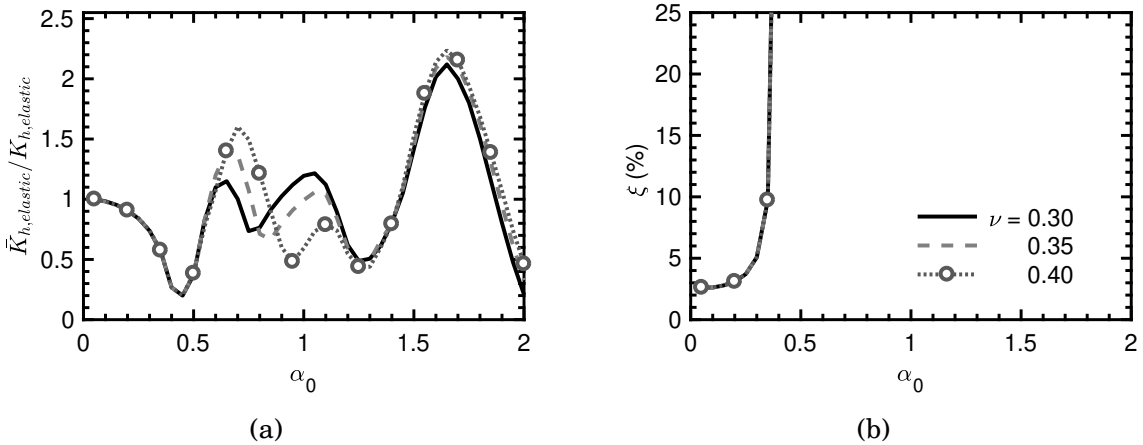

Figure 4.23: Poisson's ratio influence on: (a) normalised linear dynamic swaying stiffness over elastic static swaying stiffness and (b) damping ξ versus dimensionless frequency; $H/B = 4$, $\xi_{min} = 5\%$, $f_{min} = f_{exc}$, $V_s = 200m/s$.

not influenced as depicted in the graphs of Figure 4.24.

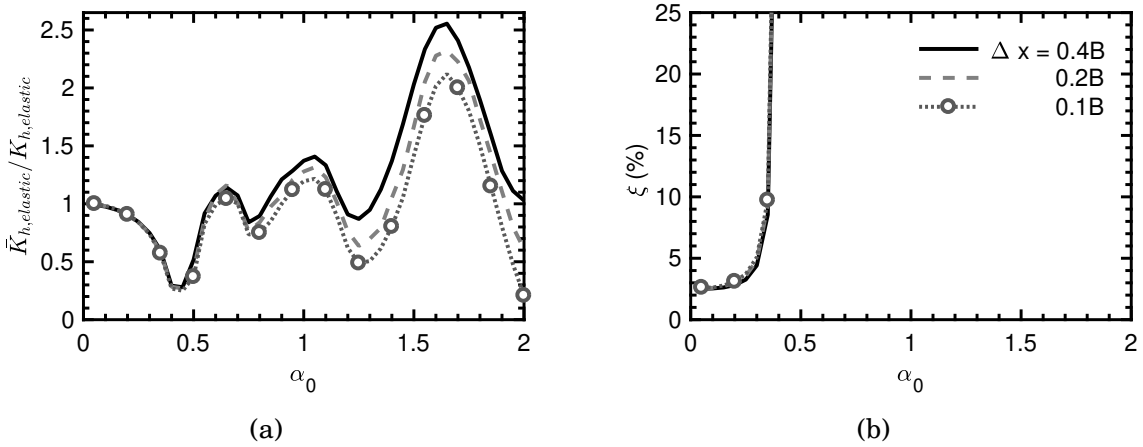

Figure 4.24: Element size, Δx, influence on: (a) normalised linear dynamic swaying stiffness over elastic static swaying stiffness and (b) damping ξ versus dimensionless frequency; $\nu = 0.30$, $H/B = 4$, $\xi_{min} = 5\%$, $f_{min} = f_{exc}$, $V_s = 200m/s$.

Lastly, for a thicker soil layer, ($H/B = 8$), the influence of Poisson' s ratio is minor. hlSome discrepancies are observed in the stiffness curves (Figure 4.25 (a)) for dimensionless frequencies between 0.3 to 0.6 but in all other cases the stiffness curves match. This phenomenon showcases stiffness sensitivity with Poisson's ratio. Volumetric waves which are inherently affected by Poisson's ratio dominate the response at the aforementioned frequency range. Outside this range, the response is shear wave dominated and that is

why no further discrepancies are observed. Natural dimensionless frequencies of the soil are again accurately depicted at 0.20, 0.60, 1.00, 1.4 and 1.8. The dynamic stiffness is gradually increasing with frequency reaching a maximum of 2.3 times the static stiffness.

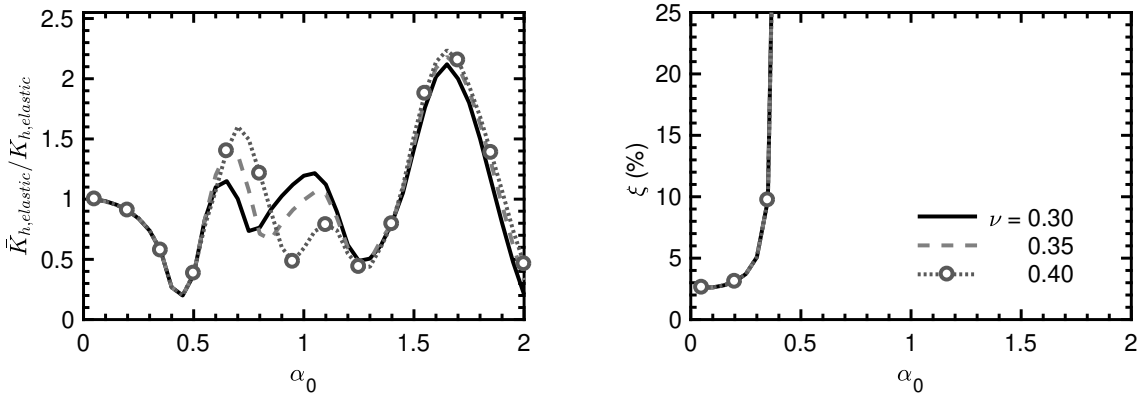

(a) (b)

Figure 4.25: Poisson's ratio influence on: (a) normalised linear dynamic swaying stiffness over elastic static swaying stiffness and (b) damping ξ versus dimensionless frequency; $H/B = 8$, $\xi_{min} = 5\%$, $f_{min} = f_{exc}$, $V_s = 200m/s$.

Similar to the previous cases studied regarding the lateral soil stiffness, element size affects the analyses in high frequencies (Figure 4.26). The discrepancy observed does not exceed 15%. Damping is evidently unaffected.

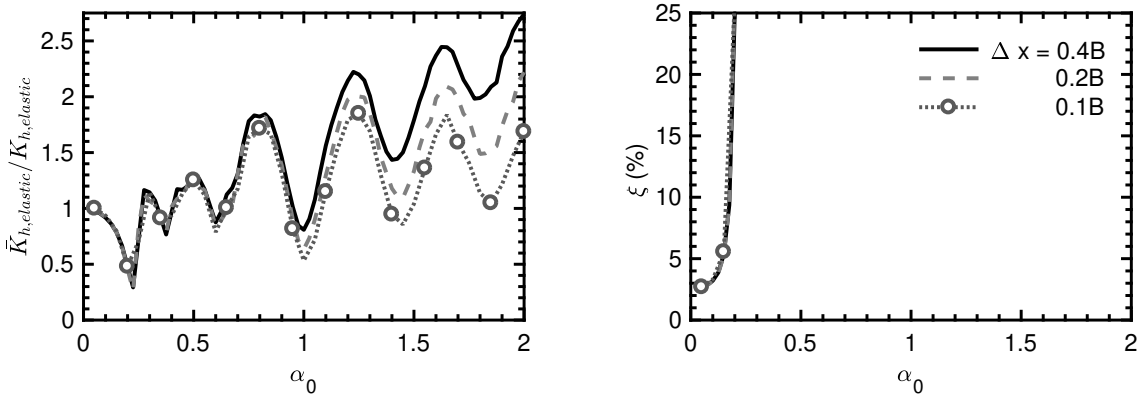

(a) (b)

Figure 4.26: Element size, Δx, influence on: (a) normalised linear dynamic swaying stiffness over elastic static swaying stiffness and (b) damping ξ versus dimensionless frequency; $\nu = 0.30$, $H/B = 8$, $\xi_{min} = 5\%$, $f_{min} = f_{exc}$, $V_s = 200m/s$.

4.2.3 Harmonic rocking oscillations

In presence of rock the rocking stiffness and the damping are influenced by soil thickness as seen in Figure 4.27. A significant dip in stiffness is observed for the shallowest soil layer examined, $H/B = 2$, close to the natural frequency of the system ($\alpha_0 = 1.45$, Figure 4.27). The dip in stiffness is matching the rapid increase in damping. This phenomenon proves that resonance occurs in a shallow soil layer over rigid bedrock. A similar behaviour is noticed for the slightly deeper soil layer ($H/B = 4$). Resonance occurs naturally at around $\alpha_0 = 0.7$.

For layer deeper than 8 times the footing halfwidth, the presence of bedrock does not affect the results due to Saint-Venant's principle. The stiffness is gradually decreasing while damping is increasing.

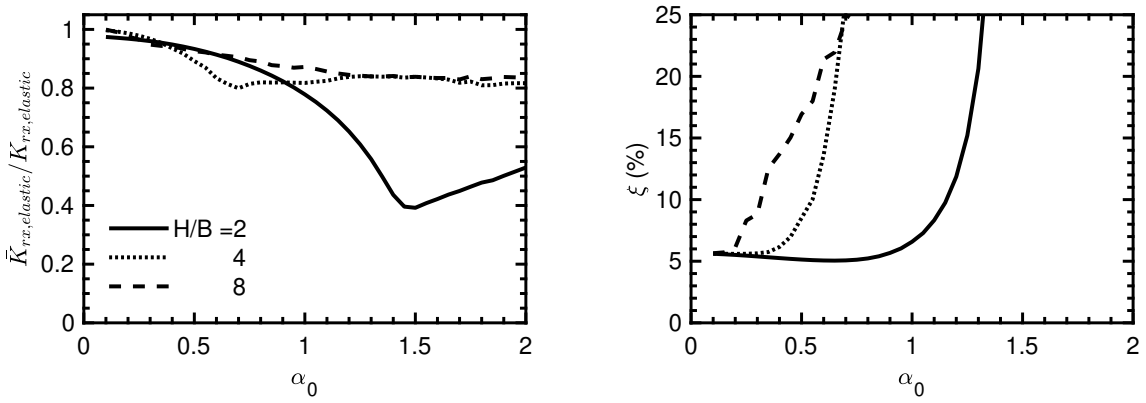

(a) (b)

Figure 4.27: (a) Normalised linear dynamic rocking stiffness over elastic static rocking stiffness and (b) damping ξ versus dimensionless frequency; $\Delta x = 0.2B$, $\nu = 0.30$, $H/B = 2$, $\xi_{min} = 5\%$, $f_{min} = f_{exc}$, $V_s = 200\ m/s$.

Linear dynamic rocking stiffness and damping are affected by element size only in high dimensionless frequencies as shown in Figures 4.28 (a) and (b), respectively. An element size of $0.2B$ is sufficient. The outcomes are less than a maximum of 5% different than the results for element half the size and the analysis is faster computationally.

Poisson's ratio does not have an effect in linear dynamic rocking stiffness neither in terms of stiffness nor damping as seen in Figures 4.29 (a) and (b), respectively. The effect in stiffness is eliminated as a result of the normalisation over the static elastic rocking stiffness and naturally Poisson's ratio does not affect damping.

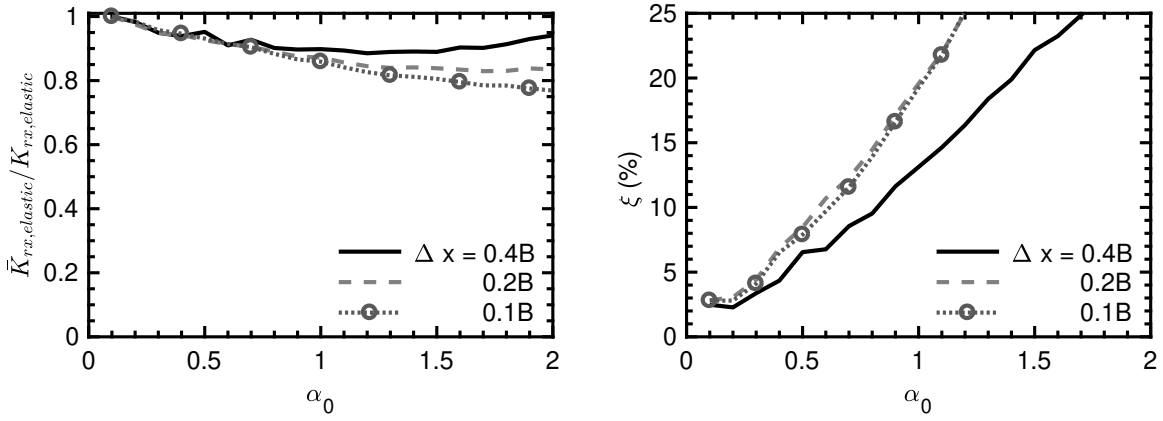

(a) (b)

Figure 4.28: Element size, Δx, influence on: (a) normalised linear dynamic rocking stiffness over elastic static rocking stiffness and (b) damping ξ versus dimensionless frequency; $\nu = 0.30$, $H/B = 8$, $\xi_{min} = 5\%$, $f_{min} = f_{exc}$, $V_s = 200\ m/s$.

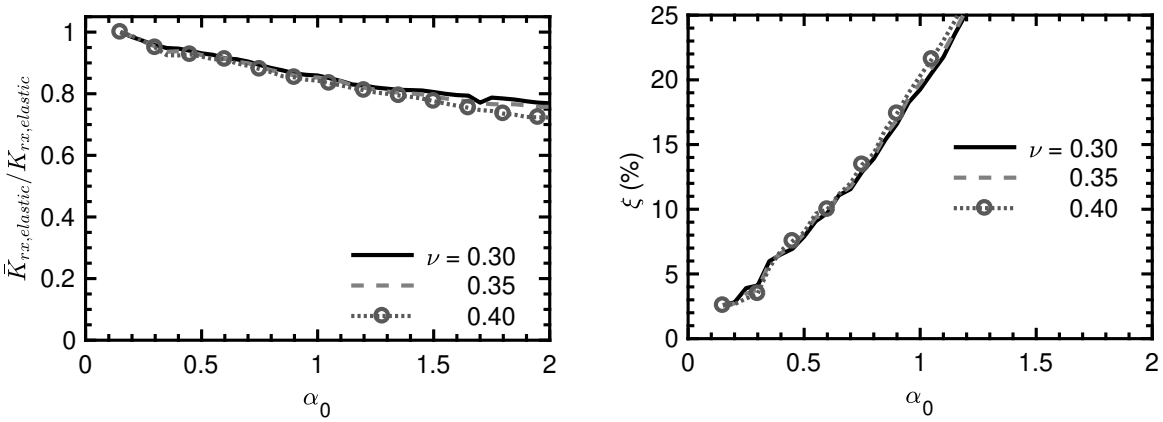

(a) (b)

Figure 4.29: Poisson's ratio influence on: (a) normalised linear dynamic rocking stiffness over elastic static rocking stiffness and (b) damping, ξ, versus dimensionless frequency; $\Delta x = 0.2B$, $H/B = 8$, $\xi_{min} = 5\%$, $f_{min} = f_{exc}$, $V_s = 200 m/s$.

4.3 Key remarks on linear dynamic analysis

The aforementioned results are discussed herein and comparisons are made where published results were available. In case of discrepancies conclusions are drawn with regards to selecting the most appropriate result. In certain cases further comparisons where made against analyses performed in the frequency domain by Karatzia [148] using Isobem.

First, the lateral dynamic stiffness is compared with published curves by Gazetas [2]. The results are illustrated in Figure 4.30 for $H/B = 2$ and 4, while Figure 4.31 accounts for $H/B = 8$.

Looking at Figure 4.30 (a), the lateral stiffness is slightly shifted compared to the literature data. The behaviour appears to be similar up to a dimensionless frequency $\alpha_0 = 1.4$. Beyond that point, lateral stiffness in numerical analysis with FLAC is exhibiting a decrease followed by a steep increase for α_0 greater than 1.6. In contrast, the stiffness curve suggested by Gazetas does not increase further for high frequencies. FLAC results can be explained by taking into consideration the natural frequency of the deposit. In all lateral stiffness figures presented herein, a valley is observed at α_0 equal to two times the natural frequency of the deposit ($\alpha_{0_1} = 0.8$ in this instance).

The agreement for $H/B = 4$ in Figure 4.30 (b) is excellent up to $\alpha_0 = 1.3$. However, the peak stiffness modifier at $\alpha_0 = 1.7$ is 45% higher in numerical analyses with FLAC2D. This phenomenon can be partially attributed to difference damping assumptions.

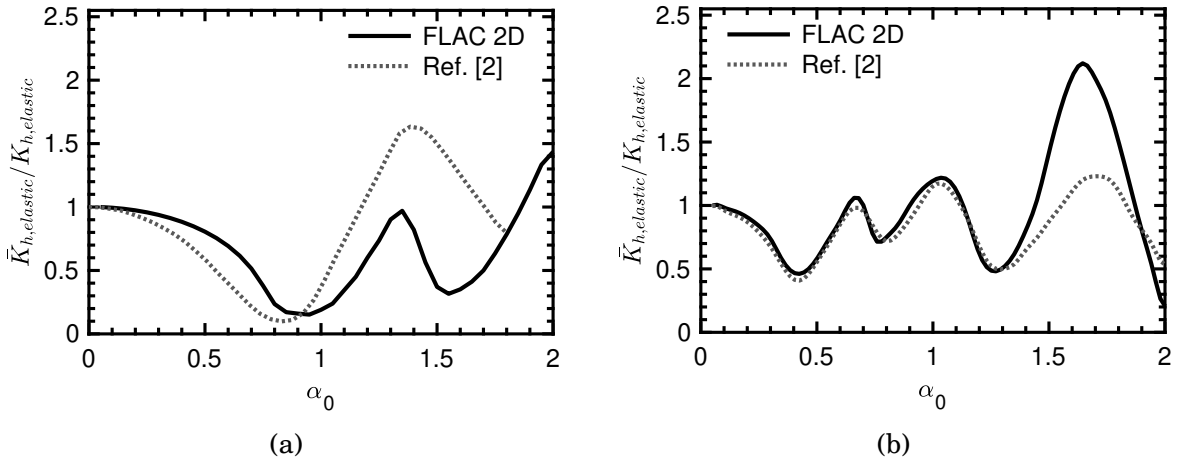

Figure 4.30: Comparison between analyses and available results in terms of horizontal dynamic stiffness for (a) $H/B = 2$, and (b) $H/B = 4$; $\nu = 0.30$.

Switching to lateral stiffness and a thicker soil deposit ($H/B = 8$), there seems to be

no correlation with published results beyond $\alpha_0 = 0.5$.

It is clear in Figure 4.31 that both FLAC and Isobem are in excellent agreement. Given that FLAC is running an explicit finite difference analysis while Isobem works in the frequency domain, the agreement can only prove their accuracy. In addition, taking into consideration the natural frequencies of the soil deposit ($\alpha_{0_1} = 0.2$, $\alpha_{0_3} = 0.6$, $\alpha_{0_5} = 1.0$, $\alpha_{0_7} = 1.4$, $\alpha_{0_9} = 1.8$), provides justification for the results produced with FLAC against those in Ref. [2].

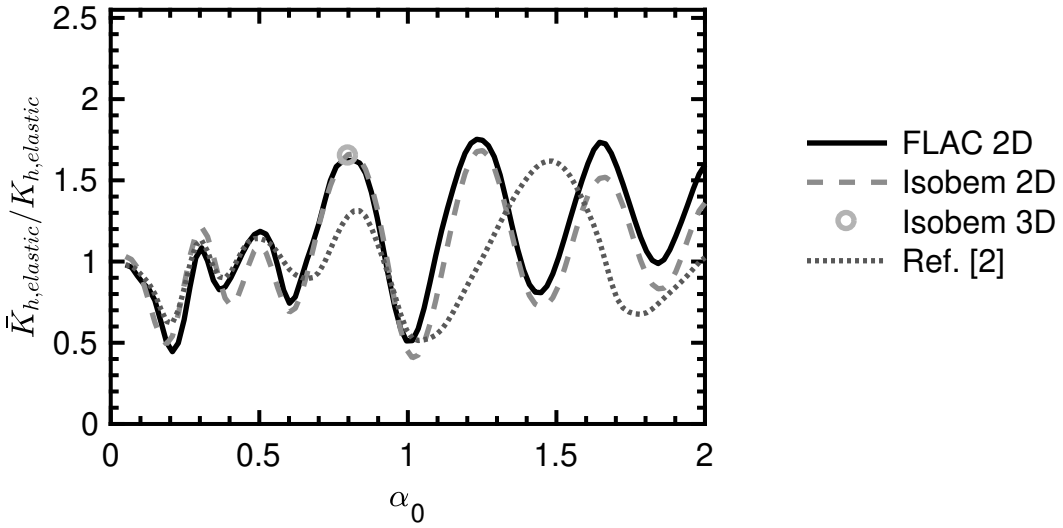

Figure 4.31: Comparison between analyses and available results in terms of horizontal dynamic stiffness; $H/B = 8$, $\nu = 0.30$.

Switching our attention to vertical dynamic stiffness, the results are shown in Figures 4.32. The agreement for both soil later depth cases studied is excellent for frequencies lower than 1.4. For higher frequencies, the stiffness is underestimated in Ref [2] by about 2 to 3 times.

In rocking oscillation the results from the numerical analyses are compared against the classical solution of Luco and Westmann [9] (Figure 4.33). Based on these results, Gazetas [2] proposed the following empirical formula (Eq. 4.18) for the stiffness modification coefficient with frequency.

$$\frac{\bar{K}_{rx,elastic}}{K_{rx,elastic}} \simeq 1 - 0.2 \cdot \alpha_0 \tag{4.18}$$

For a soil layer shallower than $8B$, the natural frequency seems to have a minor effect on rocking stiffness. It is worth noting that before resonance, the normalised stiffness is essentially identical to the published results. After resonance, the dynamic rocking

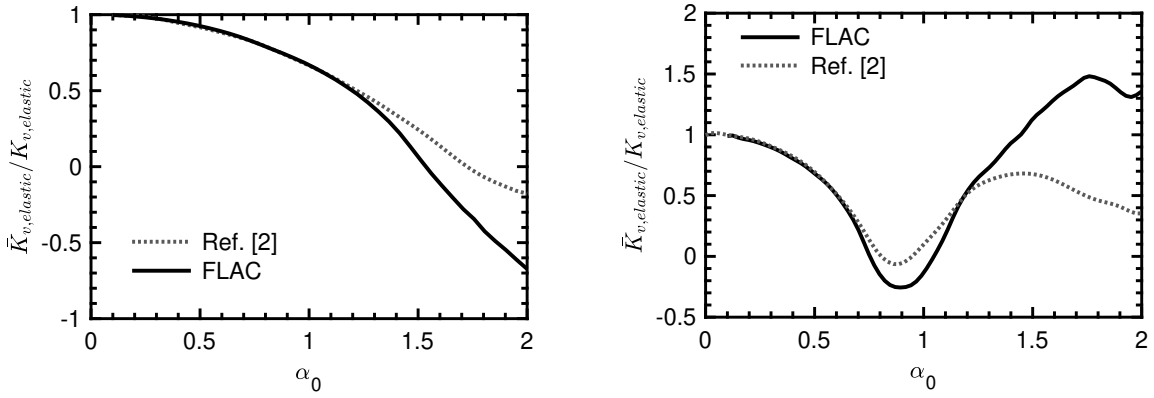

Figure 4.32: Comparison between analyses and available results in terms of vertical dynamic stiffness for (a) $H/B = 2$, and (b) $H/B = 4$; $\nu = 0.30$.

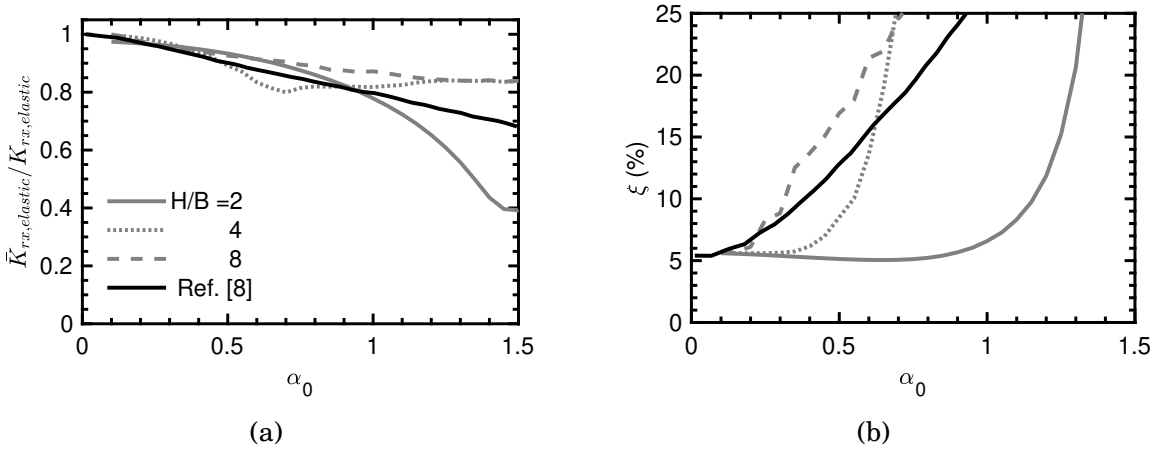

Figure 4.33: (a) Normalised linear dynamic rocking stiffness over elastic static rocking stiffness and (b) damping ξ versus dimensionless frequency (Luco and Westmann [9] results modified for fitting purposes); $\Delta x = 0.2B$, $\nu = 0.30$, $\xi_{min} = 5\%$, $f_{min} = f_{exc}$, $V_s = 200m/s$.

stiffness for $H/B = 4$ is constant at around 80% of the static counterpart, and does not follow the descending trend as suggested by Ref. [2, 9], while for $H/B = 2$ the stiffness is descending faster reaching 40% of the rocking static stiffness.

For $H/B = 8$ a very good agreement in stiffness is observed for dimensionless frequencies a_0 of less than approximately 0.6 (Figure 4.33). After that the drop in stiffness becomes smoother and approaches about 85% of the static counterpart. Damping is following an ascending trend similar to the one predicted by Luco and Westman [9], but the values are shifted as the proposed damping curve is starting from theoretically 0% damping. The discrepancies observed at higher frequencies might be attributed to differences in the boundary conditions between the two solutions (soil stratum versus halfspace).

CHAPTER 5

NON-LINEAR PARAMETRIC ANALYSES

An investigation of the effect of different governing parameters on the response of the footings described earlier is presented in this chapter. Three main parameter groups are studied: (a) Soil parameters including soil layer thickness, shear modulus, plasticity index (for clay), and Poisson's ratio. (b) Model parameters such as mesh dimensions, fixities and element size. (c) Loading parameters associated with lateral, vertical and rocking oscillations.

5.1 Non-linear analyses description

In order to accurately capture non-linear soil-structure interaction effects, it is essential to simulate non-linear soil behaviour at small and medium cyclic shear strain amplitudes. In this case, the response is governed by a hysteretic behaviour, which can be modelled using non-linear elastic stress-strain relationships. The stiffness-proportional term in Rayleigh damping is not defined. This is because the stress-strain relationships are based on tangential stiffness, while the secant shear modulus is used for the Rayleigh damping calculations. Soil shear modulus reduces with increasing strain and this reduction can be approximated by various forms of a hyperbolic function (e.g., [4, 133, 135, 153]). For the analysis presented in this thesis, soil non-linearity was explored by means of two models: the Ramberg-Osgood and the modified hyperbolic model.

5.2 Non-linear analyses based on Ramberg-Osgood model

To start with, soil non-linearity was explored according to a Ramberg-Osgood model with reference to the Vucetic and Dobry [8] experimental curves. As soil deformations in non-linear analyses accumulate in the vicinity of the footing, grid requirements are less strict than in linear static analyses. In this context, the lateral boundaries obtained from the static linear elastic analyses are adequate. For a soil layer having Poisson's ratio of 0.3 and density of $2Mg/m^3$, distances of $20B$ for swaying, $15B$ for the vertically loaded and only $10B$ for rocking foundations, are selected. The outcomes of the analyses are presented in the following subsections.

5.2.1 Calibration against Vucetic & Dobry experimental curves

The parameters of the model are predominantly determined through experiments conducted on the soil type of interest. According to Papadimitriou [5], the mean anticipated value or limit volumetric shear strain γ corresponds to the average values of G and ξ ($G = 0.64\,G_{max}$ and $\xi = 7.6\%$ for the experimental curves originally given by Vucetic and Dobry [8]). In light of this observation, the positive parameters of the Ramberg-Osgood model are determined in soils with different plasticity index PI. The values recommended by Papadimitriou are $\alpha_\gamma = 0.64$, $w = 2$. Results for τ_1 as function of PI are provided in Table 5.1.

To evaluate the implementation of the model and to verify that the Ramberg-Osgood hysteresis loop is accurately described in FLAC, one-element analyses are performed. The comparison of the hysteresis loop as produced analytically with MATLAB and numerically with FLAC are shown in Figure 5.1. The agreement is excellent, which suggests that the model was successfully implemented and the constitutive relationships follow the Ramberg-Osgood model.

The calibration of the Ramberg-Osgood model against the Vucetic and Dobry experimental curves is shown in Figure 5.2. By using the tabulated values of Table 5.1 proposed by Papadimitriou [5], the shear modulus degradation curves and the damping curves produced with Ramberg-Osgood model are compared with the curves in Ref. [8]. The agreement in terms of modulus degradation and damping curves is better with increasing plasticity index. The curves are identical of shear strain amplitudes up to $3\cdot10^{-4}$, $3\cdot10^{-3}$, $1\cdot10^{-3}$ for PI equal to 0, 15 and 30, respectively.

Table 5.1: τ_1 values for Ramberg – Osgood model (after Papadimitriou, [5])

PI	γ (%)	G_{max}/τ_1
0	0.016	9770
15	0.027	5790
30	0.058	2690

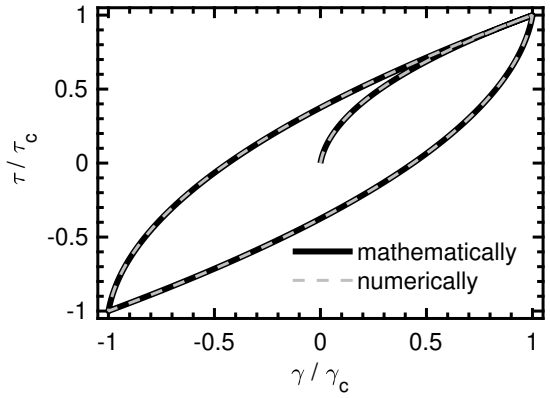

Figure 5.1: Evaluation of non-linear model Ramberg-Osgood loop in FLAC at element level

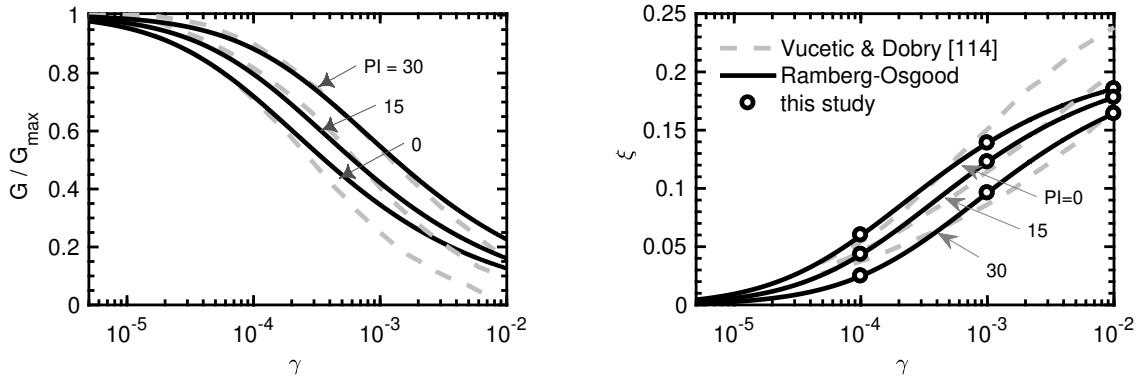

Figure 5.2: Simulation of (a) modulus reduction G/G_{max} and (b) damping curves by Vucetic and Dobry [8] with Ramberg-Osgood model [10]; $w = 2$, $\alpha_\gamma = 0.64$

5.2.2 Non-linear static analysis

Starting from a basic analysis, four parameters have been examined as to how they affect footing response in the three loading modes. The basic analysis considers a $2B_0 = 5m$ footing resting on an $8B$ thick soil layer with shear wave velocity V_{s_0} equal to $200m/s$ and a plasticity index PI equal to 0.

The first parameter is type of soil as described by the plasticity index (PI). The Ramberg-Osgood model is adjusted to match the Vucetic & Dobry [8] experimental curves. Three different values of PI $(0, 15, 30)$ are investigated. Each of these values corresponds to a limit volumetric shear strain γ_1, which is used to normalise the abscissa in the graphs by dividing footing's response.

Another key parameter is the depth of the soil stratum and the shear wave velocity. Three different values are assumed for each parameter: $H = 2B$, $4B$, $8B$ and $V_s = 100m/s$, $200m/s$, $300m/s$ respectively. These parameters have been taken into consideration for the corresponding static linear elastic analyses in the calculation of footing stiffness. Results are shown in the following subsections depending on the mode of loading.

Overall, seven basic parametric analyses were conducted by changing three key parameters (shear wave velocity, soil layer depth, and footing width). These analyses are repeated for three different types of soil and three response modes of loading, leading to 63 parametric analyses which were carried out using a grid of $0.4B$ element size in FLAC.

For the low force amplitude analyses the horizontal displacement magnitude is taken 10^{-5} m and for the large force amplitude is taken 10^{-2} m.

5.2.2.1 Vertical static loading

Considering a vertical static load acting on a massless footing resting on non-linear soil, the results are illustrated in Figure 5.3 for three soil layer thicknesses. In vertical axes static non-linear stiffness, K_v, is normalised by the static elastic stiffness, $K_{v,elastic}$, to eliminate the effect of soil properties. The normalised stiffness curves are presented versus vertical settlement, v, in the horizontal axes normalised by H to remove absolute units.

Non-linear static stiffness is gradually decreasing with the settlement amplitude and it approaches almost 15% of the static elastic stiffness when the normalised settlement reaches 1%. The soil layer thickness has no effect on this trend, as one would expect.

Similarly, the effect of the footing width is illustrated in Figure 5.4 (a). Again, the

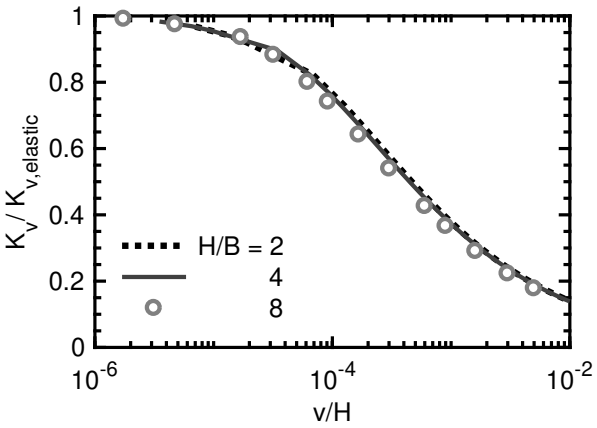

Figure 5.3: Illustration of the effect of soil layer thickness, H, on the normalised non-linear vertical static stiffness versus the normalised settlement; $w = 2$, $\alpha_\gamma = 0.64$, $PI = 0$, $\gamma_1 = 0.016$, $V_s = 200m/s$, $B = 2.5m$.

footing dimensions have no effect on the degradation of normalised stiffness. All the curves are falling into one. Same observations are made for the effect of shear wave velocity through the Figure 5.4 (b).

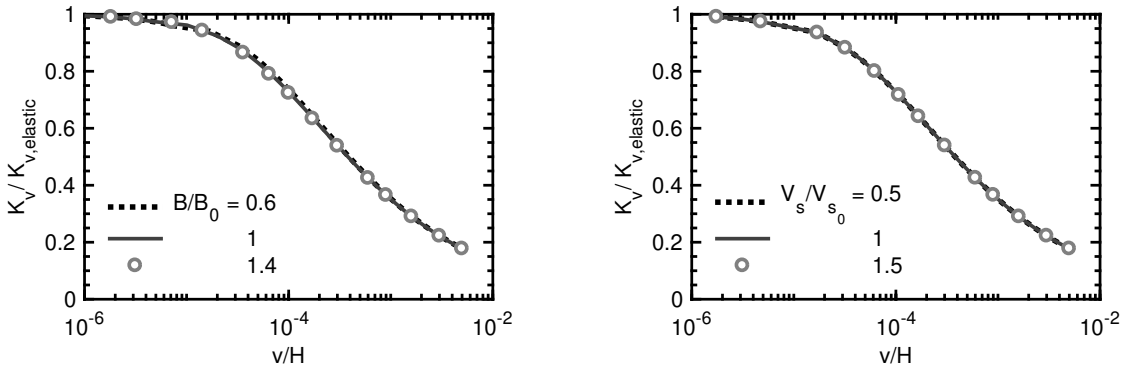

Figure 5.4: Illustration of the effect of (a) footing half-width, B, and (b) the shear wave velocity V_s on the normalised non-linear vertical static stiffness versus the normalised settlement over H; $w = 2$, $\alpha_\gamma = 0.64$, $PI = 0$, $\gamma_1 = 0.016$.

On the other hand, an increase in soil plasticity index, PI, which is accounted in Ramberg-Osgood model through parameter γ_1, naturally increases the non-linear vertical stiffness. The influence is evident in Figure 5.5 after a normalised settlement in the order of 10^{-5}. The stiffness decrease starts in smaller settlement amplitude in soils with PI equals to 0 than in soils with PI equal to 15 and 30. However, the gradient of

the decrease is similar in all three cases.

To eliminate the effect of PI from the non-linear vertical stiffness curves the horizontal axis is further normalised with the γ_1 model parameter. The results are shown in Figure 5.5 (b). Interestingly, all the analyses are falling into one universal curve.

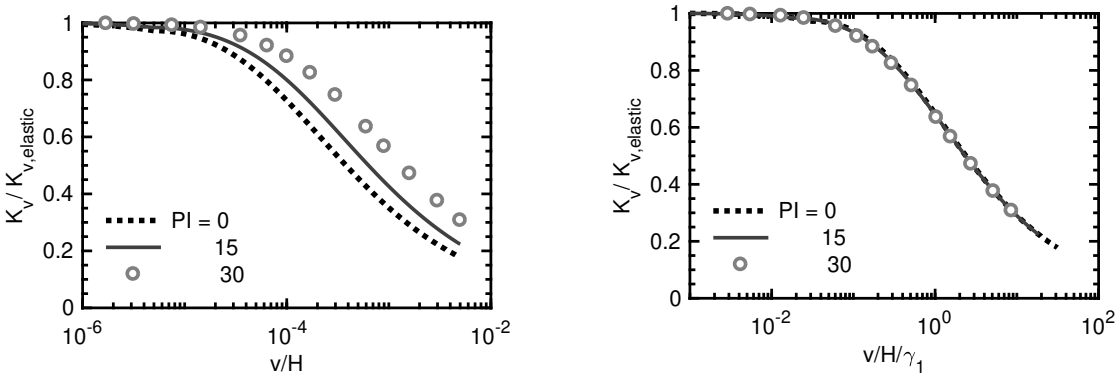

Figure 5.5: Illustration of the effect of PI on the normalised non-linear vertical static stiffness versus (a) the normalised settlement over H and (b) the normalised settlement over H over RO parameter γ_1; $w = 2$, $\alpha_\gamma = 0.64$, $V_s = 200m/s$, $H/B = 8$, $B = 2.5m$.

5.2.2.2 Lateral static loading

Switching our attention to horizontal static loading, the effect of the soil layer thickness is illustrated in Figure 5.6. Unlike the previous studied case, H seems to influence slightly the normalised lateral static stiffness. However, the trends are almost identical and the discrepancies are small.

Similarly to the vertical static stiffness, the lateral one is not affected neither by the width of the strip footing nor by the shear wave velocity as shown in Figures 5.7. This is evidence of a successful normalisation of the axes.

Following, the effect of plasticity index is investigated and the outcomes are depicted in Figure 5.8 (a). Higher PI results in higher lateral stiffness. A PI of 30% produces 40% higher static stiffness than a soil with $PI = 0\%$ when the normalised lateral displacement exceeds 10^{-4}. This difference can be supressed if the horizontal axis is normalised further with the RO model parameter γ_1, as shown in Figure 5.8 (b).

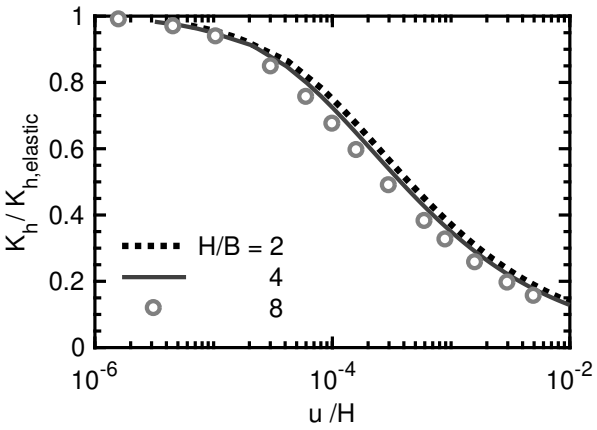

Figure 5.6: Illustration of the effect of H/B ratio on the normalised non-linear swaying static stiffness versus the normalised settlement; $w = 2$, $\alpha_\gamma = 0.64$, $PI = 0$, $\gamma_1 = 0.016$, $V_s = 200m/s$, $B = 2.5m$.

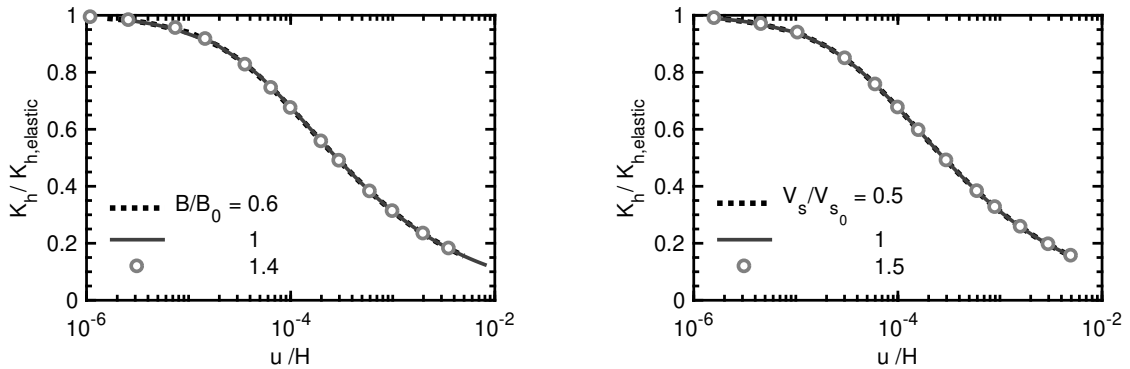

Figure 5.7: Illustration of the effect of (a) footing half-width, B, and (b) the shear wave velocity V_s on the normalised non-linear lateral static stiffness versus the normalised settlement over H; $w = 2$, $\alpha_\gamma = 0.64$, $PI = 0$, $\gamma_1 = 0.016$.

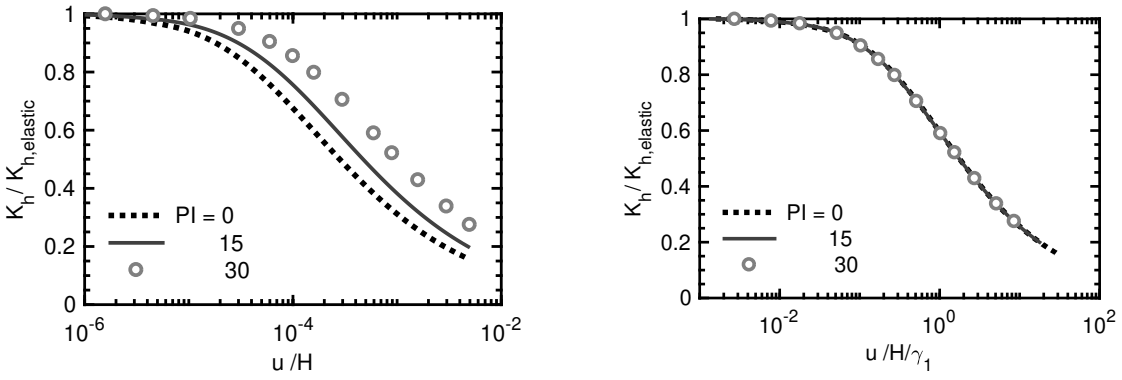

(a) (b)

Figure 5.8: Illustration of the effect of PI on the normalised non-linear lateral static stiffness versus (a) the normalised settlement over H and (b) the normalised settlement over H over RO model parameter γ_1; $w = 2$, $\alpha_\gamma = 0.64$, $V_s = 200m/s$, $H/B = 8$, $B = 2.5m$.

5.2.2.3 Rocking static loading

In the rocking mode similar trends are observed: the static stiffness decreases with increasing magnitude of the rocking angle, θ (in rad). The effect of depth of soil stratum is negligible (Figure 5.9) with the shallowest soil layer resulting in slightly lower rocking stiffness.

Interestingly, the width of the footing influences the static rocking stiffness. For a rocking angle, θ, on the order of 10^{-4} rad the non-linear static stiffness is 80%, 75% and 67% the linear counterpart for footing widths of $3.5m$, $2.5m$ and $1.5m$, respectively. That is a difference of almost 20% of the rocking stiffness of the soil between the cases when the load is applied in the widest and in the narrowest footings.

The effect of shear wave velocity is illustrated in Figure 5.10 (b). No influence is evident as the soil properties are accounted in the normalisation of the non-linear stiffness over the respective linear stiffness.

As discussed in the previous two loading cases, plasticity index effect is also evident in rocking loading (Figure 5.11 a). This effect, is again, eliminated with the proper normalisation of θ (Figure 5.11 b).

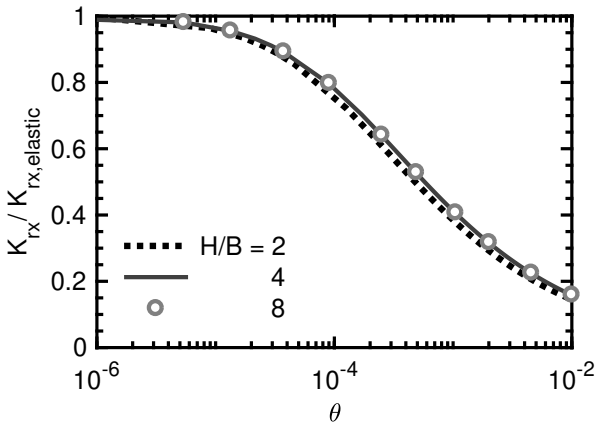

Figure 5.9: Illustration of the effect of H/B ratio on the normalised non-linear rocking static stiffness versus the rotation anglet; $w = 2$, $\alpha_\gamma = 0.64$, $PI = 0$, $\gamma_1 = 0.016$, $V_s = 200m/s$, $B = 2.5m$.

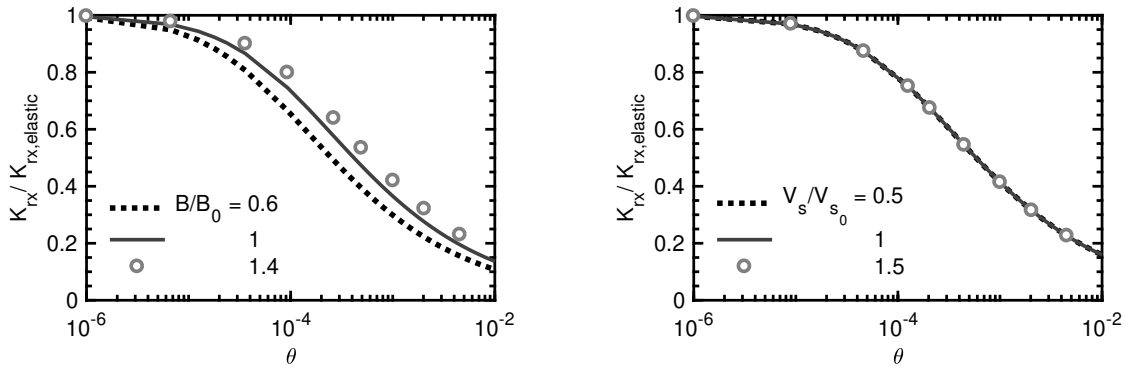

(a) (b)

Figure 5.10: Illustration of the effect of (a) footing half-width, B, and (b) the shear wave velocity V_s on the normalised non-linear rocking static stiffness versus the the rotation angle; $w = 2$, $\alpha_\gamma = 0.64$, $PI = 0$, $\gamma_1 = 0.016$.

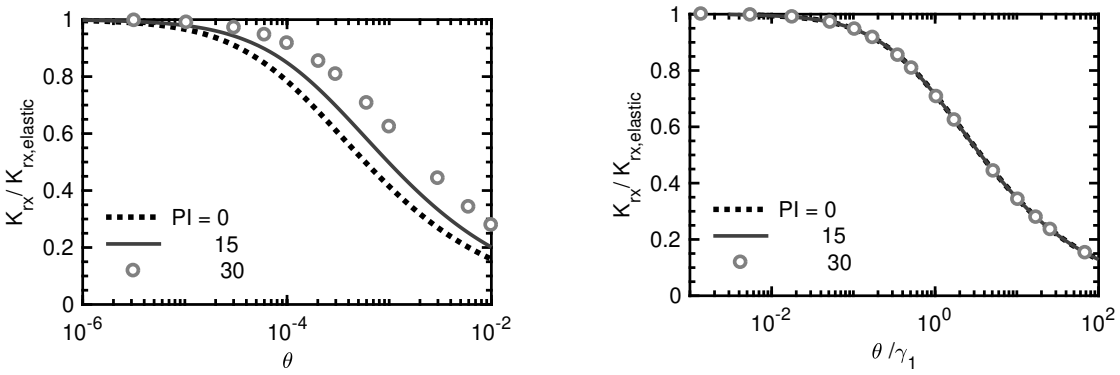

Figure 5.11: Illustration of the effect of PI on the normalised non-linear rocking static stiffness versus (a) the rotation angle and (b) versus the rotation angle over RO model parameter γ_1; $w = 2$, $\alpha_\gamma = 0.64$, $V_s = 200m/s$, $H/B = 8$, $B = 2.5m$.

5.2.2.4 Static analysis discussions

Having a closer look at graphs 5.5 (b), 5.8 (b) and 5.11 (b), one could notice that all curves are almost identical for each type of loading. Therefore, one could end up with a single curve for each mode of loading. PI value is accounted through cyclic shear strain γ_1 and its effect is eliminated from the graphs.

Taking the case of vertical static stiffness, the resulting curves could be fitted according to the formula

$$\frac{K_v}{K_{v,elastic}} = \frac{1}{1+\left(\frac{1}{\alpha_{ref}}-1\right)\left(\frac{V}{V_1}\right)} \tag{5.1}$$

where α_{ref} is the normalised stiffness value for $v/H = \gamma_1$ (it is correct) and $V = V_1$. Accordingly the above Equation 5.1 can be adjusted to account for horizontal loading and rocking by replacing V with H, M and v with u, θ, respectively.

Using MATLAB, the parameter α_{ref} is calculated with linear interpolation and presented in Table 5.2 for all the different modes of loading and PI values investigated.

Table 5.2: Parameter α_{ref} values depending on mode of loading and plasticity index.

Mode of Loading	$PI = 0$	$PI = 15$	$PI = 30$	**Average**
Vertical	0.649	0.645	0.641	0.645
Swaying	0.596	0.594	0.595	0.595
Rocking	0.707	0.714	0.714	0.712

The V_1 value is derived via the formula

$$V_1 = K_v \cdot v = \alpha_{ref} \cdot K_{v,elastic} \cdot \gamma_1 \cdot H \tag{5.2}$$

Substituting Eq. 5.2 into Eq. 5.1 one obtains the general formula to fit the curves in Figure 5.5 (a)

$$\frac{K_v}{K_{v,elastic}} = \frac{1}{1+\left(\frac{1}{\alpha_{ref}}-1\right)\left(\frac{1}{\alpha_{ref}} \cdot \frac{v/H}{\gamma_1} \cdot \frac{K_v}{K_{v,elastic}}\right)} \tag{5.3}$$

The static linear elastic stiffness $K_{v,elastic}$ is a function of G, B, H, ν and can be easily determined by the diagrams and equations provided in Section 4.1. In Summary, if v, u or θ are known the non-linear stiffness can be calculated by a trial and error procedure through equation 5.3. Alternatively, if the force or moment is given, the non-linear stiffness coefficient can be derived by Eq. 5.1.

5.2.3 Non-linear Dynamic Analysis

The following set of Ramberg-Osgood non-linear analyses concern the dynamic response of a strip footing resting on a non-linear soil layer. An initial vertical displacement is statically applied before the vertical and rotational excitation is imposed. The amplitude of the initial vertical displacement, is equal to amplitude of the excitation, v_0. Similarly to the linear dynamic analysis, the input motion is sinusoidal (Figure 4.11), expressed in terms of acceleration applied directly on the footing.

The finite difference grid utilised in the non-linear analysis is shown in Figure 5.12. Specifically, a grid of width $10B$ to $30B$ is used depending on the mode of excitation - $10B$ for rocking, $20B$ for vertical and $30B$ for swaying. The total depth is H and B is the half-width of the footing. Quiet boundaries are applied at the sides of the grid, while movements at the base are fixed in both directions. The model was discretised into six different subzones with the element dimensions for each zone being: 1. $\Delta x = 0.08B \times 0.08B$, 2. $\Delta x = 0.08B \times 0.2B$, 3. $\Delta x = 0.2B \times 0.08B$, 4. $\Delta x = 0.28B \times 0.2B$, 5. $\Delta x = 0.4B \times 0.08B$ and 6. $\Delta x = 0.4B \times 0.2B$.

Soil behaviour was simulated using the aforementioned Ramberg-Osgood model. A shear wave velocity of $V_s = 200m/s$ and a soil mass density $\rho = 2Mg/m^3$ were considered, resulting in a maximum shear modulus $G_{max} = 80MPa$. The Poisson's ratio, ν, was taken equal to $\nu = 0.30$. A Rayleigh damping $\xi = 5\%$ was considered to account for soil damping. Given that the stiffness proportional Rayleigh damping term is not

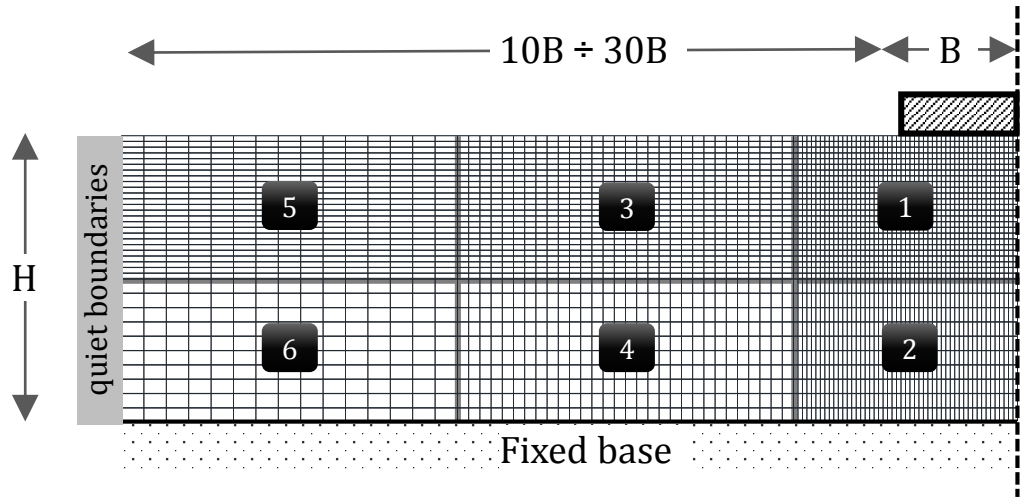

Figure 5.12: View of typical 6-zone finite difference mesh. The sketch refers to a half model due to symmetry in the vertical axis.

determined in user defined constitutive models in FLAC, and the mass proportional damping is not active in low excitation amplitudes, the damping for low amplitude excitation is zero.

5.2.3.1 Vertical dynamic response

Examining the vertical oscillations of footing on non-linear soil of various depths H, the results in terms of stiffness are presented graphically in Figure 5.13 in different vertical axes. In Figure 5.13 (a), the non-linear dynamic stiffness is normalised by the static linear elastic stiffness while the vertical axis in Figure 5.13 (b) is normalised by the static non-linear stiffness, as it was calculated in subsection 5.2.2.1.

In the same graph (Figure 5.13), it is evident that deeper soil deposits resonate in lower frequencies. Naturally, the first resonance of a soil layer of $H/B = 8$ is half of the respective value for $H/B = 4$ and one-quarter of α_1 value for $H/B = 2$.

This phenomenon is also depicted in damping curves of Figure 5.14 in which damping tends to infinity when the stiffness is zero and the phase angle is 90°. Is is also noticeable that deeper soil layers result in lower system damping. This phenomenon is not noticeable in linear dynamic analysis. This is because in linear analyses, Rayleigh damping is strain independent unlike the case of non-linear analysis. To this end, deeper soil deposits result in lower shear strain for the same applied motion amplitude.

For the normalisation of Figure 5.13 (b), the static non-linear vertical stiffness, K_v, is used as depicted in Figure 5.3. In the resulting Figure 5.13 (b), it is shown that for

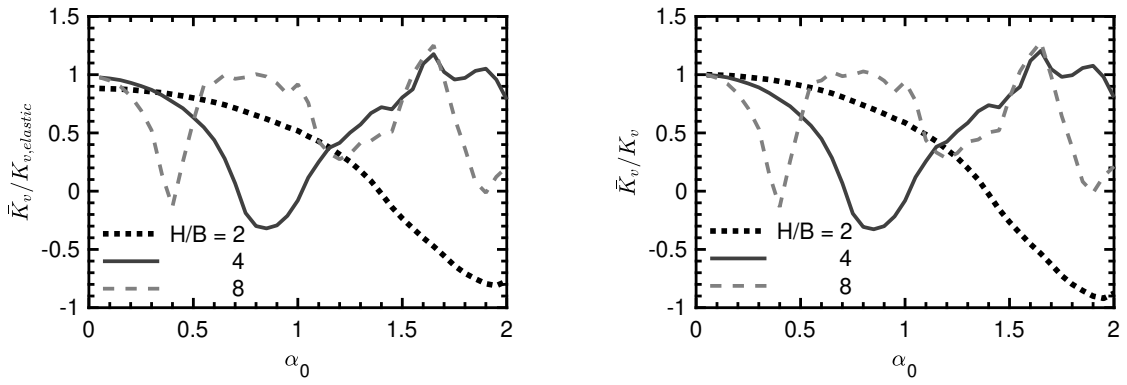

(a) (b)

Figure 5.13: Illustration of the effect of H/B on the normalised non-linear vertical dynamic stiffness (a) by the static linear elastic stiffness and (b) by the non-linear static stiffness versus the dimensionless frequency α_0; $V_s = 200m/s$, $PI = 0$, $v_0 = 10^{-4}m$, Rayleigh damping $\xi = 5\%$.

zero frequency the dynamic stiffness is equal to the static counterpart, thus verifying the theory.

As a general remark, a shallow soil layer is stiffer when the footing is subjected to low frequency vibrations (up to $\alpha_0 = 0.5$). For $\alpha_0 = 1.2$ the non-linear dynamic stiffness is equal to 40% of the static elastic stiffness, regardless of the soil layer depth. For α_0 greater than 1.2, a deeper soil stratum is stiffer. Also, the response of the shallow soil layer has more than 90°phase difference. Therefore, the presence of bedrock at a shallow depth is favourable for low frequency vibrations whilst the same is not as noticeable at higher amplitude frequencies.

Considering the effect of type of damping on footing response, Figures 5.15 and 5.16 present the stiffness and damping results, respectively. The case where $H/B = 4$ soil layer is studied considering either Rayleigh or hysteretic damping of 5%, or both. According to FLAC guidelines, hysteretic damping can be unstable in dynamic analyses. Therefore, an addition of 0.2% Rayleigh damping is suggested [13]. It is important to note that hysteretic damping significantly reduces the timestep and consequently the computational time and, for that reason, it is generally preferred. However, in this case it is evident that hysteretic damping, in addition to the limitations from the mesh element size and the analysis timestep, causes further numerical instabilities in stiffness for dimensionless frequencies greater than 0.8 or so spotted as 'noise' (Figures 5.15). Moreover, in Figure 5.16 hysteretic damping causes numerical instabilities in the calculation of system damping for α_0 as low as 0.4.

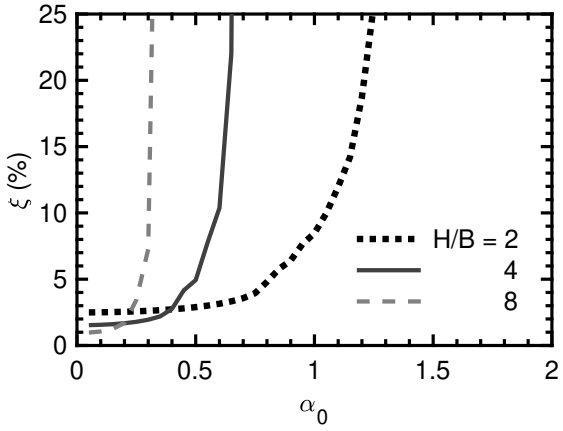

Figure 5.14: Illustration of the effect of H/B ratio on the damping ratio versus the dimensionless frequency α_0; $V_s = 200m/s$, $PI = 0$, $v_0 = 10^{-4}m$, Rayleigh damping $\xi = 5\%$.

If both hysteretic and Rayleigh damping are used in the analyses, the Rayleigh damping is predominant. One can observe that the stiffness and damping curves resulting by applying only Rayleigh damping, or by applying additional hysteretic damping are indistinguishable. In this light, Rayleigh damping is used in the analyses to follow.

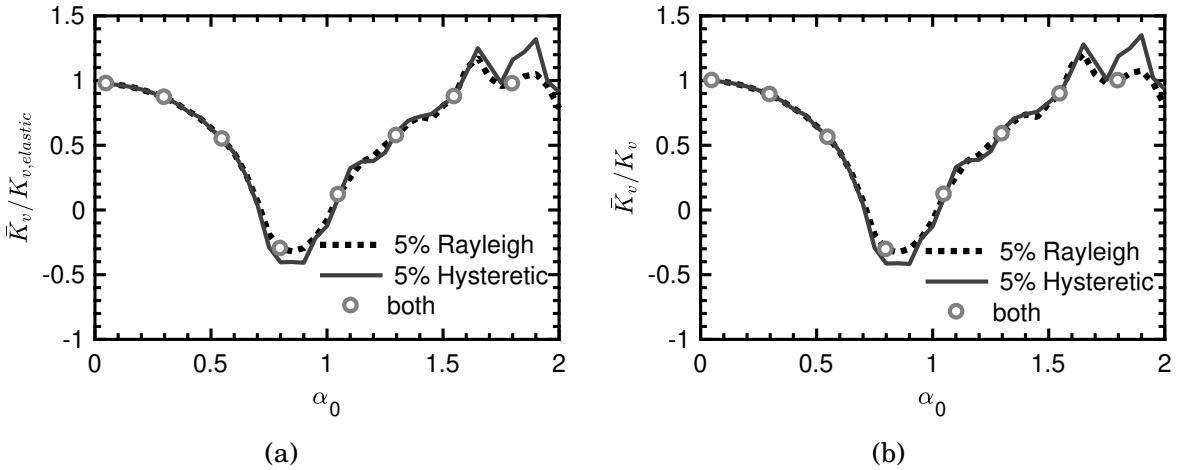

Figure 5.15: Illustration of the effect of the type of damping on the normalised non-linear vertical dynamic stiffness (a) by the static linear elastic stiffness and (b) by the non-linear static stiffness versus the dimensionless frequency α_0; $V_s = 200m/s$, $PI = 0$, $v_0/H = 10^{-5}$, $H/B = 4$.

Results for different vertical excitation amplitudes are shown in Figures 5.17. In Figure 5.17 (a) the non-linear dynamic stiffness is normalised against the static linear

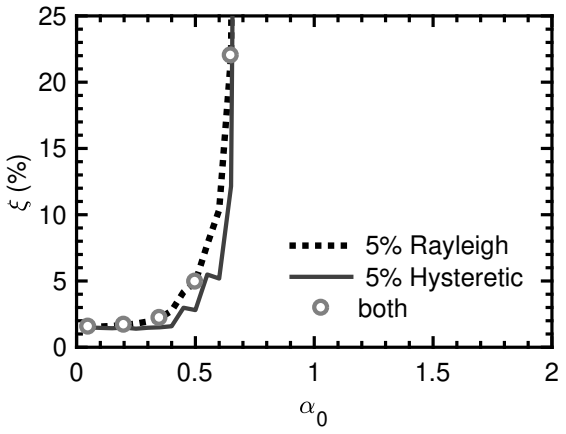

Figure 5.16: Illustration of the effect of the type of damping on the calculated damping ratio versus the dimensionless frequency α_0; $V_s = 200m/s$, $PI = 0$, $v_0/H = 10^{-5}$, $H/B = 4$.

stiffness. Evidently, the higher the magnitude of vertical excitation the lower the normalised dynamic stiffness. Non-linearity is mainly evident in high-amplitude vibrations.

By normalising the results with the non-linear static stiffness of the corresponding amplitude, the stiffness curves are falling into a single curve for dimensionless frequencies up to 0.5. A shift to the left is observed at the first resonance frequency with increasing amplitude. For values of α_0 greater than 1.5 the results are affected by numerical instabilities.

Plotting the aforementioned results versus the non-linear dimensionless excitation frequency α_{nl}

$$\alpha_{nl} = \alpha_0 \sqrt{\frac{K_{v,elastic}}{K_v}} \tag{5.4}$$

leads to Figure 5.18. In this figure the horizontal shift of the curves is eliminated as the non-linear dynamic stiffness is normalised over the corresponding non-linear static stiffness. As expected, the static non-linear stiffness is equal to the non-linear dynamic stiffness for α_0 close to zero. The stiffness curves are following identical trends up to $\alpha_0 = 1.2$. Thereafter, a fluctuation is observed which can be a spurious response of the numerical model to high frequency vibrations. Nevertheless, the footing stiffness under high-amplitude oscillations is half of the counterpart for low-amplitude vertical vibrations when $\alpha_0 = 2$.

From Figure 5.18, it is evident that up to a frequency $\alpha_{nl} = 1$ the cyclic deformation does not affect the normalised non-linear stiffness. It is also noteworthy that the nor-

malised non-linear dynamic stiffness follows the same trend as the respective linear stiffness (as seen in Figure 4.18) up to the aforementioned point.

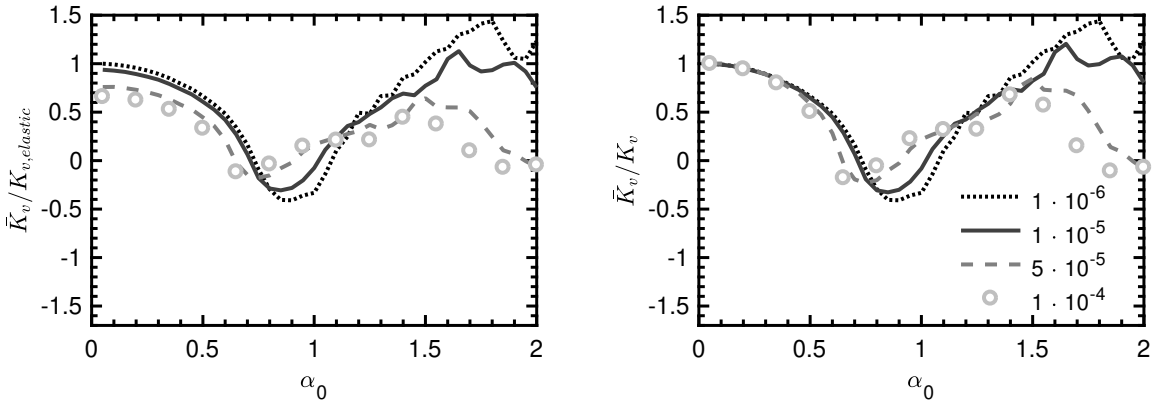

(a) (b)

Figure 5.17: Illustration of the effect of oscillations amplitude, v_0 on the non-linear vertical dynamic stiffness normalised (a) by the static linear elastic stiffness and (b) by the non-linear static stiffness (b) versus the dimensionless frequency α_0; $V_s = 200m/s$, $PI = 0$, $H/B = 4$, Rayleigh damping $\xi = 5\%$.

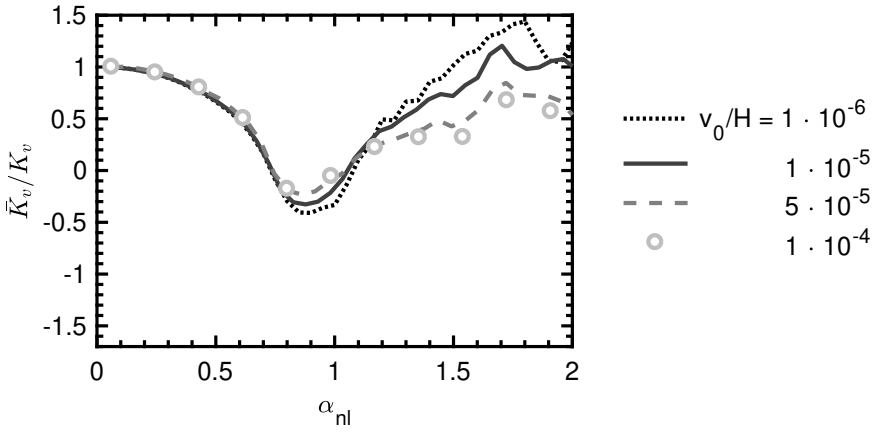

Figure 5.18: Illustration of the effect of v_0 on the normalised non-linear vertical dynamic stiffness by the non-linear static stiffness versus the non-linear dimensionless frequency α_{nl}; $V_s = 200m/s$, $PI = 0$, $H/B = 4$, Rayleigh damping $\xi = 5\%$.

The horizontal shift is also evident in the damping curves shown in Figure 5.19 (a). Similarly, it can be eliminated by plotting the results against the non-linear dimensionless frequency. In the same graphs, it is shown that the higher the amplitude of the oscillations the higher the system damping. For low amplitude vibrations (on the order

of $v_0/H = 10^{-5}$) system damping reaches 7% while for smaller vibration amplitude the same variable reaches zero for nearly static conditions of loading ($\alpha_0 \rightarrow 0$).

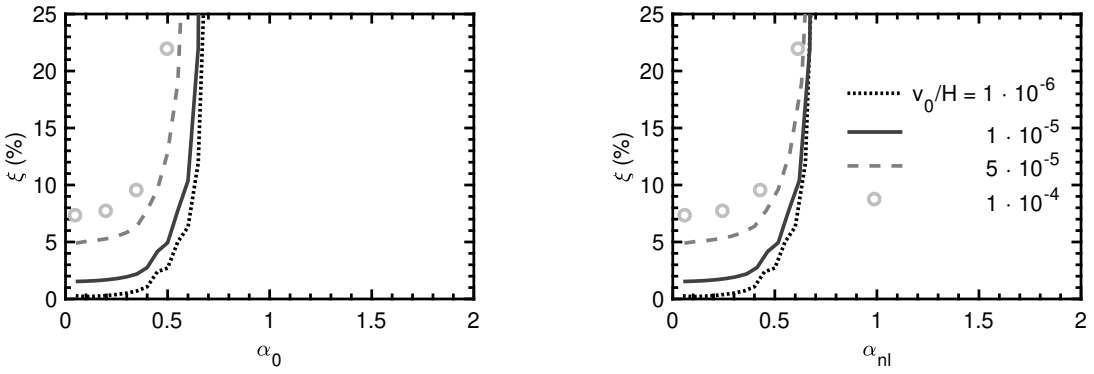

Figure 5.19: Illustration of the effect of v_0 on system damping versus (a) the dimensionless frequency α_0 and (b) the non-linear dimensionless frequency α_{nl}; $V_s = 200m/s$, $PI = 0$, $H/B = 4$, Rayleigh damping $\xi = 5\%$.

5.2.3.2 Horizontal dynamic response

Switching our attention to horizontal vibrations, the effect of the soil layer depth, H/B, is depicted in Figures 5.20 and 5.21 in terms of stiffness and damping, respectively. The effect of the excitation amplitude is investigated in Figures 5.22-5.24.

Unlike vertical response, the lateral dynamic stiffness is positive regardless of excitation frequency. That indicates a phase difference of less than 90° between excitation and response (Figures 5.20).

Looking at Figure 5.20 (a), the first resonance, α_{01}, is observed at 0.21 for $H/B = 8$, 0.42 for $H/B = 4$ and 0.85 for $H/B = 2$. The non-linear static stiffness normalises the vertical axes in Figure 5.20 (b); hence all curves are slightly lifted so they are anchored to 1.

Moving to Figure 5.21 the foundation damping ratio consisting of material and radiation damping is shown. Material damping (observed in low frequencies) increases with decreasing soil thickness under constant excitation amplitude. Damping reaches a maximum at the aforementioned resonance dimensionless frequencies.

The effect of horizontal oscillations amplitude is explored in Figures 5.22 as a function of dimensionless frequency. Higher excitation amplitudes naturally correspond to lower stiffness (Figure 5.22 a). For $u_0/H = 10^{-6}$ and $\alpha_0 \approx 0$ the non-linear dynamic stiffness is

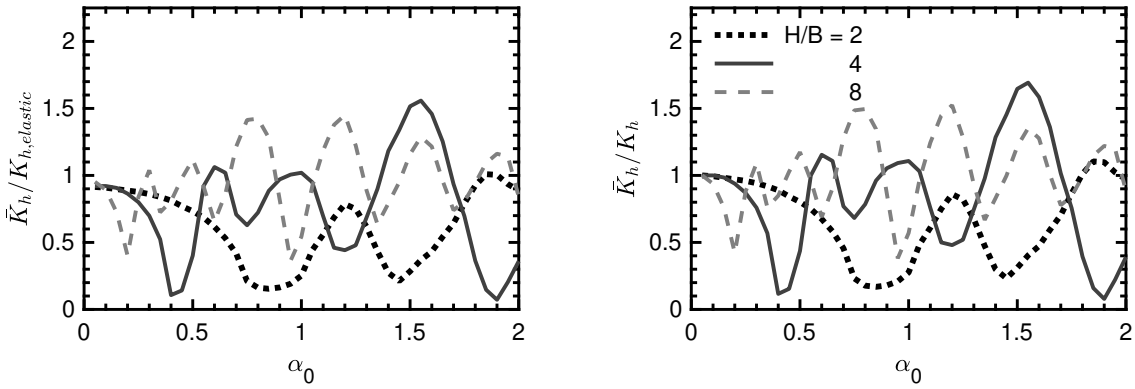

(a) (b)

Figure 5.20: Illustration of the effect of H/B on the non-linear lateral dynamic stiffness normalised (a) by the static linear elastic stiffness and (b) by the non-linear static stiffness versus the dimensionless frequency α_0; $V_s = 200m/s$, $PI = 0$, $u_0/H = 10^{-5}$, Rayleigh damping $\xi = 5\%$.

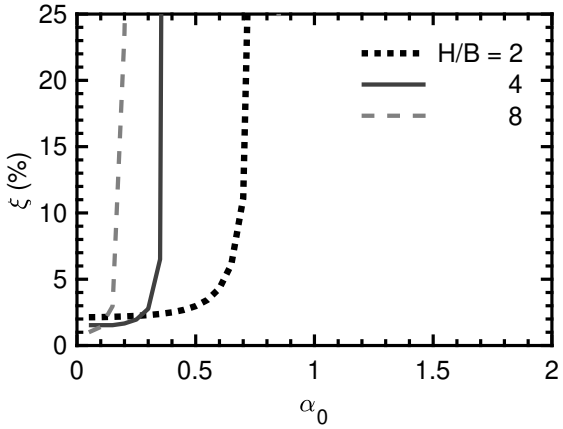

Figure 5.21: Illustration of the effect of H/B ratio on the foundation damping ratio versus the dimensionless frequency α_0; $V_s = 200m/s$, $PI = 0$, $u_0/H = 10^{-5}$, Rayleigh damping $\xi = 5\%$.

equal to the elastic static stiffness. For the maximum amplitude $u_0/H = 10^{-4}$ the dynamic stiffness is 35% lower than the corresponding static elastic. In Figure 5.17 (b) the vertical axis in normalised to eliminate the aforementioned discrepancies at low frequencies. In the same graph, the resonance frequencies shift to the right with increasing excitation amplitude.

In Figure 5.23, non-linearity is used to normalise both the horizontal and the vertical axes of the stiffness plots. The horizontal axis is normalised with the non-linear dimensionless frequency as defined in Eq. 5.4 and the vertical axis is normalised with the non-linear static stiffness. The first resonance occurs at $\alpha_{nl_1} = 0.4$, followed by $\alpha_{nl_3} = 1.2$ and $\alpha_{nl_5} = 2.0$. Although the motion amplitude does not have an effect on the resonance frequencies, the stiffness is significantly lower with increasing amplitude.

This phenomenon can be explained by looking at Figures 5.24. Material damping, which is naturally evident at low frequencies before resonance, increases with increasing excitation amplitude, adding up to the total damping. Therefore, the peaks of stiffness curves presented herein, are considerably smoother for high-amplitude excitation.

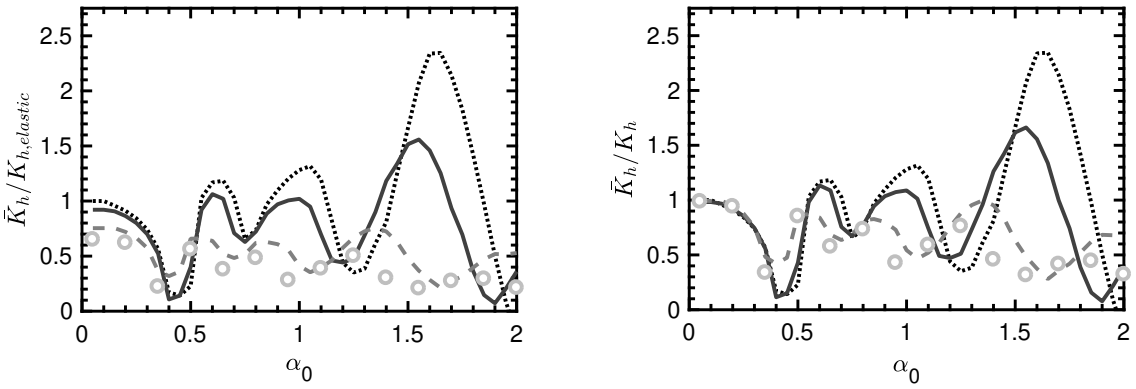

Figure 5.22: Illustration of the effect of oscillations amplitude, u_0 on the non-linear lateral dynamic stiffness normalised (a) by the static linear elastic stiffness and (b) by the non-linear static stiffness versus the dimensionless frequency α_0; $V_s = 200m/s$, $PI = 0$, $H/B = 4$, Rayleigh damping $\xi = 5\%$.

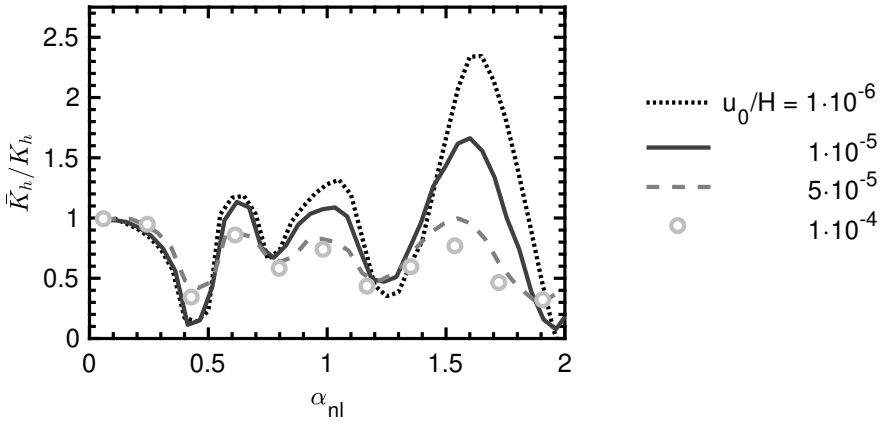

Figure 5.23: Illustration of the effect of u_0 on the normalised non-linear lateral dynamic stiffness by the non-linear static stiffness versus the non-linear dimensionless frequency α_{nl}; $V_s = 200m/s$, $PI = 0$, $H/B = 4$, Rayleigh damping $\xi = 5\%$.

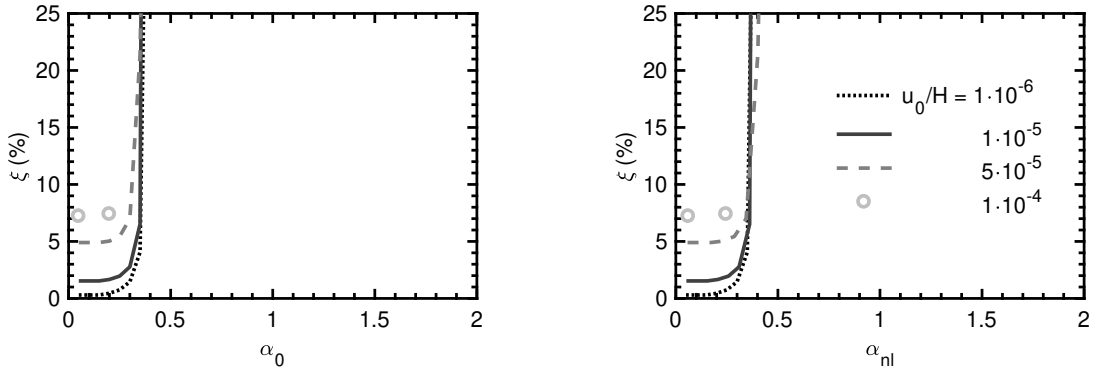

(a) (b)

Figure 5.24: Illustration of the effect of u_0 on system damping versus (a) the dimensionless frequency α_0 and (b) the non-linear dimensionless frequency α_{nl}; $V_s = 200m/s$, $PI = 0$, $H/B = 4$, Rayleigh damping $\xi = 5\%$.

5.2.3.3 Rocking dynamic response

Moving on to the rocking mode, the effect of soil layer thickness is illustrated in Figure 5.25. A dip is observed in dynamic rocking stiffness in shallow layers. For $H/B = 8$ an almost linear variation in dynamic rocking stiffness with dimensionless frequency is observed. For a_0 greater than 1.1 the dynamic stiffness of a footing resting on a soil layer of thickness $4B$ and $8B$ are identical and almost 30% smaller than that corresponding to a $2B$ thick soil layer.

In Figure 5.26 the total soil damping is plotted. In shallow layers resonance occurs resulting in a rapid increase of damping. In contrast, with increasing soil thickness there is an increase in the gradient of the damping curves.

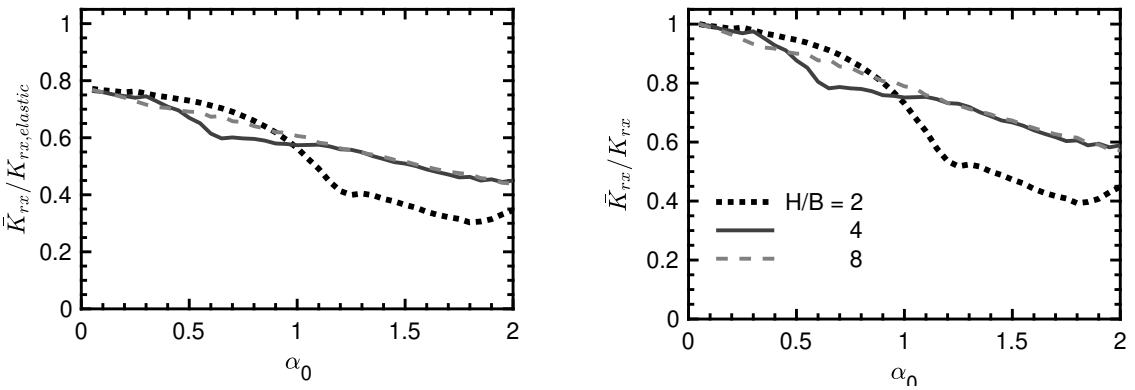

(a) (b)

Figure 5.25: Illustration of the effect of H/B on the non-linear rocking dynamic stiffness normalised (a) by the static linear elastic stiffness and (b) by the non-linear static stiffness versus the dimensionless frequency a_0; $V_s = 200m/s$, $PI = 0$, $\theta = 10^{-4}\ rad$, Rayleigh damping $\xi = 5\%$.

The effect of rotation angle amplitude is evident in Figure 5.27 (a). By increasing the rotation angle by two orders of magnitude, the dynamic stiffness decreases by as much as 55% to 75%. The discrepancy is increasing with increasing dimensionless frequency. The differences are eliminated to less than 30% in Figure 5.28, by normalising both the axis, similarly to the aforementioned loading cases.

Results for damping are shown in Figures 5.29. Similar to the previous studied loading cases, material damping is increasing with increasing rotation amplitude. For pseudo-static conditions ($\theta_{max} = 10^{-5}\ rad$), the damping starts from zero, while for $\theta_{max} = 10^{-3}\ rad$ damping reaches 13%.

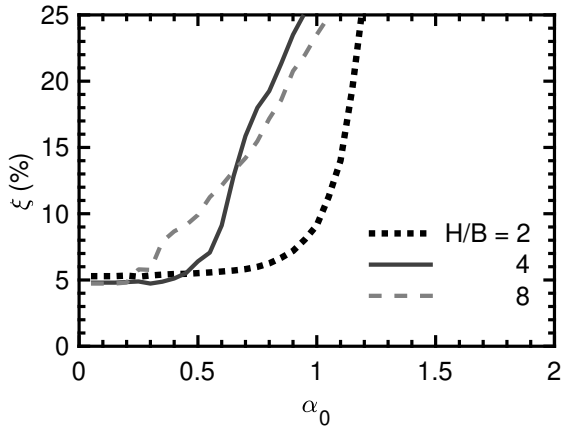

Figure 5.26: Illustration of the effect of H/B ratio on the damping ratio versus the dimensionless frequency α_0; $V_s = 200m/s$, $PI = 0$, $\theta = 10^{-4}\ rad$, Rayleigh damping $\xi = 5\%$.

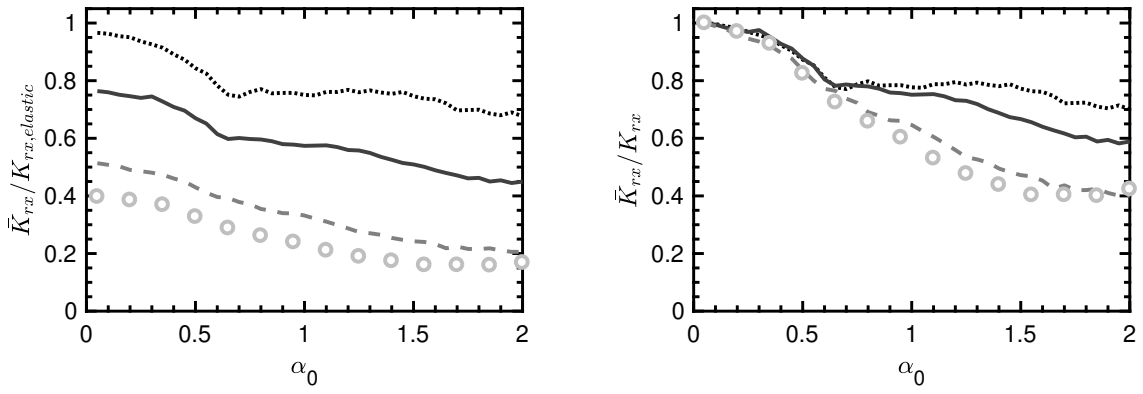

Figure 5.27: Illustration of the effect of oscillations amplitude, u_0 on the non-linear rocking dynamic stiffness normalised (a) by the static linear elastic stiffness and (b) by the non-linear static stiffness versus the dimensionless frequency α_0; $V_s = 200m/s$, $PI = 0$, $H/B = 4$, Rayleigh damping $\xi = 5\%$.

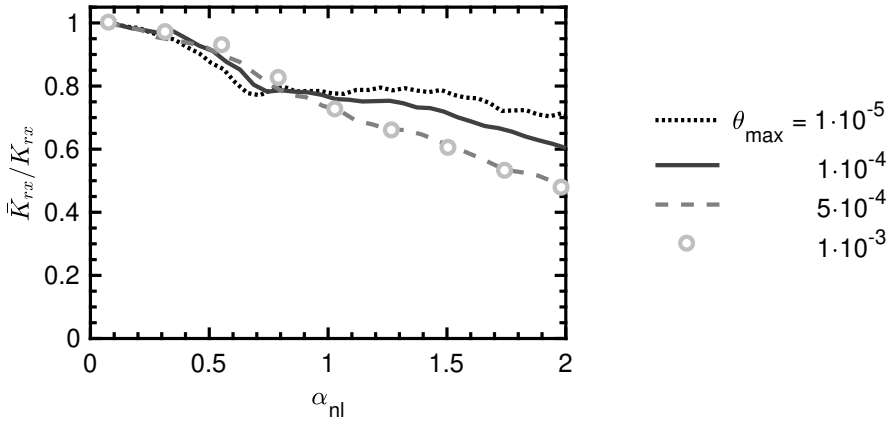

Figure 5.28: Illustration of the effect of θ amplitude (in rad) on the normalised non-linear rocking dynamic stiffness by the non-linear static stiffness versus the non-linear dimensionless frequency α_{nl}; $V_s = 200m/s$, $PI = 0$, $H/B = 4$, Rayleigh damping $\xi = 5\%$.

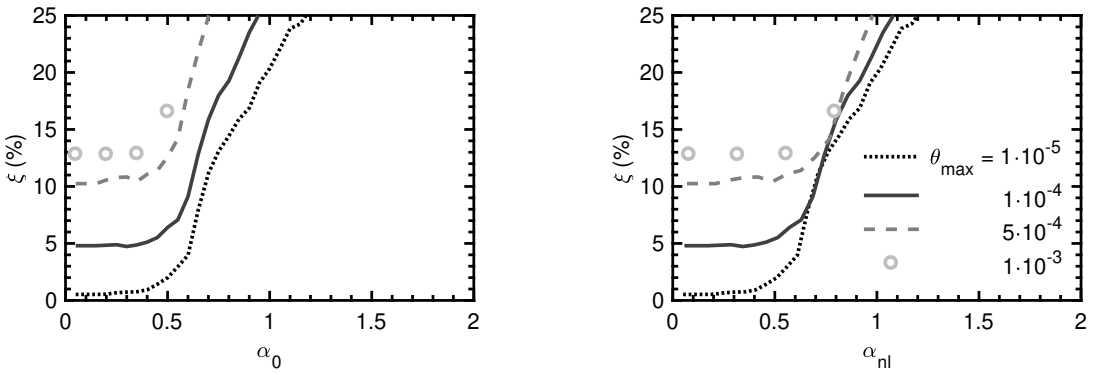

(a) (b)

Figure 5.29: Illustration of the effect of u_0 on system damping versus (a) the dimensionless frequency α_0 and (b) the non-linear dimensionless frequency α_{nl}; $V_s = 200m/s$, $PI = 0$, $H/B = 4$, Rayleigh damping $\xi = 5\%$.

5.2.3.4 Key remarks on non-linear analysis with RO model

The main conclusions of this section are:

- Static stiffness decreases as the thickness of the soil layer increases in all modes of vibration. The existence of bedrock at a shallow depth underneath the footing has a major effect on static stiffness, especially in the vertical and horizontal mode of loading. The rocking stiffness is practically unaffected by soil thickness because soil response is restricted in the vicinity of the footing.
- Dynamic stiffness is also affected by the depth to bedrock. The amplitude of foundation response increases substantially at frequencies near the natural frequency, in both vertical and horizontal modes of excitation.
- Excitation amplitude significantly affects the impedances. Naturally, high amplitudes result in lower stiffnesses and higher damping coefficients.
- The Ramberg-Osgood model used in FLAC cannot model failure, thus use of this model implies a large factor of safety. Excitation amplitudes on the order of 10^{-3} are the upper bound of the model applicability.

5.3 Non-linear analyses based on modified hyperbolic model

In this section, soil non-linearity was explored using a modified hyperbolic model calibrated against the Darendeli [4] experimental curves. Similarly with the aforementioned Ramberg-Osgood analyses, the lateral boundaries were established using static linear analyses. Consequently, the lateral boundaries are at a distance of $20B$ for swaying, $15B$ for vertical and $10B$ for rocking mode. The outcomes of the analyses are presented in the following subsections.

5.3.1 Evaluation of the model- Darendeli curves

Darendeli calibrated the experimental results he produced with modified hyperbolic model. His results were presented in detail earlier in Chapter 2 (section 2.4.2 titled

Darendeli fitted curves). He expressed the curvature coefficient and the pseudo-reference strain as a function of PI, OCR and mean effective stress σ'_0 . The fitted formula is

$$\gamma_r = \left(\phi_1 + \phi_2 \times PI \times OCR^{\phi_3}\right) \times \left(\sigma'_0 / p_\alpha\right)^{\phi_4} \tag{5.5}$$

$$\alpha = \phi_5 = 0.919 \tag{5.6}$$

where ϕ_{1-5} are constant parameters given in Table 2.10.

5.3.2 Non-linear static analysis

Starting with a basic analysis, four governing parameters have been examined in the three loading modes. The basic analysis considers a $2B = 5m$ wide footing resting on a $8B$ thick soil layer with shear wave velocity $V_s = 200\ m/s$, over-consolidation ratio $OCR = 5$ and plasticity index $PI = 0$.

The first governing parameter is type of soil as described by the plasticity index (PI). The modified hyperbolic model is used by Darendeli [4] in which the plasticity index is variable in the calculation of γ_r . Three different values for PI $(0, 15, 30)$ were investigated. The pseudo-reference strain was then used to normalise the abscissa of the graphs.

The second key parameter is depth of soil stratum and the third is over-consolidation ratio. Three different values are assumed for each parameter: $H = 2B$, $4B$, $8B$ and $OCR = 5$, 10, 15 respectively. These parameters have been taken into consideration for the respective static linear elastic analyses in the calculation of footing stiffness. Results are shown in the following subsections for all modes of loading.

To sum up, seven basic parametric analyses were conducted by changing three key parameters (OCR, PI, H). These analyses are repeated for three response modes of loading leading to 21 parametric analyses which were carried out using a grid of $0.2B$ element size in FLAC.

5.3.2.1 Vertical static loading

Considering vertical static load acting on a massless footing resting on non-linear soil the results are illustrated in Figure 5.30 for three soil layer thicknesses. In vertical axes static non-linear stiffness, K_v, is normalised by the static elastic stiffness, $K_{v,elastic}$, to eliminate the effect of soil properties. The normalised stiffness curves are presented

versus the vertical settlement, v, in the horizontal axes normalised by H to remove absolute units.

Non-linear static stiffness gradually decreases with the amplitude of settlement and approaches 5% of the static elastic stiffness when the normalised settlement reaches 1%. The soil layer thickness has no effect on this trend, as one would expect.

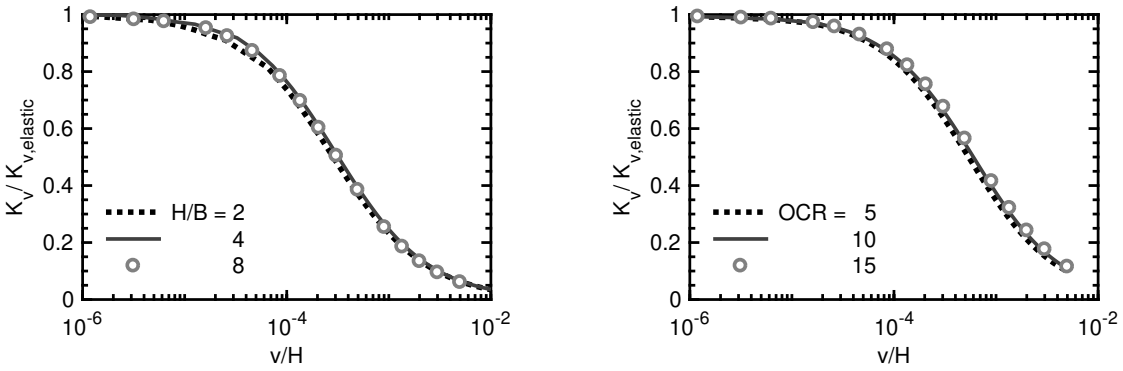

Figure 5.30: Illustration of the effect of (a) soil layer thickness, H, for $OCR = 5$ and (b) overconsolidation ratio OCR for $H/B = 8$, on the normalised non-linear vertical static stiffness versus the normalised settlement over H; $PI = 0$, $V_s = 200m/s$, $B = 2.5m$.

On the other hand, an increase in plasticity index of the soil, PI, which is accounted for through the parameter γ_r, naturally increases the non-linear vertical stiffness. The influence is evident in Figure 5.31 after a normalised settlement on the order of 10^{-5}. The stiffness decrease starts at smaller settlements in soils with $PI = 0$ over more plastic soils ($PI = 15$ and 30). However, the gradient of the decrease is similar in all three cases.

To eliminate the effect of PI on the non-linear vertical stiffness curves the horizontal axis is further normalised with γ_r. The results are shown in Figure 5.31 (b). Interestingly, all the analyses are falling into a single universal curve.

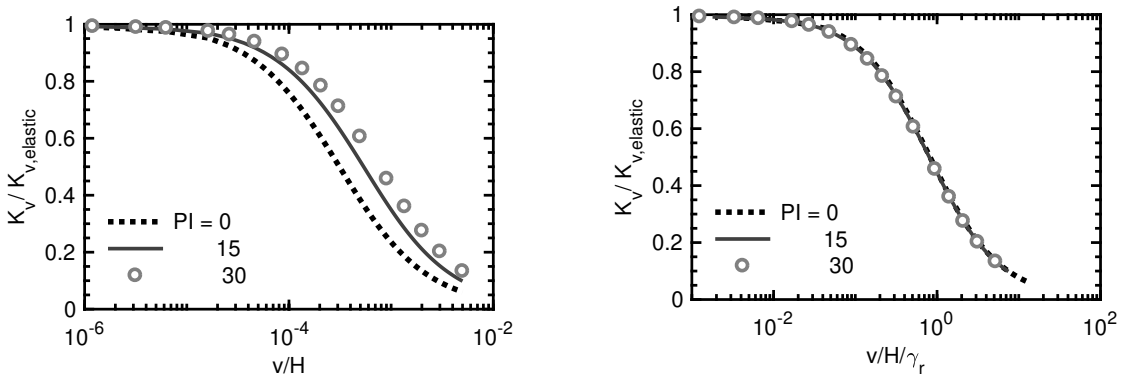

Figure 5.31: Illustration of the effect of PI on the normalised non-linear vertical static stiffness versus (a) the normalised settlement over H and (b) the normalised settlement over H over the MH parameter γ_r; $OCR = 5$, $V_s = 200m/s$, $H/B = 8$, $B = 2.5m$.

5.3.2.2 Lateral static loading

Switching our attention to the horizontal mode and static loading, the effect of soil layer thickness is illustrated in Figure 5.32 (a). Similarly to the previous case, H does not seem to influence the normalised lateral static stiffness. The trends are identical and the discrepancies are minor.

On the other hand, the non-linear lateral static stiffness is affected only slightly by OCR with smaller values of OCR producing slightly higher lateral stiffness as shown in Figure 5.32 (b).

Following, the effect of plasticity index is investigated and the outcomes are depicted in Figure 5.33 (a). Higher PI values result in higher lateral stiffness. Evidently, a PI of 30% produces 40% higher static stiffness than a soil with PI of 0 when the normalised lateral displacement exceeds 10^{-4}. This difference can be eliminated if the horizontal axis is further normalised with the MH model parameter γ_r as shown in Figure 5.33 (b).

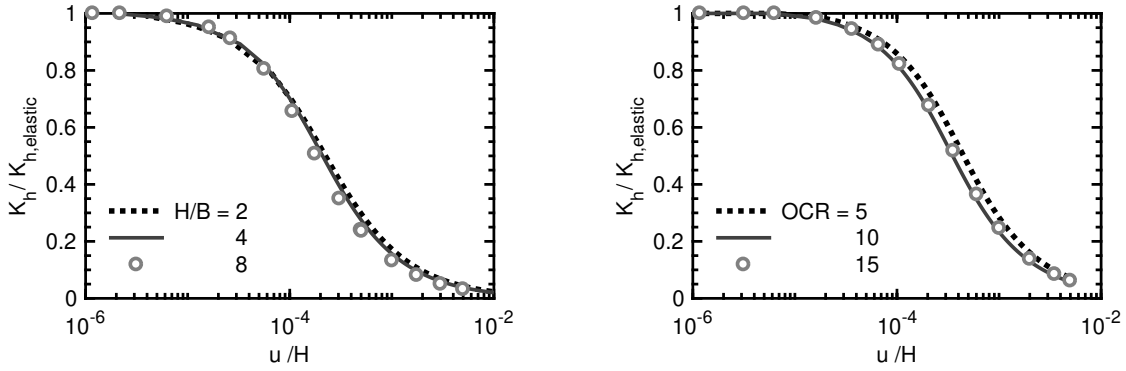

Figure 5.32: Illustration of the effect of (a) soil layer thickness, H, for $OCR = 5$ and (b) overconsolidation ratio OCR for $H/B = 8$, on the normalised non-linear lateral static stiffness versus the normalised horizontal displacement over H; $PI = 0$, $V_s = 200m/s$, $B = 2.5m$.

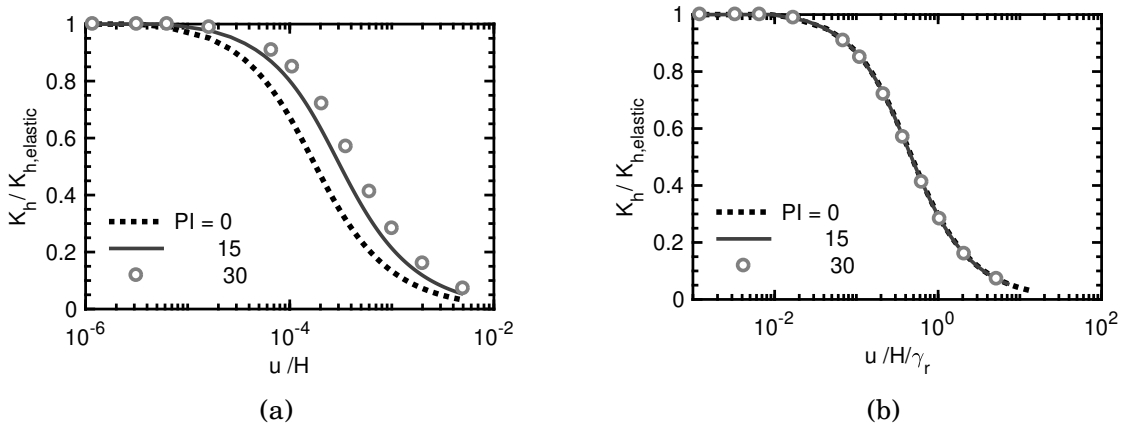

Figure 5.33: Illustration of the effect of PI on the normalised non-linear lateral static stiffness versus (a) the normalised settlement over H and (b) the normalised settlement over H over MH model parameter γ_r ; $OCR = 5$, $V_s = 200m/s$, $H/B = 8$, $B = 2.5m$.

5.3.2.3 Rocking static loading

In the rocking mode and under static conditions, similar trends are observed: stiffness decreases with increasing magnitude of rocking angle, θ. The effect of soil thickness is more noticeable (Figure 5.34 a) with the shallowest soil layer developing lower rocking stiffness. Moreover, over-consolidation does not influence static rocking stiffness (Figure 5.34 b).

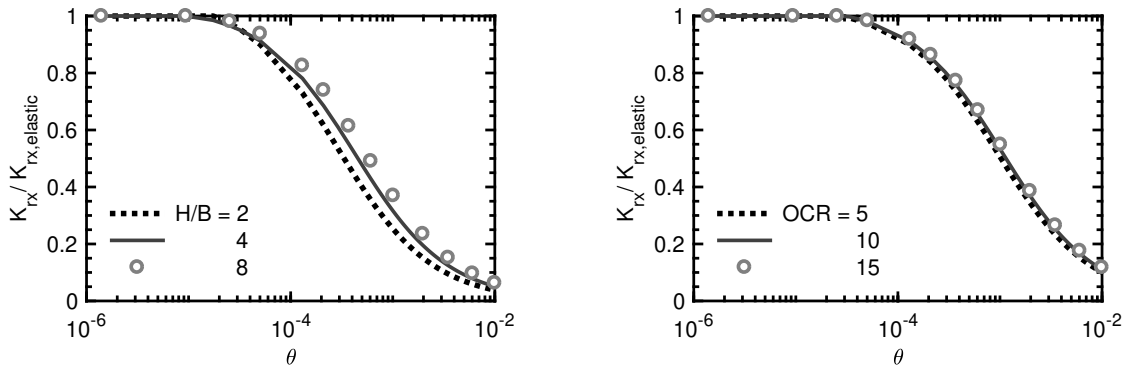

Figure 5.34: Illustration of the effect of (a) soil layer thickness, H, for $OCR = 5$ and (b) overconsolidation ratio OCR for $H/B = 8$, on the normalised non-linear rocking static stiffness versus the rotation angle; $PI = 0$, $V_s = 200m/s$, $B = 2.5m$.

As discussed in the previous two loading cases, the plasticity index effect is also evident in rocking loading (Figure 5.35 a). This effect can, again, be eliminated with the appropriate normalisation of θ by γ_r (Figure 5.35 b).

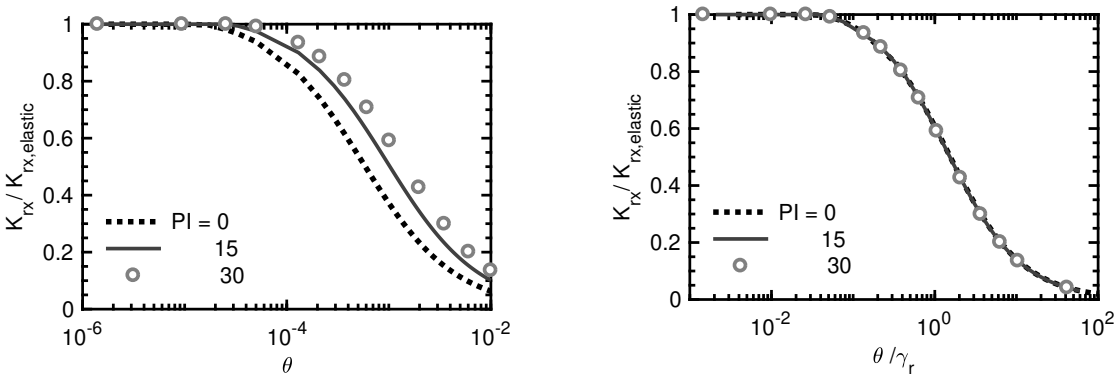

(a) (b)

Figure 5.35: Illustration of the effect of PI on the normalised non-linear rocking static stiffness versus (a) the rotation angle and (b) versus the rotation angle over MH model parameter γ_r; $OCR = 5$, $V_s = 200m/s$, $H/B = 8$, $B = 2.5m$.

5.3.2.4 Key remarks on static non-linear analysis with MH model

Similarly to the Ramberg-Osgood static analysis, the curves in Figures 5.31 (b), 5.33 (b) and 5.35 (b), are almost identical for each type of loading. Therefore, one curve for each mode of loading is sufficient to describe the non-linear soil behaviour. The plasticity index, PI, is accounted for in the modified hyperbolic model through the pseudo-reference shear strain γ_r and its effect is eliminated from the graphs.

For instance, taking the case of rocking static stiffness, the resulting curves could be fitted according to the formula

$$\frac{K_{rx}}{K_{rx,elastic}} = \frac{1}{1+\left(\frac{\theta}{\theta_r}\right)^{\alpha}} \tag{5.7}$$

where α is the familiar modified hyperbolic exponent suggested by Darendeli [4] to be equal to 0.919, and θ_r is a "pseudo-reference" rocking angle which equals $1.5 \cdot \gamma_r$. Accordingly, Equation 5.7 can be adjusted to account for vertical and horizontal loading by replacing θ with v/H and u/H, respectively.

The static linear elastic stiffness $K_{v,elastic}$ is a function of G, B, H, ν and can be easily determined by the diagrams and equations provided in Section 4.1. Therefore, if v, u or θ are known, the non-linear static stiffness can be calculated by equation 5.7 for any given plasticity index and overconsolidation ratio (accounted for through γ_r).

5.3.3 Non-linear dynamic analysis

Following, the dynamic response of a strip footing resting on a non-linear soil layer obeying a modified hyperbolic model is investigated. For the sake of simplicity and compatibility with future comparisons, all other parameters but the soil model are kept the same. The finite difference grid used herein is shown in Figure 5.12. A detailed description of the grid, the soil properties and the footing is given in Section 5.2.3.

5.3.3.1 Vertical dynamic response

The effect of soil thickness on vertical stiffness and damping is illustrated in Figures 5.36 and 5.37, respectively. Shallow soil layers result in a gradually decreasing stiffness and higher material damping. Given that the natural frequency of the deposit decreases with depth, resonance occurs in lower frequencies in deep deposits. The amplitude of foundation motion (inverse of stiffness) increases accordingly near these frequencies.

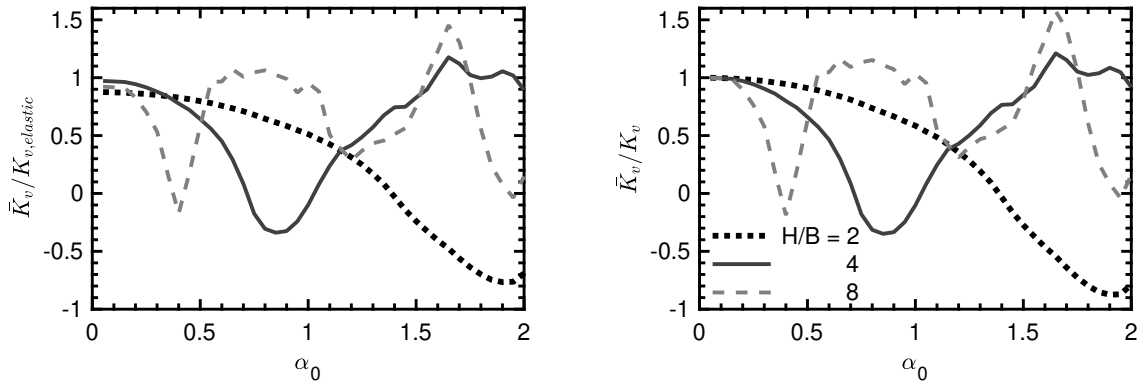

Figure 5.36: Illustration of the effect of H/B on the non-linear vertical dynamic stiffness normalised (a) by the static linear elastic stiffness and (b) by the non-linear static stiffness versus the dimensionless frequency α_0; $OCR = 5$, $V_s = 200m/s$, $PI = 0$, $v_0/H = 10^{-5}$, Rayleigh damping $\xi = 5\%$.

The effect of excitation amplitude is examined in Figures 5.38 and 5.39. After normalisation of both vertical and horizontal axes, the results are indistinguishable for α_0 less than 1.2 as shown in Figure 5.39.

In terms of damping, material damping seems to increase with increasing amplitude (Figures 5.40). Differences on the order of 90% are observed that can explain the smaller stiffness at low frequencies (Figure 5.38 a).

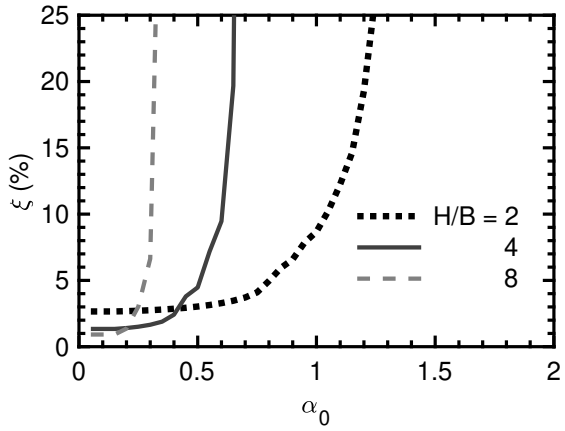

Figure 5.37: Illustration of the effect of H/B ratio on the damping ratio versus the dimensionless frequency α_0; $OCR = 5$, $V_s = 200m/s$, $PI = 0$, $v_0/H = 10^{-5}$, Rayleigh damping $\xi = 5\%$.

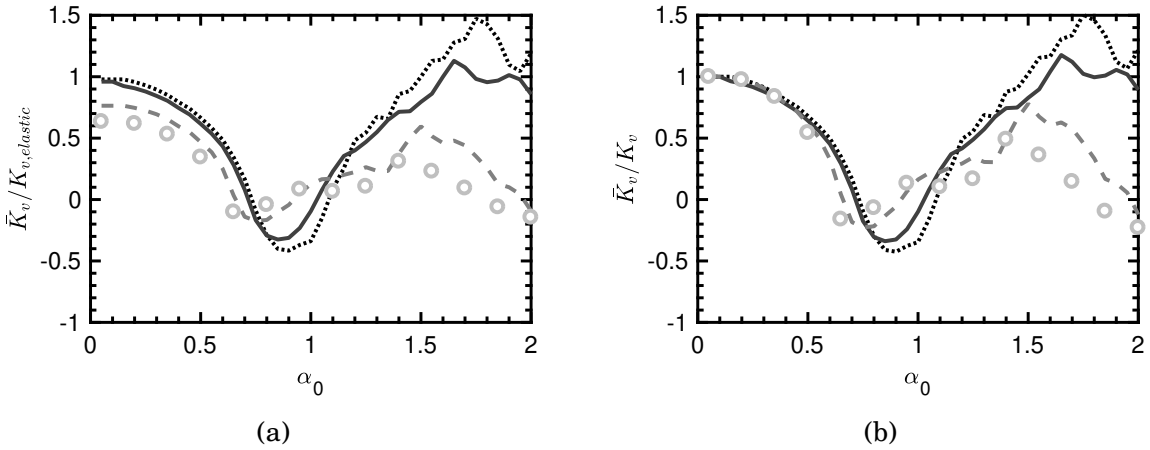

(a) (b)

Figure 5.38: Illustration of the effect of oscillations amplitude, v_0 on the non-linear vertical dynamic stiffness normalised (a) by the static linear elastic stiffness and (b) by the non-linear static stiffness versus the dimensionless frequency α_0; $OCR = 5$, $V_s = 200m/s$, $PI = 0$, $H/B = 4$, Rayleigh damping $\xi = 5\%$.

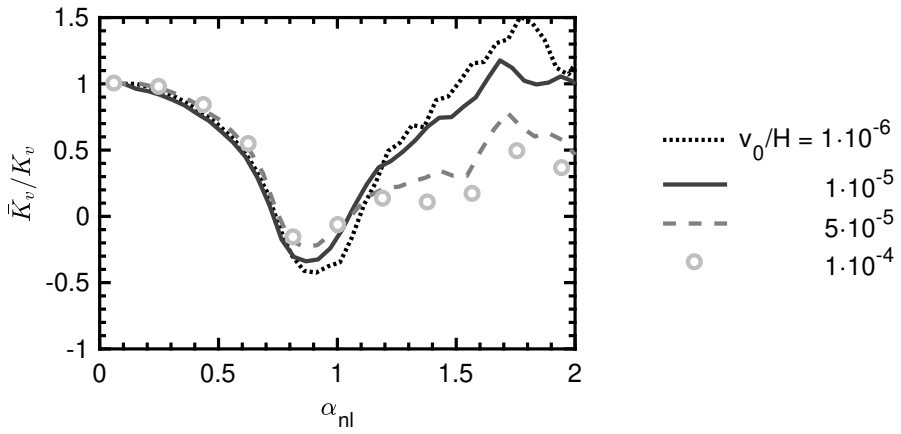

Figure 5.39: Illustration of the effect of v_0 on the normalised non-linear vertical dynamic stiffness by the non-linear static stiffness versus the non-linear dimensionless frequency α_{nl}; $OCR = 5$, $V_s = 200m/s$, $PI = 0$, $H/B = 4$, Rayleigh damping $\xi = 5\%$.

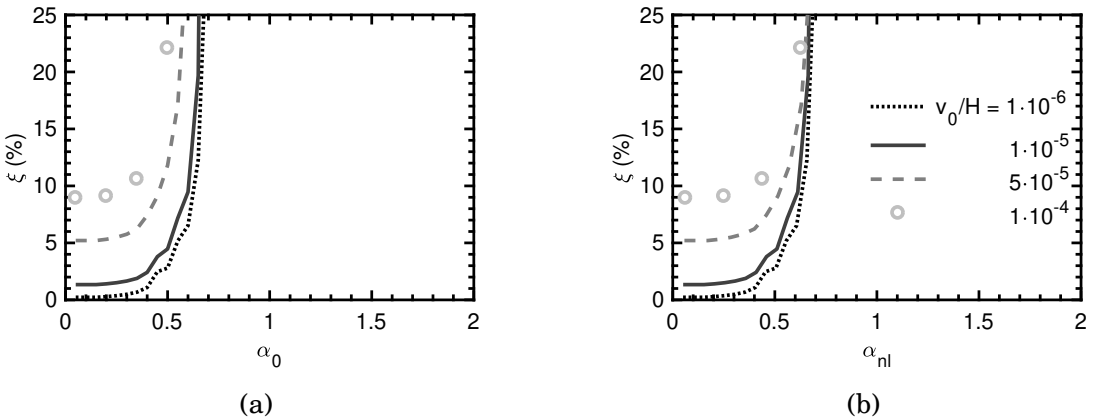

(a) (b)

Figure 5.40: Illustration of the effect of v_0 on system damping versus (a) the dimensionless frequency α_0 and (b) the non-linear dimensionless frequency α_{nl}; $OCR = 5$, $V_s = 200m/s$, $PI = 0$, $H/B = 4$, Rayleigh damping $\xi = 5\%$.

5.3.3.2 Horizontal dynamic response

Switching our attention to the horizontal mode, the effect of H is presented in Figures 5.41 and 5.42 in terms of stiffness and damping, respectively. The natural dimensionless frequencies for H/B equals to 8, 4 and 2 are analogous with values of 0.2, 0.4 and 0.8, respectively. The aforementioned values are matching the results, verifying the correct use of the constitutive model.

At low frequencies, damping increases with depth (Figure 5.42). Given that the stiffness component of Rayleigh damping is not defined in user implemented models, the observed damping is a result of the inherited damping of the model. Shallower soil deposits naturally provide more damping because of the rigid boundary close to the applied force.

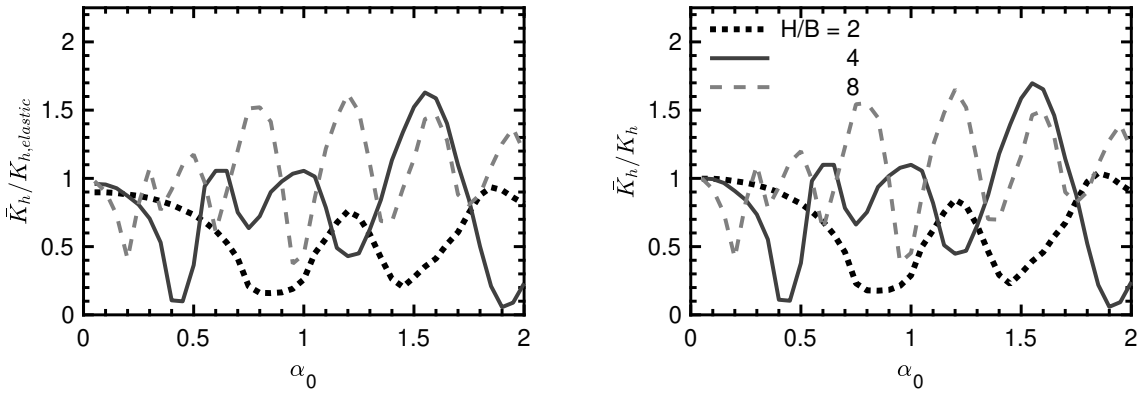

Figure 5.41: Illustration of the effect of H/B on the non-linear lateral dynamic stiffness normalised (a) by the static linear elastic stiffness and (b) by the non-linear static stiffness versus the dimensionless frequency α_0; $V_s = 200m/s$, $PI = 0$, $u_0/H = 1 \cdot 10^{-5}$, mass component of Rayleigh damping $\xi = 2.5\%$.

Following, the effect of horizontal displacement amplitude is investigated Figures 5.43, 5.44 and 5.45. Stiffness naturally decreases for higher amplitudes. Overall, horizontal dynamic stiffness for u_0/H on the order of 10^{-6} is around 30% higher than for the case of $u_0/H = 10^{-4}$ in which the stiffness peaks are smoother.

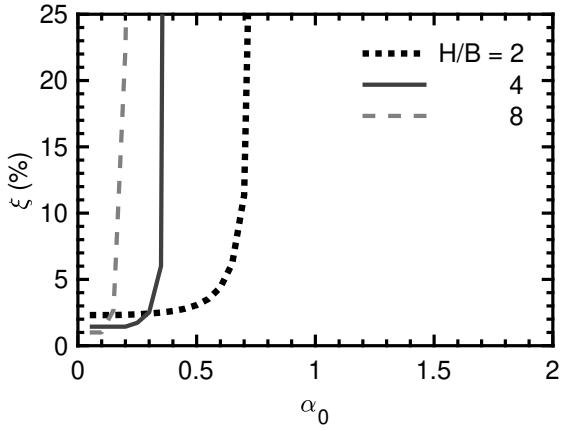

Figure 5.42: Illustration of the effect of H/B ratio on the damping ratio versus the dimensionless frequency α_0; $V_s = 200m/s$, $PI = 0$, $u_0/H = 1 \cdot 10^{-5}$, mass component of Rayleigh damping $\xi = 2.5\%$.

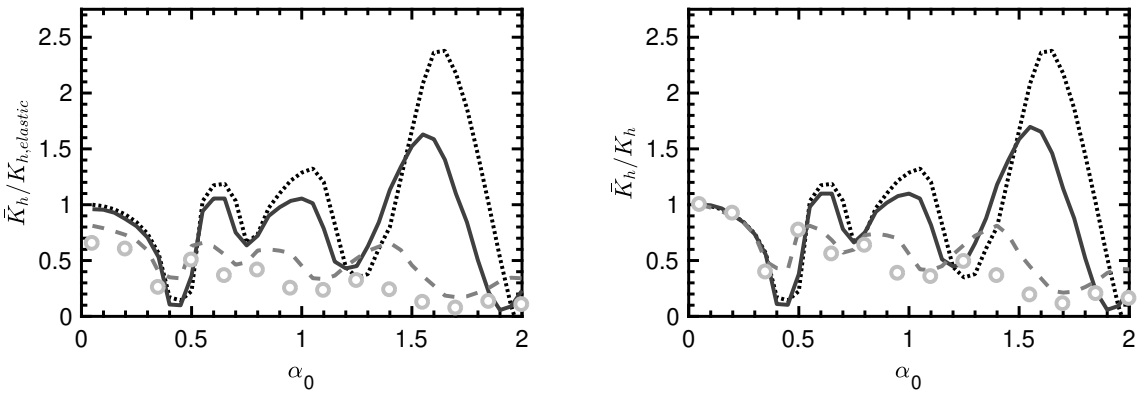

(a) (b)

Figure 5.43: Illustration of the effect of oscillations amplitude, u_0 on the non-linear lateral dynamic stiffness normalised (a) by the static linear elastic stiffness and (b) by the non-linear static stiffness versus the dimensionless frequency α_0; $V_s = 200m/s$, $PI = 0$, $H/B = 4$, mass component of Rayleigh damping $\xi = 2.5\%$.

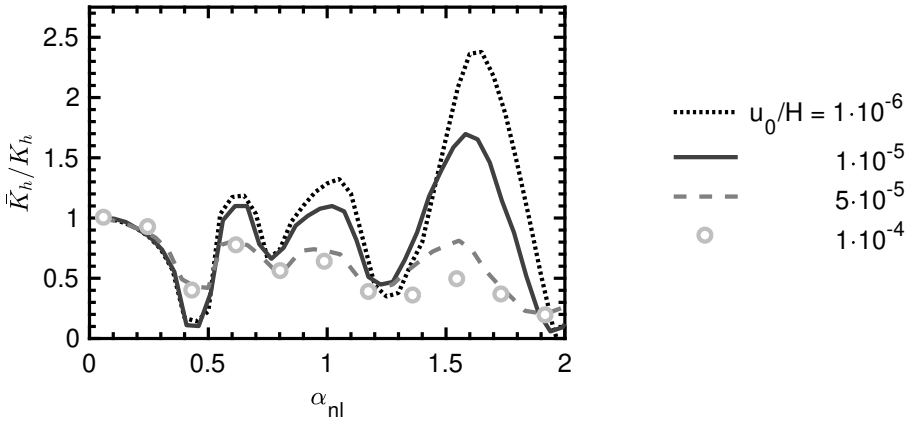

Figure 5.44: Illustration of the effect of u_0 on the normalised non-linear lateral dynamic stiffness by the non-linear static stiffness versus the non-linear dimensionless frequency α_{nl}; $V_s = 200m/s$, $PI = 0$, $H/B = 4$, mass component of Rayleigh damping $\xi = 2.5\%$.

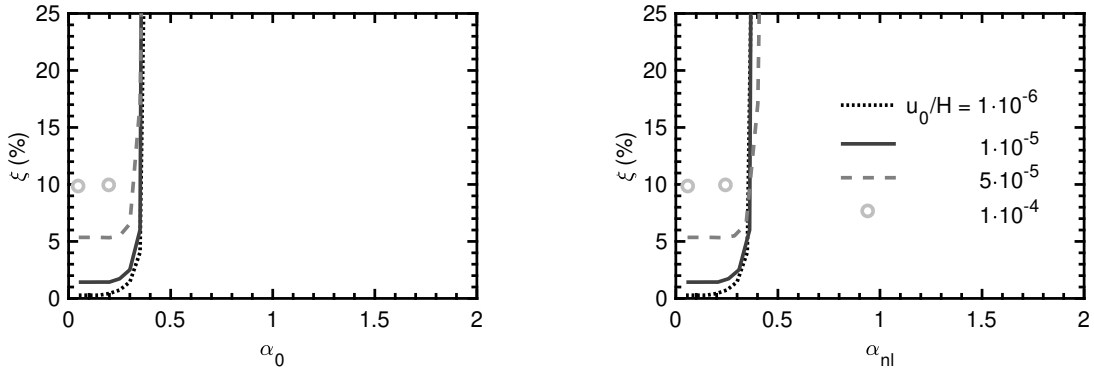

Figure 5.45: Illustration of the effect of u_0 on system damping versus (a) the dimensionless frequency α_0 and (b) the non-linear dimensionless frequency α_{nl}; $V_s = 200m/s$, $PI = 0$, $H/B = 4$, mass component of Rayleigh damping $\xi = 2.5\%$.

5.3.3.3 Rocking dynamic response

Rocking dynamic impedance is examined in this section. In the same vein as the aforementioned loading cases, soil thickness and the rotation angle amplitude are investigated.

The non-linear rocking stiffness decreases linearly with dimensionless frequency and is not affected considerably by depth before $\alpha_0 = 1$. Beyond this point, the shallowest layer considered herein results in 40% lower dimensionless stiffness. Similarly, radiation damping increases linearly for all depths but $H/B = 2$ where it suddenly increases at the soil deposit natural dimensionless frequency $\alpha_{0_1} = 1.2$.

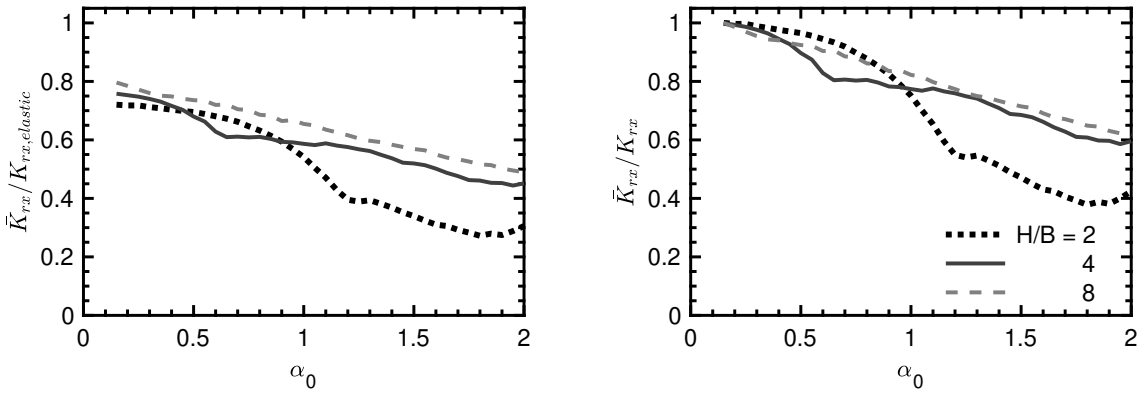

Figure 5.46: Illustration of the effect of H/B on the non-linear rocking dynamic stiffness normalised (a) by the static linear elastic stiffness and (b) by the non-linear static stiffness versus the dimensionless frequency α_0; $V_s = 200m/s$, $PI = 0$, $\theta = 10^{-4}\ rad$, Rayleigh damping $\xi = 5\%$.

For a soil layer as thick as $4B$ rotation angle amplitude effect is shown in Figures 5.48 and 5.49. The non-linear rocking stiffness is only 30% of the linear static stiffness when θ_{max} is on the order of $10^{-3}\ rad$. This effect is eliminated in Figure 5.49 where the stiffness is plotted versus the non-linear dimensionless frequency α_{nl}.

With damping, an increase is observed with increasing rotation angle amplitude with values reaching up to 25% for the highest amplitude examined. In contrast, for small amplitudes, damping is negligible before $\alpha_0 = 0.5$.

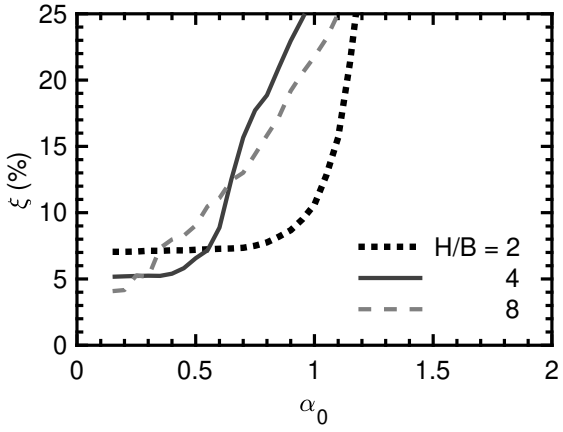

Figure 5.47: Illustration of the effect of H/B ratio on the damping ratio versus the dimensionless frequency α_0; $V_s = 200m/s$, $PI = 0$, $\theta = 10^{-4}\ rad$, Rayleigh damping $\xi = 5\%$.

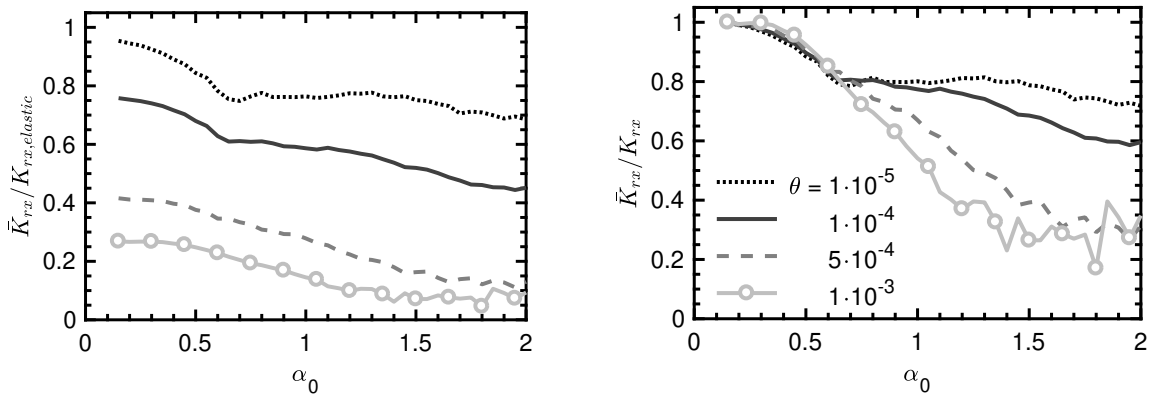

(a) (b)

Figure 5.48: Illustration of the effect of oscillations amplitude, θ (in rad) on the non-linear rocking dynamic stiffness normalised (a) by the static linear elastic stiffness and (b) by the non-linear static stiffness versus the dimensionless frequency α_0; $V_s = 200m/s$, $PI = 0$, $H/B = 4$, Rayleigh damping $\xi = 5\%$.

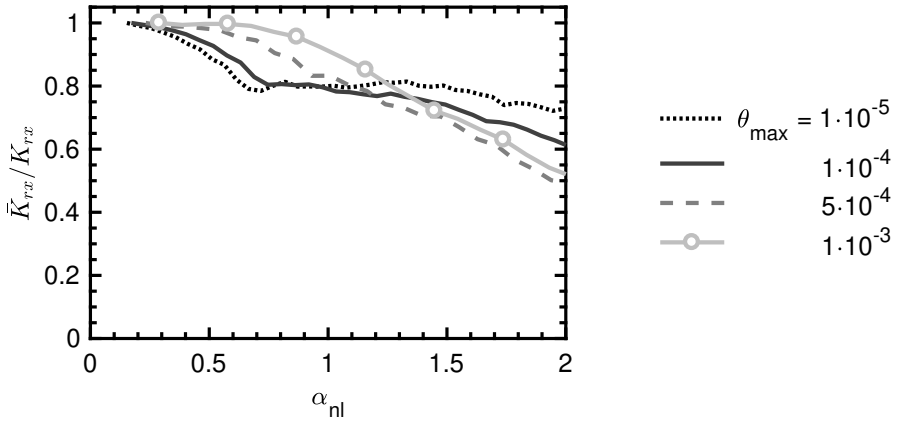

Figure 5.49: Illustration of the effect of θ_{max} (in rad) on the normalised non-linear rocking dynamic stiffness by the non-linear static stiffness versus the non-linear dimensionless frequency α_{nl}; $V_s = 200m/s$, $PI = 0$, $H/B = 4$, Rayleigh damping $\xi = 5\%$.

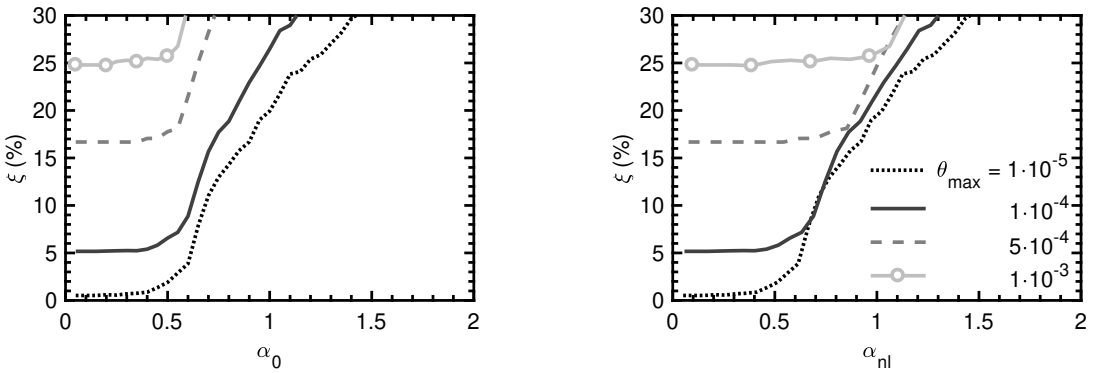

(a) (b)

Figure 5.50: Illustration of the effect of θ_{max} (in rad) on system damping versus (a) the dimensionless frequency α_0 and (b) the non-linear dimensionless frequency α_{nl}; $V_s = 200m/s$, $PI = 0$, $H/B = 4$, Rayleigh damping $\xi = 5\%$.

5.3.3.4 Key remarks on non-linear analysis with MH model

Summing up, the key points of this section are:

- The static stiffness increases as the thickness of the soil layer decreases in all modes of vibration. The presence of bedrock at a shallow depth underneath the footing has a major effect on static stiffness, especially in the vertical and horizontal mode of loading. The rocking stiffness is practically unaffected by soil thickness because soil response is limited to the vicinity of the footing.
- The dynamic stiffness is also affected by the bedrock. The amplitude of foundation motion can increase substantially at frequencies close to natural frequency of the deposit, both in vertical and horizontal modes. This phenomenon is only observed in shallow soil layers during rocking oscillations.
- Excitation amplitude significantly affects stiffness and damping in all excitation modes. In general, high amplitudes produce lower stiffnesses and higher damping coefficients.
- Given that the modified hyperbolic model used in FLAC cannot model failure, this model implies large factors of safety. The model is applicable for shear strains on the order of 10^{-3} or so.

5.4 Comparison of RO and MH constitutive models

The previous sections were focused on the parametric non-linear analysis of rigid, massless, strip footings resting on a soil layer. The non-linear, hysteretic soil behaviour was based on two constitutive models, the Ramberg-Osgood and the modified hyperbolic.

In this section, the normalised non-linear static stiffness over the linear elastic stiffness of a soil governed by the Ramberg-Osgood constitutive relationships is compared with the corresponding values of a soil following modified hyperbolic stress-strain expressions. The comparison is made for all three modes of loading and the respective outcomes are plotted in Figures 5.51 to 5.52. Both non-linear constitutive models result in a decrease of static stiffness with increasing displacement/rotation.

More specifically, in Figure 5.51 (a) the non-linear vertical stiffness is plotted versus normalised settlement. Up to a normalised settlement of $v/H = 2 \cdot 10^{-4}$ the two constitutive models result in indistinguishable results. Beyond this point the discrepancy

between the two is increasing. The non-linear static stiffness governed by RO model is almost four times the corresponding value governed by MH model at large settlements.

Similar behaviour is observed for the other translational stiffness as shown in Figure 5.51 (b). The horizontal stiffness following RO constitutive model is higher beyond $u/H = 1 \cdot 10^{-4}$. Before that point the non-linear static stiffness defined by means of MH model is slightly higher.

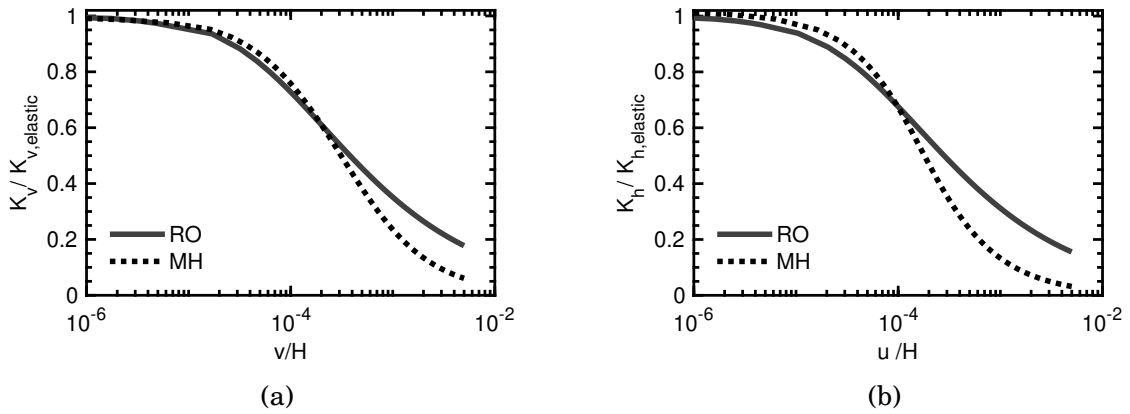

Figure 5.51: Comparison of Ramberg-Osgood and modified hyperbolic constitutive models in terms of normalised non-linear static (a) vertical and (b) horizontal stiffness versus the normalised respective displacement; $PI = 0$, $H/B = 8$, $V_s = 200m/s$, $\nu = 0.3$.

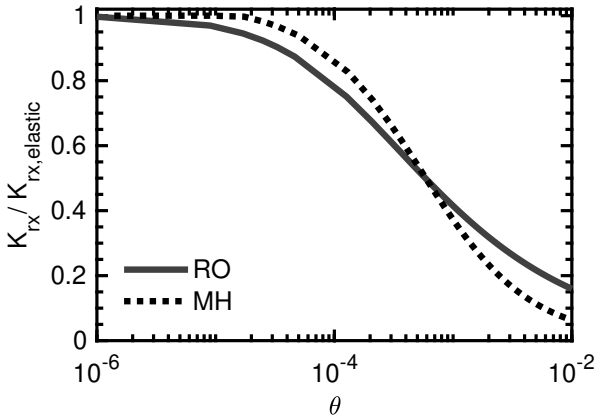

Figure 5.52: Comparison of Ramberg-Osgood and modified hyperbolic constitutive models in terms of normalised non-linear static rocking stiffness versus the rotation angle; $PI = 0$, $H/B = 8$, $V_s = 200m/s$, $\nu = 0.3$.

The same behaviour but in a more pronounced fashion is noticed for the static rocking stiffness 5.52. MH model results in higher rocking stiffness up to a rotation angle of

$\theta = 5 \cdot 10^{-4}\ rad$. The trend is flipped beyond that point and RO model results in higher static rocking stiffness. The discrepancy noticed is almost 10% of $K_{rx.elastic}$.

Overall, the soil described by RO constitutive relationships is stiffer when subjected to static translational loading in higher displacement amplitudes. However, in rocking mode of loading the discrepancy is fluctuating with MH model resulting in larger stiffness up to the curve's turning point. Beyond this the RO produces higher stiffness.

Switching our attention to dynamic impedance components, stiffness and damping, the results are presented for all three modes of loading in Figures 5.53 to 5.55. In general, due to normalisation of the abscissa, the influence of the model is omitted. On the contrary the effect of the non-linear constitutive model is evident in the static stiffness plots (Figures 5.51, 5.52).

For vertical oscillations, the impedance components with the assumption of a Ramberg-Osgood model or a modified hyperbolic are indistinguishable and very similar to the elasto-dynamic corresponding values (Figures 5.53). Material damping is slightly lower in the non-linear regime as a result of the difficulty to define stiffness proportional Rayleigh damping.

On the other hand, horizontal impedance components are in perfect agreement only at low frequencies (Figures 5.54). Beyond $\alpha_0 = 1$ a shift to the left is observed. The discrepancies between the two non-linear models are not as significant as the difference between them and the elasto-dynamic solution.

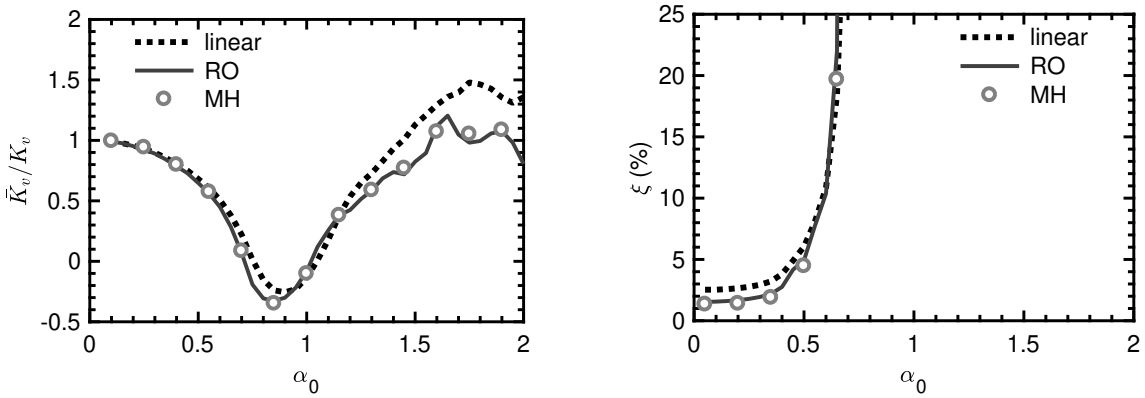

Figure 5.53: Comparison of linear, Ramberg-Osgood and modified hyperbolic constitutive models in terms of (a) normalised dynamic vertical stiffness and (b) damping coefficient versus dimensionless frequency; $PI = 0$, $H/B = 4$, $V_s = 200m/s$, $\nu = 0.3$, $\xi = 5\%$.

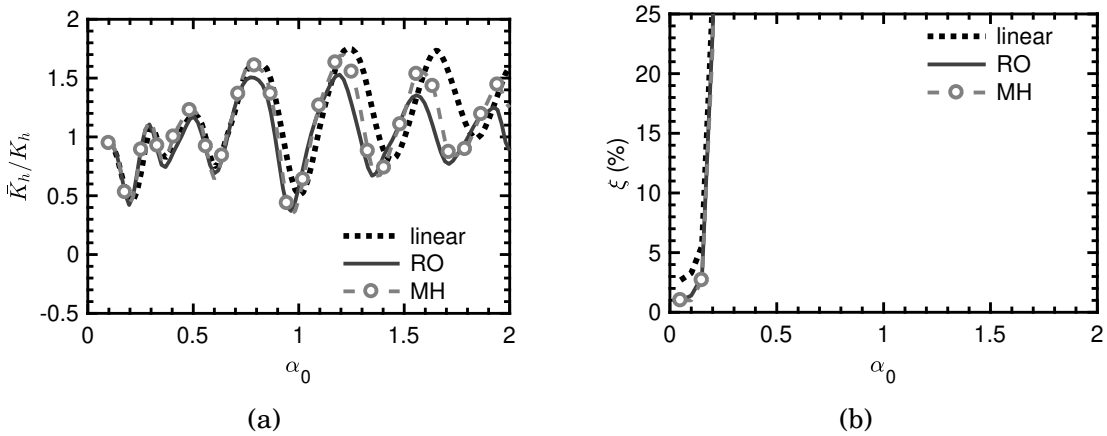

(a) (b)

Figure 5.54: Comparison of linear, Ramberg-Osgood and modified hyperbolic constitutive models in terms of (a) normalised dynamic lateral stiffness and (b) damping coefficient versus dimensionless frequency; $PI = 0$, $H/B = 8$, $V_s = 200m/s$, $\nu = 0.3$, $\xi = 5\%$.

As far as the rocking impedance parts are concerned, differences are getting more obvious for dimensionless frequencies beyond $\alpha_0 = 0.5$, as shown in Figures 5.55. Non-linear stiffness is decreasing with frequency at a faster rate than the corresponding linear stiffness. On the other hand, damping in the linear regime exceeds by more than 25% the non-linear system damping. The difference between the two studied non-linear models is negligible. Ramberg-Osgood model produces insignificantly larger damping and lower stiffness at high frequencies.

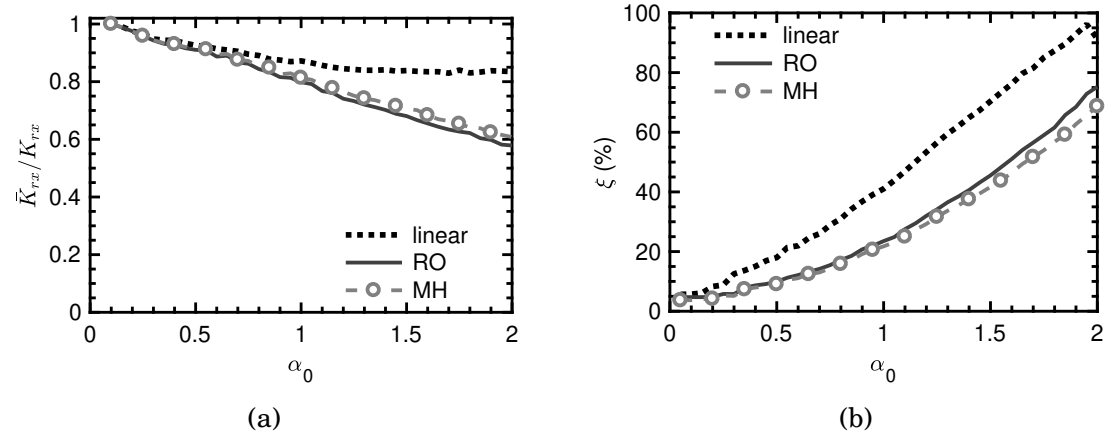

(a) (b)

Figure 5.55: Comparison of linear, Ramberg-Osgood and modified hyperbolic constitutive models in terms of (a) normalised dynamic rocking stiffness and (b) damping coefficient versus dimensionless frequency; $PI = 0$, $H/B = 8$, $V_s = 200m/s$, $\nu = 0.3$, $\xi = 5\%$.

5.5 Investigation of strain rate effects

This section has been published in the proceedings of the 16th European Conference on Earthquake Engineering by Katsiveli et al [154].

5.5.1 Calibration against Vardanega et al

Vardanega and Bolton [139] processed a database of 67 tests on 21 fine grained soils for the influence of rate effects assuming a 5% reduction per log cycle (an assumption made based on the findings of Lo Presti et al [141] and d'Onofrio et al [142]). The analysis of the database produced expressions for the reference stain linked to plasticity index (following the observations of [8]). For the static adjustment, the curvature parameter and the reference strain were shown to be linked to changes in plasticity via the empirical relationships shown as equation 5.8

$$\alpha = 0.736 \qquad \gamma_r = 2.2\frac{PI}{1000} \tag{5.8}$$

while for the dynamic adjustment the curvature parameter and the reference strain were shown to be linked to changes in plasticity via the empirical relationships shown as equation 5.9

$$\alpha = 0.943 \qquad \gamma_r = 3.7\frac{PI}{1000} \tag{5.9}$$

which correspond to a strain rate of $10^{-2}/s$. Note that PI is expressed numerically for both equations 5.8 and 5.9.

The modified hyperbolic model parameters α, γ_r vary depending on the strain rate correction applied. In the initial set analysis the α and γ_r was held constant at $\alpha = 0.736$ and $\gamma_r = 1.1 \cdot 10^{-3}$ (using Equations 5.8), which describes a static adjustment (STA). A second set of analyses is conducted with the parameter values $\alpha = 0.943$ and $\gamma_r = 1.85 \cdot 10^{-3}$ (using Equations 5.9), which describes a pseudo shear strain rate adjustment (PSSR) in the model. Using these sets of parameters, analyses were carried out for both static and dynamic loads.

Nevertheless, a rigorous analysis of the problem also requires considering the variation of shear strain rates across the foundation subsoil. To achieve this, a third set of analyses was carried out, more accurately accounting for shear strain rate effects, by appropriately varying the model parameters with location and with time, a function of the shear strain rate in each element of the mesh. As a first approximation, the expres-

sions used for intermediate values of strain rates were obtained from linear interpolation between the two aforementioned sets of limiting values (STA and PSSR) see Figure 5.56.

To this end, FISH is used to prescribe the variation of model properties across the grid (mesh), as a function of the strain-rate given by FLAC for every zone (element) during every time-step. This allows the accurate implementation of strain-rate effects, as presented in Figure 5.56.

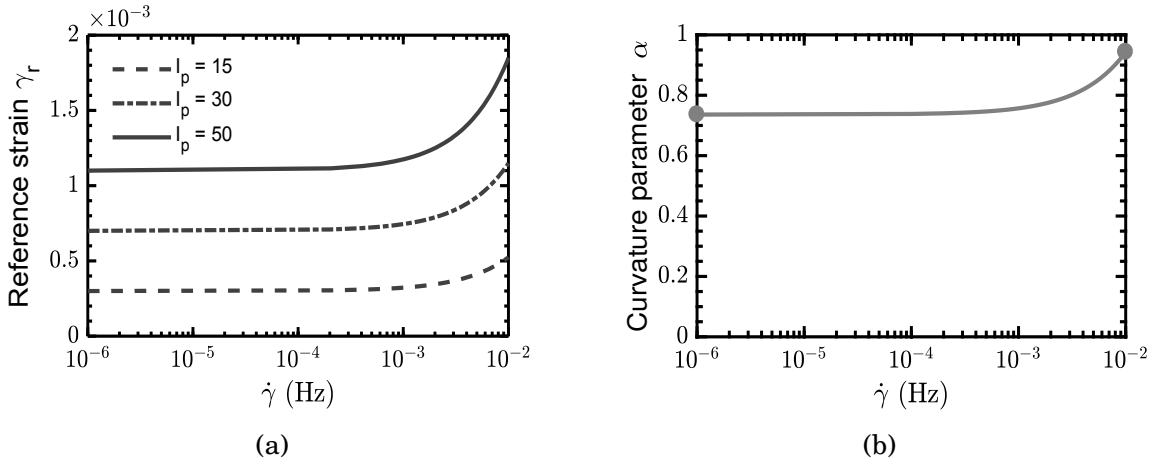

Figure 5.56: Modified hyperbolic model parameter (a) γ_r and (b) α as functions of the strain rate (units of frequency).

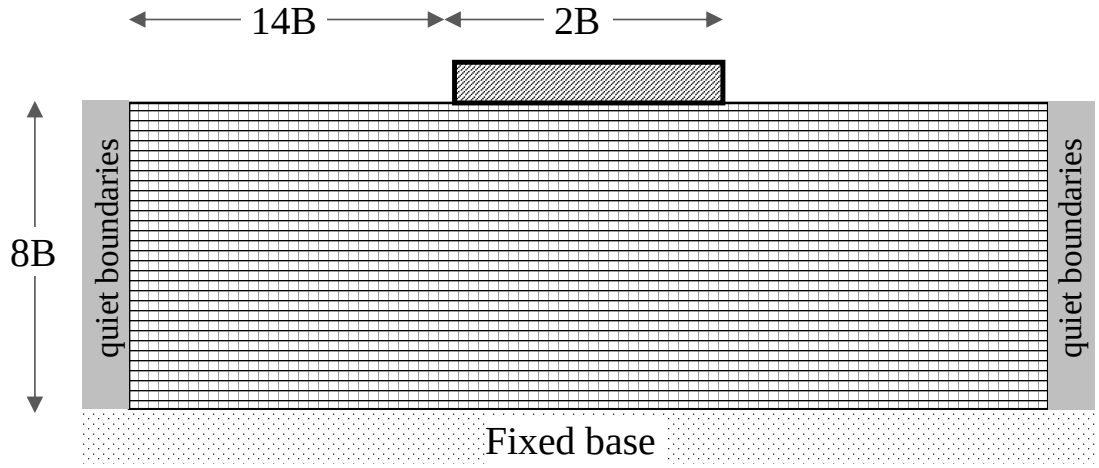

Figure 5.57: Evaluation of linear static analyses

The finite difference grid utilised in the analyses is shown in Figure 5.57. More specifically, a grid of width (14 B) was used, with a total depth of (8B), where B is the

half-width of the footing. In this case, a value of $B = 2.5m$ was selected, although the results can be readily generalised to other footing widths. Quiet boundaries were employed at the sides of the model, while movements at the base were fixed in both directions. The model was discretised into square elements of (0.4 B). Note that the accuracy of this discretisation was verified through rigorous mesh sensitivity analyses.

Soil behaviour was simulated using the aforementioned Modified Hyperbolic Model. A shear wave velocity $V_s = 158m/s$ and a soil mass density $\rho = 2Mg/m^3$ were considered, corresponding to a maximum shear modulus $G_{max} = 50MPa$. The Poisson's ratio was taken as $\nu = 0.35$. In dynamic analyses, a Rayleigh damping $\xi = 3\%$ was also incorporated to account for soil damping at small shear strain amplitudes. For larger amplitudes, additional hysteretic damping was obtained inherently from the non-linear response of the implemented soil model. It should be noted that damping has a minor influence on the stiffness values reported in this work and won't be discussed further.

Finally, the footing movement was applied as a prescribed velocity or acceleration imposed to the corresponding model nodes. The reactions at these nodes allowed to calculate, using FLAC's inbuilt programming language FISH, the corresponding overturning moment. Since the implemented model does not account for failure, the initial loading applied to the model does not affect the obtained results. Nevertheless, the obtained response is only valid for medium factor-of-safety values (e.g., FS = 2 to 3) and small-to-medium forces/displacements (or moments/rotations), when the applied cyclic loading does not induce bearing capacity failure or foundation uplifting.

5.5.2 Rocking static loading

Firstly, a linear static analysis was carried out to evaluate FLAC's performance in rocking response. The scope of this analysis is to prove the suitability of model dimensions and boundary fixities on the accuracy of stiffness calculation. For the case examined herein, static rocking stiffness equation in Table 4.1 predicts a rocking stiffness $K_{rx,elastic} = 7.74 \cdot 10^5 kN/m^2$. This is in notably good agreement (less than 0.7% discrepancy) with the numerically obtained value of $7.79 \cdot 10^5 kN/m^2$.

The non-linear rocking stiffness is illustrated in Figure 5.58. In vertical axes, static values of normalised non-linear rocking stiffness $K_{rx}/K_{rx,elastic}$ are plotted versus the rocking angle θ (a) and θ normalised by the reference strain γ_r (b). Evidently, stiffness degradation might be stronger for the case of pseudo-shear strain rate parameters, notably beyond $\theta = 10^{-4}\ rad$ and $\theta/\gamma_r = 10^{-1}\ rad$. In these curves, the effect of model

parameters is also evident. Overall, the increase in stiffness due to pseudo strain rate effects does not exceed 10% or so.

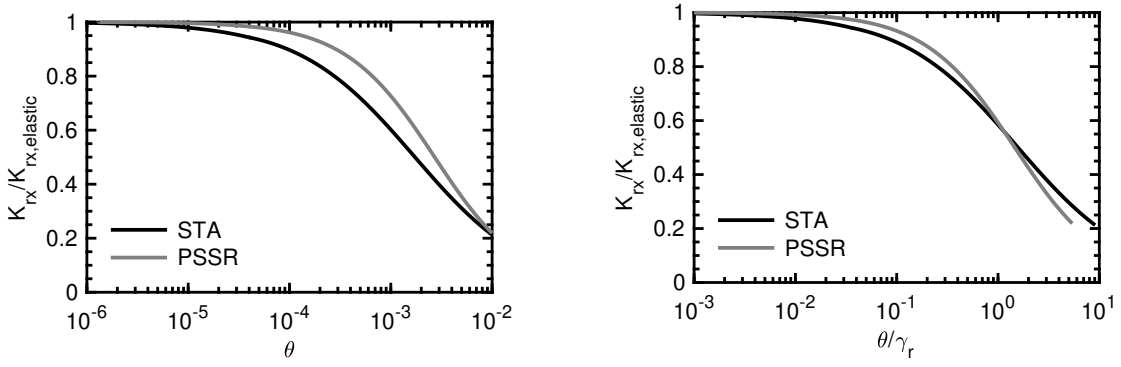

(a) (b)

Figure 5.58: Normalised static rocking stiffness for STA and PSSR conditions (eqs 5.8 and 5.9,respectively) versus (a) rocking angle and (b) normalised rocking angle.

The curves in Figure 5.58 can be fitted by a modified hyperbolic expression of normalised non-linear rocking stiffness as a function of rocking angle normalised by a "pseudo-reference" rocking angle, θ_r

$$\frac{K_{rx}}{K_{rx,elastic}} = \frac{1}{1+\left(\frac{\theta}{\theta_r}\right)^{\alpha}} \tag{5.10}$$

where θ_r is the "pseudo-reference" rocking angle equals to $1.5 \cdot \gamma_r$, and γ_r, α as specified in equations 5.8 and 5.9 for static and dynamic adjustment, respectively.

5.5.3 Rocking dynamic response

Results for dynamic conditions are reported in Figure 5.59, where the non-linear dynamic rocking stiffness is plotted in normalised form as (a) $\bar{K}_{rx}/K_{rx}$, elastic and (b) $\bar{K}_{rx}/K_{rx}$ versus the dimensionless excitation frequency $a_0 = 2fB/V_s$ for three different rocking amplitudes θ_{max} ($10^{-5}, 10^{-4}, 10^{-3}$ rad).

No rate effects have been considered on this plot (STA conditions). Despite the different levels of soil non-linearity involved in the analysis, the frequency variation in the three curves follows that of the elastic model in Figure 4.33. This is particularly evident on Figure 5.59 (b) and suggests that the non-linearity mainly affects the static stiffness K_{rx}, while the dynamic stiffness modifier k_{rx} can still be obtained from the elastodynamic Equation 2.18 for dimensionless frequencies a_0 as high as 0.8.

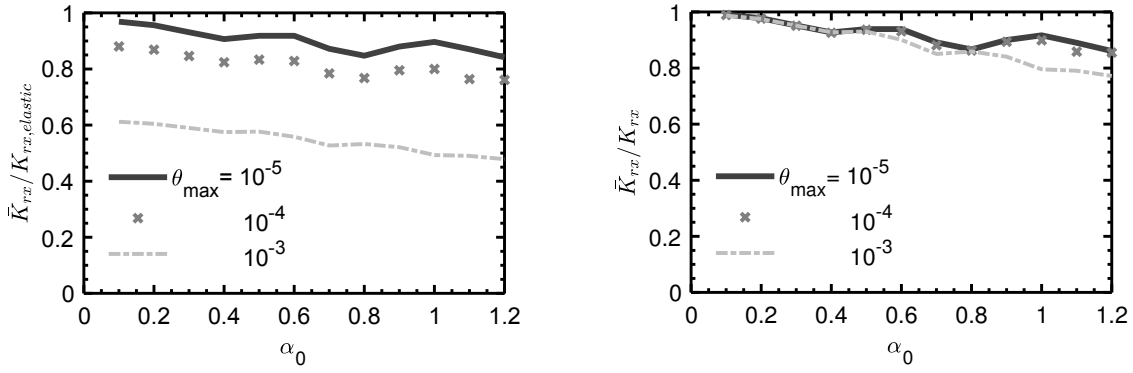

(a) (b)

Figure 5.59: Normalised non-linear dynamic rocking stiffness over (a) elastic and (b) non-linear static rocking stiffness versus dimensionless frequency for different rotation amplitudes. Modified hyperbolic model parameters correspond to STA conditions according to Equation 5.8.

Analogous patterns are observed in Figure 5.60 where the normalised non-linear dynamic rocking stiffness is plotted versus dimensionless frequency using the pseudo shear strain rate (PSSR) adjustment according to Equations 5.9. The behaviour is like in the previous case, with all curves exhibiting similar frequency variations, independent of strain level, and non-linearity affecting primarily the static stiffness term K_{rx}.

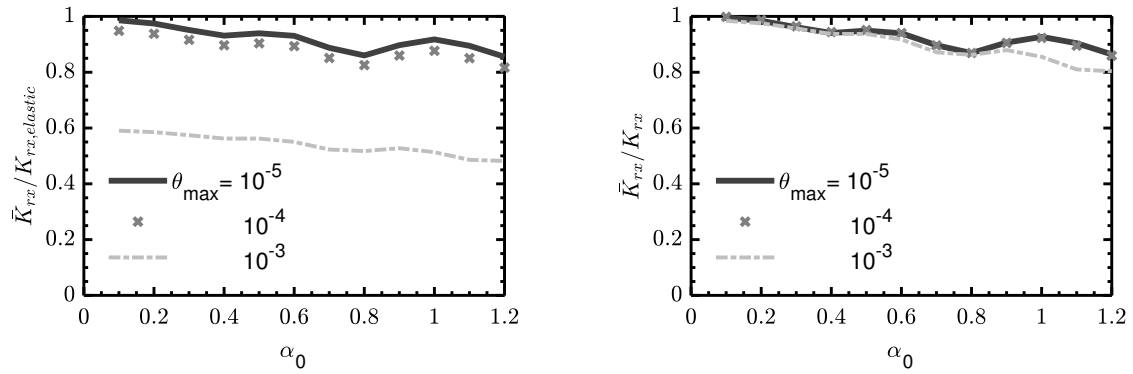

(a) (b)

Figure 5.60: Normalised non-linear dynamic rocking stiffness over (a) elastic and (b) non-linear static rocking stiffness versus dimensionless frequency for different rotation amplitudes. Modified hyperbolic model parameters correspond to PSSR conditions according to Equation 5.9

Results for shear strain rate (SSR) effects on non-linear dynamic footing stiffness $\bar{K}_{rx}$

are provided in Figure 5.61. Since the model is formulated in terms of absolute strain rate (measured in units of 1/Time, Figure 5.56), use of dimensionless frequency α_0 is not possible. For the small rocking amplitudes $\theta_{max} = 10^{-5}\ rad$ and $10^{-4}\ rad$, the curves exhibit patterns analogous to those observed for STA and PSSR conditions in Figures 5.59 and 5.60. For the largest rocking amplitude ($\theta_{max} = 10^{-3}$ rad), however, a different pattern is observed, with the non-linear rocking stiffness increasing with frequency. The causes of this behaviour could be sought to stress-induced in-homogeneities in the soil mass, as strain rate varies for point to point in proportion to strain. Further research is required to quantify this effect, which lies beyond the scope of this work.

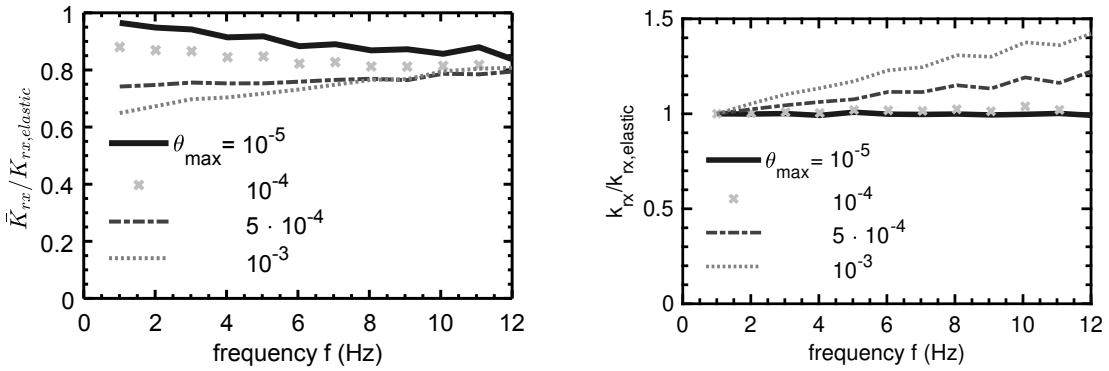

Figure 5.61: (a) Normalised non-linear dynamic rocking stiffness over elastic static rocking stiffness and (b) normalised non-linear over linear stiffness modifier versus absolute frequency versus absolute frequency for different rotation amplitudes. Modified hyperbolic model parameters correspond to SSR conditions according to Figure 5.56.

5.5.4 Key remarks on strain rate effects

The main conclusions on the effect of strain rates are summarised below:

- A practical numerical methodology for non-linear analysis of rigid surface footings under rocking oscillations, was presented. A modified hyperbolic model originally calibrated using an experimental database was implemented into the finite difference code FLAC, to account for stress-strain and shear strain rate behaviour of soil. The two required model parameters, and γ_r, can either be constant, pertaining to static or dynamic conditions, or vary as a function of shear strain rate.

- Parametric analyses on shear rate effects showed that for rocking amplitudes $\theta_{max} = 10^{-5}\ rad$ and $10^{-4}\ rad$ non-linear dynamic rocking stiffness fluctuates past $a_0 =$ 0.4 following a very similar trend to the linear case. For the rocking amplitude of $10^{-3}\ rad$ the values are dropping significantly, and curves are smoother. This suggests that non-linearity mainly affects the static stiffness K_{rx}, while the dynamic stiffness modifier k_{rx} can be obtained from the elastodynamic Equation 4.18 for dimensionless frequencies a_0 as high as 0.8. The drop in static stiffness can be explained by shear modulus degradation effects, as shown in Figure 2.11 (a).

- Regarding Shear Strain Rate (SSR) effects, an increase in rocking stiffness is observed with increasing frequency for the largest rocking amplitude ($\theta_{max} = 10^{-3}\ rad$). The causes of this behaviour may be related to stress-induced inhomogeneity in the soil mass, as shear strain rate varies for point to point in proportion to strain. On the other hand, for small rotation amplitudes stiffness is unaffected by shear strain rate which shows that, in this case, soil non-linearity would be of minor importance.

- SSR effects are becoming evident from very low frequencies for rocking amplitudes larger than $\theta_{max} = 10^{-4}\ rad$, and are increasingly more significant with increasing frequency. For rocking amplitudes equal or under $\theta_{max} = 10^{-4}\ rad$, non-linearity and SSR effects have a negligible impact on dynamic stiffness.

CHAPTER 6

EXTENSION TO THREE DIMENSIONS

In *Chapter 6* a brief verification of the finite difference 3D software, FLAC3D, is presented by extending the two-dimensional solutions discussed in *Chapters 4* and *5* to three dimensions. In addition, the elastic response of massless, rigid, square footings is examined and comparisons are made in terms of stiffness and damping with solutions from the literature. Furthermore, the non-linear response of square and rectangular foundations is investigated.

6.1 Verification of compatibility with 2D analysis

6.1.1 Linear analysis

The first step in developing a three-dimensional model is to verify the analysis against a two-dimensional counterpart. To this end, plane strain conditions are simulated in FLAC3D by restricting the out-of-plane degrees of freedom in a thin vertical slice of material. Two models are investigated in this regard: (a) one-element wide plane strain model, and (b) multiple-elements ($L/B = 4$) plane strain model. The plane strain models with grid-point fixities are shown in Figure 6.1.

6.1.1.1 Linear static analysis verification

The plane strain models shown in Figure 6.1 are examined in static rocking, vertical and horizontal mode of loading. The results are presented in Table 6.1, 6.2 and 6.3,

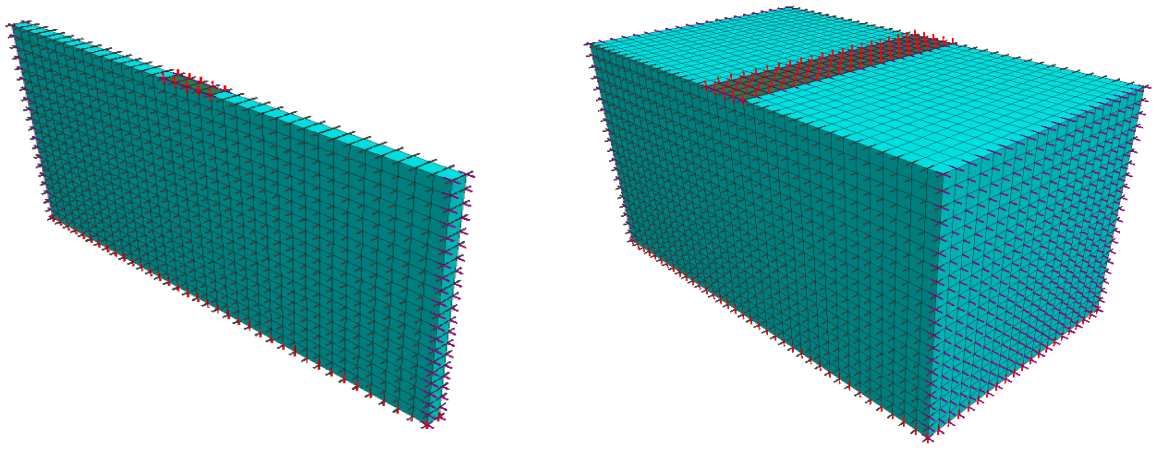

(a) (b)

Figure 6.1: FLAC3D plane strain models with grid-point fixities illustrated: (a) one-element wide model and (b) twenty-elements wide model.

respectively, alongside with the discrepancies over the two-dimensional solution in percentage. The results are compared with corresponding results from FLAC2D, the empirical formulas from literature ([2], [9]) and the fitted formulas Eq. 2.14 and 4.6 suggested in *Chapter 4*.

Generally speaking, the FLAC3D results are in good agreement with the corresponding results produced with FLAC2D. The greater discrepancy is observed for rocking loading condition and it is on the order of 2%. Furthermore, it is clear from the comparison between the FLAC3D (a) and FLAC3D (b) that the width of the grid does not affect the results in plane strain conditions.

The discrepancies between the numerical results provided by FLAC2D and the results by FLAC3D arise from the different shapes of the elements. In FLAC2D the solid is divided into a finite difference mesh composed of quadrilateral elements which are then subdivided internally into two overlaid sets of constant-strain triangular elements [13, 143]. In contrast, in FLAC3D the discretisation of the solid is done into hexahedral zones each of which is subdivided into two different configurations of five tetrahedra. This process is often called *mixed discretisation* over the combination of two overlays. Consequently, in FLAC2D calculations are based on four subzones, while in FLAC3D in ten subzones.

Table 6.1: Normalised linear static rocking stiffness calculated by means of FLAC3D and FLAC2D. FLAC3D (a) and (b) refer to Figure 6.1.

Method	Stiffness $K_{rx}/G \cdot B^2$	Discr. over Eq. 2.16	Discr. over FLAC2D
FLAC 3D (a)	2.43	2.06%	2.47%
FLAC 3D (b)	2.43	2.06%	2.47%
FLAC 2D	2.49	-0.40%	0%
Semi-empirical [2]: Eq 2.16	2.48	0%	0.40%

Table 6.2: Normalised linear static vertical stiffness calculated by FLAC3D and FLAC2D. FLAC3D (a) and (b) refer to Figure 6.1.

Method	Stiffness K_v/G	Discr. over the Eq. 2.14	Discr. over the Eq. 4.5	Discr. over FLAC2D
FLAC 3D (a)	1.98	-24.24%	-1.01%	-1.52%
FLAC 3D (b)	1.98	-24.24%	-1.01%	-1.52%
FLAC 2D	1.95	-23.08%	0.51%	0%
Fitted (this study): Eq. 4.5	1.96	-23.47%	0%	-0.51%
Fitted [2]: Eq. 2.14	1.50	0%	30.67%	30.0%

Table 6.3: Normalised linear static lateral stiffness calculated by FLAC3D and FLAC2D. FLAC3D (a) and (b) refer to Figure 6.1.

Method	Stiffness K_h/G	Discr. over the Eq 2.15	Discr. over the Eq 4.6	Discr. over FLAC2D
FLAC 3D (a)	1.42	3.52%	-1.41%	-0.70%
FLAC 3D (b)	1.42	3.52%	-1.41%	-0.70%
FLAC 2D	1.41	4.26%	-0.71%	0%
Fitted (this study): Eq. 4.6	1.40	5.0%	0%	0.71%
Fitted [2]: Eq. 2.15	1.47	0%	-4.76%	-4.08%

6.1.1.2 Linear dynamic analysis verification

For dynamic rocking loading conditions, normalised linear dynamic rocking stiffness, $\bar{K}_{rx}$, over elastic static rocking stiffness, $K_{rx,elastic}$, as shown in Table 6.1, versus dimensionless frequency, a_0, is presented in Figure 6.2. The numerical results refer to a soil layer of depth, $H = 2B$. A very good agreement between the halfspace ($H/B \rightarrow \infty$) solution by Luco and Westmann [9] is observed for dimensionless frequencies a_0 of less than approximately 0.4. The discrepancies observed at higher frequencies might be attributed to differences in the boundary conditions. The FLAC3D results are in good agreement with the corresponding results calculated by means of FLAC2D. The minor differences

observed are attributed to discretisation.

FLAC3D produces identical results for the normalised stiffness regardless of the width of the grid, as expected for plane strain conditions. To this end and for the sake of computational efficiency, only the grid pictured in Figure 6.1 (a) is used to verify the 3D code against the two-dimensional for the other two loading cases, namely vertical and horizontal.

Both the vertical and the swaying dynamic stiffness are in excellent agreement with the values provided using the two-dimensional finite difference code, as shown, respectively, in Figures 6.3 (a) and (b).

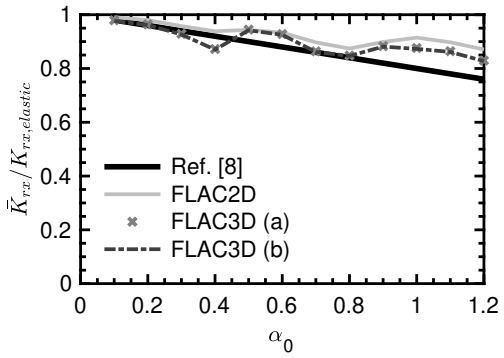

Figure 6.2: Normalised linear dynamic rocking stiffness over elastic static rocking stiffness versus dimensionless frequency; numerical results: $H/B = 8$, Luco & Westmann [9] solution: $H/B \to \infty$ (halfspace).

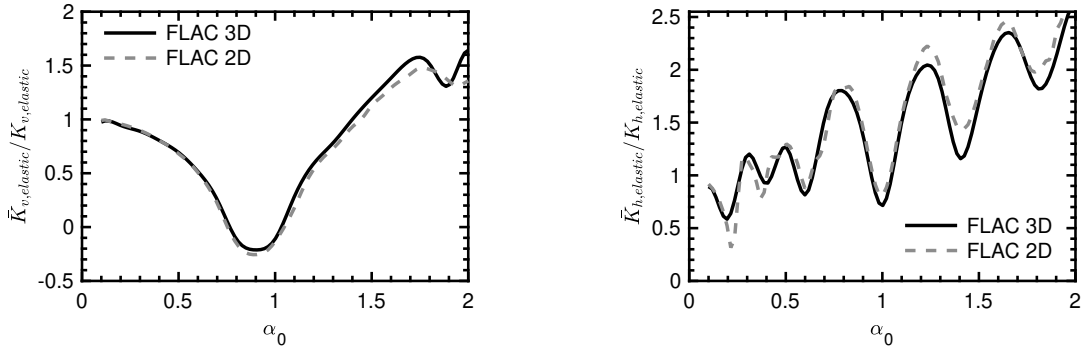

(a) (b)

Figure 6.3: Normalised linear dynamic stiffness over elastic static stiffness versus dimensionless frequency for a footing subjected to (a) vertical and (b) horizontal oscillations ; (a) $H/B = 4$, (a) $H/B = 8$, $\nu = 0.30$, $\Delta x = 0.4B$.

6.1.2 Non-linear analysis

In the previous section, the linear verification of a two dimensional analysis executed with FLAC3D was presented. Similarly, in this section, the soil behaviour described by either the modified hyperbolic or the Ramberg-Osgood constitutive model is verified against the outcomes of FLAC2D.

6.1.2.1 Non-linear static analysis verification

The results concerning the static non-linear analysis are graphically illustrated in terms of normalised non-linear stiffness versus the normalised footing response when the footing is statically loaded. There is an excellent agreement between the results obtained with FLAC3D and FLAC2D in all response modes, namely vertical, lateral, and rocking as seen in Figures 6.4, 6.5 and 6.6, respectively. The outcomes are in agreement for both constitutive models, Ramberg-Osgood and modified hyperbolic with the corresponding results shown in (a) and (b) graphs below, respectively. In this light, the non-linear models are verified in FLAC3D.

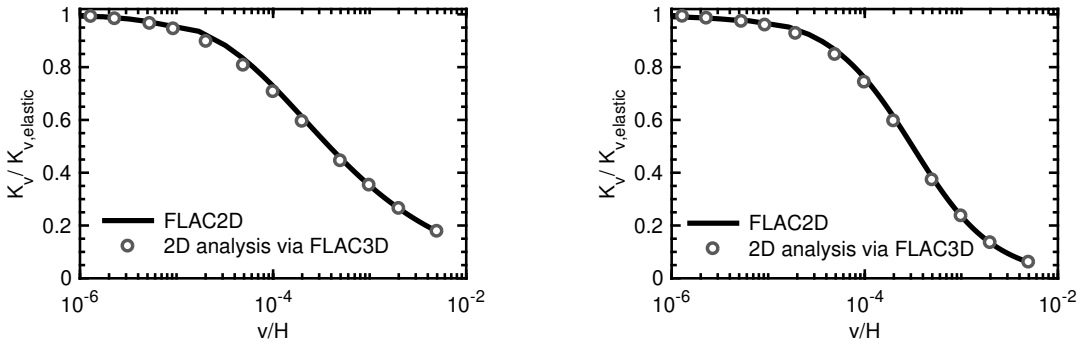

Figure 6.4: Normalised non-linear static vertical stiffness versus normalised settlement assuming non-linear soil behaviour is described by a (a) Ramberg-Osgood and (b) Modified hyperbolic model; $H/B = 8$, $\nu = 0.3$, $\Delta x = 0.4B$.

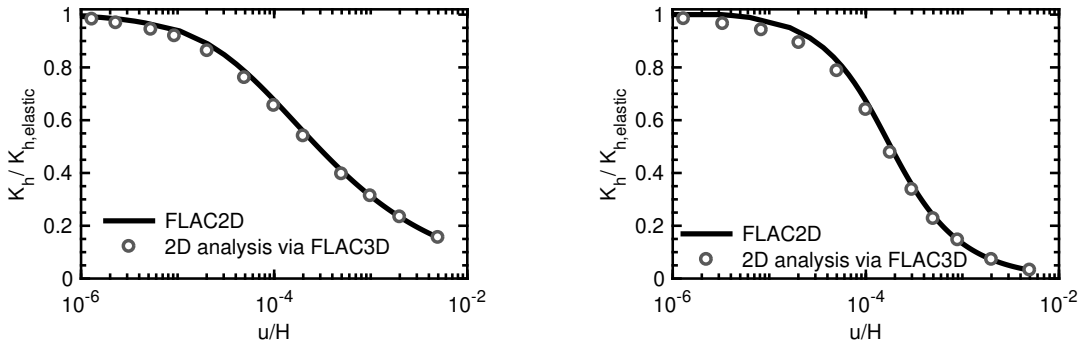

Figure 6.5: Normalised non-linear static lateral stiffness versus normalised horizontal displacement assuming non-linear soil behaviour is described by a (a) Ramberg-Osgood and (b) Modified hyperbolic model; $H/B = 8$, $\nu = 0.3$, $\Delta x = 0.4B$.

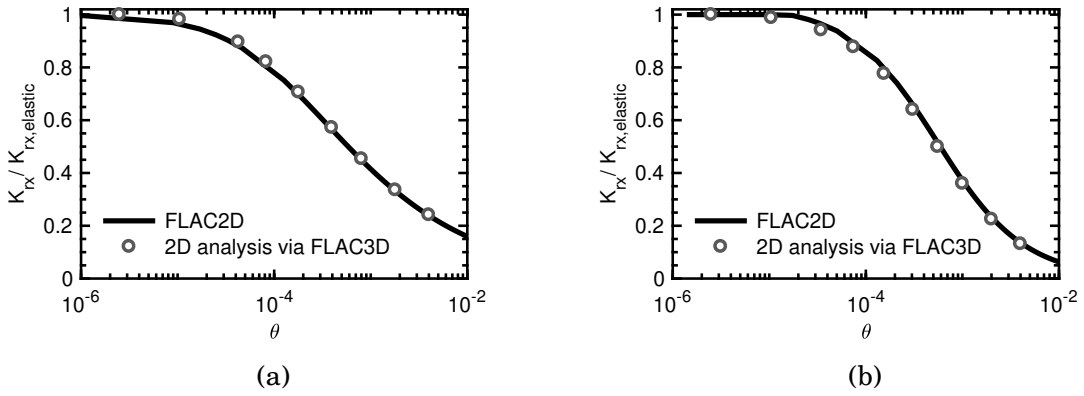

Figure 6.6: Normalised non-linear static rocking stiffness versus rotation angle assuming non-linear soil behaviour is described by a (a) Ramberg-Osgood and (b) Modified hyperbolic model; $H/B = 8$, $\nu = 0.3$, $\Delta x = 0.4B$.

6.2 Elastic response of square foundations

The elastic response of square footings resting on a homogeneous soil layer is investigated next and compared with solutions from the literature. Two studies are taken into consideration for the comparison, namely Pais and Kausel [1] and Gazetas [2] (revisited by Mylonakis et al [3]). The suggested formulas for the static and dynamic stiffness are shown in *Chapter 2* in Tables 2.8 and 2.9 , respectively.

6.2.1 Static elastic response

The three-dimensional problem of a square footing resting on a soil layer is compared, in terms of static stiffness, with published studies. The model used for the numerical analyses is shown in Figure 6.7, half the square footing is used due to the axial symmetry in the geometry and applied loading. For the case of vertical loading, a quarter of the problem would lead to same results but for the sake of homogeneity across all modes of loading the half model is taken. The results shown in Table 6.4 concern the vertical static stiffness. The agreement is excellent with FLAC3D slightly overestimating the vertical static stiffness. FLAC3D analysis results are closer to Pais and Kausel [1] findings. The discrepancies are a result of the difference in boundary conditions (soil layer versus halfspace).

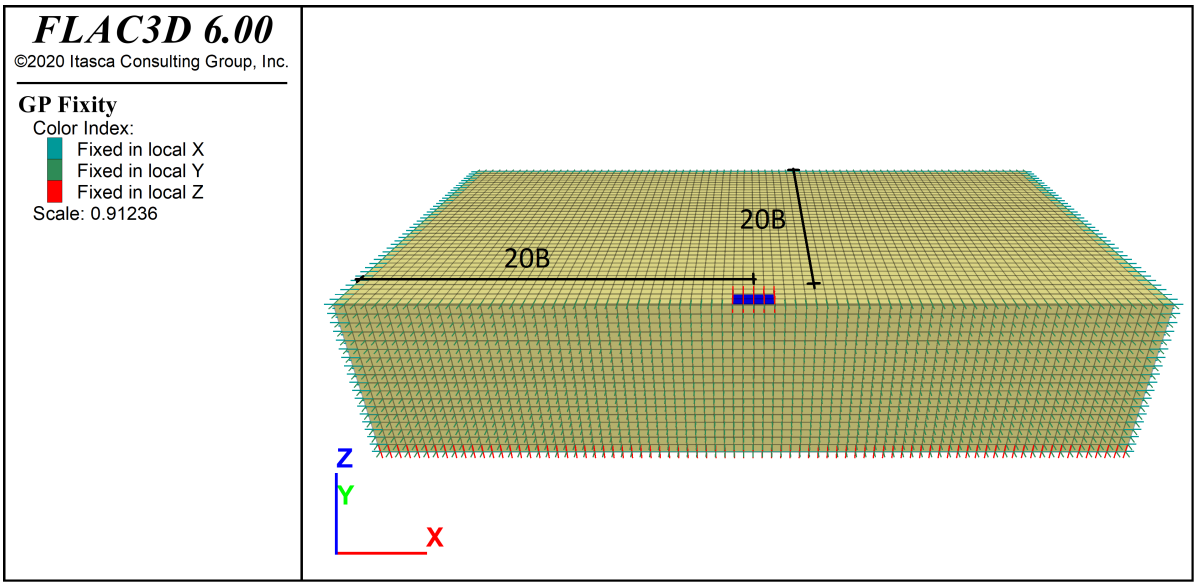

Figure 6.7: FLAC3D square footing model geometry with grid-point fixities illustrated. Fixities on the footing correspond to horizontal static loading conditions; $\Delta x = 0.5B$, $s = 20B$, $H = 8B$.

The same analysis is performed considering the lateral static stiffness instead of the vertical static stiffness. Similarly to the previous case, the results are in agreement (Table 6.5). The value obtained by FLAC3D analysis is insignificantly higher than the suggested values. The agreement is excellent.

Switching our focus to rocking static stiffness, the outcomes are tabulated in Table 6.6. A slightly higher discrepancy is noticed with respect to the previous cases but the comparisons are excellent.

The results concerning all the stiffness of square foundations cases treated above demonstrate that between our analysis performed with FLAC3D and the published results of [2] and [9] are in excellent agreement; hence the software is a valid alternative for standard techniques currently used in static analysis.

Table 6.4: Normalised linear static vertical stiffness of square foundations.

Method	Stiffness K_v/G	Discr. over Pais & Kausel [1]	Discr. over Gazetas [2]
FLAC3D	18.67	-3.3%	-6.9%
Pais & Kausel [1]: Table 2.9	18.08	0%	-3.5%
Gazetas [2]: Table 2.9	17.46	3.4%	0%

Table 6.5: Normalised linear static horizontal stiffness of square foundations.

Method	Stiffness K_v/G	Discr. over Pais & Kausel [1]	Discr. over Gazetas [2]
FLAC3D	14.24	-2.18%	-4.46%
Pais & Kausel [1]: Table 2.9	13.94	0%	-2.22%
Gazetas [2]: Table 2.9	13.64	2.17%	0%

Table 6.6: Normalised linear static rocking stiffness of square foundations

Method	Stiffness K_{rx}/GB^3	Discr. over Pais & Kausel [1]	Discr. over [2]
FLAC3D	5.93	3.67%	-7.04%
Pais & Kausel [1]: Table 2.9	6.15	0%	-11.11%
Gazetas [2]: Table 2.9	5.54	10%	0%

6.2.2 Dynamic elastic response

The dynamic elastic response of square footings is investigated and the results are shown below. The outcomes are compared with the halfspace solution for the case of rotational excitation. In contrast, the impedance in translational mode is compared with the respective results of the two-dimensional problem of strip footing.

The results of footings subjected to rocking are shown in Figure 6.8. The halfspace solution is suggested by Pais and Kausel [1]. The outcomes are comparable because of Saint-Venant's principle. Some discrepancies appear after $\alpha_0 = 0.7$ for both stiffness and

damping. The stiffness of a footing resting on a soil layer is greater for high dimensionless frequencies. Naturally, the radiation damping is lower in the case of soil layer over rock.

Switching our attention to horizontal stiffness, fewer reflections are observed for the three-dimensional problem. Radiation damping is higher in the two-dimensional problem and reflections are more obvious through the peaks and the valleys. Stiffness follows a similar ascending trend regardless of the studied problem.

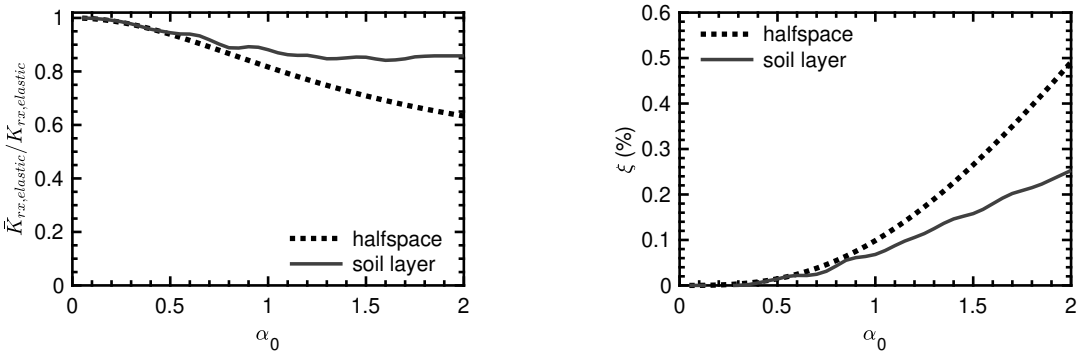

(a) (b)

Figure 6.8: (a) Normalised linear dynamic rocking stiffness and (b) damping coefficient versus dimensionless frequency; numerical: $H/B = 8$, $\nu = 0.3$, $\Delta x = 0.4B$.

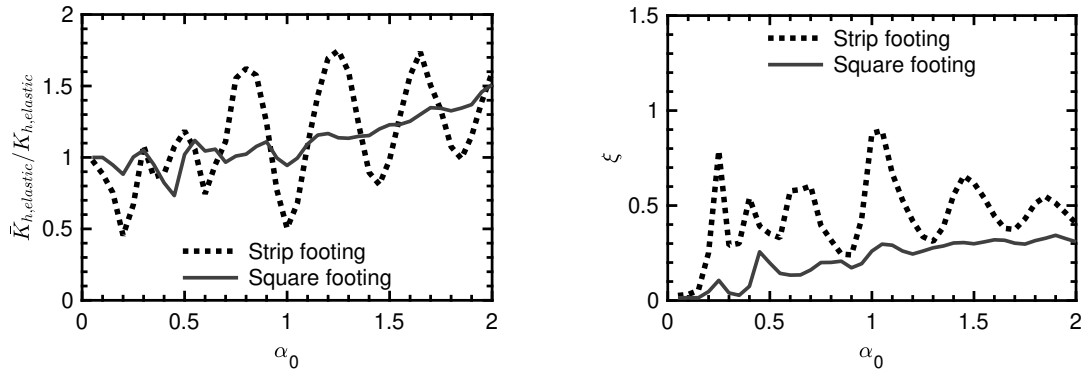

(a) (b)

Figure 6.9: (a) Normalised linear dynamic horizontal stiffness over elastic static horizontal stiffness and (b) damping versus dimensionless frequency for strip and square footings; $H/B = 8$, $\nu = 0.3$, $\Delta x = 0.4B$.

6.3 Nonlinear response

The non-linear dynamic response of square (aspect ratio, $L/B = 1$ - Figure 6.7) and rectangular ($L/B = 2$ and 4 - Figure 6.10) footings resting on a soil layer over bedrock and subjected to vertical, horizontal and rocking oscillations, is investigated here. For the sake of brevity, horizontal oscillations along transverse direction (X axis) and rocking around the longitudinal direction (Y axis) are considered.

Soil non-linearity was explored by means of a Ramberg-Osgood model calibrated against Vucetic and Dobry [8], as presented in section 5.2 for $PI = 0$, $w = 2$ and $\alpha_\gamma = 0.64$.

The analyses are conducted up to a dimensionless frequency $a_0 = 1.5$ at frequency intervals of 0.1. The outcomes are illustrated in terms of normalised stiffness over dimensionless frequency and damping ratio over dimensionless frequency. In the vertical axis, the dynamic non-linear stiffness, $\bar{K}_{v,h,rx}$, for each oscillation mode is normalised with the corresponding non-linear stiffness for $a_0 = 0.1$, which is meant to represent pseudo-static conditions. Element size in all three dimensions is taken as $0.5B$. Corresponding results presented in *Chapter 5, section 5.2* for two dimensions are also plotted to facilitate comparisons between the two and the three-dimensional counterparts of the non-linear problem.

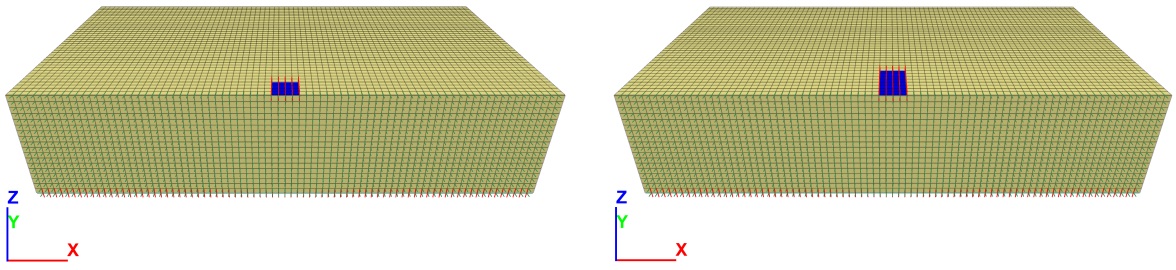

(a) (b)

Figure 6.10: FLAC3D rectangular footings model geometry with aspect ratio (a) two and (b) four with grid-point fixities illustrated. Fixities on the footing correspond to horizontal static loading conditions; $\Delta x = 0.5B$, $s = 20B$, $H = 8B$.

6.3.1 Vertical dynamic response

The effect of soil thickness on vertical non-linear dynamic stiffness and damping ratio of a square footing ($L/B = 1$) is presented graphically in 6.11. For $H/B = 2$ vertical stiffness

remains almost constant up to $\alpha_0 = 0.8$. Beyond this point stiffness is decreasing with increasing excitation frequency dropping almost to 0 for $\alpha_0 = 1.5$. Similar trends are observed for deeper soil deposits ($H/B = 4$ and 8) with resonance observed at smaller excitation frequencies. The drop in stiffness at resonance decreases with increasing layer thickness reaching only 20% for $H/B = 8$. Away from resonance, stiffness is practically frequency independent (Figure 6.11 (a)).

Opposite trends are observed for damping ratio with local maxima developing at resonance (Figure 6.11 (b)). Similar trends are observed for rectangular footings of aspect ratio 2 and 4 as shown in Figures 6.12 and 6.13, respectively.

The effect of footing aspect ratio on the vertical non-linear impedance is demonstrated in Figures 6.14, 6.15 and 6.16 for layer thickness, H/B, 2, 4 and 8, respectively.

For the shallowest soil layer ($H/B = 2$), footing aspect ratio has little effect on stiffness and damping (Figure 6.14). On the other hand, for deeper soil layers longer footings demonstrate higher drops in dynamic vertical stiffness close to resonance (Figures 6.15 and 6.16).

The differences between the two and three dimensional set-ups of the problem can be observed for high excitation frequencies in terms of normalised vertical stiffness. More wave reflections are obvious through the peaks and the valleys on the stiffness graphs. On the other hand, damping curves are indistinguishable, only exception being the shallow soil layer. For $H/B = 2$, radiation damping in the case of the two dimensional problem of a strip footing is noticeably higher.

Switching our attention to the effect of vertical displacement amplitude, v_0, the rectangular footing $L/B = 2$ resting on soil layer with $H/B = 8$ is investigated. The results are illustrated in Figure 6.17. For low frequencies (up to resonance), normalised stiffness is little affected by excitation amplitude. Beyond resonance, a drop in stiffness is observed with increasing amplitude. Resonant frequency is the same for all cases as its value is controlled by the properties of the soil layer away from the footing.

As far as damping ratio is concerned, higher amplitudes result in higher energy dissipation with damping ratio being almost 4 times higher when v_0/H is 10^{-4} compared to v_0/H equal to 10^{-5}.

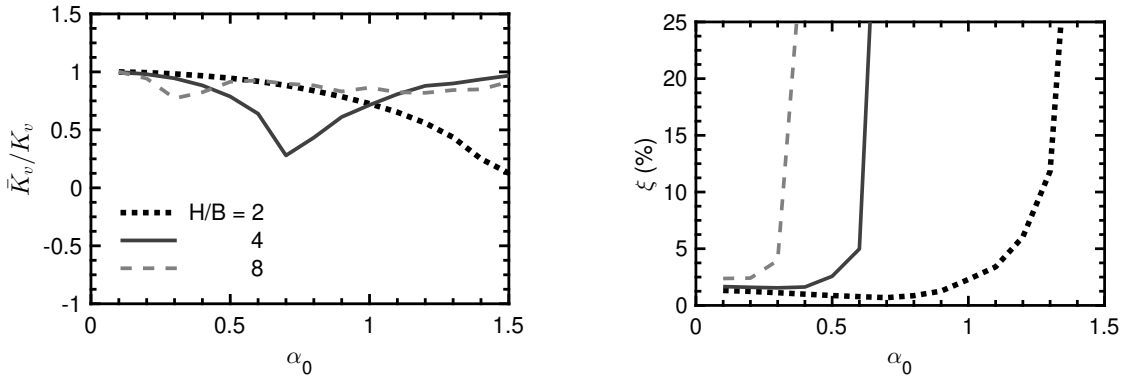

(a) (b)

Figure 6.11: Illustration of the effect of footing half-with B on the (a) normalised nonlinear vertical dynamic stiffness and (b) the damping ratio versus the dimensionless frequency a_0; $PI = 0$, $L/B = 1$, $v_0/H = 10^{-5}$, $V_s = 200m/s$, $\nu = 0.3$, Rayleigh damping $\xi = 5\%$.

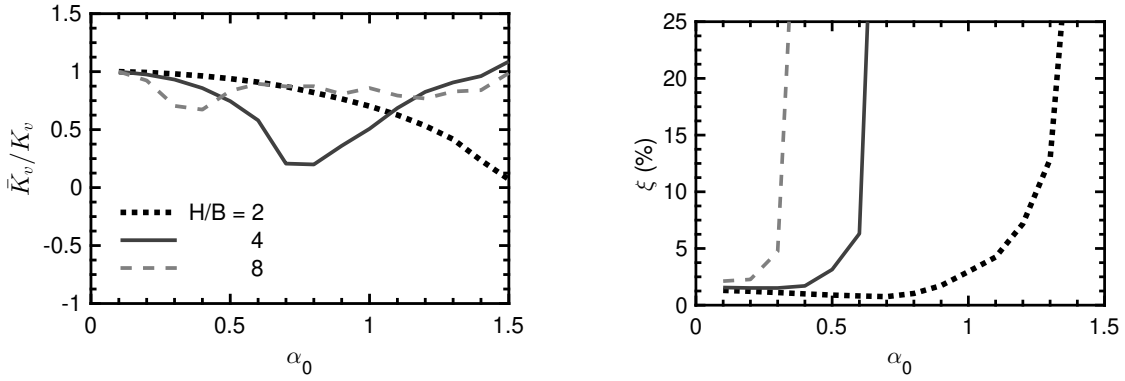

(a) (b)

Figure 6.12: Illustration of the effect of footing half-with B on the (a) normalised nonlinear vertical dynamic stiffness and (b) the damping ratio versus the dimensionless frequency a_0; $PI = 0$, $L/B = 2$, $v_0/H = 10^{-5}$, $V_s = 200m/s$, $\nu = 0.3$, Rayleigh damping $\xi = 5\%$.

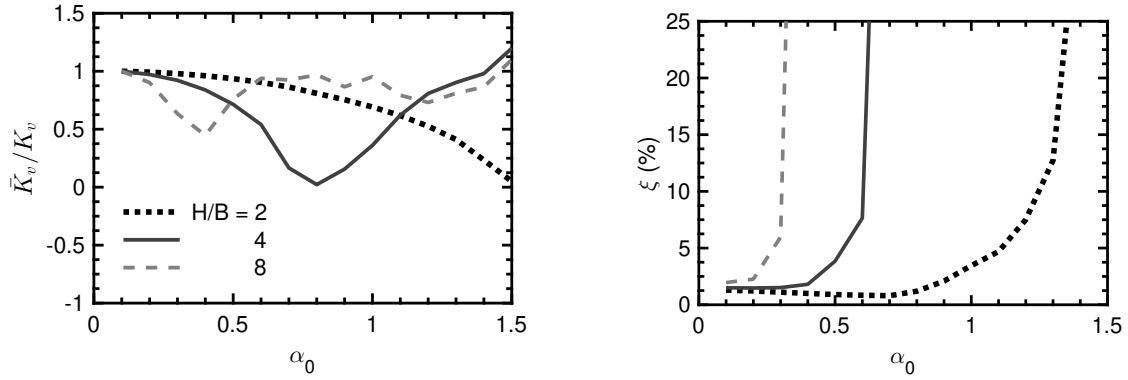

(a) (b)

Figure 6.13: Illustration of the effect of footing half-with B on the (a) normalised non-linear vertical dynamic stiffness and (b) the damping ratio versus the dimensionless frequency α_0; $PI = 0$, $L/B = 4$, $v_0/H = 10^{-5}$, $V_s = 200m/s$, $\nu = 0.3$, Rayleigh damping $\xi = 5\%$.

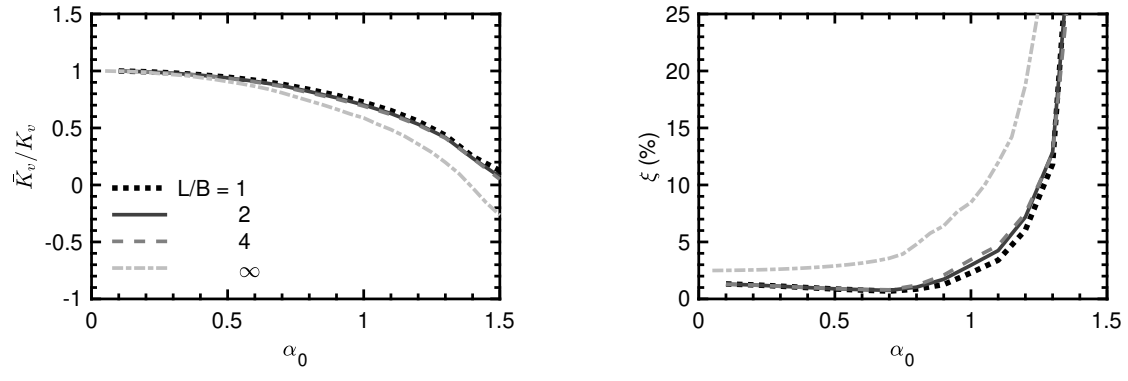

(a) (b)

Figure 6.14: Illustration of the effect of footing half-length L on the (a) normalised non-linear vertical dynamic stiffness and (b) the damping ratio versus the dimensionless frequency α_0; $PI = 0$, $H/B = 2$, $v_0/H = 10^{-5}$, $V_s = 200m/s$, $\nu = 0.3$, Rayleigh damping $\xi = 5\%$.

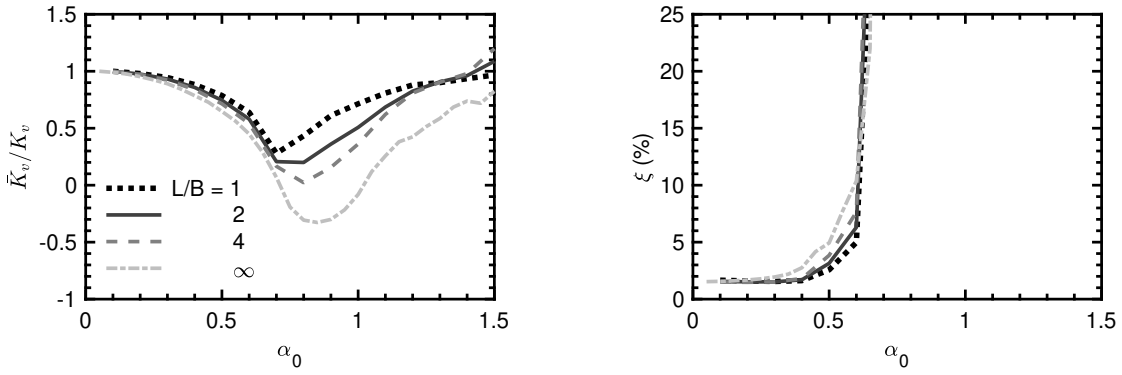

(a) (b)

Figure 6.15: Illustration of the effect of footing half-length L on the (a) normalised non-linear vertical dynamic stiffness and (b) the damping ratio versus the dimensionless frequency a_0; $PI = 0$, $H/B = 4$, $v_0/H = 10^{-5}$, $V_s = 200m/s$, $\nu = 0.3$, Rayleigh damping $\xi = 5\%$.

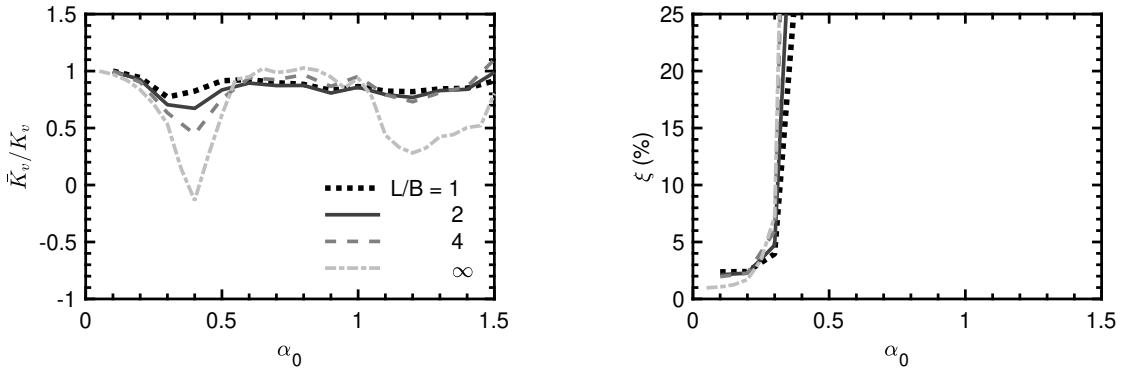

(a) (b)

Figure 6.16: Illustration of the effect of footing half-length L on the (a) normalised non-linear vertical dynamic stiffness and (b) the damping ratio versus the dimensionless frequency a_0; $PI = 0$, $H/B = 8$, $v_0/H = 10^{-5}$, $V_s = 200m/s$, $\nu = 0.3$, Rayleigh damping $\xi = 5\%$.

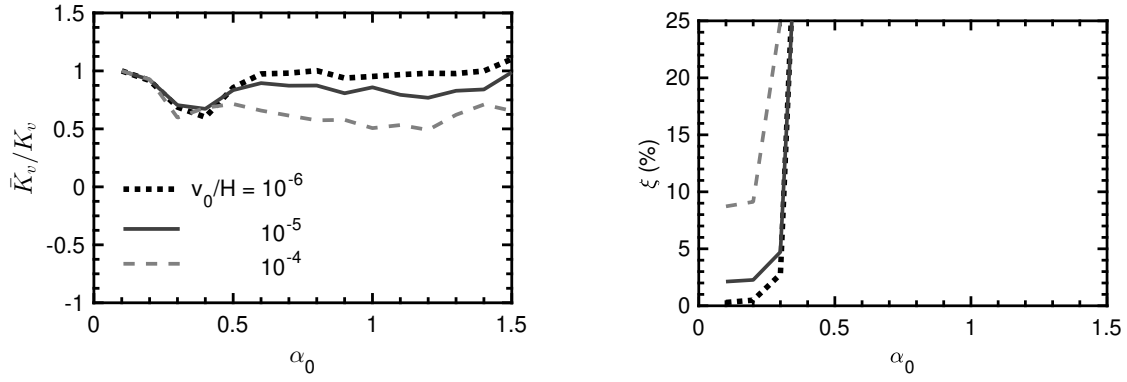

(a) (b)

Figure 6.17: Illustration of the effect of displacement amplitude v_0 on the (a) normalised non-linear vertical dynamic stiffness and (b) the damping ratio versus the dimensionless frequency α_0; $PI = 0$, $L/B = 2$, $H/B = 8$, $V_s = 200m/s$, $\nu = 0.3$, Rayleigh damping $\xi = 5\%$.

6.3.2 Horizontal dynamic response

Considering horizontal (swaying) oscillations of a square footing resting on non-linear soil the results are presented in Figures 6.18 for three soil layer thicknesses and $u_0/H = 10^{-5}$. For $H/B = 2$ horizontal stiffness decreases with frequency up to $\alpha_0 = 0.8$. Between $\alpha_0 = 0.8$ to 1.3 stiffness increases with increasing excitation frequency. At $alpha_0 = 1.3$ stiffness drops again, reaching 20% of its static value at $\alpha_0 = 1.5$. In contrast, for deeper soil layers, normalised stiffness is only slightly affected and it fluctuates around 1 (Figure 6.18 (a)).

Analogous trends are observed for rectangular footings of aspect ratios $L/B = 2$ and 4 as shown in Figures 6.19 and 6.20, respectively, for lateral loading acting in the transverse - X direction (Figure 6.10). In this case, however, the drop in normalised stiffness at high frequencies for shallow soil layers $H/B = 2$ is not replicated for rectangular footings.

The effect of footing aspect ratio, L/B, on the horizontal non-linear impedance function is presented in Figures 6.21, 6.22 and 6.23 for layer thickness, $H/B = 2$, 4 and 8, respectively. For shallow soil layers ($H/B = 2$ and 4), longer footings demonstrate a slightly higher drop in dynamic horizontal stiffness close resonance (Figures 6.21 and 6.22). For deep deposits, footing aspect ratio has no effect on stiffness but the damping ratio increase is smoother for square footings (Figure 6.23).

Looking at the same graphs, one can notice fewer wave reflections on the normalised lateral stiffness for the three-dimensional problem, regardless of footing aspect ratio.

Naturally, higher radiation damping was observed in the two-dimensional model.

Switching our attention to the effect of horizontal displacement amplitude, u_0, the case of a rectangular footing with aspect ratio $L/B = 2$ resting on soil layer with $H/B = 8$ is investigated. The results are illustrated in Figure 6.24. For low frequencies and up to resonance ($a_0 = 0.2$), the normalised stiffness is not affected by excitation amplitude. Beyond that point, a drop in stiffness is observed with increasing amplitude. Similarly with the vertical loading case, resonant frequency is the same for all cases as it is dominated by the soil layer behaviour on the far field.

As far as the damping ratio is concerned, higher amplitudes result in higher energy dissipation. As with the vertical mode, damping is almost 4 times higher when u_0/H is 10^{-4} compared to $u_0/H = 10^{-5}$.

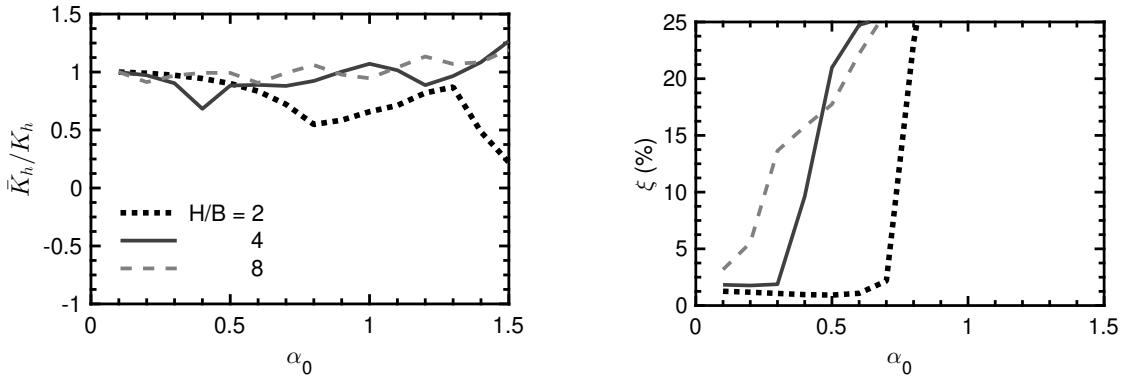

(a) (b)

Figure 6.18: Illustration of the effect of footing half-with B on the (a) normalised non-linear horizontal dynamic stiffness and (b) the damping ratio versus the dimensionless frequency a_0; $PI = 0$, $L/B = 1$, $u_0/H = 10^{-5}$, $V_s = 200m/s$, $\nu = 0.3$, Rayleigh damping $\xi = 5\%$.

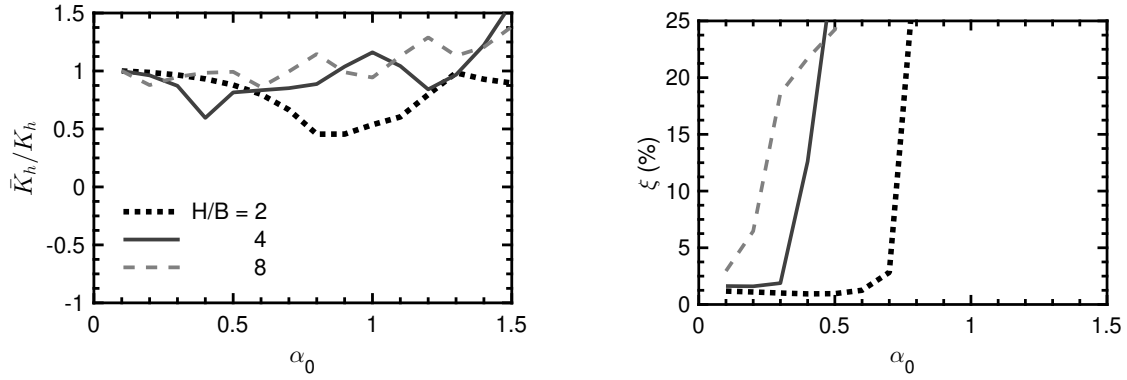

(a) (b)

Figure 6.19: Illustration of the effect of footing half-with B on the (a) normalised nonlinear horizontal dynamic stiffness and (b) the damping ratio versus the dimensionless frequency α_0; $PI = 0$, $L/B = 2$, $u_0/H = 10^{-5}$, $V_s = 200m/s$, $\nu = 0.3$, Rayleigh damping $\xi = 5\%$.

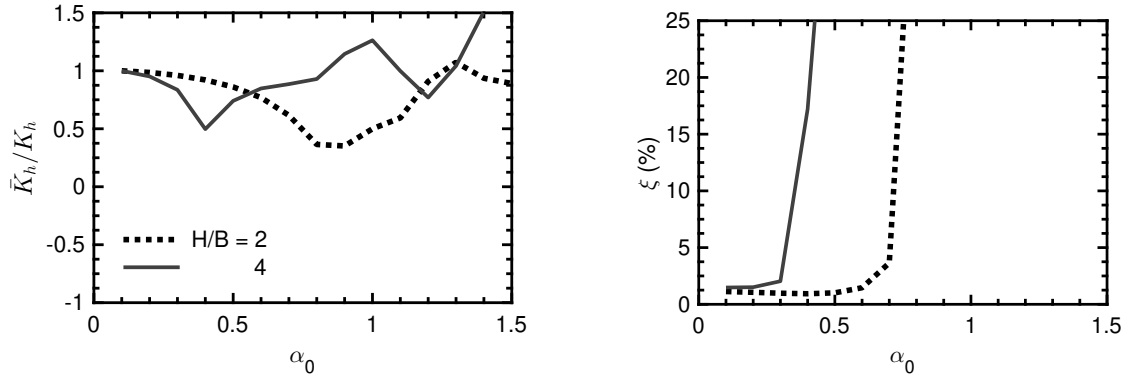

(a) (b)

Figure 6.20: Illustration of the effect of footing half-with B on the (a) normalised nonlinear horizontal dynamic stiffness and (b) the damping ratio versus the dimensionless frequency α_0; $PI = 0$, $L/B = 4$, $u_0/H = 10^{-5}$, $V_s = 200m/s$, $\nu = 0.3$, Rayleigh damping $\xi = 5\%$.

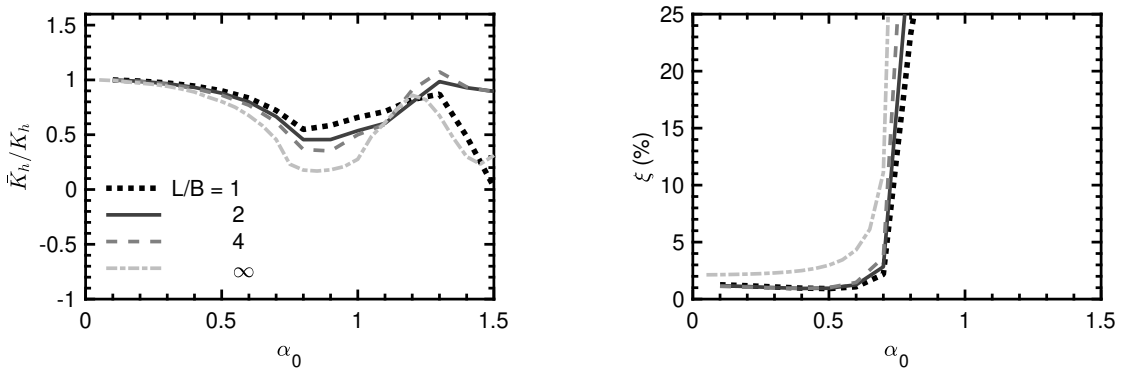

(a) (b)

Figure 6.21: Illustration of the effect of footing half-length L on the (a) normalised nonlinear horizontal dynamic stiffness and (b) the damping ratio versus the dimensionless frequency a_0; $PI = 0$, $H/B = 2$, $u_0/H = 10^{-5}$, $V_s = 200m/s$, $\nu = 0.3$, Rayleigh damping $\xi = 5\%$.

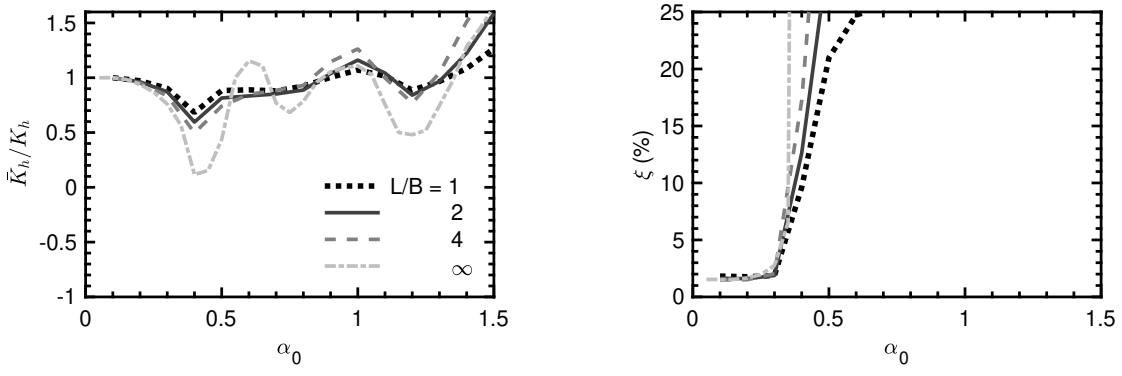

(a) (b)

Figure 6.22: Illustration of the effect of footing half-length L on the (a) normalised nonlinear horizontal dynamic stiffness and (b) the damping ratio versus the dimensionless frequency a_0; $PI = 0$, $H/B = 4$, $u_0/H = 10^{-5}$, $V_s = 200m/s$, $\nu = 0.3$, Rayleigh damping $\xi = 5\%$.

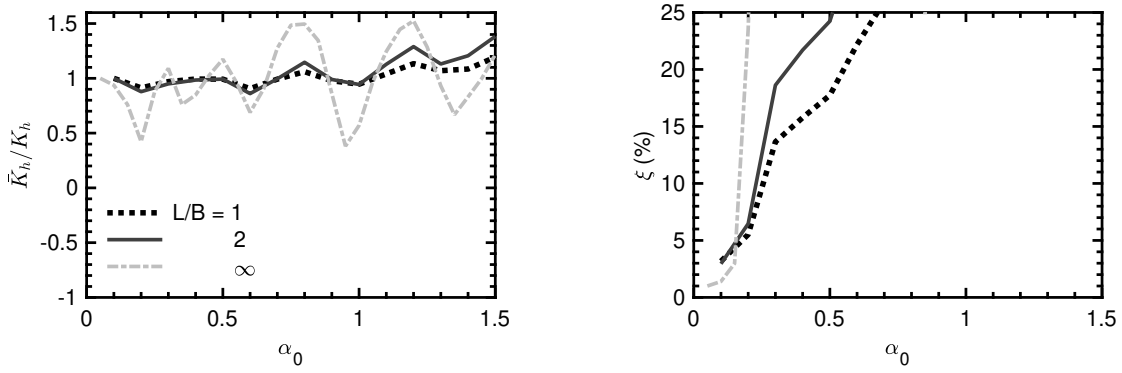

(a) (b)

Figure 6.23: Illustration of the effect of footing half-length L on the (a) normalised non-linear horizontal dynamic stiffness and (b) the damping ratio versus the dimensionless frequency a_0; $PI = 0$, $H/B = 8$, $u_0/H = 10^{-5}$, $V_s = 200m/s$, $\nu = 0.3$, Rayleigh damping $\xi = 5\%$.

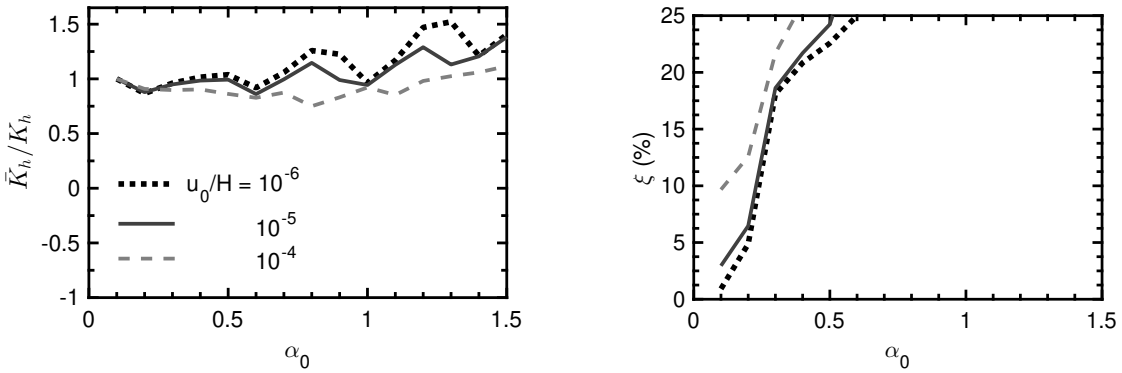

(a) (b)

Figure 6.24: Illustration of the effect of displacement amplitude v_0 on the (a) normalised non-linear horizontal dynamic stiffness and (b) the damping ratio versus the dimensionless frequency a_0; $PI = 0$, $L/B = 2$, $H/B = 8$, $V_s = 200m/s$, $\nu = 0.3$, Rayleigh damping $\xi = 5\%$.

6.3.3 Rocking dynamic response

Switching our attention to rocking vibrations around longitudinal axis (Y axis), the effect of soil layer thickness on non-linear dynamic stiffness and damping ratio of square footings ($L/B = 1$) is presented graphically in Figure 6.25. As shown previously in *Chapters 4 and 5*, due to Saint-Venant's principle the depth of the soil deposit (and thus excitation frequency) have a negligible effect on rocking stiffness. Minor discrepancies are observed for high frequencies corresponding to a_0 greater than 1.2.

In contrast, material damping increases with increasing layer depth from almost 5% for $H/B = 2$, to 9% when $H/B = 8$. Damping strongly increases with excitation frequency following a parabolic trend (Figure 6.25 (b)).

Identical trends are observed for rectangular footings of aspect ratio $L/B = 2$ and 4 as shown in Figures 6.26 and 6.27, respectively.

The effect of footing aspect ratio on non-linear rocking impedance is demonstrated in Figures 6.28, 6.29 and 6.30 for layer thickness, $H/B = 2$, 4 and 8, respectively. For the shallowest soil layer, footing aspect ratio has no effect on either stiffness or damping (Figure 6.28). On the other hand, for deeper soil layers larger aspect ratio footings exhibit a steep increase in damping with frequency (Figures 6.29 and 6.30).

Moving to the effect of rotation angle, θ, the rectangular footing $L/B = 2$ resting on a soil layer with $H/B = 8$ is examined. The results are illustrated in Figure 6.31. Naturally, rotation angle amplitude on the order of 10^{-6} rad results in higher normalised stiffness which does not drop lower than 0.9. For low frequencies (a_0 up to 0.5), the normalised stiffness is not affected by the excitation amplitude. Beyond that point, a drop in stiffness is observed with increasing rotation amplitude.

As far as the damping ratio is concerned, higher rotational angle amplitudes result in higher damping with damping ratio being almost double for $\theta = 10^{-4}$ rad compared to $\theta = 10^{-5}$ rad. The higher damping values reflect on lower stiffness. Even though the effect is normalised in Figure 6.31 (a), it is important to note that dynamic rocking stiffness for $a_0 = 0.1$ and $\theta = 10^{-5}$ is 70% of the respective value for $\theta = 10^{-6}$ while for $\theta = 10^{-4}$ is only 30% of its counterpart for $\theta = 10^{-6}$.

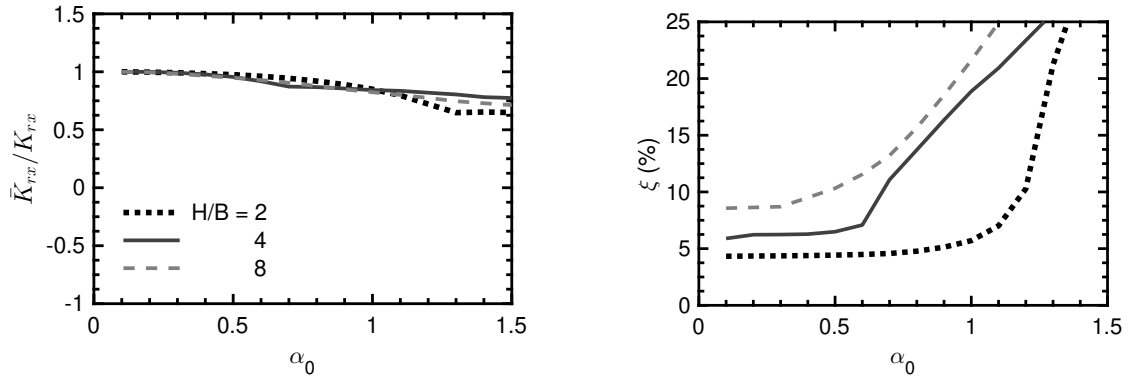

(a) (b)

Figure 6.25: Illustration of the effect of footing half-with B on the (a) normalised nonlinear rocking dynamic stiffness and (b) the damping ratio versus the dimensionless frequency α_0; $PI = 0$, $L/B = 1$, $u_0/H = 10^{-5}$, $\theta_0 = 10^{-5}$ rad, $V_s = 200m/s$, $\nu = 0.3$, Rayleigh damping $\xi = 5\%$.

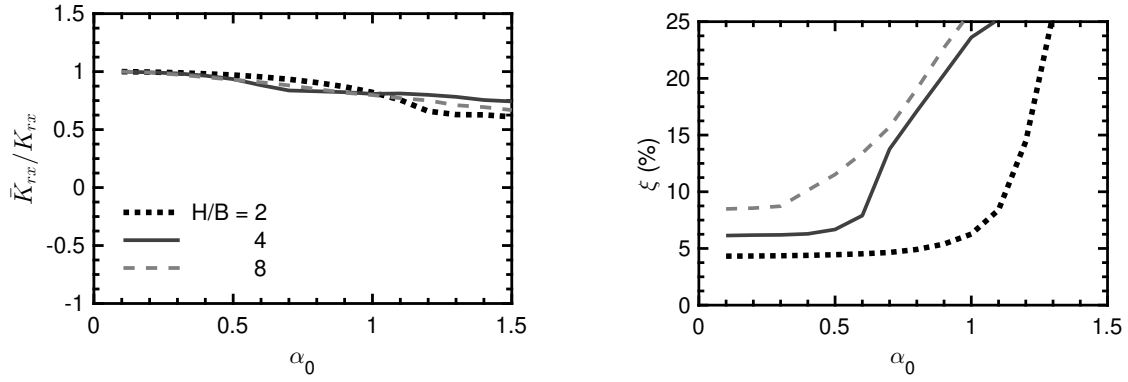

(a) (b)

Figure 6.26: Illustration of the effect of footing half-with B on the (a) normalised nonlinear rocking dynamic stiffness and (b) the damping ratio versus the dimensionless frequency α_0; $PI = 0$, $L/B = 2$, $\theta_0 = 10^{-5}$ rad, $V_s = 200m/s$, $\nu = 0.3$, Rayleigh damping $\xi = 5\%$.

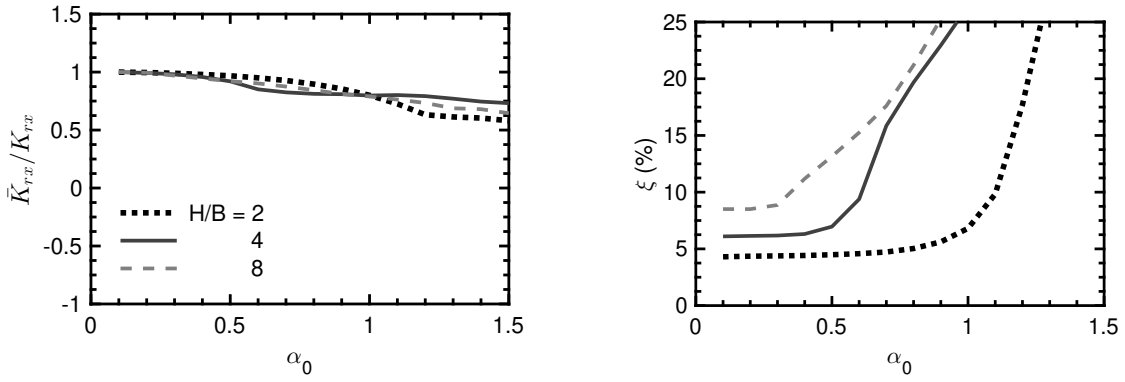

(a) (b)

Figure 6.27: Illustration of the effect of footing half-with B on the (a) normalised non-linear rocking dynamic stiffness and (b) the damping ratio versus the dimensionless frequency α_0; $PI = 0$, $L/B = 4$, $\theta_0 = 10^{-5}\ rad$, $V_s = 200m/s$, $\nu = 0.3$, Rayleigh damping $\xi = 5\%$.

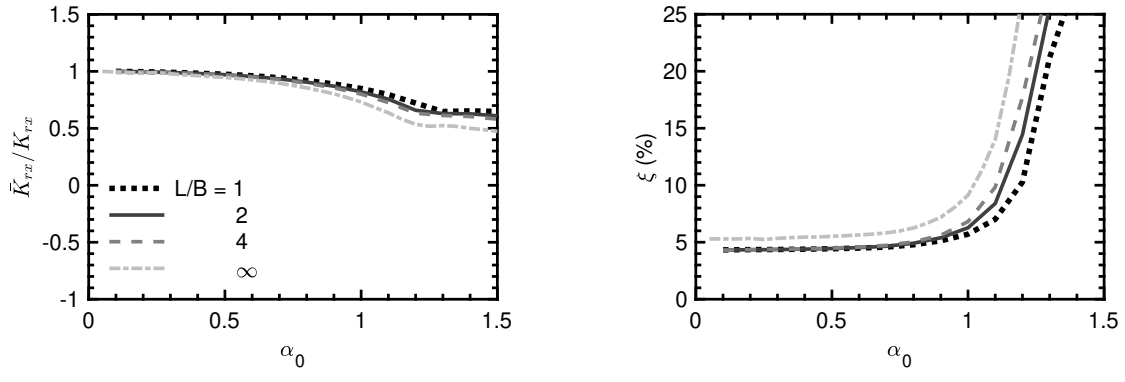

(a) (b)

Figure 6.28: Illustration of the effect of footing half-length L on the (a) normalised non-linear rocking dynamic stiffness and (b) the damping ratio versus the dimensionless frequency α_0; $PI = 0$, $H/B = 2$, $\theta_0 = 10^{-5}\ rad$, $V_s = 200m/s$, $\nu = 0.3$, Rayleigh damping $\xi = 5\%$.

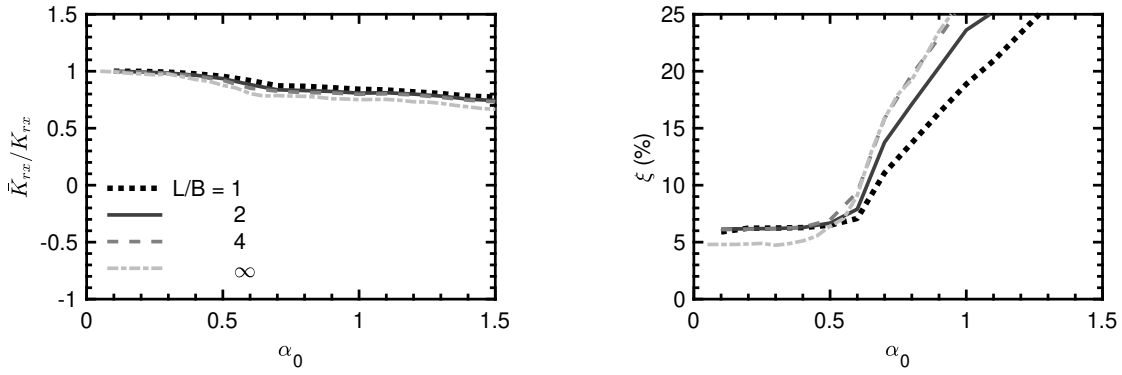

(a) (b)

Figure 6.29: Illustration of the effect of footing half-length L on the (a) normalised non-linear rocking dynamic stiffness and (b) the damping ratio versus the dimensionless frequency a_0; $PI = 0$, $H/B = 4$, $\theta_0 = 10^{-5}\ rad$, $V_s = 200 m/s$, $\nu = 0.3$, Rayleigh damping $\xi = 5\%$.

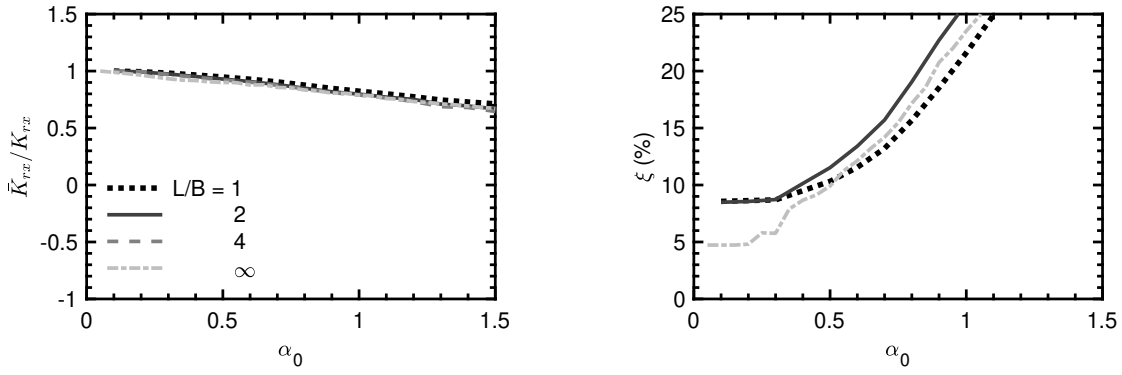

(a) (b)

Figure 6.30: Illustration of the effect of footing half-length L on the (a) normalised non-linear rocking dynamic stiffness and (b) the damping ratio versus the dimensionless frequency a_0; $PI = 0$, $H/B = 8$, $\theta_0 = 10^{-5}\ rad$, $V_s = 200 m/s$, $\nu = 0.3$, Rayleigh damping $\xi = 5\%$.

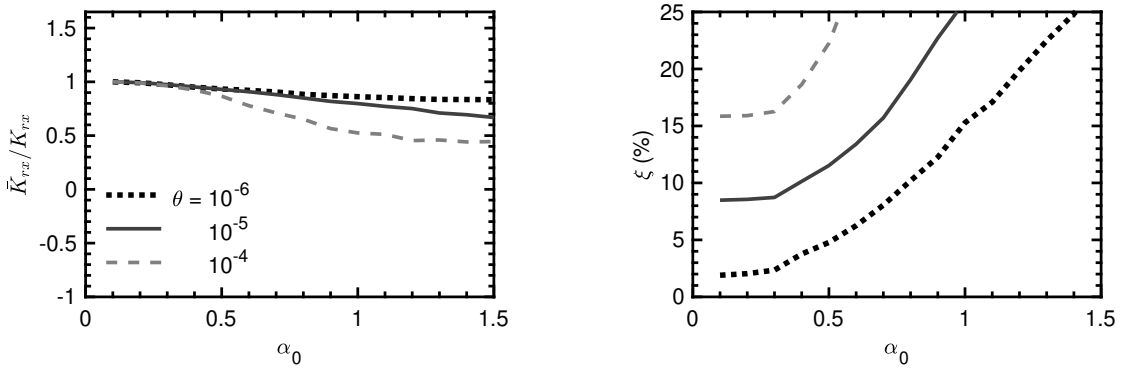

(a) (b)

Figure 6.31: Illustration of the effect of rotation angle θ (in rad) on the (a) normalised non-linear rocking dynamic stiffness and (b) the damping ratio versus the dimensionless frequency α_0; $PI = 0$, $L/B = 2$, $H/B = 8$, $V_s = 200m/s$, $\nu = 0.3$, Rayleigh damping $\xi = 5\%$.

6.4 Discussions - Key findings

To sum up, the key findings of this chapter are:

- Outcomes produced by means of finite difference code FLAC in two and three dimensions are in good agreement both in static and dynamic loading conditions. Linear elastic as well as non-linear constitutive soil behaviour described by modified hyperbolic and Ramberg-Osgood models is verified in FLAC3D against the corresponding results in FLAC2D. The minor discrepancies observed are attributed to the different element shapes. Calculations in FLAC3D are based on ten subzones, while in FLAC2D in four.

- In plane strain conditions modelled in FLAC3D, where the out-of-plane degrees of freedom are fixed, the width of the grid does not influence the results.

- Moving to the three dimensional problem the elastic response of square footings resting on a homogeneous soil layer is verified against solutions from the literature (Pais and Kausel [1] and Gazetas [2] revisited by Mylonakis et al [3]). Minor discrepancies are a result of the difference in boundary conditions (soil layer versus halfspace). To this end, the software is a valid alternative for standard techniques currently employed in static analysis.

- Dynamic stiffness in the translational modes of shaking in three dimensions follows similar trends as the two dimensional problem of a strip footing, but stronger wave

reflections are observed in the later case. Therefore, peaks and valleys are more obvious for the stiffnesses of the strip footings. Radiation damping is naturally less pronounced in three dimensions.

- Rocking stiffness and damping ratio of a footing resting on a soil layer are unaffected by the foundation aspect ratio. Two and three dimensional FLAC simulations produce indistinguishable results.

- Damping ratio is higher for the two dimensional problem of a strip footing compared to the three dimensional case of rectangular foundations in all modes of excitation. That is because in plane strain conditions, waves propagate in two dimensions whereas in the 3D case waves can escape to every direction thus generating stronger destructive interference effects. As a result, two dimensional analyses are deemed unconservative for foundation vibrations.

CHAPTER 7

ANALYSIS OF EXPERIMENTAL RESULTS

Chapter seven includes comparative studies between numerical 3D analyses and experimental data. The experimental data used are part of the Network for Earthquake Engineering Simulations Research (NEESR) project which have been orchestrated by the University of California, Los Angeles. The chapter begins with a brief description of the sites and the structure tested, and continues with a presentation of the modelling procedure in three dimensions. All simulations were conducted with FLAC3D version 6.

7.1 NEESR project overview

7.1.1 NEESR project objective

The objective of the project was to evaluate soil-structure interaction (SSI) effects on systems founded on real soil. To this end, a steel and reinforced concrete structure supported on a shallow foundation was used. The scope of this set-up was to measure horizontal and rocking impedances of the footings. A common problem in those experimental settings is noise disturbance which was reduced by applying high-precision forced lateral vibrations straight on the test structure. Therefore, the structure was experiencing both base shear and moment. The project involved three different experiments on three sites; one in the lab and two in the field. The structural influence on the results was eliminated by keeping the testing structure identical in all three sites. An exemption was the lab where

the structure was fixed on the floor.

More specifically, the test sites included a structural laboratory (LAB) setting to effectively simulate fixed base conditions, the Wildlife Liquefaction Array (WLA) site with a soft clay layer over sands prone to liquefaction and Garner Valley Downhole Array (GVDA) with a firm alluvium material as shown in Figure 7.1. The last two cases represent flexible base conditions with arbitrary soil stiffness.

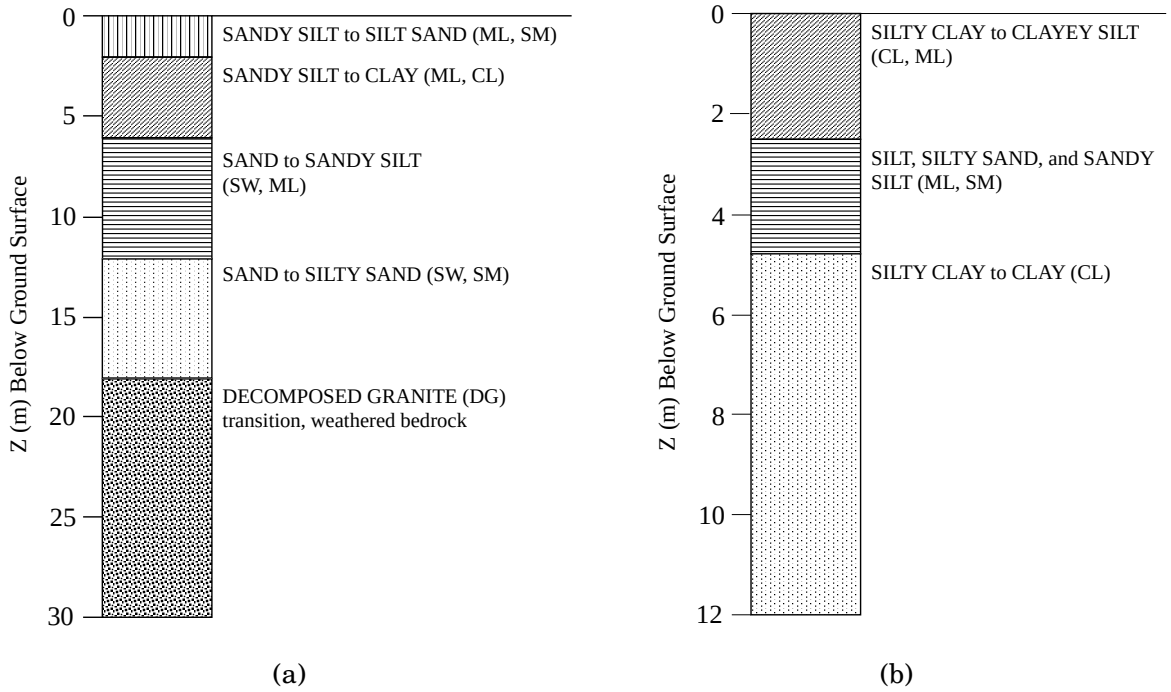

Figure 7.1: (a) Material profile in GVDA, (b) Material profile in WLA. Reproduced from [6]

The testing structure and the three different testing sites are described below in some detail. An extensive documentation of the NEESR project is provided in Design Safe-CI as part of the project 'Mitigation of Collapse Risk in Vulnerable Concrete Buildings' as experiments number 25 through number 27 [155].

7.1.2 Test Structure

A simple, rectangular test structure was designed specifically to accommodate forced vibration testing of a shallow foundation. The structure consists of a 4.28 m × 2.13 m × 0.61 m reinforced concrete foundation mat, a top slab of the same plan dimensions, yet 0.25 m thick, four steel columns and removable cross braces. The aspect ratio of the structure

in plan view is 2 : 1. The total height of the structure and the foundation mat is 3 m. A photograph of the structure in GVDA testing site is shown in Figure 7.2.

Figure 7.2: Test structure in GVDA

The foundation mat was cast in place, its mass was calculated to be 13.340 Mg and it is considered nearly rigid. The top slab weighs 5.47 Mg. Its mass is assumed to be sufficient to induce non-linear soil response and be sufficiently rigid against flexural and shear deformations. The four columns are made of square hollow steel sections HSS (30.5 cm × 30.5 cm × 1.3 cm), the total height is 2.13 m and their mass is calculated to be around 1 Mg in total. The removable cross braces consist of steel sections HSS (10.2 cm × 10.2 cm × 1.3 cm) and the total weight is 0.8 Mg.

7.1.3 Test Sites

7.1.3.1 University of California, Los Angeles Laboratory - LAB test site

The UCLA Laboratory - LAB is fitted with a strong reinforced concrete floor of 1.5m thickness. The floor has DYWIDAG threaded bars on a 0.6m grid which allows the test structure to fixed directly to the floor. The shear modulus of the concrete floor is estimated at 10 GPa and represents fixed base conditions.

7.1.3.2 Wildlife Liquefaction Array - WLA test site

The Wildlife Liquefaction Array is maintained by NEES@UCSB and is representing the case of soft soil layers prone to liquefaction. The objective of the current study is not concerning liquefaction, but the test site is modelled to represent very flexible base conditions.

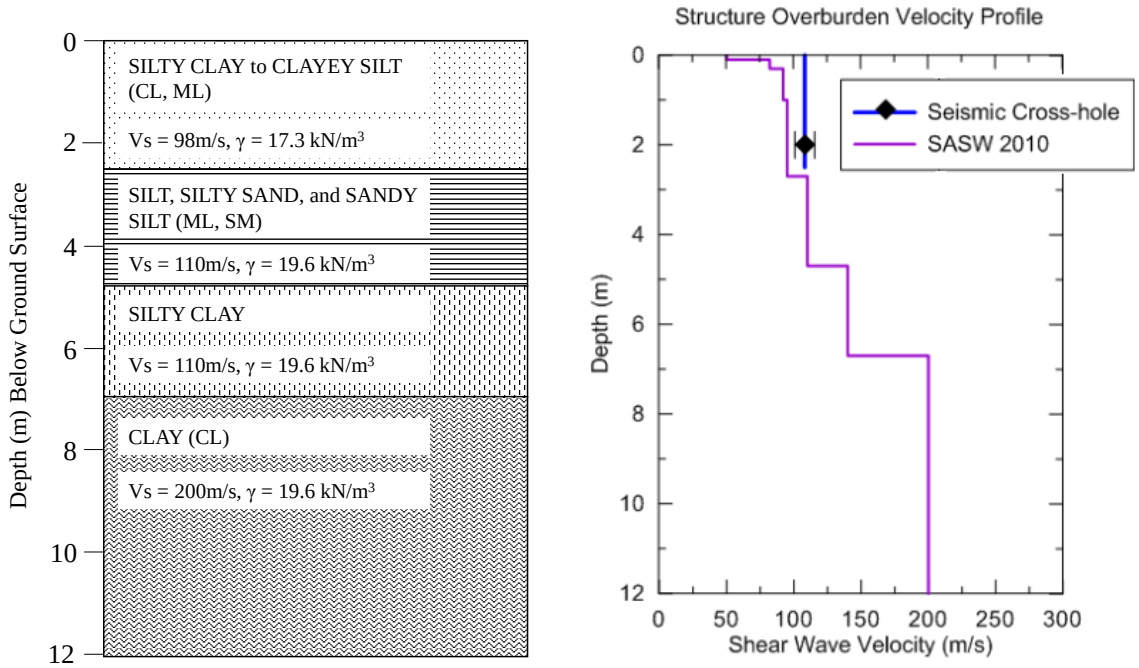

(a) (b)

Figure 7.3: (a) Soil and (b) shear wave profile at WLA based on non-invasive spectral-analysis of surface waves testing (SASW). Source [6].

Documentation on the test site suggests that the soil consists mainly by clay, silty clay and clayey silt up to a depth of $12m$ as shown in 7.3. The moist unit weight of the soil is at 17.3 kN/m^3 at the first layer and increases to 19.6 kN/m^3 thereafter. The water table varies between 1 to $2m$ on the rainy seasons.

The shear wave velocity is measured prior and after the construction of the testing structure and is 98 m/s and 106 m/s for the upper 2 m, respectively. The shear wave velocity is almost doubled at 7 m below the ground surface where the transition to silty clay to clay occurs.

7.1.3.3 Garner Valley Downhole Array - GVDA test site

The Garner Valley Downhole Array (GVDA) test site is essentially representing the problem of soft soil horizontal layers over bedrock. The site has been studied before the set of experiments at hand, in 1989 by NEES@UCSB. Consequently, the GVDA site is very well documented and studied. A square-plan test structure exists on the site in addition to the rectangular-plan studied. The setting in this test site can also help to investigate the influence of adjacent structures on soil and structure interaction, but this

exceeds the purpose of this study.

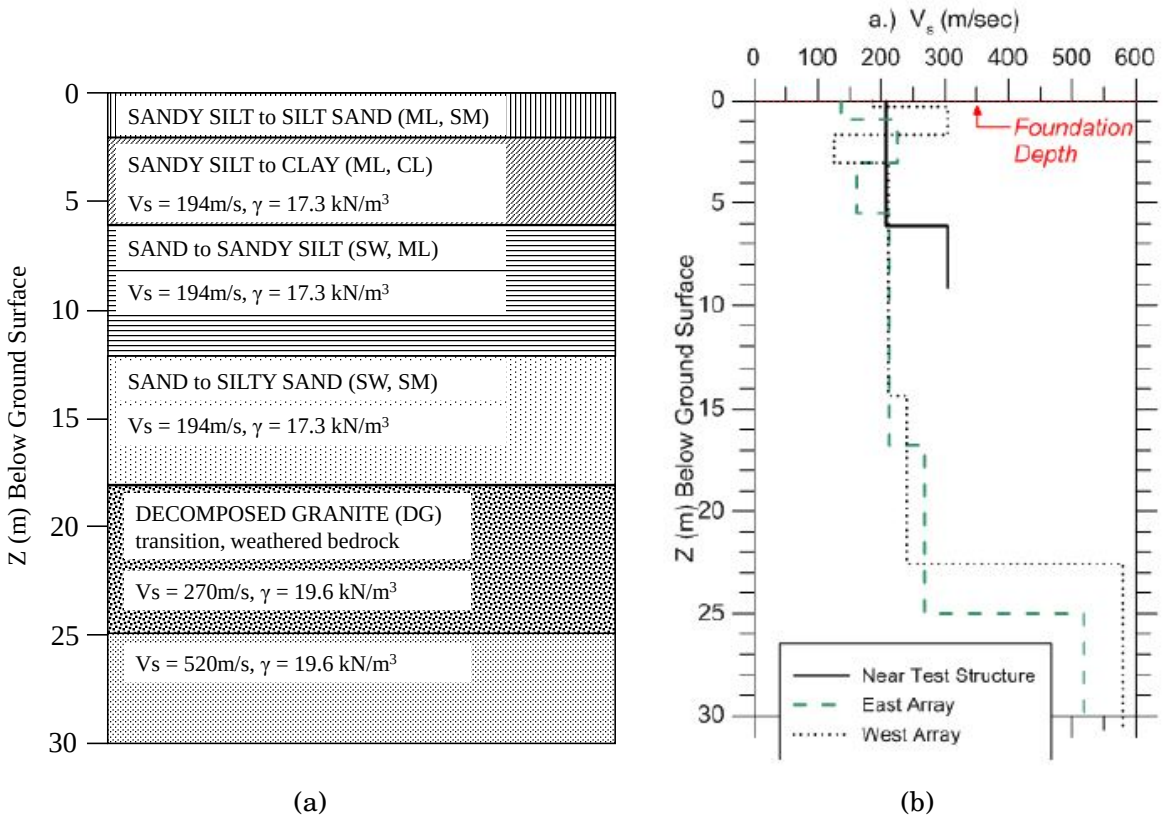

Figure 7.4: (a) Soil and (b) shear wave profile at WLA based on non-invasive spectral-analysis of surface waves testing (SASW). Source [11].

As shown in Figure 7.4, the soil consists of alluvium up to 18 m to 25 m depth followed by decomposed granite. Weathered granodiorite is encountered below the decomposed granite layers.The NEES team at UCSB conducted a series of Spectral Analysis of Surface Waves (SASW) measurements and suggested an average moist unit weight between 17.3 to 19.6 kN/m^3 and the water table was found to be at 3 m depth [11].

Cross-hole seismic surveys were conducted on the top 2 m of soil before and after the set up of the examined rectangular-plan test structure to evaluate the effect that structural weight has on shear wave propagation velocity. It is found that the shear wave velocity with the foundation mat in place is 187 m/s and 194 m/s when the complete structure is installed. According to Youd et al [156] the shear wave velocity is increasing with depth to a maximum of 520 to 570 m/s at around 25 m depth.

7.1.4 Loading equipment

Dynamic harmonic load was applied to the test structure by portable shakers attached to either the roof or the foundation slab, oriented either in the longitudinal or the transverse direction of the structure. Two shakers were utilised: (a) an eccentric mass shaker referred to as 'Mighty Mouse' (MM), and (b) a linear mass shaker referred to as 'Atom Ant' (AA) shown in Figure 7.5.

The electromagnetic linear mass shaker (AA) loads the structure with a maximum force of 440 N at fast sine sweeps with frequency ranging from 4 to 44Hz and provides constant force amplitude across the whole frequency range.

On the other hand, the eccentric mass shaker can reach up to 90kN over a frequency range of $0-20Hz$ but the force amplitude varies as it is proportional to the square of frequency. However, large amplitude vibrations exceed the scope of this work and the outcomes are not further discussed herein.

Figure 7.5: Linear mass shaker used for small amplitude shaking of test structure. Source: [6].

The bracing and loading set-ups studied in this chapter are illustrated in 7.6.

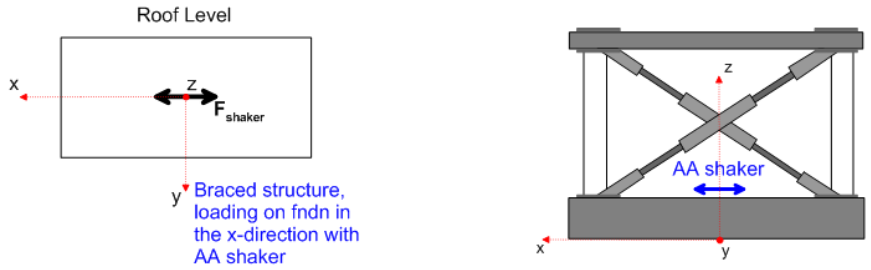

(a)

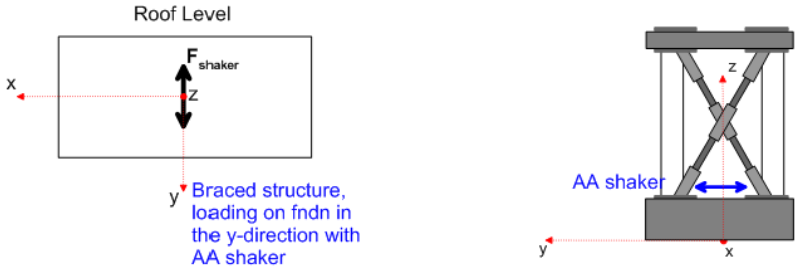

(b)

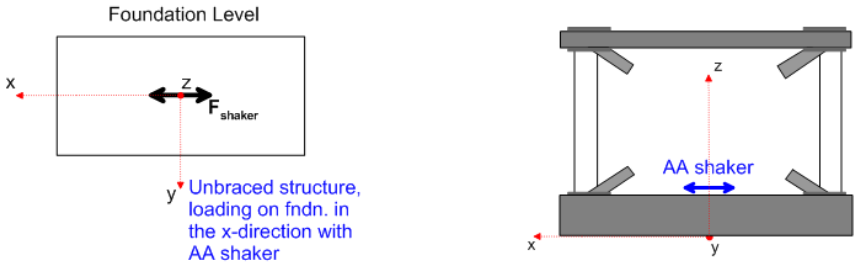

(c)

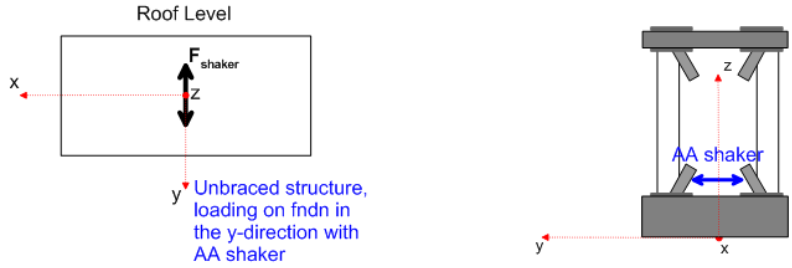

(d)

Figure 7.6: Experiment bracing and loading conditions: a) Braced loading case in the longitudinal direction, b) Braced loading case in the transverse direction, c) Unbraced loading case in the longitudinal direction and d) Unbraced loading conditions in the transverse direction. Source: [11].

7.2 Numerical simulation of UCLA field data

7.2.1 WLA test site soil conditions - Half-space

7.2.1.1 Modelling of experimental setup

A rectangular rigid footing resting on halfspace at WLA test site is investigated by means of FLAC3D. According to the case study [6], the geometric and soil properties are given in Table 7.1 and shown in Figure 7.3.

FLAC3D modelled geometry taking into consideration the layering, is presented in Figure 7.7. The model extends to a depth of $35m$ and quiet boundaries are used laterally and in depth to simulate half-space conditions. The mesh consists of elements of size $0.2m$ x $0.1m$ x $0.5m$ in the vicinity of the footing, resulting in 8 zones per B and L. To increase computational efficiency, the grid coarsens laterally away from the studied footing. Based on the sensitivity studies presented in *Chapter 4*, lateral boundaries are set $15L$ from the edge of the footing.

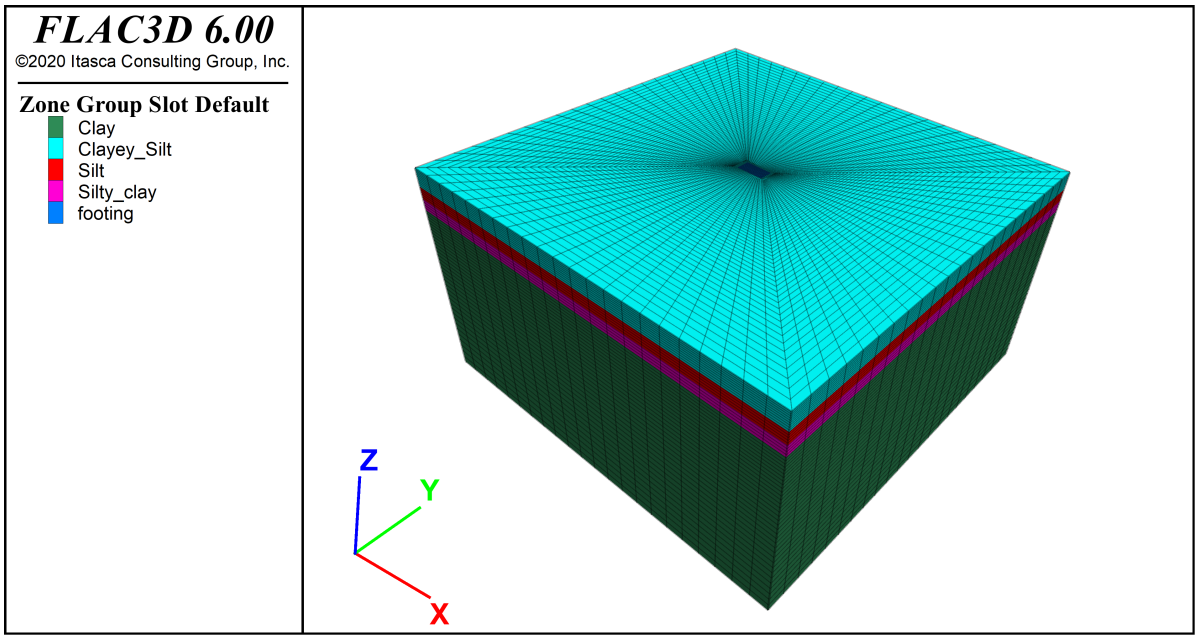

Figure 7.7: FLAC3D modelled geometry accounting for the layered soil profile at WLA.

Comparisons are made against the experimental impedance functions as described in [6, 76]. The method for deriving impedance functions from field test data is presented in detail in [76] while extensions to that procedure were also discussed in [6].

Low force amplitudes are examined resulting in displacements (in meter) and rotations (in rad) on the order of 10^{-5}, induced by the linear mass shaker "AA". Therefore,

it is expected to demonstrate an almost linear elastic behaviour within the frequency range 4 to 25 Hz.

The impedance values derived from the field data and numerical analyses are compared with analytical solutions from the literature [1], assuming homogeneous halfspace conditions. Two values for shear wave velocity were adopted for these comparisons: (a) $V_{s_1} = 106$ m/s which accounts for structure overburden effects on seismic velocities, and (b) $V_{s_2} = 98$ m/s which only partially accounts for structure overburden effects because it is measured adjacent to the structure and not beneath. Based on the data in Table 7.1, the shear and bulk modulus are calculated for both shear wave velocities considered. The results are given in Table 7.2 and Table 7.3.

A modified hyperbolic constitutive model, calibrated against Darendeli [4], is implemented for the analyses. Model parameters are calculated as described in 2.4.2 based on the information on Table 7.1. To this end, the curvature coefficient α is equal to 0.919 and the pseudo-reference strain γ_r is calculated from equation 2.34 to be 0.043%.

Table 7.1: Geometric and soil properties in WLA test site used to calibrate modified hyperbolic model against Darendeli [4]. Source: [6].

Property	Symbol	Value	Units
footing width	$2B$	2.13	m
footing length	$2L$	4.26	m
soil density	ρ	1.73	Mg/m^3
Poisson's ratio	ν	0.45	[ ]
Plasticity index	PI	20	[ ]
Mean effective confining pressure	σ'_v	49	kPa
Over-consolidation ratio	OCR	1.15	[ ]
Material damping	ξ	2%	[ ]
Resonant frequency	f_1	7	Hz

Table 7.2: Shear wave velocity, shear and bulk moduli used for the homogeneous halfspace calculations accounting for structure overburden effects on seismic velocities (measured beneath the structure).

Property	Symbol	Value	Units
Shear wave velocity	V_{s_1}	106	m/s
Shear modulus	G_1	19400	kPa
Bulk modulus	K_1	188000	kPa

Table 7.3: Shear wave velocity, shear and bulk moduli used for homogeneous halfspace calculations only partially accounting for structure overburden effects (measured adjacent to the structure).

Property	Symbol	Value	Units
Shear wave velocity	V_{s_2}	98	m/s
Shear modulus	G_2	16600	kPa
Bulk modulus	K_2	161000	kPa

7.2.1.2 Low amplitude forced vibration impedance

Stiffness and damping derived from WLA field test data back-calculated using the methodology described in [76], as presented in [6], are compared with predictions based on Pais and Kausel [1] equations for homogeneous halfspace and impedance functions derived from numerical modelling with FLAC3D. Two V_s profiles were taken into account for the homogeneous halfspace: (a) $V_s = 106m/s$ accounting for structure overburden effects (Table 7.2), and (b) $V_s = 98m/s$ which only partially accounting for structure overburden effects (measured adjacent to the structure - Table 7.3). Three sets of analyses were conducted with FLAC3D utilising modified hyperbolic constitutive model calibrated against the experimental results by Darendeli [4]. First, the homogeneous halfspace was investigated for two shear wave propagation velocities: (a) $V_s = 106m/s$ and (b) $V_s = 98m/s$. Additionally, the layered profile is modelled based on soil properties shown in Figure 7.3. Impedance functions for a) lateral translation and b) rotation are shown in Figures 7.10 to 7.9.

In all the studied cases, the experiments had been repeated at least three times to minimise errors. It is interesting to note that despite the simplicity of the test structure, the consistency of the equipment and the very low shaking amplitude, it is clear that not all the experiment results are reproducible. This is more pronounced for the case of a

braced structure shaken in the longitudinal direction (Figure 7.10) and the unbraced test structure oscillating in the transverse direction (Figure 7.9). This malfunction could be attributed to the data acquisition system.

The numerical analyses at both examined shear wave velocities demonstrate a clear ascending trend with frequency that is not in agreement with the solution provided in the literature [1].

For the lateral stiffness (graphs (a) and (b) in Figures 7.10 to 7.9), it is clear from both the field data and the numerical analyses that stiffness increases with frequency. This effect is more pronounced under the assumption of a homogeneous layer and less evident - though still noticeable- when soil layering is taken into account.

As mentioned in [6] foundation stiffness is relatively stable up to approximately $15Hz$ under longitudinal shaking (Figures 7.10 and 7.11) and $10Hz$ under transverse shaking (Figures 7.8 and 7.9). At higher frequencies, the results become unstable, possibly due to errors in shaker force measurement and the limitations of the data acquisition system. The effect is more obvious for the damping ratio. The behaviour past 10 Hz is suspect and it is deemed unreliable. The lack in synchronisation might be attributed to the conversion from the analog signal of the accelerometers and cabling to digital.

A further proof that the results have been compromised, is the negative damping ratios observed in Figures 7.10, 7.8 and 7.9 for the rocking mode.

The experimental data are in better agreement with the numerical results for the unbraced case as clearly seen in Figures 7.9 and 7.11. This indicates that impedance is affected by bracing. Therefore, the results for unbraced are more reliable up to $12Hz$. Beyond that point malfunctions occur. It appears that at 15 Hz a local resonance occurs which is possibly due to the response of the bracing.

Considering the case of longitudinal excitation (Figures 7.10 and 7.11), the system is naturally stiffer and less sensitive to rotations. The experimental dataset is stable over a wider frequency range, up to $15Hz$.

Within the aforementioned range, foundation stiffness is relatively constant for translation exhibiting minor frequency dependence. On the other hand, rocking stiffness drops significantly with frequency. Those trends are predicted in the equations in literature [1] and are successfully replicated in FLAC3D although the drop in rocking stiffness with frequency is not as steep as in the field data.

Stiffness predictions based on literature [1] are sensitive to the shear wave velocity, and the test data as well as the data obtained from the layered soil profile appear to be closer to the analytical predictions with $V_s = 98m/s$. Translational stiffnesses for the

transverse and longitudinal shaking are approximately equal, which is anticipated from model predictions.

Interestingly, the damping results appear to be stable over a wider frequency range (up to $15Hz$) than the stiffness results, at least for the case of longitudinal shaking (Figures 7.10, 7.11). For frequency up to $15Hz$, the experimental data show steep increases of damping with frequency, highlighting the importance of radiation damping for energy dissipation. The observed damping slightly exceeds analytical model predictions for translation but is lower for rocking, an effect also documented in [6]. With regard to the numerical model values, the layered model which is a better representation of the soil conditions, is in great agreement with the field test data within the stable range of frequencies.

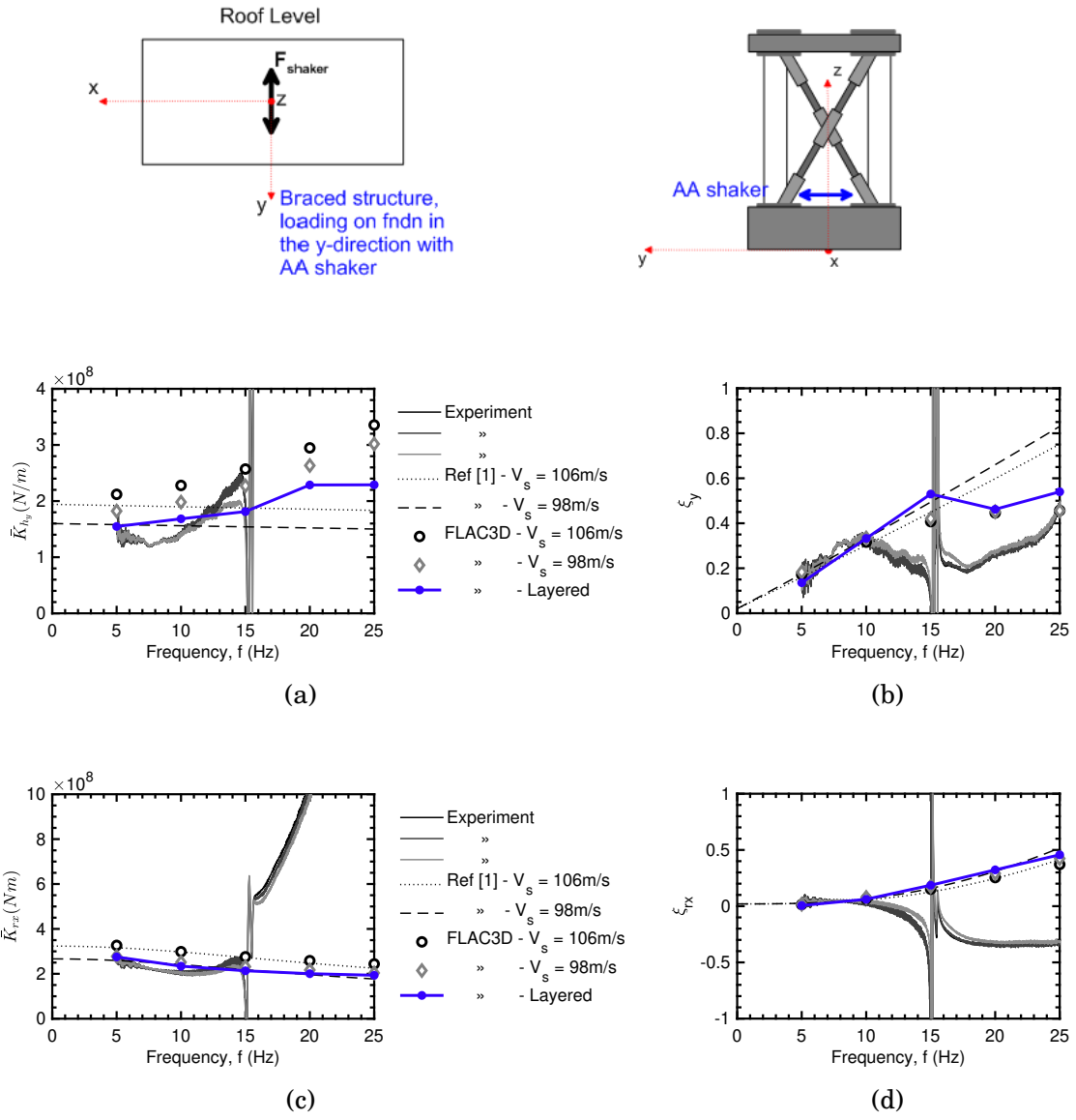

Figure 7.8: (a) Lateral dynamic stiffness and (b) damping ratio, along with (c) rocking dynamic stiffness and (d) damping ratio derived from experimental data for the braced AA loading case in the transverse direction reproduced from [6], compared to predicted models based on Pais and Kausel [1] for $V_s = 106m/s$ and $98m/s$ and the numerical solutions produced with FLAC3D for homogeneous and layered non-linear medium; modified hyperbolic, $\gamma_r = 0.0043\%$.

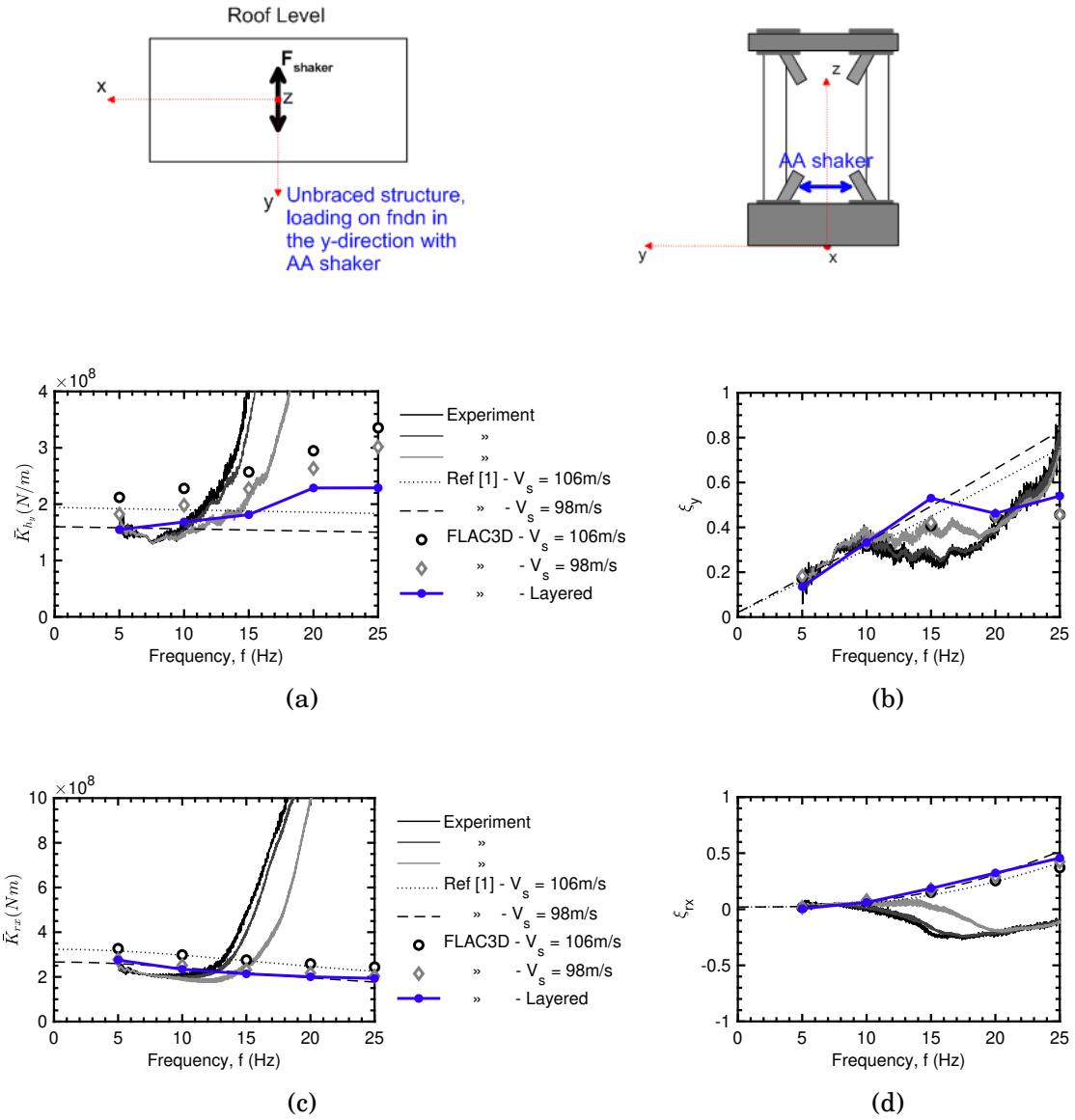

Figure 7.9: (a) Lateral dynamic stiffness and (b) damping ratio, along with (c) rocking dynamic stiffness and (d) damping ratio derived from experimental data for the unbraced AA loading case in the transverse direction reproduced from [6], compared to predicted models based on Pais and Kausel [1] for $V_s = 106m/s$ and $98m/s$ and the numerical solutions produced with FLAC3D for homogeneous and layered non-linear medium; modified hyperbolic, $\gamma_r = 0.0043\%$.

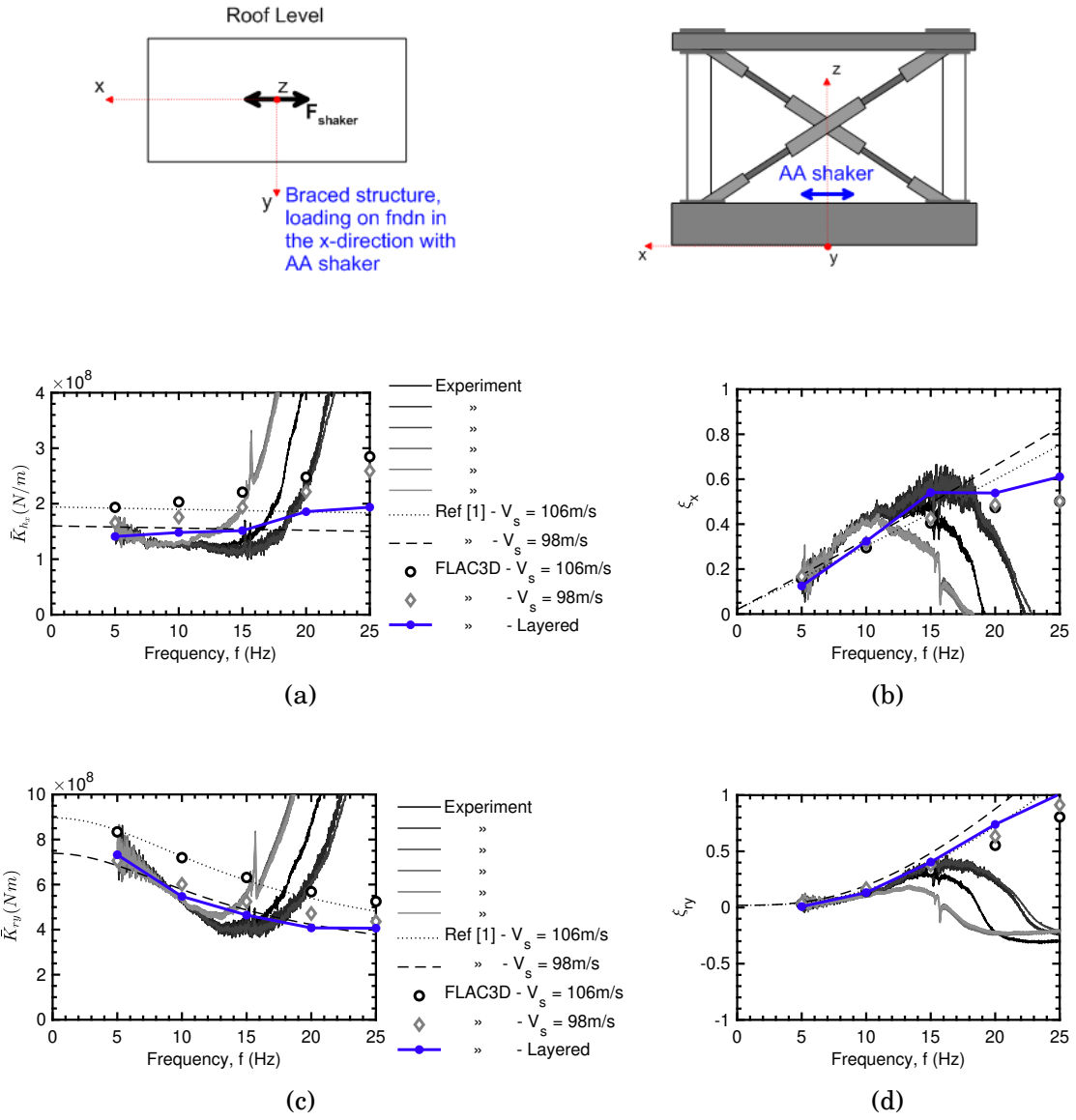

Figure 7.10: (a) Lateral dynamic stiffness and (b) damping ratio, along with (c) rocking dynamic stiffness and (d) damping ratio derived from experimental data for the braced AA loading case in the longitudinal direction reproduced from [6], compared to predicted models based on Pais and Kausel [1] for $V_s = 106m/s$ and $98m/s$ and the numerical solutions produced with FLAC3D for homogeneous and layered non-linear medium; modified hyperbolic, $\gamma_r = 0.0043\%$.

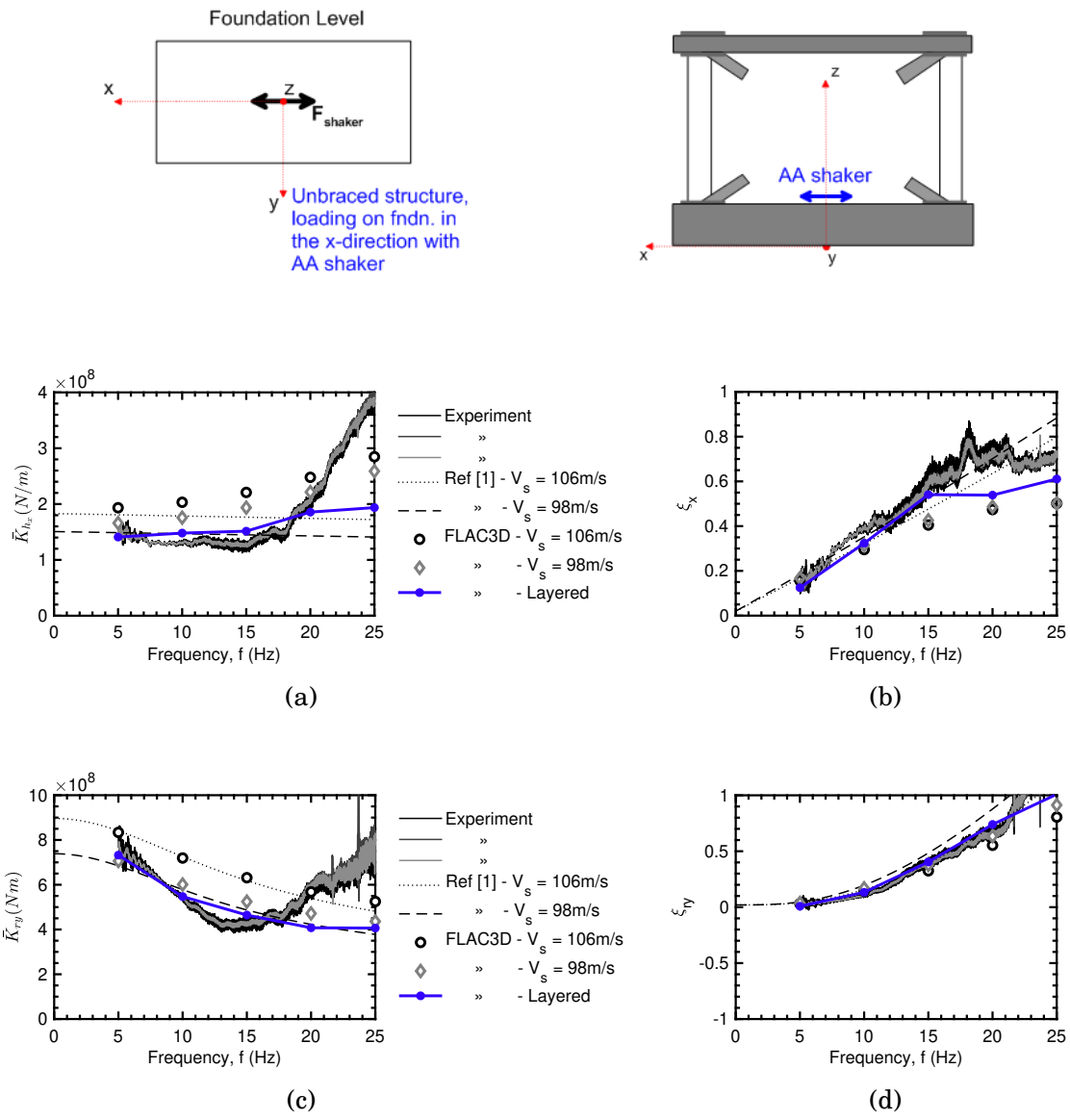

Figure 7.11: (a) Lateral dynamic stiffness and (b) damping ratio, along with (c) rocking dynamic stiffness and (d) damping ratio derived from experimental data for the unbraced AA loading case in the longitudinal direction reproduced from [6], compared to predicted models based on Pais and Kausel [1] for $V_s = 106m/s$ and $98m/s$ and the numerical solutions produced with FLAC3D for homogeneous and layered non-linear medium; modified hyperbolic, $\gamma_r = 0.0043\%$.

7.2.2 GVDA test site soil conditions - Layer over bedrock

7.2.2.1 Modelling of experimental setup

Similarly, a rectangular rigid footing resting on halfspace at GVDA test site is investigated by means of FLAC3D. According to the case study [11] the geometric and soil properties are shown in Figure 7.4.

FLAC3D modelled geometry of this test case, taking into consideration soil layering, is presented in Figure 7.12. The model extends to a depth of $35m$ and quiet boundaries are used laterally. The mesh consists of elements of size $0.2m$ x $0.1m$ x $0.5m$ in the vicinity of the footing resulting in 8 zones per B and L. To increase computational efficiency, the grid coarsens laterally away from the studied footing. Based on the sensitivity studies presented in *Chapter 4*, lateral boundaries are set $15L$ from the edge of the footing.

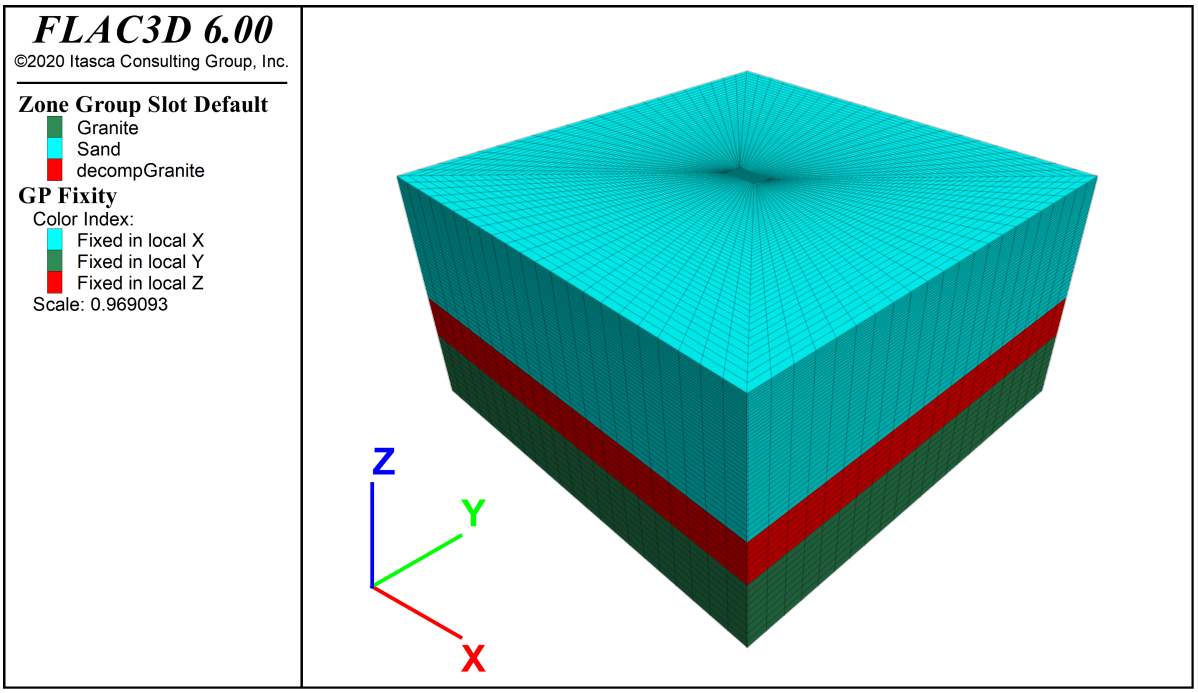

Figure 7.12: FLAC3D modelled geometry accounting for the layered soil profile at GVDA.

Comparisons are made against the derived from field forced vibration test data impedance functions as described in [11, 76]. The method for deriving impedance functions from field test data is presented in detail in [76].

Low force amplitudes are examined resulting in displacements (in meter) and rotations (in rad) in the order of 10^{-5}, induced by linear mass shaker "AA". Therefore, it is expected to demonstrate an almost linear elastic behaviour within the frequency range 4 to 25 Hz.

The impedance values derived from the field data and numerical analyses are compared with analytical solutions from the literature [1] assuming homogeneous halfspace conditions. Two values for shear wave velocity are proposed for these comparisons: (a) $V_{s_1} = 194\ m/s$ accounts for structure overburden effects on seismic velocities, and (b) $V_{s_2} = 176\ m/s$ which back-calculated to fit the experimental outcomes as described in [11].

7.2.2.2 Low amplitude forced vibration impedance

Similarly to the WLA test site, stiffness and damping derived from GVDA field test data back-calculated using the methodology described in [76], as presented in [11], are compared with predictions based on Pais and Kausel [1] equations for homogeneous halfspace and impedance functions derived from numerical modelling with FLAC3D. Two V_s profiles were taken into account for the homogeneous halfspace: (a) $V_s = 194m/s$ accounting for structure overburden effects, and (b) $V_s = 176m/s$ which represents equivalent free-field velocities. For the sake of brevity, FLAC3D numerical simulations were conducted only for the layered profile shown in Figure 7.4.

The shaker location of applied force and structure stiffness introduced by bracing resulted to local complexities near the bracing frequency. That is because the linear mass shaker was secured in place during testing at the roof slab, whereas shaking applied at the foundation slab only used the weight of the shaker. The lack of an external mount during shaking at the foundation slab introduced noise into the data compromising the impedance results. The experiments having the cleanest data sets at GVDA are those from the structure in an unbraced condition with forcing at the roof as documented in [11]. To this end, the unbraced condition with the shaker on the roof is investigated herein.

Considering the horizontal stiffness, experimental values are lower than predicted by analytical and numerical means for shaking in the longitudinal and the transverse direction as shown in Figure 7.13 (a) and 7.14 (a), respectively. In all cases, lateral dynamic stiffness is little affected by frequency. The translational damping ratio are in agreement, although slightly lower compared to the ones obtained with FLAC3D.

It is noted that for the case of shaking in the longitudinal direction, the outcomes match well for $V_s = 176m/s$ which is a 10% reduction of the the overburden in-situ shear wave velocity while a 15% reduction would be required to match the experimental swaying stiffness for shaking in the transverse direction. One speculation is that the reduction from the expected stiffnesses arises from localised shearing of the soil underlying the

foundation. The dynamic interaction of the concrete-soil contact could cause disturbances to the shear stiffness of a thin layer of soil in the immediate vicinity of the foundation that are not captured by the cross-hole seismic testing at $1m$ depth [11].

Switching our attention to rocking stiffness and damping ratio a frequency-dependency is observed in Figures 7.13 (c), (d) and 7.14 (c), (d). Dynamic rocking stiffness decreases with increasing frequency in an almost linear manner. For shaking in the longitudinal direction, rocking stiffness matches the analytical results for $V_s = 194m/s$ and follows similar trend with the numerically obtained stiffness. FLAC3D numerical simulations based on the documented soil profile overpredicts dynamic rocking stiffness. On the other hand, shaking in the transverse direction produces a lower rocking stiffness. In contract with the translational mode, rocking damping ratio are higher compared to the analytically and numerically obtained results. This phenomenon indicates the imperfect cancellation of shear waves laterally in the inhomogeneous medium. Even though in the case of lateral loading the same inhomogeneity is in favour the disruptive interference resulting in lower damping ratios, in the case of rocking oscillations it works against it and higher damping ratios are observed.

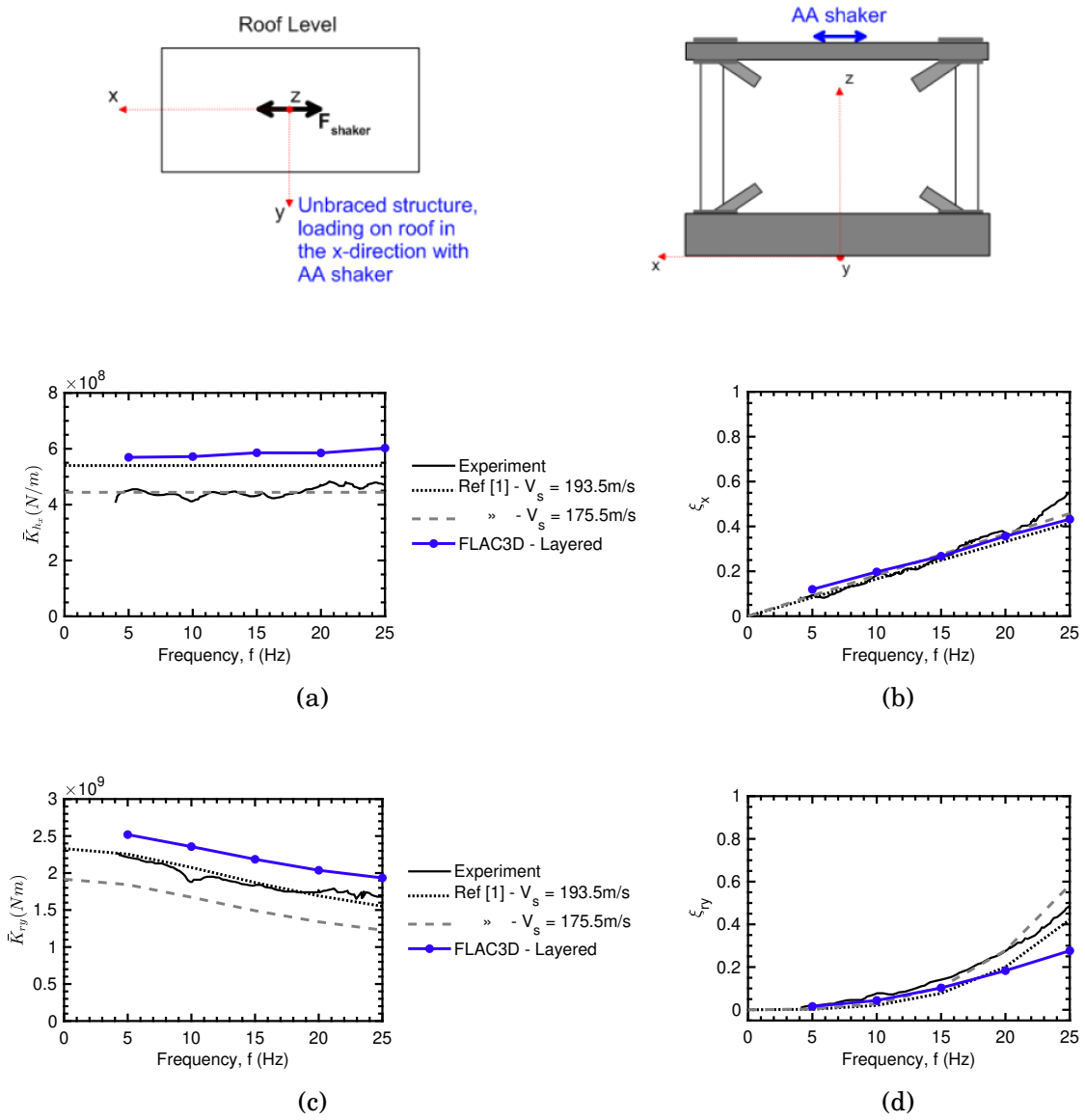

Figure 7.13: (a) Lateral dynamic stiffness and (b) damping ratio, along with (c) rocking dynamic stiffness and (d) damping ratio derived from experimental data for the unbraced AA loading case in the longitudinal direction reproduced from [11], compared to predicted models based on Pais and Kausel [1] for $V_s = 193.5m/s$ and $175.5m/s$ and the numerical solutions produced with FLAC3D for layered non-linear medium.

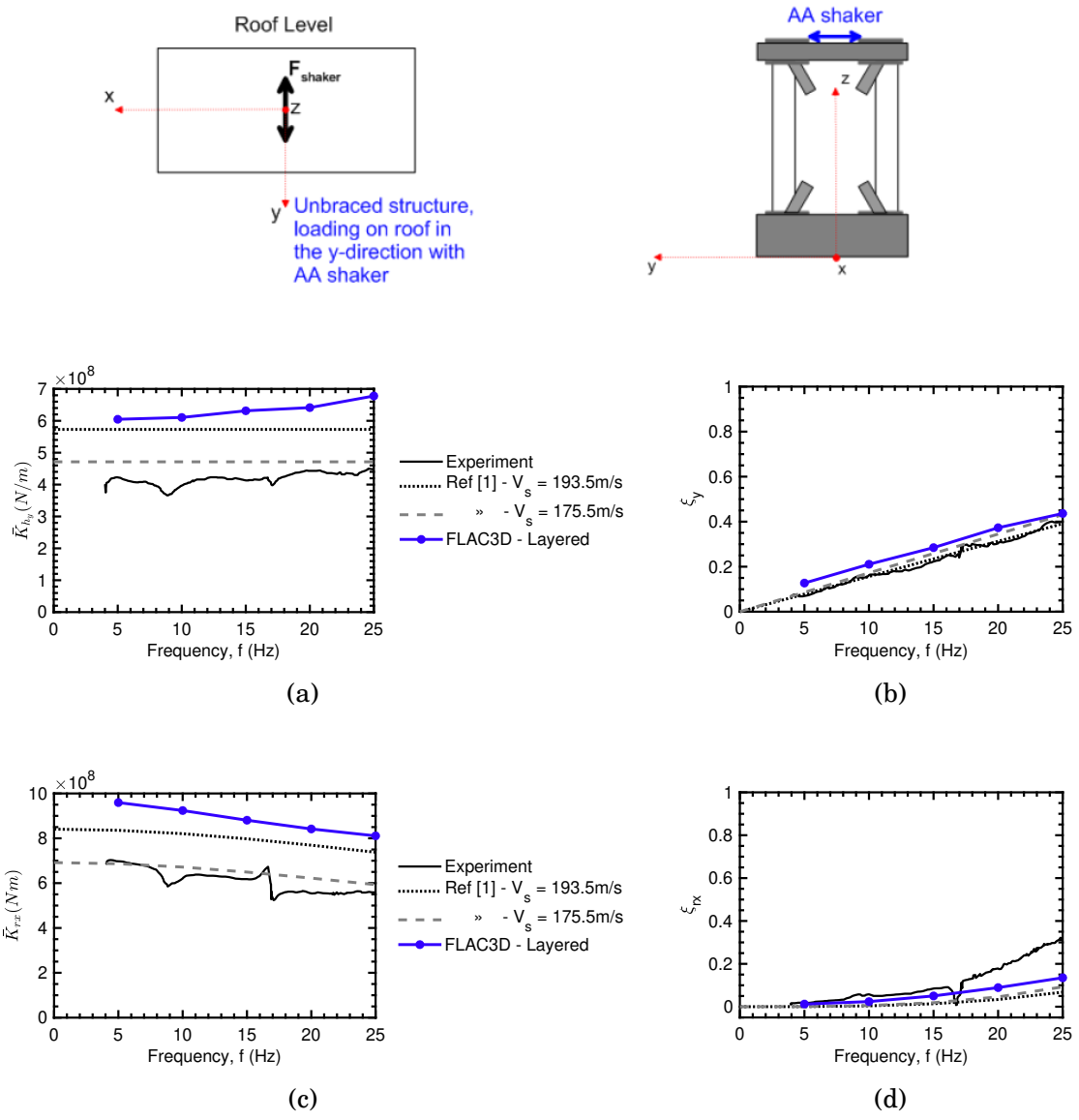

Figure 7.14: (a) Lateral dynamic stiffness and (b) damping ratio, along with (c) rocking dynamic stiffness and (d) damping ratio derived from experimental data for the unbraced AA loading case in the transverse direction reproduced from [11], compared to predicted models based on Pais and Kausel [1] for $V_s = 193.5m/s$ and $175.5m/s$ and the numerical solutions produced with FLAC3D for layered non-linear medium.

7.3 Key remarks

To sum up, the key findings of this chapter are:

- For the WLA test site, it is evident that despite the simplicity of the test structure, the consistency of the equipment and the very low shaking amplitude, it is clear that not all the experiment results are reproducible. This malfunction could be mainly attributed to the data acquisition system.
- FLAC3D simulations produce rocking stiffness and damping ratio in convincing agreement with analytical solutions for homogeneous halfspace conditions. However, for the translational mode numerical results showcase frequency dependence, also obvious in the field test dataset, yet not predicted analytically [1].
- In both test sites, the measured data are more stable for excitation frequencies up to $15Hz$. The shaker location as well as the structure stiffness i.e. bracing introduce local complexities.
- For GVDA test site, numerical simulations based on the documented soil layering and properties, over-predict swaying and rocking stiffness. This can be attributed to disturbances to the shear stiffness of a thin layer of soil in the immediate vicinity of the foundation that are not captured by the cross-hole seismic testing at $1m$ depth. On the other hand, FLAC3D simulations successfully replicate the damping ratio as the shear modulus cancels out from the numerator and the denominator of $ImK/2ReK$. In this light, damping ratio is an indicator of a geometric (radiation) problem and the effect of material properties is eliminated.
- Model-based radiation damping is limited because it applies for homogeneous soil conditions in which upward and downward excitation from a rocking slab effectively cancels out at large distances (St. Venant's principle). In contrast, in real site conditions the near-perfect cancellation of the radiated waves does not occur, increasing radiation damping relative to numerical model predictions.

CHAPTER 8

DISCUSSION

In this chapter the main points of research are summarised alongside the key findings and the contributions. The numerical methodology application is also included and recommended dimensionless design charts are presented.

8.1 Scope of the research

The scope of the progress research is to provide insight into non-linear soil-foundation-structure interaction and propose recommendations for the analysis and design. In order to achieve this, a numerical methodology is developed and it is validated against existing experimental data, obtained by academic collaborators at UCLA.

Firstly, two numerical models, namely the Ramberg-Osgood and the modified hyperbolic, are implemented into FLAC, focusing on the effects of non-linear soil-structure interaction under small and medium excitation amplitudes. Following a rigorous mesh sensitivity analysis, the numerical models were calibrated against existing analytical solutions for elastic soil behaviour. A parametric investigation was subsequently conducted, focusing on the decrease in soil stiffness and the increase of damping, due to shear modulus degradation and damping increase for small and medium shear strains developing in the foundation subsoil.

To this end, the Ramberg-Osgood model calibrated to match the Vucetic and Dobry [8] experimental curves, implemented as a User-Defined Model into the Explicit Finite

Difference code FLAC 2D. Similarly, modified hyperbolic model is used in agreement with the recommendations by Darendeli [4] experimental findings.

8.2 Research key findings

The main focus of this research was to explore the dynamic response of shallow foundations when subjected to static and dynamic loads. The project's objectives have been pursued by carrying out an extensive parametric investigation on soil properties, foundation geometry and numerical parameters. The emphasis of this research was directed to explore the influence of two non-linear constitutive models on the evolution of the principal mechanical properties, such as stiffness and, in the case of dynamic loading, on the evolution of impedance with excitation frequency. The following sections summarise the conclusions drawn from the work described in the previous chapters.

8.2.1 Key remarks on linear analysis

The linear static solutions in literature were revisited and following are the main observations:

- For swaying foundations when s/B is equal or higher than approximately 20, the stiffness reaches a constant value no matter the boundary fixities. The corresponding value of s/B is around 15 and 8 for vertically-loaded and rocking footings, respectively. For (s/B) values lower than the aforementioned limits, stiffness is either increasing (for free side boundaries) or decreasing (for fixed side boundaries). This can be explained as the restrictions of fixed boundaries results in a stiffer medium and vice versa.
- The expressions for the calculation of the vertical and the horizontal stiffness provided in the literature are revisited and new expressions are suggested to fully account for the influence of Poisson's ratio and soil layer thickness. The expressions are repeated herein for vertical static stiffness

$$K_{v,elastic} = \frac{G}{1-\nu}\left[1+\frac{3.5}{1-\nu}\left(\frac{B}{H}\right)^{1.25}\right] \tag{8.1}$$

And for the horizontal static stiffness

$$K_{h,elastic} \simeq \frac{2G}{2-\nu}\left[1+3\nu\,(2-\nu)\frac{B}{H}\right] \tag{8.2}$$

- The dynamic lateral stiffness is revisited for and a thick soil deposit ($H/B = 8$), as there seems to be no correlation with the published results [2] beyond $\alpha_0 = 0.5$.

  It is clear in Figure 8.1 that both FLAC and Isobem are in excellent agreement. Given that FLAC is running an explicit finite difference analysis while Isobem works in the frequency domain, the agreement can only prove their accuracy. In addition, taking into consideration the natural frequencies of the soil deposit ($\alpha_{0_1} = 0.2$, $\alpha_{0_3} = 0.6$, $\alpha_{0_5} = 1.0$, $\alpha_{0_7} = 1.4$, $\alpha_{0_9} = 1.8$), provides justification for the results produced with FLAC against those in Ref. [2].

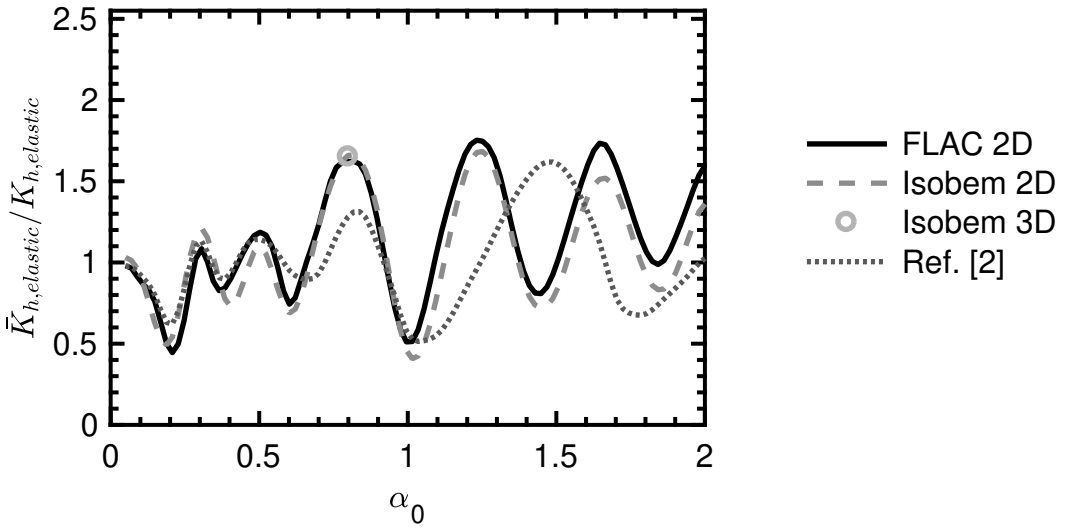

Figure 8.1: Comparison between analyses and available results in terms of horizontal dynamic stiffness; $H/B = 8$, $\nu = 0.30$.

8.2.2 Key remarks on non-linear analysis with Ramberg-Osgood

The main conclusions regarding the Ramberg-Osgood non-linear analysis are as follows:

- For static conditions regardless of the mode of loading, a single fitted formula is suggested for the normalised non-linear static stiffness. The static linear elastic stiffness, $K_{ij,elastic}$, is a function of G, B, H, ν and can be easily determined by the diagrams and equations provided in Section 4.1 e.g. Equations 8.2 and 8.1. If the applied force or moment is given, the non-linear stiffness coefficient can be derived by Eq. 5.1 (repeated below).

The fitted formula is following the expression

$$\frac{K_{ij}}{K_{ij,elastic}} = \frac{1}{1+\left(\frac{1}{\alpha_{ref}}-1\right)\left(\frac{F_{ij}}{F_{ij,1}}\right)} \tag{8.3}$$

where α_{ref} is the normalised stiffness value for u_{ij} equals to γ_1 and F_{ij} equals to $F_{ij,1}$ and it is given in Table 8.1. The above Equation 8.3 can be adjusted to account for vertical, horizontal and rocking loading by replacing F_{ij} with V, H, M and u_{ij} with v/H, u/H or θ, respectively.

Table 8.1: Parameter α_{ref} values depending on mode of loading and plasticity index.

Mode of Loading	$PI = 0$	$PI = 15$	$PI = 30$	**Average**
Vertical	0.649	0.645	0.641	0.645
Swaying	0.596	0.594	0.595	0.595
Rocking	0.707	0.714	0.714	0.712

If the response is known, the non-linear stiffness can be calculated by a trial and error procedure through equation 8.4.

$$\frac{K_{ij}}{K_{ij,elastic}} = \frac{1}{1+\left(\frac{1}{\alpha_{ref}}-1\right)\left(\frac{1}{\alpha_{ref}}\cdot\frac{v/H}{\gamma_1}\cdot\frac{K_{ij}}{K_{ij,elastic}}\right)} \tag{8.4}$$

- Firstly, the static stiffness decreases as the thickness of the soil layer increases in all modes of vibration. The existence of bedrock at a shallow depth underneath the footing has a major effect on static stiffness, especially in the vertical and horizontal mode of loading. The rocking stiffness is practically unaffected by soil stratum thickness because the soil response is limited to the vicinity of the footing.

- The dynamic stiffness is also affected by bedrock elevation. The amplitude of foundation response increases substantially at frequencies near the natural frequency, in both vertical and horizontal modes of excitation.

- Excitation amplitude significantly affects the impedances. High amplitudes naturally result in lower stiffnesses and higher damping coefficients.

8.2.3 Key remarks on non-linear analysis with modified hyperbolic

Summing up, the key points of this section are:

- Similarly to the Ramberg-Osgood static analysis, it is shown that a single curve is sufficient to describe the non-linear soil behaviour regardless of the loading mode. If (i.e. v, u or θ) is known the non-linear static stiffness can be calculated by equation 8.5 for any given plasticity index and overconsolidation ratio (accounted in γ_r). The resulting curves could be fitted according to the formula

$$\frac{K_{ij}}{K_{ij,elastic}} = \frac{1}{1+\left(\frac{u_{ij}}{u_{ij,r}}\right)^{\alpha}} \tag{8.5}$$

  where α is the familiar modified hyperbolic exponent suggested by Darendeli [4] to be equal to 0.919, and $u_{ij,r}$ is a "pseudo-reference" rocking angle equal to $1.5 \cdot \gamma_r$.

- It is shown that the static stiffness increases as the thickness of the soil layer decreases in all modes of loading. The presence of bedrock at a shallow depth underneath the footing has a major effect on static stiffness, especially in the vertical and horizontal mode of loading. The rocking stiffness is practically unaffected by soil stratum thickness because the soil response is limited to the vicinity of the footing.

- The dynamic stiffness is also affected by the bedrock. The amplitude of foundation motion can increase substantially at frequencies close to natural frequency of the deposit, both in vertical and horizontal modes. This phenomenon is only observed in shallow soil layers during rocking oscillations. Excitation amplitude is significantly affecting both stiffness and damping in all modes of excitation. In general, high amplitudes produce lower stiffnesses and higher damping coefficients.

8.2.4 Comparison of RO and MH constitutive models

Overall, the aforementioned non-linear constitutive models to simulate the problem of a rigid, massless, strip footing resting on a soil layer, are compared as follows:

- Both non-linear constitutive models result in the decrease of static stiffness with increasing displacement/rotation.

- As a rule of thumb, the soil described by RO constitutive relationships is stiffer when subjected to static translational loading with increasing displacements. However, in rocking mode the discrepancy is fluctuating with MH model resulting in larger stiffness up to the curve's turning point and beyond this the RO produces higher stiffness. The effect of the non-linear constitutive model is evident in static stiffness plots.

- On the contrary, in non-linear dynamic stiffness, it is observed that, due to normalisation of abscissa, the influence of the model is omitted.

- As far as the rocking impedance parts are concerned, differences are getting more obvious for medium to high dimensionless frequencies. Non-linear stiffness decreases with frequency at a faster rate than the corresponding linear stiffness. On the other hand, damping in the linear regime exceeds by more than 25% the non-linear system damping. The difference between the two studied non-linear models is negligible. Ramberg-Osgood model produces insignificantly larger damping and lower stiffness at high frequencies.

- Both the Ramberg-Osgood and the modified hyperbolic model used in FLAC cannot model failure, thus use of these models implies large factors of safety. Excitation amplitudes in the order of 10^{-3} are the upper bound of the models applicability.

8.2.5 Key remarks on strain rate effects

With reference to the shear strain rates effects, the following key points are shown:

- A practical numerical methodology for non-linear analysis of rigid surface footings under rocking oscillations, was presented. A modified hyperbolic model originally calibrated using an experimental database was implemented into the finite difference code FLAC, to account for stress-strain and shear strain rate behaviour of soil. The two required model parameters, and γ_r, can either be constant, pertaining to static or dynamic conditions, or vary as a function of shear strain rate.

- Parametric analyses on shear rate effects showed that for rocking amplitudes $\theta_{max} = 10^{-5}$ and 10^{-4} non-linear dynamic rocking stiffness fluctuates past $\alpha_0 = 0.4$ following a very similar trend to the linear case. For the rocking amplitude of 10^{-3} the values are dropping significantly, and the curves are smoother. This suggests that non-linearity mainly affects the static stiffness K_{rx}, while the dynamic

stiffness modifier k_{rx} can be obtained from the elastodynamic Equation 4.18 for dimensionless frequencies a_0 as high as 0.8. The drop in static stiffness can be explained by shear modulus degradation effects, as shown in Figure 2.11 (a).

- Regarding SSR effects, an increase in rocking stiffness is observed with increasing frequency for the largest rocking amplitude ($\theta_{max} = 10^{-3}$). The causes of this behaviour may be related to stress-induced in-homogeneity in the soil mass, as shear strain rate varies for point to point in proportion to strain. On the other hand, for small rotation amplitudes stiffness is unaffected by shear strain rate which shows that, in this case, soil non-linearity would be of minor importance.

- SSR effects are becoming evident from very low frequencies for rocking amplitudes larger than $\theta_{max} = 10^{-4}$ and they are increasingly more significant with increasing frequency. For rocking amplitudes equal or under $\theta_{max} = 10^{-4}$, non-linearity and SSR effects have negligible impact on dynamic stiffness.

8.2.6 Key remarks on three dimensional problem

Considering dynamic oscillations for the three-dimensional problem of square and rectangular footings, the following key findings are shown:

- Outcomes produced by means of finite difference code FLAC in two and three dimensions are in good agreement both in static and dynamic loading conditions. Linear elastic as well as non-linear constitutive soil behaviour described by modified hyperbolic and Ramberg-Osgood models is verified in FLAC3D against the corresponding results in FLAC2D. The minor discrepancies observed are attributed to the different element shapes. Calculations in FLAC3D are based on ten subzones, while in FLAC2D in four.

- In plane strain conditions modelled in FLAC3D, where the out-of-plane degrees of freedom are fixed, the width of the grid does not influence the results.

- Moving to the three dimensional problem the elastic response of square footings resting on a homogeneous soil layer is verified against solutions from the literature (Pais and Kausel [1] and Gazetas [2] revisited by Mylonakis et al [3]). Minor discrepancies are a result of the difference in boundary conditions (soil layer versus halfspace). To this end, the software is a valid alternative for standard techniques currently employed in static analysis.

- Dynamic stiffness in the translational modes of shaking in three dimensions follows similar trends as the two dimensional problem of a strip footing, but stronger wave reflections are observed in the later case. Therefore, peaks and valleys are more obvious for the stiffnesses of the strip footings. Radiation damping is naturally less pronounced in three dimensions.

- Rocking stiffness and damping ratio of a footing resting on a soil layer are unaffected by the foundation aspect ratio. Two and three dimensional FLAC simulations produce indistinguishable results.

- Damping ratio is higher for the two dimensional problem of a strip footing compared to the three dimensional case of rectangular foundations in all modes of excitation. That is because in plane strain conditions, waves propagate in two dimensions whereas in the 3D case waves can escape to every direction thus generating stronger destructive interference effects. As a result, two dimensional analyses are deemed unconservative for foundation vibrations.

8.2.7 Key remarks on numerical simulation of UCLA field data

The key points drawn from the comparative studies between numerical 3D analyses and experimental data are as follows:

- For the WLA test site, it is evident that despite the simplicity of the test structure, the consistency of the equipment and the very low shaking amplitude, it is clear that not all the experiment results are reproducible. This malfunction could be mainly attributed to the data acquisition system.

- FLAC3D simulations produce rocking stiffness and damping ratio in convincing agreement with analytical solutions for homogeneous halfspace conditions. However, for the translational mode numerical results showcase frequency dependence, also obvious in the field test dataset, yet not predicted analytically [1].

- In both test sites, the measured data are more stable for excitation frequencies up to $15Hz$. The shaker location as well as the structure stiffness i.e. bracing introduce local complexities.

- For GVDA test site, numerical simulations based on the documented soil layering and properties, over-predict swaying and rocking stiffness. This can be attributed

to disturbances to the shear stiffness of a thin layer of soil in the immediate vicinity of the foundation that are not captured by the cross-hole seismic testing at $1m$ depth. On the other hand, FLAC3D simulations successfully replicate the damping ratio as the shear modulus cancels out from the numerator and the denominator of $ImK/2ReK$. In this light, damping ratio is an indicator of a geometric (radiation) problem and the effect of material properties is eliminated.

- Model-based radiation damping is limited because it applies for homogeneous soil conditions in which upward and downward excitation from a rocking slab effectively cancels out at large distances (St. Venant's principle). In contrast, in real site conditions the near-perfect cancellation of the radiated waves does not occur, increasing radiation damping relative to numerical model predictions.

8.3 Significance of research findings for geotechnical practice

It is believed that some of the outcomes of this numerical study may have a positive input for improving current geotechnical practice in numerical modelling. In particular, the following impacts can be foreseen:

- The linear static problem of a massless, strip footing resting on the surface of a soil layer and the corresponding elastodynamic problem are revisited and simulated with finite difference code, FLAC in two- and three-dimensions.
- New fitted formulas for the vertical and lateral static stiffness are proposed to account for the effect of Poisson's ratio and the thickness of the soil layer. The suggested formulas are confirmed with other software such as PLAXIS and IsoBEM.
- An extensive analysis has been conducted with reference to lateral elasto-dynamic stiffness and a new design charthas been proposed.
- Two non-linear numerical models are implemented into FLAC2D and FLAC3D to simulate the non-linear behaviour of soil from small to medium shear strains. The models can be calibrated against experimental findings or site response analysis measurements.

8.4 Recommendations for future research

The recommendations presented in this section have been derived from the personal experience gained during this research project. It is hoped that such suggestions will benefit further research. The recommendations presented here could be followed to further extend the scope of research in order to better understand the soil structure interaction during static and dynamic loading.

The following are recommended for future investigation:

- The non-linear analyses are modelled for high factors of safety as failure is not defined in the models used. This is a limitation of the Ramberg-Osgood and modified hyperbolic model and therefore, seeking a way to overcome this limitation is key to obtain realistic results. The necessity for developing a more elaborate constitutive model is arising.
- Another worth examined topic is to apply the excitation to the base of the soil layer in order to simulate earthquake excitation, including the effect of a superstructure. In this study the loading is applied at the top of the footing to simulate machine operation.
- Other worth-examined cases are concerning footings resting on multiple non-linear soil layers, inhomogeneous soil layers described by different shear velocities with depth. Moreover, the interaction with other structures in the vicinity of the footing must be of concern.
- Cover dynamic soil structure interaction effects with a 1-storey superstructure and add excitation in all three examined locations; at the base of the structure, the top slab of the structure and as earthquake excitation at the base of the soil layer.
- Finally, the numerical results, especially the effect of shear strain rate, should be verified experimentally. Carefully designed model tests in controlled environments (e.g., in geotechnical centrifuges, shaking tables and soil pits) would be useful in this regard.
- A wider set of field tests would be worth examining.

8.5 Closure

The ultimate objective of this research project is to make a contribution toward a better understanding of soil-structure interaction effects of spread footings and its engineering applications. Invariably, this must involve extensive research in search for parameters governing footing response. This research has explored the cyclic soil behaviour by means of two constitutive models and has proposed a methodology for predicting soil response based on soil properties such as Poisson's ratio, shear modulus, shear wave velocity and Plasticity Index. The dynamic stiffness analyses were also integrated to trace the footing behaviour to small to medium soil strain. It is hoped that the outcomes of this research will contribute to a greater understanding of soil-foundation-interaction. The direct beneficiaries of this study would be ground engineering contractors, asset owners and software developers, who may be able to exploit the analytical developements reported in this work to inform their projects.

APPENDIX A

SOIL COLUMN VERIFICATION PROBLEM

Appendix A presents a comparison between the mathematical and the numerical solution of the soil column problem subjected to harmonic vertical oscillations. The mathematical solution is provided with the assistance MATLAB and the numerical solution is given by FLAC analysis.

A.1 Soil column problem

The static vertical stiffness of an elastic soil column, fixed at one end, is given by well-known the expression

$$K_{st} = \frac{EA}{H} \tag{A.1}$$

The corresponding normalised dynamic stiffness is

$$\frac{K_{dyn}}{K_{st}} = \frac{(1+i2\xi)H\lambda}{tanh(H\lambda)} \tag{A.2}$$

where

$$\lambda = \sqrt{-\frac{\omega^2\rho}{E^*}} \tag{A.3}$$

and

$$E^* = E(1+i2\xi) \tag{A.4}$$

where ξ is the material hysteretic damping ratio. As the above expression A.4 is frequency independent and does not involve structural mass ξ, can be interpreted as a performance index.

In case of viscous damping, the expression A.4 becomes

$$E^* = E\left[1 + i2\zeta\left(\frac{\omega}{\omega_1}\right)\right] \tag{A.5}$$

with ζ being the percentage of viscous damping applied.
The normalised vertical displacement over the static vertical counterpart is given by the expression

$$\frac{u(\omega)}{u_{st}} = \frac{tanh(H\lambda)}{(1+i2\xi)H\lambda} \tag{A.6}$$

The damping of the system is calculated using the well-known formula

$$\xi_{system} = \frac{Im(K_{dyn})}{2Re(K_{dyn})} = \frac{1}{2} \times \frac{|K_{dyn}|sin\phi}{|K_{dyn}|cos\phi} = \frac{1}{2} \times tan\phi \tag{A.7}$$

By numerically investigating equations A.6 and A.7 with MATLAB one can produce the following plots

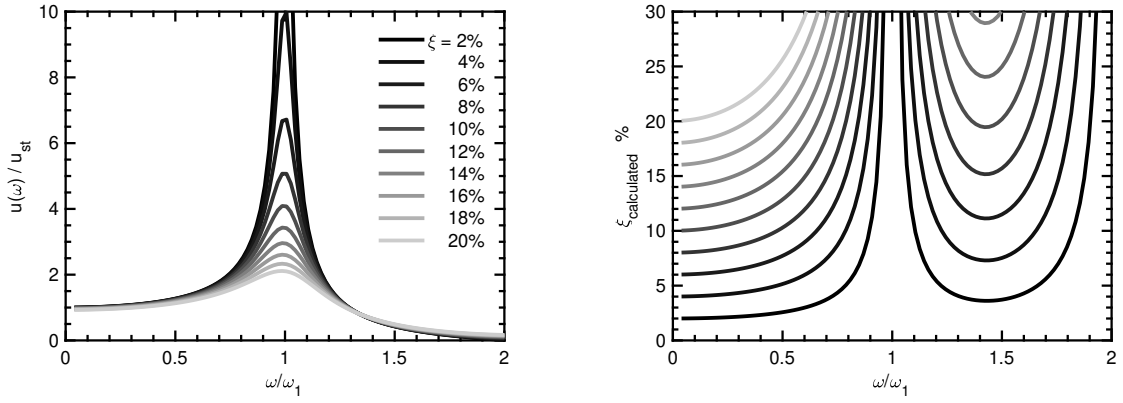

(a) (b)

Figure A.1: Influence of damping ratio, ξ, on (a) flexibility, $u(\omega)/u_{st}$, and (b) the system damping, ξ_{system}, calculated mathematically with MATLAB

By numerically investigating the above solutions yields Figures A.2 to A.4. Two damping values, 6% and 8% are investigated in Figure A.2. Two Rayleigh damping formulation were considered, mass proportional Rayleigh damping only and both stiffness and mass proportional Rayleigh damping. The m close to the damping value indicates mass proportional damping. It is clear in the first figure that mass proportional Rayleigh

damping is zero for low dimensionless frequencies and both components of Rayleigh damping are producing half of the applied damping ratio.

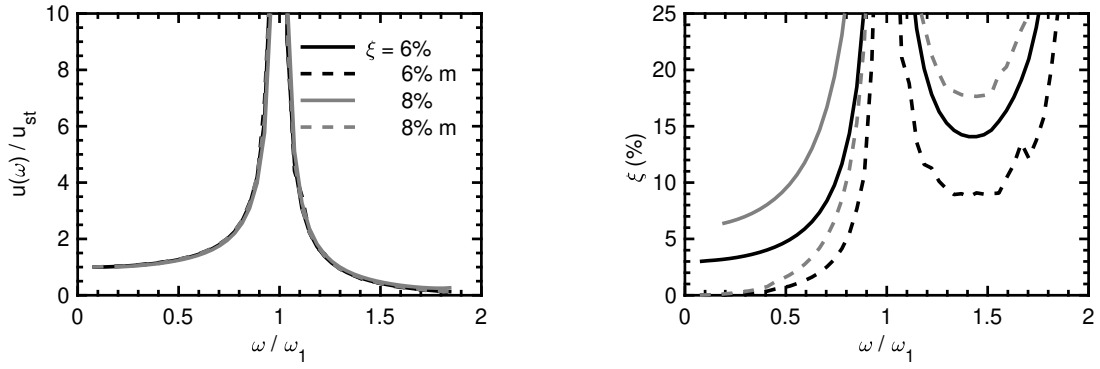

(a) (b)

Figure A.2: Influence of damping ratio, ξ, on (a) flexibility, $u(\omega)/u_{st}$, and (b) the system damping, ξ_{system}, calculated numerically with FLAC; $H/B = 8$, $\nu = 0.30$, $f_{min} = f_{exc}$.

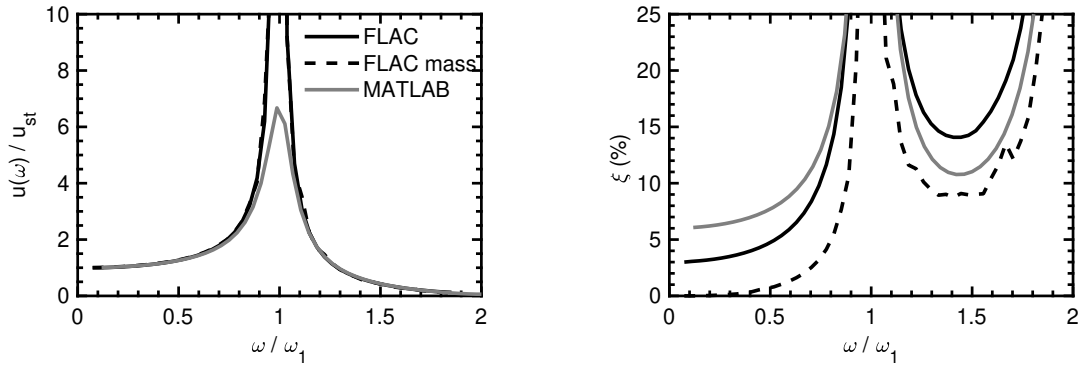

Figure A.3: Influence of damping ratio, ξ, on (a) flexibility, $u(\omega)/u_{st}$, and (b) the system damping, ξ_{system}, calculated numerically with FLAC; $H/B = 8$, $\nu = 0.30$, $f_{min} = f_{exc}$, $\xi = 6\%$.

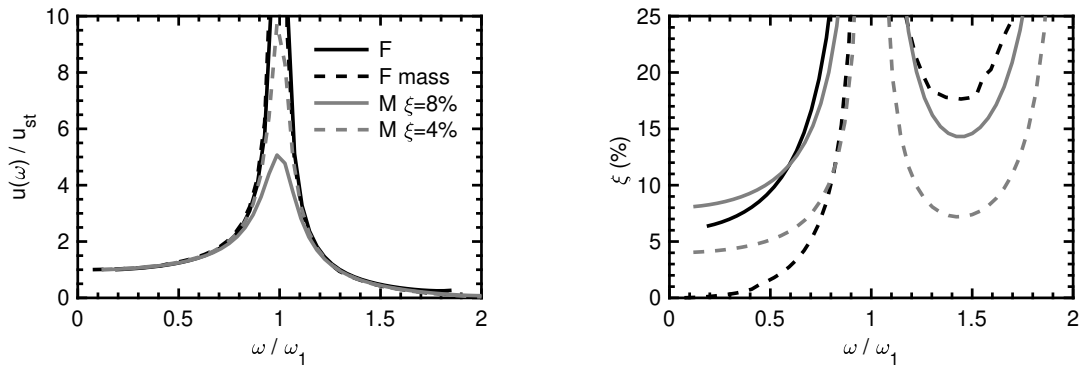

Figure A.4: Influence of damping ratio, ξ, on (a) flexibility, $u(\omega)/u_{st}$, and (b) the system damping, ξ_{system}, calculated numerically with FLAC (F) and mathematically with MATLAB (M); $H/B = 8$, $\nu = 0.30$, $f_{min} = f_{exc}$, $\xi = 8\%$.

APPENDIX B

CONE THEORY - FOOTING SUBJECTED TO HORIZONTAL LOADING

Cone theory was developed to provide a simple and computationally easy solution on shallow foundations under dynamic loading by avoiding complex, elasto-dynamic solutions. It is an approximate closed-form method to calculate the dynamic response of shallow foundations. This method was first used by Ehlers in 1942 for a swaying footing resting on an elastic halfspace. Since then, there are many solutions either regarding footings on an elastic halfspace or on soil layers ([108, 109, 157]). The solution of the problem of a swaying footing resting on a soil layer is following below. In a similar way the problem of a vertically loaded footings can be solved.

The studied case is illustrated in Figure B.1. A massless strip footing with width $2B$, resting on a soil stratum with height H, is subjected to the horizontal load P. The footing is perfectly rigid as well as the bedrock underlying the soil stratum. According to the cone theory, only a part of the soil layer shaped as a truncated cone is affected by the load P as it is shown at the Figure B.1. The top of the cone is at z_0 over the soil surface. The soil surrounding the cone is considered to have negligible influence and it is disregarded in the derivations below.

One strip of the soil cone at depth z with elementary thickness dz is taken into examination. With the assumption that soil could only be sheared, the aforementioned soil strip functions as a 'shear beam' with shear modulus soil's shear modulus G. Summing

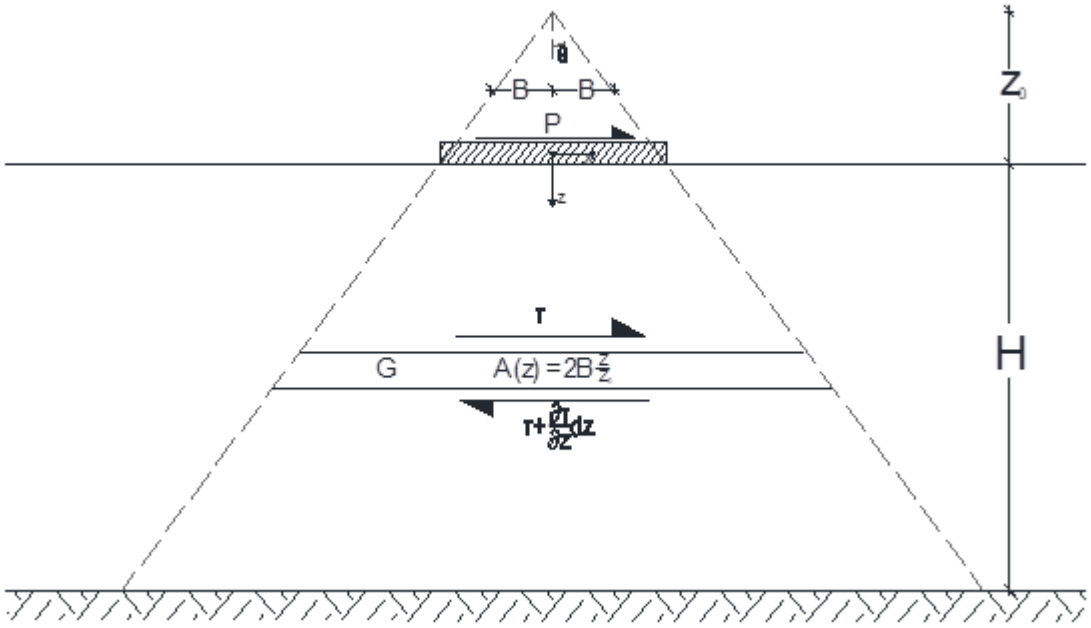

Figure B.1: Strip footing subjected to horizontal loading resting on homogeneous soil layer

up forces in the horizontal direction yields:

$$\tau A(z) - \left(\tau + \frac{\partial \tau}{\partial z} dz\right) A(z + dz) = 0 \tag{B.1}$$

Upon simplification one gets:

$$\tau + z \frac{\partial \tau}{\partial z} = 0 \tag{B.2}$$

Combining equation B.2 with the linear constitutive law:

$$\tau = G\gamma \tag{B.3}$$

and the field equation:

$$\gamma = -\frac{\partial u_x}{\partial z} \tag{B.4}$$

leads to the governing equation

$$\frac{d}{dz}\left(z \frac{\partial u_x}{\partial z}\right) = 0 \tag{B.5}$$

Upon twice integrating with respect to z yields:

$$u_x(z) = C_1 lnz + C_2 \tag{B.6}$$

Both coefficients C_1 and C_2 can be calculated using the boundary conditions

$$u_x(z_0 + H) = 0,\ \tau(z_0) = \frac{P}{2B} \tag{B.7}$$

which leads to

$$C_1 = -\frac{P}{G}\frac{z_0}{2B} \tag{B.8}$$

and

$$C_2 = \frac{P}{G}\frac{z_0}{2B} ln(z_0 + H) \tag{B.9}$$

So the horizontal displacement is

$$u_x(z) = \frac{P}{G}\frac{z_0}{2B} ln\left(\frac{z_0 + H}{z}\right) \tag{B.10}$$

Setting $z = z_0$, the horizontal movement of the footing is obtained as

$$u_x(z_0) = \frac{P}{G}\frac{z_0}{2B} ln\left(1 + \frac{H}{z_0}\right) \tag{B.11}$$

By definition

$$K \equiv \frac{P}{u_x(z_0)} = G\frac{2B}{z_0}\frac{1}{ln\left(1 + \frac{H}{B}\frac{B}{z_0}\right)} \tag{B.12}$$

Introducing 2θ as the opening angle of the cone

$$tan\theta = \frac{B}{z_0} \tag{B.13}$$

Yields the dimensionless expression

$$\frac{K}{G} = \frac{2tan\theta}{ln\left(1 + \frac{H}{B}tan\theta\right)} \tag{B.14}$$

Thus, footing stiffness is affected by cone geometry and normalised soil thickness. Another approximate formula fitted to FE results has been proposed by Gazetas [7] as follows

$$\frac{K}{G} = \frac{2}{2 - \nu}\left(1 + 2\frac{B}{H}\right) \tag{B.15}$$

Interestingly, the cone model predicts the anticipated value $K/G \to 0$ as $H/B \to \infty$, whereas the fitted formula does not. For Poisson's ration $\nu = 0.3$ to 0.4 and $H/B = 2$, one could match the cone solution with the one proposed by Gazetas [7] using $\theta \cong 60°$. Additional results are tabulated on Table B.1. Different opening angles are anticipated in other response modes as the associated expressions are different.

Table B.1: Opening angle of the cone to match Gazetas [7] approximate formula.

Poisson's ratio, ν	H/B	K/G	θ (in °)
0.3	1	3.53	61.5
	2	2.35	60.8
	4	1.76	62.2
	8	1.47	64.8
0.4	1	3.75	65.1
	2	2.50	63.7
	4	1.88	64.5
	8	1.56	66.7
0.5	1	4.00	68.3
	2	2.67	66.4
	4	2.00	66.8
	8	1.67	68.6

APPENDIX C

MODIFIED HYPERBOLIC MODEL: TAYLOR EXPANSION APPROACH

Appendix D presents the first, second and third order approximate solution of modified hyperbolic constitutive model based on Taylor expansion. Comparisons are made to assess the accuracy of the suggested solutions.

C.1 Introduction

According to the modified hyperbolic model, the modulus reduction curve is described by the expression

$$\frac{G}{G_{max}} = \frac{1}{1+\left(\frac{\gamma}{\gamma_r}\right)^{\alpha}} \tag{C.1}$$

G being the secant shear modulus used in the basic soil shear stress equation and α a free parameter controlling curvature. Note that in the conventional hyperbolic model, α is taken equal to 1.

$$\tau = G\gamma \tag{C.2}$$

Combining the above equations and normalising with respect to product $G_{max} \cdot \gamma_r$, one gets the dimensionless form

$$\frac{\tau}{G_{max}\gamma_r} + \frac{\tau}{G_{max}\gamma_r}\left(\frac{\gamma}{\gamma_r}\right)^{\alpha} - \frac{\gamma}{\gamma_r} = 0 \tag{C.3}$$

Defining

$$x = \frac{\tau}{G_{max}\gamma_r} \tag{C.4a}$$

$$y = \frac{\gamma}{\gamma_r} \tag{C.4b}$$

$$\alpha = 1 + \epsilon \tag{C.4c}$$

leads to the simpler equation

$$x + xy^{1+\epsilon} - y = 0 \tag{C.5}$$

ϵ being a (positive or negative) parameter of magnitude much less than 1 i.e. $|\epsilon| << 1$. It is an elementary matter to solve (C.5) in the form $x = f(y)$. The objective of this section is to solve the non-trivial inverse problem $y = g(x)$.

C.2 Investigation of non linear equation

The modified hyperbolic model is explored for all three different cases of α; less than, equal to, and greater than 1. All three cases are treated differently due to the non-linearity of the equation. A depiction of the equation is shown below through a normalised shear stress versus normalised shear strain plot

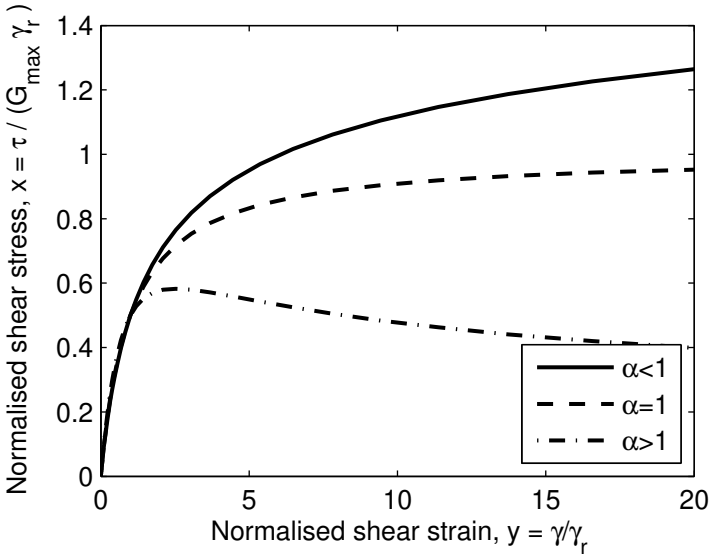

Figure C.1: Illustration of the effect of α on the shape of the normalised shear strain curves

Evidently for $\alpha < 1$ or $\epsilon < 0$, the maximum shear stress, τ_{max}, is approaching infinity, while for $\alpha > 1$ or $\epsilon > 0$, the shear stress goes to zero and for $\alpha = 1 (\epsilon = 0)$, the maximum shear stress reaches the constant product $G_{max} \cdot \gamma_r$ at infinite strain.

For $\alpha = 1$ or $\epsilon = 0$ there is an elementary analytical solution to (C.5)

$$y = \frac{x}{1-x} \tag{C.6}$$

For $\alpha \neq 1$ the equation can only be solved approximately except of the finite values of 1/4, 1/3, 1/2, 2/3, 3/2, 2, 3 and 4. Note that for $\alpha > 1$ a function in the form of $y = g(x)$ cannot be uniquely defined as there are two values of y for every value of the variable x. In addition, in the above case x is bounded and does not cover all the range of positive real numbers.

In all the above cases one can notice that:

Using the easy to derive $x = f(y)$ form:

$$x = \frac{y}{1+y^{1+\epsilon}} \tag{C.7}$$

It is simple matter to show -using asymptotic analysis- that for very large shear strains (y »1) the normalised shear strain is given by asymptotic formula a

$$x \rightarrow y^{-\epsilon} \; or \; y \sim x^{-\frac{1}{\epsilon}} \tag{C.8}$$

Likewise, for very small shear strains (y «1) the normalised shear strain can be obtained by what is referred as asymptotic formula b

$$x \rightarrow y \; or \; y \sim x \tag{C.9}$$

C.3 Taylor expansion approach

A Taylor series is the power series of an infinitely differentiated function f(x), like those studied in this section, about a point α given by

$$f(x) = f(a) + \frac{f'(a)}{1!}(x-a) + \frac{f''(a)}{2!}(x-a)^2 + \frac{f'''(a)}{3!}(x-a)^3 + \ldots + R_n \tag{C.10}$$

where R_n is the remainder term.

Depending on the term the user decides to stop the series hence the maximum power of variable x, Taylor series approximation can be first, second, third order, etc.

In this current work, the term $y^{1+\epsilon}$ in (C.5) can be expanded into Taylor series of first, second or third order to transform (C.5) into an algebraic equation.

C.3.1 Taylor approximation formulae

The first Taylor expansion approximation formula of the function $f(y) = y^{1+\epsilon}$ about an arbitrary point y_0 is

$$f(y) = {y_0}^{\epsilon+1} + {y_0}^{\epsilon}\,(\epsilon+1)\,(y-y_0) \tag{C.11}$$

Similarly, the second and the third Taylor expansion approximation formula of the function $f(y) = y^{1+\epsilon}$ about y_0 are

$$f(y) = {y_0}^{\epsilon+1} + {y_0}^{\epsilon}\,(\epsilon+1)\,(y-y_0) + \frac{\epsilon\,(\epsilon+1)\,{y_0}^{\epsilon-1}}{2}(y-y_0)^2 \tag{C.12}$$

and

$$f(y) = {y_0}^{\epsilon+1} + {y_0}^{\epsilon}\,(\epsilon+1)\,(y-y_0) + \frac{\epsilon\,(\epsilon+1)\,{y_0}^{\epsilon-1}}{2}(y-y_0)^2 + \frac{\epsilon\,(\epsilon+1)\,(\epsilon-1)\,{y_0}^{\epsilon-2}}{6}(y-y_0)^3 \tag{C.13}$$

By substituting the above expressions in (C.5) explicit solutions in the form $y = f(x)$ can be obtained. In the interest of space only the first two solutions are presented herein

$$y = -\frac{x - \epsilon\,x\,y_0\,{y_0}^{\epsilon}}{x\,{y_0}^{\epsilon} - 1 + \epsilon\,x\,{y_0}^{\epsilon}} \tag{C.14}$$

$$y = \frac{{y_0}^{1-\epsilon}\left(\sqrt{-\frac{2\epsilon^2x^2{y_0}^{\epsilon}-y_0-x^2y_0{y_0}^{2\epsilon}+2xy_0{y_0}^{\epsilon}+2\epsilon x^2{y_0}^{\epsilon}+\epsilon^2x^2y_0{y_0}^{2\epsilon}-2\epsilon^2xy_0{y_0}^{\epsilon}}{y_0}} - x\,{y_0}^{\epsilon} + \epsilon^2\,x\,{y_0}^{\epsilon} + 1\right)}{\epsilon\;x\;(\epsilon+1)} \tag{C.15a}$$

$$y = -\frac{y_0\left(x\,{y_0}^{\epsilon} + \sqrt{-\frac{2\epsilon^2x^2{y_0}^{\epsilon}-y_0-x^2y_0{y_0}^{2\epsilon}+2xy_0{y_0}^{\epsilon}+2\epsilon x^2{y_0}^{\epsilon}+\epsilon^2x^2y_0{y_0}^{2\epsilon}-2\epsilon^2xy_0{y_0}^{\epsilon}}{y_0}} - \epsilon^2\,x\,{y_0}^{\epsilon} - 1\right)}{\epsilon\,x\,{y_0}^{\epsilon} + \epsilon^2\,x\,{y_0}^{\epsilon}} \tag{C.15b}$$

The solution corresponding to (C.13) is presented in the Appendix. The expansion point y_0 is obtained from the solution of the reduced equation (C.6)

$$y_0 = \frac{x}{1-x} \tag{C.16}$$

It is clear from the above expression that using Taylor expansion approximate formulae results in one closed analytical solution. The normalized shear strain, y, is expressed as a function of the acting normalized shear stress, x, the regression parameters of the modified hyperbolic model; pseudo-reference shear strain γ_r and curvature coefficient ϵ and the point around which the Taylor expansion series is expanded, y_0.

C.4 Results

The results are presented as plots of normalized shear stress, x over the normalized shear strain, y.

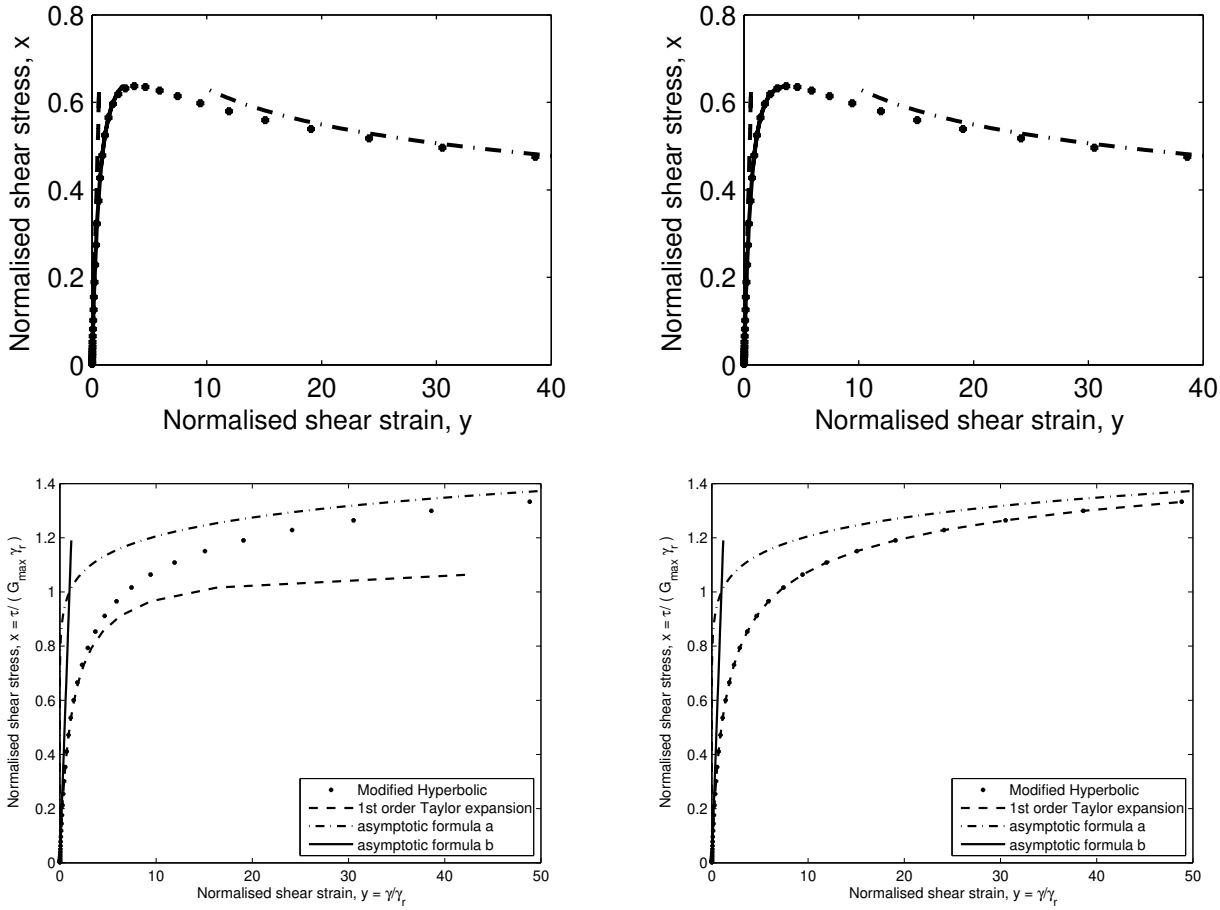

Figure C.2: First order Taylor expansion about $y_0 = \frac{x}{1-x}$ for $\alpha = 1.2$ (top), 0.919 (bottom). All for $\gamma_r = 5 \cdot 10^{-4}$. The left column shows the results for 1 iteration and the left for the optimum number of iterations (5-8).

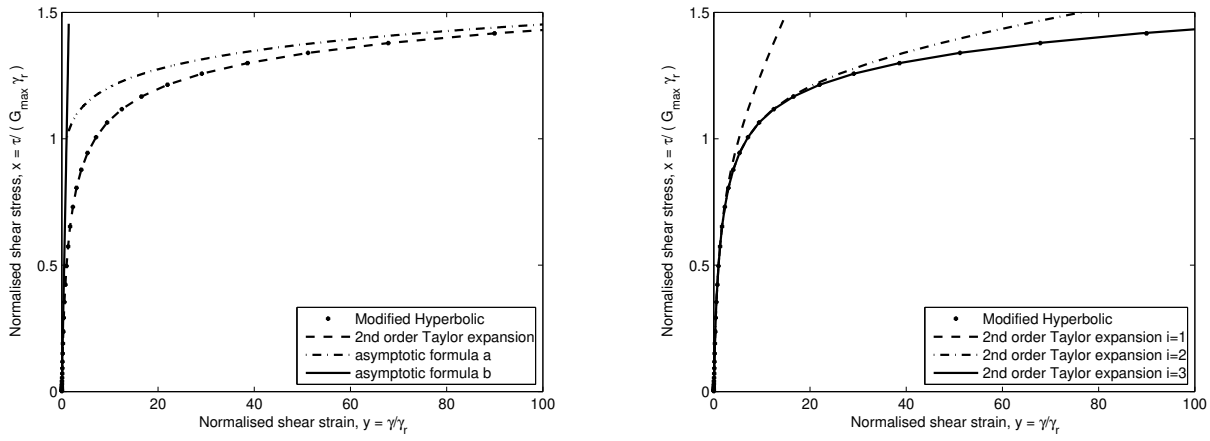

Figure C.3: Second order Taylor expansion about $y_0 = \frac{x}{1-x}$ for $\alpha = 0.919$. All for $\gamma_r = 5{\cdot}10^{-4}$. The Taylor expansion approach solution with the optimum number of iterations is shown on the left and the number of iterations effect on the left.

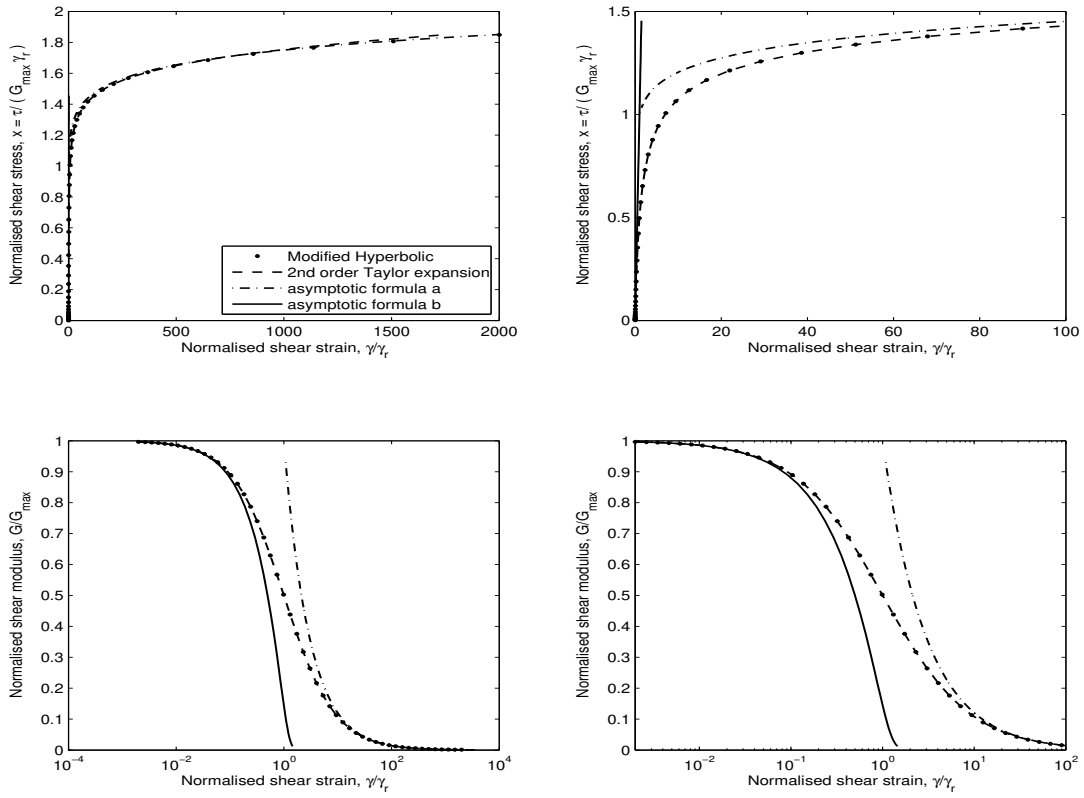

Figure C.4: Second order Taylor expansion about y_0 for $\alpha = 0.919$. Normalized shear stress versus normalized shear strain (top) and MR curves (bottom) for extended spectra (right) and for shear strain range 10^{-6} to 10^{-2} (left). All for $\gamma_r = 5 \cdot 10^{-4}$ and the optimum number of iterations (5).

C.5 Appendix

C.5.1 Perturbation Theory Approach

Perturbation theory has been used to solve the non-trivial equation (C.5) with regards to y. The results are unsatisfactory but they are presented in this appendix in favor of completeness.
Eq. (C.5), which is repeated below, is defined for $|\epsilon| \leq 1$

$$x + xy^{1+\epsilon} - y = 0 \tag{C.17}$$

For $\epsilon = 0$ one can get the elementary exact solution for y

$$y_0 = \frac{x}{1-x} \tag{C.18}$$

According to perturbation theory, one can get an approximate solution to a problem by starting from the exact solution of a simpler problem. Perturbation theory leads to an expression for the desired solution in terms of a power series which quantifies the deviation from the exactly solvable problem. In this current problem perturbation theory can be applied by replacing y with the expression

$$y = \epsilon^0 y_0 + \epsilon^1 y_1 + \epsilon^2 y_2 + \epsilon^3 y_3 + ... \tag{C.19}$$

while y_0 is the already known analytical solution expressed in eq. (C.18), the higher order terms y_1, y_2, y_3... can only be found iteratively. However, as ϵ is small, higher order terms become negligible and an approximate solution can be obtained by keeping only the first two terms. By replacing the shortened version of eq. (C.19) in eq. (C.5) one gets

$$x + (y_0 + \epsilon y_1)^{1+\epsilon} x - (y_0 + \epsilon y_1) = 0 \tag{C.20}$$

BIBLIOGRAPHY

[1] Pais, A. and Kausel, E. (1988) Approximate formulas for dynamic stiffnesses of rigid foundations. *Soil Dynamics and Earthquake Engineering,* **7**(4), 213–227.

[2] Gazetas, G. (1991) Foundation Vibrations. In Fang, H.-Y., (ed.), *Foundation Engineering Handbook*, chapter 15, pp. 890–902 Springer US Boston, MA 2nd edition.

[3] Mylonakis, G., Nikolaou, S., and Gazetas, G. (2006) Footings under seismic loading: Analysis and design issues with emphasis on bridge foundations. *Soil Dynamics and Earthquake Engineering,* **26**(9), 824–853.

[4] Darendeli, M. B. Development of a new family of normalized modulus reduction and material damping curves PhD thesis University of Texas Austin (2001).

[5] Papadimitriou, A. Elastoplastic modeling of monotonic and dynamic behavior of soils PhD thesis National Technical University of Athens (1999).

[6] Star, L. M. Seismic Vulnerability of Structures: Demand Characteristics and Field Testing to Evaluate Soil-Structure Interaction Effects PhD thesis University of California, Los Angeles (2011).

[7] Gazetas, G. (1991) Formulas and Charts for Impedances of Surface and Embedded Foundations. *Journal of Geotechnical Engineering,* **117**(9), 1363–1381.

[8] Vucetic, M. and Dobry, R. (1991) Effect of Soil Plasticity on Cyclic Response. *Journal of Geotechnical Engineering,* **117**(1), 89–107.

[9] Luco, J. E. and Westmann, R. a. (1972) Dynamic Response of a Rigid Footing Bonded to an Elastic Half Space. *Journal of Applied Mechanics,* **39**(2), 527.

[10] Ramberg, W. and Osgood, W. R. (1943) Description of stress-strain curves by three parameters. *National Advisory Committee For Aeronautics,* p. Technical Note No. 902.

[11] Givens, M. J. Dynamic Soil-Structure Interaction of Instrumented Buildings and Test Structures PhD thesis UCLA (2013).

[12] Barkan, D. D. (1948) Dynamics of Bases and Foundations [in Russian], Stroyvoenmorizdat, Moscow.

[13] Itasca Consulting Group Inc. (2011) FLAC — Fast Lagrangian Analysis of Continua in Two-Dimensions, Version 7, Itasca, Minneapolis, Minnesota, United States of America.

[14] Barkan, D. D. (1962) Dynamics of bases and foundations [Translated], McGraw-Hill Book Company, Inc., United States of America.

[15] Fry, Z. B., Development and evaluation of soil bearing capacity foundations. Technical report, U.S. Army Engineer Waterways Experiment Station Vicksburg, Mississippi (1963).

[16] Margason, B. E., McNeill, R. L., and Babcock, F. M., Case histories in foundation vibrations. Technical report, Vibration effects of earthquakes on soils and foundations ASTM International (1969).

[17] Thompson (Lord Kelvin), W. (1848) Note on the integration of the equations of equilibrium of an elastic solid. *Cambridge and Dublin Mathematical Journal,* **3**, 87–89.

[18] Boussinesq, J. V. (1878) Équilibre d'élasticité d'un sol isotrope sans pesanteur, supportant différents poids. *Comptes Rendus,Paris,Gauthier-Villars,* **LXXXVI**, 1260–1263.

[19] Boussinesq, J. V. (1878) Sur la dépression que produit, à la surface d'un sol horizontal élastique et isotrope, un poids qu'on dépose, et sur la répartition de ce poids entre ses divers point d'appui. *Comptes Rendus, Paris, Gauthier-Villars,* **LXXXVII**, 402–405.

[20] Boussinesq, J. V. (1878) Sur la manière dont se distribue entre ses points d'appui le poids d'un corps dur, posé sur un sol poli, horizontal et élastique: identité de ce mode de répartition, pour une base de sustentation plane et horizontale, avec celui d'une charge électrique en. *Comptes Rendus, Paris, Gauthier-Villars,* **LXXXVII**, 519–522.

[21] Cerruti, V. (1882) Ricerche intorno all'equilibrio de'corpi elastici isotropi: memoria. *Coi tipi del Salviucci,*.

[22] Flamant, A. (1892) Sur la répartition des pressions dans un solide rectangulaire chargé transversalement.. *CR Acad. Sci. Paris,* **114**, 1465–1468.

[23] Terazawa, K.-i. On the Elastic Equilibrium of a Semi-Infinite Solid Under Given Boundary Conditions, with Some Applications. (1916).

[24] Schleicher, F. (1926) Zur theorie des baugrundes. *Bauingenieur,* **48**, 931–935.

[25] Love, A. E. H. (1929) The Stress Produced in a Semi-Infinite Solid by Pressure on Part of the Boundary. *Philosophical Transactions of the Royal Society A: Mathematical, Physical and Engineering Sciences,* **228**(659-669), 377–420.

[26] Melan, E. (1932) Der Spannungszustand der durch eine Einzelkraft im Innern beanspruchten Halbscheibe. *ZAMM - Zeitschrift für Angewandte Mathematik und Mechanik,* **12**(6), 343–346.

[27] Mindlin, R. D. (1936) Force at a point in the interior of a semi-infinite solid. *Journal of Applied Physics,* **7**(5), 195–202.

[28] Boussinesq, J. V. (1885) Application des potentiels à l'étude de l'équilibre et du mouvement des solides élastiques: principalement au calcul des déformations et des pressions que produisent, dans ces solides, des efforts quelconques exercés sur une petite partie de leur surface . *Gauthier-Villars,* **4**.

[29] Borowicka, H. (1943) Uber ausmittig belastete, starre Platten auf elastisch-isotropem Untergrund. *Ingenieur-Archiv,* **14**(1), 1–8.

[30] Reissner, E. and Sagoci, H. F. (1944) Forced Torsional Oscillations of an Elastic Half-Space. I.. *Journal of Applied Physics,* **15**(9), 652–654.

[31] Mindlin, R. D. (1949) Compliance of Elastic Bodies in Contact. *Journal of Applied Mechanics, ASME,* **16**, 259–268.

[32] Muskhelishvili, N. I. (1953) Singular Integral Equations: Boundary Problems of Functions Theory and Their Application to Mathematical Physics, P. Noordhoff, Groningen.

[33] Muskhelishvili, N. I. (1963) Some basic problems of the mathematical theory of elasticity, P. Noordhoff, Translated from the Russian by Radok, J. R. M., Groningen, The Netherlands fourth edition.

[34] Steinbrenner, W. (1934) Tafeln zur Setzungsberechnung. *Die Strasse,* **1**, 121–124.

[35] Burmister, D. M. (2, 1945) The General Theory of Stresses and Displacements in Layered Systems. I. *Journal of Applied Physics,* **16**(2), 89–94.

[36] Kassir, M. K. and Chuaprasert, M. F. (1974) A Rigid Punch in Contact With a Nonhomogeneous Elastic Solid. *Journal of Applied Mechanics,* **41**(4), 1019.

[37] Booker, J. R., Balaam, N. P., and Davis, E. H. (7, 1985) The behaviour of an elastic non-homogeneous half-space. Part I-line and point loads. *International Journal for Numerical and Analytical Methods in Geomechanics,* **9**(4), 353–367.

[38] Booker, J. R., Balaam, N. P., and Davis, E. H. (7, 1985) The behaviour of an elastic non-homogeneous half-space. Part II-circular and strip footings. *International Journal for Numerical and Analytical Methods in Geomechanics,* **9**(4), 369–381.

[39] Cerruti, V. (1884) Sulla deformazione di uno strato isotropo indefinito limitato da due piani paralleli. *Atti Acad. Nazl. Lincei. Rend.,* **4.1**.

[40] Burmister, D. M., Palmer, L. A., Barber, E. S., and Middlebrooks, T. (1944) The theory of stress and displacements in layered systems and applications to the design of airport runways. In *Highway Research Board Proceedings (Vol. 23)*.

[41] Burmister, D. M. (1945) The general theory of stresses and displacements in layered soil systems. II. *Journal of Applied Physics,* **16**(3), 126–127.

[42] Burmister, D. M. (1945) The general theory of stresses and displacements in layered soil systems. III. *Journal of Applied Physics,* **16**(5), 296–302.

[43] Poulos, H. and Davis, E. (1974) Poulos and Davis Elastic solutions for soil and rock mechanics, Centre for Geotechical Research, University of Sydney.

[44] Eason, G., Noble, B., and Sneddon, I. N. (1955) On Certain Integrals of Lipschitz-Hankel Type Involving Products of Bessel Functions. *Philosophical Transactions of the Royal Society A: Mathematical, Physical and Engineering Sciences,* **247**(935), 529–551.

[45] Hanson, M. T. and Puja, I. W. (9, 1997) The evaluation of certain infinite integrals involving products of Bessel functions: a correlation of formula. *Quarterly of Applied Mathematics,* **55**(3), 505–524.

[46] Lambe, T. W. and Whitman, R. V. (1969) Soil Mechanics, Wiley India Pvt. Ltd., .

[47] Richart, F. E., Hall, J. R., and Woods, R. D. (1970) Vibrations of Soils and Foundations. *Prentice-Hall,* p. 437.

[48] Davis, R. O. and Selvadurai, A. P. S. (1996) Elasticity and Geomechanics, Cambridge University Press, .

[49] Kausel, E. (2010) Early history of soil-structure interaction. *Soil Dynamics and Earthquake Engineering,* **30**(9), 822–832.

[50] Stokes, G. (1849) On the dynamical theory of diffraction. *Cambridge Philosophical Society,* **9**, 1–62.

[51] Lamb, H. (1, 1904) On the Propagation of Tremors over the Surface of an Elastic Solid. *Philosophical Transactions of the Royal Society A: Mathematical, Physical and Engineering Sciences,* **203**(359-371), 1–42.

[52] Pekeris, C. L. (1955) The seismic surface pulse. *Proceedings of the National Academy of Sciences of the USA,* **41**, 469–480.

[53] Chao, C.-C. (1960) Dynamical Response of an Elastic Half-Space to Tangential Surface Loadings. *Journal of Applied Mechanics,* **27**(3), 559.

[54] Mooney, H. M. (1974) Some numerical solutions for Lamb's problem. *Bulletin of the Seismological Society of America,* **64**(2), 473–491.

[55] Richards, P. G. (10, 1979) Elementary solutions to Lamb's problem for a point source and their relevance to three-dimensional studies of spontaneous crack propagation. *Bulletin of the Seismological Society of America,* **69**(4), 947–956.

[56] Kausel, E. (11, 2012) Lamb's problem at its simplest. *Proceedings of the Royal Society A: Mathematical, Physical and Engineering Sciences,* **469**(20120462).

[57] Reissner, E. (1936) Stationare, axialsymmetrische, durch eine schut-telnde Masse erregte Schwingungen eines homogenen elastischen Halbraumes. *Ingenieur-Archiv,* **7**(6), 381–396.

[58] Quinlan, P. M. (1953) The Elastic Theory of Soil Dynamics. *Symposium on Dynamic Testing of Soils,* **156**(1953), 3–34.

[59] Sung, T. (1953) Vibrations in semi-infinite solids due to periodic surface loadings. *Symposium on Dynamic Testing of Soils,* **156**, 35–64.

[60] Hsieh, T. K. (1962) Foundation Vibrations. *Proceedings of the Institution of Civil Engineers,* **22**, 211–226.

[61] Lysmer, J. Vertical Motion of Rigid Footings PhD thesis University of Michigan (1968).

[62] Reissner, E. (1937) Freie und erzwungene Torsionsschwingungen des elastischen Halbraumes. *Ingenieur-Archiv,* **8**(4), 229–245.

[63] Bycroft, G. N. (1956) Forced vibrations of a rigid circular plate on a semi-infinite elastic space and on an elastic stratum. *Philosophical Transactions of the Royal Society A: Mathematical, Physical and Engineering Sciences,* **248**(948), 327–368.

[64] Richart, F. E. (1962) Foundation Vibrations. *Transactions of the American Society of Civil Engineers,* **127**(1), 863–897.

[65] Gazetas, G. (1983) Analysis of machine foundation vibrations: State of the art. *Soil Dynamics and Earthquake Engineering,* **2**(1), 1–42.

[66] Hsieh, T. K. and Richart, F. E. (1962) Discussion on Foundation Vibrations. *Proceedings of the Institution of Civil Engineers,* **22**, 211–226.

[67] NIST (2012) Soil-structure interaction for building structures, NIST GCR 12-917-21, .

[68] Novak, M. (1970) Prediction of footing vibrations. *Journal of the Soil Mechanics and Foundations,* **96**(3), 837–861.

[69] Novak, M. and Beredugo, Y. O. (1971) The effect of embedment on footing vibrations. In *Proceedings of the First Canadian Conference on Earthquake Engineering Research* Vancouver: .

[70] Beredugo, Y. O. and Novak, M. (1972) Coupled Horizontal and Rocking Vibration of Embedded Footings. *Canadian Geotechnical Journal,* **9**(4), 477–497.

[71] Novak, M. (1985) Experiments with shallow and deep foundations. *Vibration problems in geotechnical engineering, ASCE,* pp. 1–26.

[72] Lin, B. A. N., Asce, A. M., Jennings, P. C., and Asce, M. (1984) Effect of embedment on foundation-soil impedances. *Journal of Engineering Mechanics,* **110**(7), 1060–1075.

[73] Luco, J. E., Trifunac, M. D., and Wong, H. L. (1988) Isolation of soil-structure interaction effects by full-scale forced vibration tests. *Earthquake Engineering & Structural Dynamics,* **16**(1), 1–21.

[74] Crouse, C. B., Hushmand, B., Luco, J. E., and Wong, H. L. (3, 1990) Foundation Impedance Functions: Theory Versus Experiment. *Journal of Geotechnical Engineering,* **116**(3), 432–449.

[75] de Barros, F. C. and Enrique Luco, J. (1995) Identification of foundation impedance functions and soil properties from vibration tests of the Hualien containment model. *Soil Dynamics and Earthquake Engineering,* **14**(4), 229–248.

[76] Tileylioglu, S., Stewart, J. P., and Nigbor, R. L. (2011) Dynamic Stiffness and Damping of a Shallow Foundation from Forced Vibration of a Field Test Structure. *Journal of Geotechnical and Geoenvironmental Engineering,* **137**(4), 344–353.

[77] Star, L. M., Givens, M. J., Nigbor, R. L., and Stewart, J. P. (11, 2015) Field-Testing of Structure on Shallow Foundation to Evaluate Soil-Structure Interaction Effects. *Earthquake Spectra,* **31**(4), 2511–2534.

[78] Erden, S. M. Influence of shape and embedment on dynamic foundation response PhD thesis University of Massachusetts (1974).

[79] Stokoe, K. H. and Erden, S. M., Influence of base shape on dynamic response of surface foundations. Technical report, Geotechnical Engineering report GP85-1 Univ of Texas at Austin (1985).

[80] Dobry, R. and Gazetas, G. (2, 1986) Dynamic Response of Arbitrarily Shaped Foundations. *Journal of Geotechnical Engineering,* **112**(2), 109–135.

[81] Gadre, A. and Dobry, R. (1998) Lateral Cyclic Loading Centrifuge Tests on Square Embedded Footing. *Journal of Geotechnical and Geoenvironmental Engineering,* **124**(11), 1128–1138.

[82] Maugeri, M., Musumeci, G., Novità, D., and Taylor, C. A. (2000) Shaking table test of failure of shallow foundation subjected to an eccentric load. *Soil Dynamics and Earthquake Engineering,* **20**(5-8), 435–444.

[83] Ghosh, B. and Madabhushi, S. P. G. (2007) Centrifuge modelling of seismic soil structure interaction effects. *Nuclear Engineering and Design,* **237**(8), 887–896.

[84] Gajan, S. and Kutter, B. L. (8, 2008) Capacity, Settlement, and Energy Dissipation of Shallow Footings Subjected to Rocking. *Journal of Geotechnical and Geoenvironmental Engineering,* **134**(8), 1129–1141.

[85] Dobry, R., Gazetas, G., and Stokoe, K. H. (2, 1986) Dynamic Response of Arbitrarily Shaped Foundations: Experimental Verification. *Journal of Geotechnical Engineering,* **112**(2), 136–154.

[86] Gazetas, G. and Stokoe, K. H. (1991) Free Vibration of Embedded Foundations: Theory versus Experiment. *Journal of geotechnical engineering,* **117**(9), 1382–1401.

[87] Luco, J. E. and Wong, H. L. (11, 1986) Response of Hemispherical Foundation Embedded in Half-Space. *Journal of Engineering Mechanics,* **112**(12), 1363–1374.

[88] Wong, H. L., Trifunac, M. D., and Luco, J. E. (1988) A comparison of soil-structure interaction calculations with results of full-scale forced vibration tests. *Soil Dynamics and Earthquake Engineering,* **7**(1), 22–31.

[89] Crouse, C. B., Liang, G. C., and Martin, G. R. (1984) Experimental Study of Soil-Structure Interaction at an Accelerograph Station. *Bulletin of the Seismological Society of America,* **74**(5), 1995–2013.

[90] Crouse, C. B., Liang, G. C., and Martin, G. R. (6, 1985) Experimental Foundation Impedance Functions. *Journal of Geotechnical Engineering,* **111**(6), 819–822.

[91] Crouse, C. B. and Hushmand, B. (1989) Soil - structure interaction at CDMG and USGS accelerograph stations. *Bulletin of the Seismological Society of America,* **79**(1), 1–14.

[92] Massimino, M. R. and Maugeri, M. (2013) Physical modelling of shaking table tests on dynamic soil-foundation interaction and numerical and analytical simulation. *Soil Dynamics and Earthquake Engineering,* **49**, 1–18.

[93] Paolucci, R., Shirato, M., and Yilmaz, M. T. (4, 2008) Seismic behaviour of shallow foundations: Shaking table experimentsvs numerical modelling. *Earthquake Engineering & Structural Dynamics,* **37**(4), 577–595.

[94] Star, L. M., Tileylioglu, S., Givens, M. J., Mylonakis, G., and Stewart, J. P. (2017) Evaluation of Soil-Structure Interaction Effects from System Identification of Structures Subject to Forced Vibration Tests. *Earthquake Engineering and Structural Dynamics,*.

[95] Luco, J. E. and Westman, R. A. (1971) Dynamic Response of Circular Footings. *Journal of the Engineering Mechanics Division,* **97**(5), 1381–1395.

[96] Gazetas, G. (1981) Strip foundations on a cross-anisotropic soil layer subjected to dynamic loading. *Géotechnique,* **31**(2), 161–179.

[97] Wong, H. L. and Luco, J. E. (1976) Dynamic response of rigid foundations of arbitrary shape. *Earthquake Engineering & Structural Dynamics,*.

[98] Jakub, M. and Roesset, J. M., Nonlinear Stiffness of foundations. Technical report, MIT (1977).

[99] Wolf, J. P. and Obernhuber, P. (1985) Non-linear soil-structure analysis using dynamic stiffness or flexibility of soil in the time domain. *Earthquake Engineering & Structural Dynamics,* **13**, 195–212.

[100] Wolf, J. P. (1989) Soil-structure-interaction analysis in time domain. *Nuclear Engineering and Design,* **111**(3), 381–393.

[101] Wolf, J. P. and Meek, J. W. (8, 1993) Cone models for a soil layer on flexible rock half-space. *Earthquake Engineering & Structural Dynamics,* **23**(8), 909–925.

[102] Schnabel, P., Lysmer, J., and Seed, H. (1972) SHAKE a computer program for earthquake response analysis of holizontally layered sites. *ERRC,*.

[103] Kanai, K. (1951) Relation Between the Nature of Surface Layer and the Amplitude of Earthquake Motions. *Bulletin Tokyo Earthquake Research Institute,*.

[104] Roesset, J. M. and Whitman, R. V., Theoretical Background for Amplification Studies. Technical report, Massachusetts Institute of Technology Cambridge (1969).

[105] Tsai, N. C. (1970) A Note on the Steady-State Response of an Elastic Half-Space. *Bulletin of the Seismological Society of America,* **60**(3), 795–808.

[106] Gerolymos, N. and Gazetas, G. Constitutive Model for 1-D Cyclic Soil Behaviour Applied To Seismic Analysis of Layered Deposits. (2005).

[107] Novak, M., Aboul-Ella, F., and Nogami, T. (1978) Dynamic soil reactions for plane strain case. *Journal of the Engineering Mechanics Division,* **104**(4), 953–959.

[108] Meek, J. W. and Wolf, J. P. (5, 1992) Cone Models for Homogeneous Soil. I. *Journal of Geotechnical Engineering,* **118**(5), 667–685.

[109] Meek, J. W. and Wolf, J. P. (5, 1992) Cone Models for Soil Layer on Rigid Rock. II. *Journal of Geotechnical Engineering,* **118**(5), 686–703.

[110] Anastasopoulos, I., Gelagoti, F., Kourkoulis, R., and Gazetas, G. (2011) Simplified Constitutive Model for Simulation of Cyclic Response of Shallow Foundations: Validation against Laboratory Tests. *Journal of Geotechnical and Geoenvironmental Engineering,* **137**(12), 1154–1168.

[111] Frederick, C. and Armstrong, P. (2007) A mathematical representation of the multiaxial Bauschinger effect. *Materials at High Temperatures,* **24**(1), 1–26.

[112] Ishibashi, I. and Zhang, X. (1993) Unified dynamic shear moduli and damping ratios of sand and clay. *Japanese Society of Soil Mechanics and Foundation Engineering,* **33**(1), 182–191.

[113] Jakub, M. and Roesset, J. M., Dynamic stiffness of foundations: 2-D vs 3-D solutions. Technical Report MIT-CE R77-36, Massachusettes Institure of Technology (MIT) Massachusettes (1977).

[114] Borja, R. I. and Wu, W.-H. (9, 1994) Vibration of Foundations on Incompressible Soils with No Elastic Region. *Journal of Geotechnical Engineering,* **120**(9), 1570–1592.

[115] Borja, R. I., Wu, W.-H., and Smith, A. H. (1993) Nonlinear response of vertically oscillating foundations. *Journal of Geotechnical Engineering,* **119**(5), 893–911.

[116] Borja, R. I., Wu, W.-H., Amies, A. P., and Smith, H. A. (3, 1994) Nonlinear Lateral, Rocking, and Torsional Vibration of Rigid Foundations. *Journal of Geotechnical Engineering,* **120**(3), 491–513.

[117] Stewart, J. P., Kwok, A. O.-L., Hashash, Y. M. a., Matasovic, N., Pyke, R., Wang, Z., and Zhaouhi, Y., Benchmarking of Nonlinear Geotechnical Ground Response Analysis Procedures. Technical report, Pacific Earthquake Engineering Research Center Univ. of California, Berkeley (2008).

[118] Phillips, C. and Hashash, Y. M. a. (2008) A Simplified Constitutive Model to Simultaneously Match Modulus Reduction and Damping Soil Curves for Nonlinear Site Response Analysis. *Geotechnical Earthquake Engineering and Soil Dynamics IV,*.

[119] Phillips, C. and Hashash, Y. M. (2009) Damping formulation for nonlinear 1D site response analyses. *Soil Dynamics and Earthquake Engineering,*.

[120] Groholski, D. R., Hashash, Y. M. A., Kim, B., Musgrove, M., Harmon, J., and Stewart, J. P. (9, 2016) Simplified Model for Small-Strain Nonlinearity and Strength in 1D Seismic Site Response Analysis. *Journal of Geotechnical and Geoenvironmental Engineering,* **142**(9), 04016042.

[121] Gazetas, G., Anastasopoulos, I., Adamidis, O., and Kontoroupi, T. (2013) Nonlinear rocking stiffness of foundations. *Soil Dynamics and Earthquake Engineering,* **47**, 83–91.

[122] Adebar, P. (11, 2015) Nonlinear Rotation of Capacity-Protected Foundations: The 2015 Canadian Building Code. *Earthquake Spectra,* **31**(4), 1885–1907.

[123] Ishihara, K. (1996) Soil behavior in earthquake geotechnics, Clarendon Press, .

[124] Kramer, S. L. (1996) Geotechnical Earthquake Engineering, Vol. 6, Prentice-Hall, .

[125] Masing, G. (1926) Eigenspannungen und verfestigung beim messing. In *Proceedings, second international congress of applied mechanics* Zurich: .

[126] Pyke, R. (1979) Nonlinear soil models for irregular cyclic loadings. *Journal of the Geotechnical Engineering Division ASCE,* **105**(GT6), 715–726.

[127] Wang, Z., Han, Q. Y., and Zhou, G. S. (1980) Wave propagation method of site seismic response by visco-elastoplastic model. In *Proc., Seventh World Conf. on Earthquake Engineering. Vol. 2.* pp. 379–386.

[128] Vucetic, M. (1990) Normalized behavior of clay under irregular cyclic loading. *Canadian Geotechnical Journal,* **27**(1), 29–46.

[129] Mostaghel, N. and Byrd, R. A. (2002) Inversion of Ramberg-Osgood equation and description of hysteresis loops. *International Journal of Non-Linear Mechanics,* **37**(8), 1319–1335.

[130] Vucetic, M. and Dobry, R. (2, 1988) Degradation of Marine Clays under Cyclic Loading. *Journal of Geotechnical Engineering,* **114**(2), 133–149.

[131] Karamitros, D. K., Bouckovalas, G. D., Chaloulos, Y. K., and Andrianopoulos, K. I. (2013) Numerical analysis of liquefaction-induced bearing capacity degradation of shallow foundations on a two-layered soil profile. *Soil Dynamics and Earthquake Engineering,* **44**, 90–101.

[132] Durante, M. G., Karamitros, D., Di Sarno, L., Sica, S., Taylor, C. A., Mylonakis, G., and Simonelli, A. L. (8, 2015) Characterisation of shear wave velocity profiles of non-uniform bi-layer soil deposits: Analytical evaluation and experimental validation. *Soil Dynamics and Earthquake Engineering,* **75**, 44–54.

[133] Kondner, R. L. (1963) Hyperbolic stress-strain response: cohesive soils. *Journal of the Soil Mechanics and Foundations Division,* **89**(1), 115–144.

[134] Duncan, J. M. and Chang, C.-Y. (1970) Nonlinear analysis of stress and strain in soils. *Journal of the Soil Mechanics and Foundations Division,* **96**(5), 1629–1653.

[135] Hardin, B. O. and Drnevich, V. P. (1972) Shear Modulus and Damping in Soils: Design Equations and Curves. *Soil Mechanics and Foundations Division,* **SM7**, 667–692.

[136] Menq, F.-Y. Dynamic Properties of Sandy and Gravelly Soils PhD thesis The University of Texas at Austin (2003).

[137] Seed, B. H. B. and Idriss, I. M., Soil Moduli and Damping Factors for Dynamic Response Analyses. Technical Report EERC 70-10, California University, Berkeley (1970).

[138] Iwasaki, T., Tatsuoka, F., and Takagi, Y. (1978) Shear moduli of sand under cyclic torsional shear loading. *Soils and Foundations,* **18**(1), 39–56.

[139] Vardanega, P. J. and Bolton, M. D. (9, 2013) Stiffness of Clays and Silts: Normalizing Shear Modulus and Shear Strain. *Journal of Geotechnical and Geoenvironmental Engineering,* **139**(9), 1575–1589.

[140] Stewart, J. P., Afshari, K., and Hashash, Y. M. A., Guidelines for Performing Hazard-Consistent One-Dimensional Ground Response Analysis for Ground Motion Prediction. Technical Report October, Pacific Earthquake Engineering Research Center (2014).

[141] Lo Presti, D. C. F., Jamiolkowski, M., Pallara, O., Cavallaro, A., and Pedroni, S. (1997) Shear modulus and damping of soils. *Géotechnique,* **47**(3), 603–617.

[142] D'Onofrio, A., Silvestri, F., and Vinale, F. (1999) Strain rate dependent behaviour of natural stiff clay. *Soils and Foundations,* **39**(2), 69–82.

[143] Itasca Consulting Group Inc. (2017) FLAC3D — Fast Lagrangian Analysis of Continua in Three-Dimensions, Version 6, Itasca, Minneapolis, Minnesota, United States of America.

[144] Wilkins, M. L. (1964) Fundamental methods in hydrodynamics. In *Methods in Computational Physics* chapter Vol.3, pp. 211–263 Academic Press New York.

[145] Lysmer, J. and Kuhlemeyer, R. L. (1969) Finite-dynamic model for infinite media. *Journal of the Engineering Mechanics Division,* pp. 859–877.

[146] Rayleigh, J. and Lindsay, R. (1945) The theory of sound, Dover Publications, New York.

[147] Plaxis (2018) PLAXIS Material Models Manual 2018, PLAXIS, Netherlands.

[148] Karatzia, X. personal communication. (2018).

[149] Heidarzadeh, B. Dynamic Stresses in Foundation Soils from Soil-Structure Interaction PhD thesis University of California, Los Angeles (UCLA) (2016).

[150] Karatzia, X. Theoretical investigation of geotechnical seismic isolation of bridge piers on footings and piles PhD thesis University of Patras (2016).

[151] Anoyatis, G., Mylonakis, G., and Lemnitzer, A. (2016) Soil reaction to lateral harmonic pile motion. *Soil Dynamics and Earthquake Engineering,* **87**, 164–179.

[152] Dobry, R. and Gazetas, G. (1988) Simple method for dynamic stiffness and damping of floating pile groups. *Géotechnique,*.

[153] Zhang, J., Andrus, R. D., and Juang, C. H. (2005) Normalized Shear Modulus and Material Damping Ratio Relationships. *Journal of Geotechnical and Geoenvironmental Engineering,*.

[154] Katsiveli, E., Karamitros, D., Vardanega, P. J., and Mylonakis, G. (2018) Strain and strain rate effects on the rocking response of footing subjected to machine vibrations. In *Proceedings of the 16th European Conference on Earthquake Engineering* Thessaloniki: European Association for Earthquake Engineering (EAEE) p. 10760.

[155] Givens, M. J., Star, L. M., and Stewart, J. P. Mitigation of Collapse Risk in Vulnerable Concrete Buildings. (2012).

[156] Youd, T. L., Bartholomew, H. A. J., Proctor, J. S., and Steidl, J. H., Geotechnical Logs and Data from Permanently Instrumented Sites: Garner Valley Downhole Array (GVDA) and Wildlife Liquefaction Array (WLA). Technical report, The Network for Earthquake Engineering Simulation (NEES) (2004).

[157] Veletsos, A. S. and Meek, J. W. (1974) Dynamic behaviour of building-foundation systems. *Earthquake Engineering & Structural Dynamics,*.